Mixing of Transverse Jets in Open Channel Bends

Helene Katherine Schreiner

Thesis submitted to the University of Ottawa
in partial fulfillment of the requirements for the
Doctorate in Philosophy Environmental Engineering

Department of Civil Engineering
Faculty of Engineering
University of Ottawa

Acknowledgements

First and foremost, I would like to thank my supervisors, Dr. Colin Rennie and Dr. Majid Mohammadian. Their support and guidance was invaluable not only for their expertise but also for encouraging me to take on work that I would not have considered possible, and advising me when I took on too much at a time.

I would like to acknowledge all the technical staff at the University of Ottawa, especially Mark Lapointe, as well as the technicians at LaVision. I would also like to acknowledge all my fellow students who worked with me in the lab, and the co-op students and interns who assisted with lab work.

I would like to acknowledge the Natural Sciences and Engineering Research Council, the Ontario Graduate Scholarship program, and the University of Ottawa for providing funding.

I would like to thank my parents, Heather and John, and my sisters, Bethie and Chrissy, for their encouragement, their enthusiasm about my research, and their willingness to be a test audience for my presentations.

I would like to thank my housemates, Robin, Kyle, and Jaime Lawrence, for listening when I needed a sounding board, sustaining me through the difficult times, and encouraging me at the best times. I would also like to thank rest of the Lawrence family for their support, especially Kathryn for her proofreading.

I would like to extend thanks to many people in my wider community without whom I could not have completed this thesis: the St. Joseph's choir, for their encouragement and for their collective effort not to ask questions about my thesis at stressful times; the Grovites; my neighbours; and my friends from Henderson and Frontenac.

Finally, I would like to thank Amy Hanes, who was probably the first person I ever spoke to about grad school, long before I started this thesis. The joy she found in learning was infectious, and I wish I could have shared this thesis with her. May her memory live on through those she touched.

Abstract

Water quality in river systems is an important issue, and relies on various factors including our ability to predict how effluents from outfalls mix with river water. However, predicting mixing in rivers, and especially in river bends, remains a difficult problem to solve. The goal of this project is to develop a comprehensive picture of the mixing mechanisms of an effluent jet in a river bend. This is done with experiments in both bend flumes in the University of Ottawa Water Resources Engineering Laboratory. The large bend flume is 1 m in width, and contains a single 135° bend of radius 1.5 m, and the small flume has a channel width of 0.2 m with a 135° bend of radius 0.3 m. The experiments in the large flume used acoustic Doppler velocimeters to measure velocity, and the experiments in the small flume used particle image velocimetry to track flow fields. Large eddy simulation (LES) were also completed using the same channel geometry as the small flume.

To complete the parametric analysis on mixing of a neutrally buoyant effluent jet in a channel bend, 35 flow conditions, from seven channel aspect ratios and five momentum ratios, are modelled using LES. Each flow condition is also modelled without the jet present. Particle image velocimetry data from the small bend flume validates the LES models. Additionally, acoustic Doppler velocimeter tests were completed in the large bend flume under two different flume flow rates, two jet flow rates, and two aspect ratios. These models and measurements provide a broad range of the parameters under investigation.

The experiments in the large bend flume establish the shape of the jet's trajectory within the channel bend, and how it differs from a trajectory in a straight crossflow. From these experiments, it is established that the centre position of the secondary circulation cell is an important parameter for determining the position of the jet.

Through the LES models, more details of the 3D velocity and effluent distributions are available, allowing for a detailed analysis of how the secondary circulation develops and how the jet vortices change the development patterns. A method for clustering instantaneous vortices to separate sub-cells of secondary circulation is established, and is used to set a baseline for the development of secondary flow in a channel bend without a jet.

The effect of an added jet was investigated in detail for a single flow condition, and then with machine learning techniques to develop a parametrical model incorporating both channel and jet flow conditions. The best performing machine learning model for the parametrisation of secondary flow cells with the jet is the ANFIS model coupled with a decision tree classifying the presence of each sub-cell; without the jet, the best-performing model is the ANFIS model without any additional classification. The effluent distribution is well-characterised using multiple linear regression. The addition of a jet changes the relative strengths of secondary circulation sub-cells and their circulation development and retention characteristics, though the total circulation in the bend is not strongly affected by the jet.

Contents

List of Figures

List of Tables

Glossary

ADV acoustic Doppler velocimeter

ANFIS adaptive neuro-fuzzy inference system

ANN artificial neural network

CC centre cell

CVP counter-rotating vortex pair

DBSCAN density-based spatial clustering of applications with noise

DMD dynamic mode decomposition

IBC inner bank cell

LES large eddy simulation

LIF laser-induced fluorescence

MLP multi-later perceptron

MLR multiple linear regression

NRMSE normalised root mean squared error

OBC outer bank cell

PIV particle image velocimetry

POD proper orthogonal decomposition

RANS Reynolds averaged Navier Stokes

RMSE root mean squared error

SGS subgrid scale

surface LIC surface line integral convolution

TPD transition point distance

VOF volume of fluids

Symbols

$\langle\cdot\rangle$	depth average	
$\hat{\cdot}$	spatial filter	
$\bar{\cdot}$	time average	
$\cdot'$	difference between instantaneous and average	
$\cdot_{cf}$	bulk property of crossflow	
$\cdot_{jet}$	property of jet at outlet	
B	channel width	m
C	concentration	m^{-}3
cc	normalized position of centre of circulation cell	Dimensionless
c_{ϵ}	coefficient in dynamic k equation model	Dimensionless
c_{ν}	coefficient in dynamic k equation model	Dimensionless
Cr	curvature ratio	Dimensionless
d	jet dimension	mm
De	Dean number	Dimensionless
Δ	LES filter width	Length units
δ_{ij}	Kronecker delta	Dimensionless
D_{ij}	components of diffusion tensor	m^2/s
D_n	transverse diffusion coefficient	m^2/s
D_s	longitudinal diffusion coefficient	m^2/s
D_z	vertical diffusion coefficient	m^2/s

ϵ	rate of turbulence dissipation	$\mathrm{m}^2/\mathrm{s}^3$
ε	clustering parameter defining radius of neighbourhood	Dimensionless
Fr	Froude number	Dimensionless
g	gravitational acceleration	m/s^2
Γ_1	parameter for defining vortex centres	Dimensionless
Γ_2	parameter for defining vortex area	Dimensionless
$\vec{g}$	gravitational acceleration vector	m/s^2
h	water depth	cm
J_{jet}	jet buoyancy flux	$\mathrm{m}^4/\mathrm{s}^3$
k	turbulent kinetic energy	J/kg
κ	von Karman constant	Dimensionless
$k_{resolved}$	directly resolved portion of turbulent kinetic energy	J/kg
k_s	height of roughness element	mm
k_{SGS}	subgrid scale turbulent kinetic energy	J/kg
l	mixing length	m
λ_2	criterion for the detection of vortex cores	Dimensionless
l_m	characteristic length of jet mixing	m
M_{jet}	jet momentum flux	$\mathrm{m}^4/\mathrm{s}^2$
M_{pt}	clustering parameter defining minimum points in neighbourhood	Dimensionless
m_r	jet-to-crossflow momentum ratio	Dimensionless
N	number samples in a series	Dimensionless
n	cross-stream coordinate	m
n_{cc}	cross stream position of centre of secondary circulation	Dimensionless
ν	kinematic viscosity	m^2/s
ν_T	eddy viscosity	m^2/s
$\mathbf{\Omega}$	antisymmetric component of velocity gradient tensor	s^-1

ω	vorticity	s^{-1}
p	pressure	Pa
Π	wake function parameter	m/s
Q	flow rate	m^3/s or mL/s
Q-criterion	criterion for identifying vortex cores	s^{-2}
R	channel radius of curvature	m
r	jet-to-crossflow velocity ratio	Dimensionless
Re	Reynolds number	Dimensionless
ρ	density of fluid	kg/m^3
R^2	fit parameter for regression models	Dimensionless
$\boldsymbol{S}$	symmetric component of velocity gradient tensor	s^{-}1
s	streamwise coordinate	m
S_n	sinuosity	Dimensionless
T	temperature	°C
t	time	s
τ_0	bed shear stress	Pa
τ_{ij}	subgrid scale stresses	Pa
θ	opposite wall contact angle	°
TPD	transition point distance, defining cross-stream position of jet trajectory	cm
U	bulk velocity	m/s
$\vec{u}$	velocity vector	m/s
u_*	shear velocity	m/s
$\tilde{u}$	convection velocity	m/s
W	wake function	m/s
z	vertical coordinate	m

Chapter 1

Introduction

River systems are used as drinking water sources and for recreation, and protecting them from pollution is important for public health and environmental preservation. Water systems are also used in the disposal of treated wastewater and industrial effluent. If the effluents are not managed correctly, there can be many consequences for water systems, including toxic algae blooms and harmful effects on fish. As the human population grows and becomes more concentrated in urban centres, and the need for industry and wastewater treatment facilities grows correspondingly, it is increasingly important to build outfalls sustainably in order to protect water systems and public health (Grace, 2009). This includes a responsibility to ensure that effluent is quickly diluted once it enters the receiving body of water.

The importance of effluent dilution in river systems is often emphasized in the laws and regulations governing effluent disposal in rivers and streams. Some jurisdictions, for example British Columbia, use initial dilution zones as a basis for regulating the speed at which an effluent must disperse into rivers or streams (e.g., BC Reg 87/2012). Even in the absence of any concentration requirements, jets entering rivers with their own momentum and associated vortices have the potential to disrupt flow and thus affect erosion and other river processes, whether intentionally (Tamoradi et al., 2019) or not.

There are several mixing mechanisms at work in river bends, including molecular and turbulent diffusion and advection from secondary circulation, so understanding the hydrodynamics of river bends is an important starting point for the study of mixing in river bends. Water flows through river bends in a helical pattern, with the water at the surface moving toward the outer bank and the water at the bed toward the inner bank, in a pattern called the secondary circulation (Blanckaert and Graf, 2001). This structure has been well studied, especially its effect on the momentum distribution and the geometry of the bend (Blanckaert and Graf, 2004; Constantinescu et al., 2013a; de Vriend and Geldof, 1983; Ottevanger et al., 2012; van Balen et al., 2010; Wei et al., 2016). In high curvature bends, it is possible to have more complex patterns of circulation cells (Kashyap et al., 2012).

Mixing in rivers also depends largely on the parameters of the effluent jet discharged to the river. The trajectory of jets in crossflows has been widely studied (Pratte and Baines, 1967; Smith and Mungal, 1998; Yuan and Street, 1998), though never in channel bends until the start of this project. With the advent of more precise measurement methods, studies on jets in crossflows have focused largely on identifying turbulent structures of the jet as it mixes with the ambient flow (Chang and Cowen, 2002; Iyer and Mahesh, 2016; Markovich et al., 2016; Meyer et al., 2007; Smith and Mungal, 1998; Wu et al., 2019). The interaction between these turbulent structures and those in the ambient flow, such as ones found in river bends, are largely unknown.

The few studies that have been done on mixing in river bends have all focused on the same approach: the concentration of effluent at every point in the bend is predicted using mixing coefficients and velocity fields (Baek and Seo, 2013; Elhadi et al., 1984; Pilechi et al., 2014; Rutherford, 1994; Zahiri and Nezaratian, 2020). Finding velocity fields and mapping out the mixing coefficients within a bend require intensive, time consuming measurements or simulations (Lee and Seo, 2012). Measuring concentration fields in rivers is also quite difficult (Pilechi et al., 2014; Zhang and Zhu, 2011), as there is often a large measurement area for the experiment and a large amount of tracer is required.

It could be argued that since secondary flow in general increases mixing, conservative outfalls should be designed neglecting the effects of river bends. However, this is an oversimplification: while overall mixing is increased by secondary flow, local mixing in separated cell structures and flow separation zones may decrease, and these effects should not be neglected. For conservative outfall design, one should instead consider the condition with the lowest flow and water depth. Low flow rate, low overall secondary circulation strength, and increased cell separation would all lead to low dilution. In order to implement this condition for design, one must first understand the effects of secondary circulation on mixing.

The importance of understanding the effects of bends on mixing, as well as the difficulties in the current approach to studying mixing in rivers, are the motivations behind this project. This thesis will identify the physical mechanisms at work, and investigate easier-to-apply prediction methods such as artificial neural networks, fuzzy logic, and empirical equations. In order to understand the processes involved in jet-bend interactions, it is fist necessary to have a general understanding of many contributing fields of study. To that end, a brief literature review is presented in the following section to give the reader the necessary background on fluid dynamics; circulation and vortices; the dynamics of straight open channels, river bends, and jets in crossflows; the study of mixing in rivers; and artificial intelligence methods and applications.

1.1 Fluid Dynamics and Turbulence

In general, the dynamics of incompressible fluids are described by the incompressible Navier-Stokes equations:

$$\frac{\partial \vec{u}}{\partial t} + (\vec{u} \cdot \nabla)\vec{u} = -\frac{1}{\rho}\nabla p + \nu \nabla^2 \vec{u} + \vec{g} \tag{1.1}$$

Together with the continuity equation:

$$\nabla \cdot \vec{u} = 0 \tag{1.2}$$

Where $\vec{u}$ is the velocity vector, t is time, ρ is the density of the fluid, p is pressure, ν is viscosity, and $\vec{g}$ is gravitational acceleration.

These equations are not analytically solvable, and models must therefore incorporate additional strategies. Broadly, these fall into two categories: Reynolds averaged Navier Stokes (RANS), which models the average velocities and their fluctuations separately, and introduces the Reynolds stresses in order to model the velocity fluctuation cross-terms; and large eddy simulation (LES), which directly resolves large eddies numerically on a grid, and uses subgrid scale (SGS) models to incorporate the effects on smaller scales than the grid can resolve.

In the limit of infinitesimal grid spacing, where the SGS effects vanish, LES is equivalent to direct numerical simulations of the Navier-Stokes equations. When the grid size is not infinitesimal, LES models solve the Navier-Stokes equations convoluted with a spatial filter, usually using the grid resolution as the characteristic filter width Δ. As per Kim and Menon (1995), the resulting equation is:

$$\frac{\partial \hat{u}_i}{\partial t} + \hat{u}_j \frac{\partial \hat{u}_i}{\partial x_j} = -\frac{\partial}{\partial x_j}\left(\hat{p}\delta_{ij} + \tau_{ij}\right) + \nu \frac{\partial^2 \hat{u}_i}{\partial x_j^2} \tag{1.3}$$

where a hat indicates a spatially filtered quantity, and τ_{ij} is the SGS stress tensor.

There are many possible ways to model the SGS stress in LES. The simplest approaches use eddy viscosity models to allow energy to dissipate naturally into subgrid scales following a typical energy cascade. In more complex flow fields, energy can be transferred from SGS to resolved scales, or nonlocal and historical effects can become important, requiring the use of special SGS models. Many SGS models have therefore been developed for use in particular cases (Germano et al., 1991; Iliescu and Fischer, 2004; Kim and Menon, 1995).

1.2 Circulation and vortices

It is often necessary to differentiate between flow which rotates around an axis and flow whose gradients are due to shear. In two dimensions, the simplest way to do so is using vorticity, defined as:

$$\omega = \frac{du_1}{dx_2} - \frac{du_2}{dx_1} \tag{1.4}$$

The vorticity can also be integrated over an area to give the circulation, which provides a useful way of comparing rotational flow over areas instead of at individual points.

In three dimensions this becomes more complicated, as flow can rotate around any axis and therefore any measure of the rotation of flow must account for all possible axes simultaneously. One often-used measure of rotation in three dimensions is the Q-criterion, defined as the second invariant of the velocity gradient tensor (Hunt et al., 1988):

$$\text{Q-criterion} = \frac{1}{2}\left[\left(\frac{du_i}{dx_i}\right)^2 - \frac{du_i}{dx_j}\frac{du_j}{dx_i}\right] \tag{1.5}$$

This can be conceptualised as an extension of vorticity into more dimensions: a direct comparison of velocity gradients in different directions to differentiate between rotation and shear, summed over all directions in such a way as to make it invariant under rotation. In practice, the Q-criterion gives a useful visualization of vortex cores, which are defined as regions where the Q-criterion exceeds an arbitrary positive threshold value.

A similar criterion for identifying vortex cores is the λ_2 criterion, which defines a vortex core as a connected region with at least two negative eigenvalues of the tensor $\mathbf{S}^2 + \mathbf{\Omega}^2$, where $\mathbf{S}$ and $\mathbf{\Omega}$ are the symmetric and antisymmetric components of the velocity gradient tensor, respectively (Jeong and Hussain, 1995).

Both criteria outlined above provide useful ways to visualise vortex cores, but they fall short in their ability to distinguish between different vortex structures once connected regions begin to overlap. Such distinction becomes important when trying to separate adjacent rotating structures, such as sub-cells of secondary circulation, which may stem from different driving mechanisms. In this case it is useful to identify not only the area of the vortex core, but also the centre of rotation. In the case of secondary circulation, the three dimensional problem can be simplified into two dimensions by only considering rotation around the streamwise axis. Then, a two dimensional vortex detection method such as the one presented in Graftieaux et al. (2001) can be applied. This method begins with the calculation of two parameters:

$$\Gamma_1(O) = \frac{1}{S}\int_{M\in S} \sin(\phi_M)dS \qquad \Gamma_2(O) = \frac{1}{S}\int_{M\in S} \frac{\overrightarrow{OM} \wedge (\vec{u}_M - \tilde{u}_O)}{||\overrightarrow{OM}|| \cdot ||\vec{u}_M - \tilde{u}_O||}dS \qquad (1.6)$$

Where S is an area around any point O, ϕ_M is the angle between the velocity vector ($\vec{u}_M$) at point M and the vector between O and M ($\overrightarrow{OM}$), and $\tilde{u}_O$ is the convection velocity $(1/S)\int_S \vec{u}dS$ around O. The vortex core is defined as the area where $|\Gamma_2| > 2/\pi$, and is associated with a centre of rotation at a local maximum of Γ_1.

1.3 Straight Open Channels

Open channel flow in straight channels has been the subject of much study, and its characteristic velocity and turbulence profiles are well defined. The coordinates of an open channel are defined by the direction of channel flow, and are denoted s, n, and z for the streamwise, cross-stream, and vertical directions respectively. The open channel profile can be subdivided into the “wall region”, where the wall effects dominate; the “free-surface region”, which is under the influence of free surface effects; and the “intermediate region” between the two (Nezu and Nakagawa, 1993). For an open channel with water depth h, the wall region is considered to be from $z = 0$ to $z = 0.2h$, the intermediate region from $z = 0.2h$ to $z = 0.6h$, and the free surface region above $z = 0.6h$.

The mean streamwise velocity profile in the wall region is described by the law of the wall, also called the log law, which is the defining characteristic of all boundary layer flows:

$$u_s = \frac{u_*}{\kappa} \ln\left(\frac{u_* z}{\nu}\right) + D \tag{1.7}$$

Where D is an empirical constant dependent on the channel roughness, κ is the von Karman constant, and u_* is the shear velocity $u_* = \sqrt{\tau_0/\rho}$ given bottom shear stress τ_0.

Outside of the wall region, the velocity profile deviates from this formula, so the defect must also be accounted for. This is done by adding a wake function to the value obtained in eq. (1.7):

$$u_s = \frac{u_*}{\kappa} \ln\left(\frac{u_* z}{\nu}\right) + D + W(z/h) \tag{1.8}$$

The wake function usually employed is Coles' wake function:

$$W(z/h) = \frac{2\Pi}{\kappa} \sin^2\left(\frac{\pi z}{2h}\right) \tag{1.9}$$

Where Π is the wake strength parameter. Using Π as an adjustable parameter gives the log law more flexibility to deal with accelerating and decelerating flow, but it does not account for the full complexity of flow in a channel bend, as will be shown in Section 1.4.1.

Turbulence statistics in open channels are easiest to define in the intermediate region, where effects of the free surface and the wall are relatively small. Turbulent kinetic energy in this region can be described by the equation:

$$k = 4.78 u_*^2 \exp(-2z/h) \tag{1.10}$$

The constant is empirical. The principal Reynolds stress in the same region takes a linear distribution (Voulgaris and Trowbridge, 1998):

$$-\overline{u_s' u_z'} = u_*^2 \left(1 - \frac{z}{h}\right) \tag{1.11}$$

And the eddy viscosity in this region follows a parabolic distribution (Nezu and Nakagawa, 1993):

$$\nu_T = \kappa h u_* \frac{z}{h} \left(1 - \frac{z}{h}\right) \tag{1.12}$$

The eddy viscosity can also be modelled by a mixing length model:

$$\underbrace{l = \kappa z}_{\text{in wall region}} \qquad\qquad \underbrace{l \propto h}_{\text{outside wall region}} \tag{1.13}$$

Where the constant of proportionality outside the wall region depends on the Reynolds number, $Re = Uh/\nu$ for bulk velocity U.

1.4 Hydrodynamics of River Bends

The basic helical flow pattern found in river bends, with surface flow tending to the outer bank and flow at the bed toward the inner bank, has been known for well over a hundred years (Thomson, 1877), but developments in measurement techniques now make it possible to easily resolve flow structures that were not commonly visible even a few decades ago.

1.4.1 Mean Velocities

The coordinate system used to describe river bends (shown in figure 1.1) uses s to represent the streamwise direction, n for the cross stream direction, and z for the vertical.

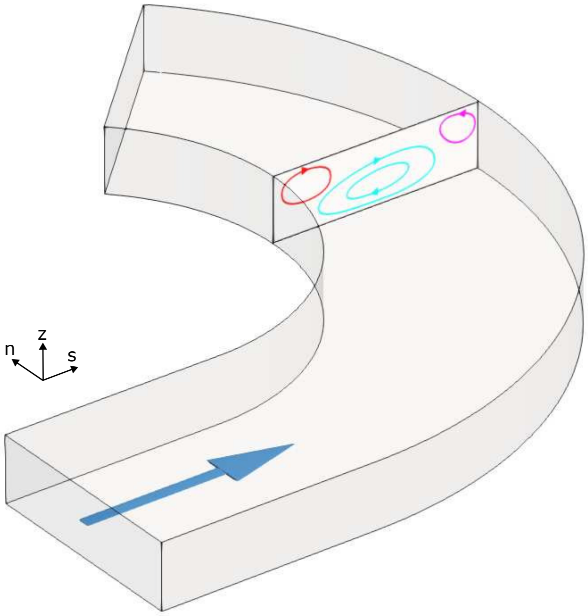

Figure 1.1: Coordinates and secondary circulation in a river bend, showing an inner bank cell in red, a centre cell in blue, and an outer bank cell in pink

The velocity of the water going into a river bend causes a centrifugal force effect, pushing the water toward the outer bank and causing the water surface at the outer bank to be higher than at the inner bank. The superelevation at the outer bank causes a pressure gradient that drives the water toward the inner bank. This force balances with the centrifugal force on average, as it must to maintain continuity, but they do not balance at every individual location. At the water surface, where the streamwise velocity is greater, the centrifugal force dominates and causes a secondary flow toward the outer bank. At the bed, the pressure gradient dominates, and the water tends toward the inner bank. The combined effect is one of helical motion through the bend.

The channel beds of river bends tend to deform under the force of the flow to what is called bar-pool topography. The bar refers to a shallow point bar along the inside wall of the bend, and the pool refers to a scour hole at the outer wall. The bathymetry then interacts with the flow field through a process called topographic steering which redirects the flow around the point bar and through the deepest part of the channel (Dietrich and Smith, 1983). The flow is forced over the point bar, resulting in high pressure over the point bar and low over the pool. This pressure gradient, combined with the centrifugal force, can overcome the pressure gradient from the surface elevation, even at the bed, resulting in a net outward flow. Blanckaert (2010) showed that the redirection of flow can mainly be attributed to mass conservation.

The centre cell is not the only cell that can develop in river bends, but it is certainly the most consistently seen and has the strongest circulation, allowing it to be observed even without sophisticated equipment. In addition to the centre cell, there is often a cell circulating in the opposite direction near the surface at the outer bank, driven by turbulent anisotropy (Bathurst et al., 1977). The outer bank cell has not been observed as extensively as the centre cell, as its small size and velocities and its intermittent behaviour make it difficult to resolve (Blanckaert and Graf, 2001). It typically has cross-stream velocities of $O(0.03U)$, in contrast to the centre cell that has velocities of $O(0.1U)$, U being the bulk velocity (Blanckaert and de Vriend, 2005). In the past few decades, developments in measurement techniques have allowed for better resolution of the outer bank cell in both experiments (Bai et al., 2019; Farhadi et al., 2018) and in the field (Foerst and Rüther, 2018; Russell and Vennell, 2019). In general, the outer bank cell is thought to protect the outer bank by preventing the high velocity core from reaching the outer bank, and therefore keeping the shear stress and erosion down. There is also a school of thought that the outer bank cell may increase erosion by deflecting high momentum fluid from the surface into the lower part of the outer bank, causing bank undercutting (Bathurst et al., 1979).

In high curvature bends, it is possible to have even more complex patterns of circulation cells. Kashyap et al. (2012) showed two ways in which the centre cell can split, one with a sub-cell that splits off at the inner bank and one with a split at the outer bank. When the main cell splits, all the sub-cells rotate in the same direction, though their individual contribution to total circulation varies for each cell and for location through the bend. M2, the cell that splits off near the outer bank, forms shortly after the bend entrance but remains small until 120° where it quickly grows until its circulation is comparable to that of the main cell at the bend exit. Figure 1.2 shows the paths that M2 and the centre cell follow through the bend. Note that this figure shows flow over a deformed bed, and therefore the paths of the cells are affected by topographic steering. The split off cell at the inner bank, V1, is characteristic of flow in high curvature bends with a flat bed, and is associated with the area of high shear stress magnitude at the inner bank. V1 forms on the inner bank close to the apex of the bend, but does not grow later as M2 does. V1, along with M2 and the main circulation cell, is shown in figure 1.3. The counter-rotating cell at the outer bank was not tracked for either figure.

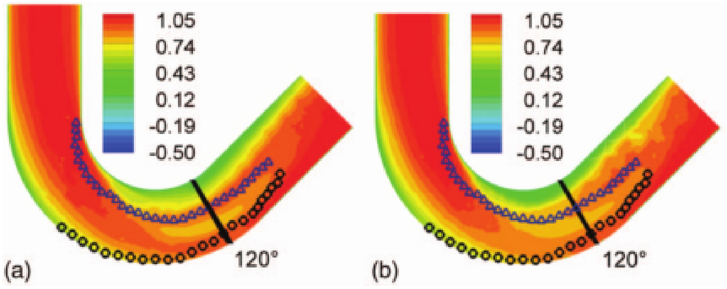

Figure 1.2: Depth-averaged downstream velocity, normalised with the bulk velocity, for experiments on a deformed bed under two different width-to-depth ratios, 5 and 6.67 for (a) and (b) respectively. The centrelines of the clockwise-rotating cells are also shown: the main cell, M1, in blue triangles and the outer bank split off of the main cell, M2, in black squares (Kashyap et al., 2012)

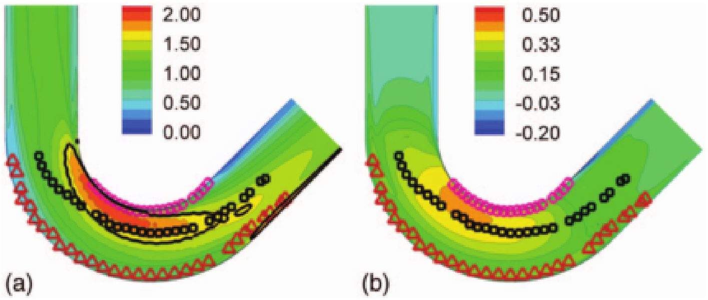

Figure 1.3: Bed shear stress (a) magnitude, normalised using the average bed shear stress in the inlet, and (b) cross-stream component, normalised using the magnitude, for simulations of flow in a bend with a flat bed. Centrelines of clockwise-rotating cells are also shown: the main cell, M1, in black squares; the inner bank split off of the main cell, V1, in pink circles; and the outer bank split off of the main cell, M2, in red triangles (Kashyap et al., 2012)

The paths of the main cells through the bend follow the areas of high discharge, as can be seen in figure 1.2.

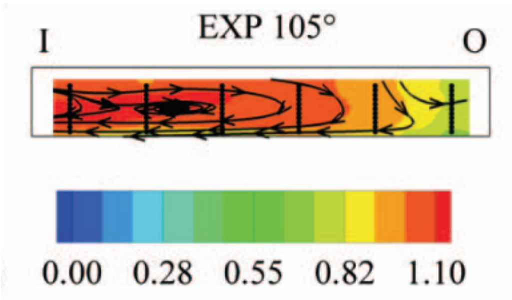

Figure 1.4: Streamlines showing split cells of secondary circulation over a flat bed after Kashyap et al. (2012)

Figure 1.4 demonstrates how split cells appear in secondary circulation streamlines in cross section. Though neither the inner bank cell nor the outer bank cell are entirely captured in the measurements, streamline structures that do not connect are distinctly visible.

Cell splitting such as was observed by Kashyap et al. (2012) can be further affected by the geometry of the bend, both in the planform shape of the bend (Blanckaert et al., 2013) and in its bed geometry (Constantinescu et al., 2011).

The streamwise velocity profile in a straight channel is defined in eq. (1.8), but this equation does not apply in channel bends. As shown in figure 1.5, the maximum velocity core follows the deepest part of the channel toward the outer bank and moves down from the surface. The maximum velocity core starts close to the inner bank before moving outward through the bend, eventually reaching the outer bank after the bend. The shift toward the inner bank at the beginning of a bend was first thought to only be an effect of upstream bends, but de Vriend and Geldof (1983) showed that that is not the case, and that non-uniformity of flow in the bend and the redistribution of streamwise momentum are likely factors in causing the shift.

Though the basic assumption that the downstream velocity profile follows eq. (1.8) is not true in bends, linear models of flow in bends such as the Rozovskii model developed by de Vriend (1977) rely on this assumption holding true. Consequently, results from these models often show significant overestimation of advective momentum transport. A nonlinear model developed by Blanckaert and de Vriend (2003) and Blanckaert (2003) corrects the overestimation by including feedback from

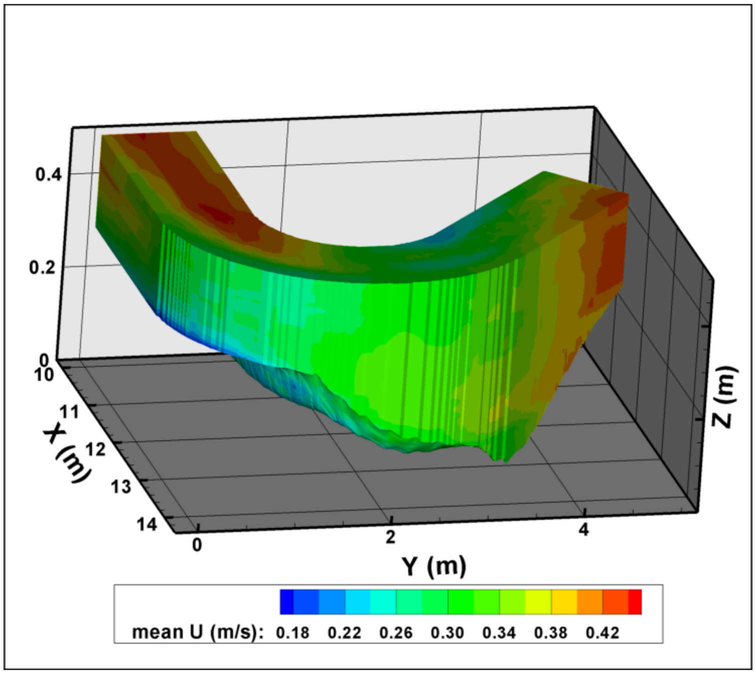

Figure 1.5: 3D view of streamwise velocity $\overline{u}$, with flow from left to right (Post, 2007)

the vertical velocity distribution, and is considered the most reliable model for calculating both streamwise velocity and secondary circulation in river bends without resorting to full simulations. There are still limitations to Blanckaert's model, most notably the fact that it predicts flow at the channel centreline and thus cannot account for cross stream variations. The complexity of channel bend flows and the number of parameters at play make it very difficult to develop all-encompassing models for bend flow. Recent developments in machine learning have made it possible to develop more comprehensive models; for example Bali et al. (2019, 2020) developed formulae for velocity components in bends with a model tree using data from RANS simulations as input.

1.4.2 Turbulence Statistics

With the development of helical flow in bends, the magnitudes and relative importance of the Reynolds stresses change. In general, locations of Reynolds stress extrema correlate with locations of the centres of circulation cells (Post, 2007). Likewise, turbulent kinetic energy distributions are also related with the presence of secondary circulation cells. Figure 1.6 shows all Reynolds shear stress component distributions for two different flow conditions, as well as sample distributions of turbulent kinetic energy and the placement of the secondary circulation cell.

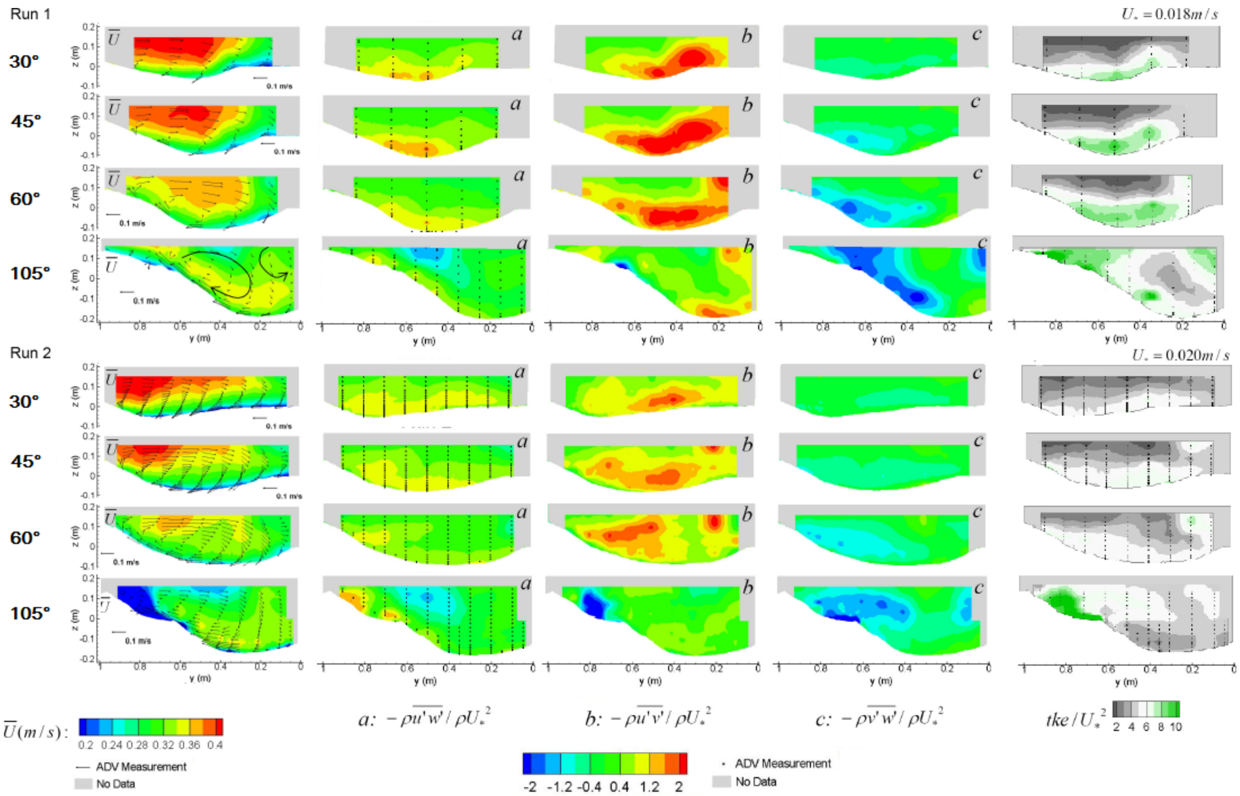

Figure 1.6: Mean streamwise velocity (column 1), Reynolds stress components (columns 2 to 4) and turbulent kinetic energy (column 5) in a bend at 30, 45, 60, and 105 degrees (Jamieson, 2011)

In understanding the turbulent structure of channel bends, it is also important to acknowledge that the cells of secondary circulation are not stationary, but rather coherent structures that move in time. Blanckaert and de Vriend (2005) measured velocity fluctuations and showed that they were coherent across the channel width, indicating oscillation of the whole circulation cell. This oscillation had different spectral characteristics from the background turbulence, and contributed a significant proportion of the normal stresses but very little shear stress.

1.4.3 Simulating Flow in River Bends

Understanding the hydrodynamics of river bends is vital for the development of simulations capable of reproducing accurate flow fields. Specifically, the turbulence closure model and the treatment of the water surface should be chosen to best represent the physical processes outlined in the previous section.

LES has been shown to resolve transient structures much better than RANS models. Specifically in river bends, most RANS simulations cannot reproduce the anisotropy-driven secondary outer bank cell. By contrast, LES can reproduce this cell, and also yields better agreement with experiment for turbulence distributions (Booij, 2003). Kashyap (2012) confirmed that RANS models cannot discern the outer bank counter-rotating cell, and also found that they cannot reproduce some main cell splitting effects. Therefore LES models are preferable for simulations in river bends.

Two of the most common water surface treatments in computational fluid dynamics are the rigid lid model and the volume of fluids (VOF) model. VOF defines the fraction of each cell occupied by a given fluid, and determines the free surface by modelling the transport of fluid at the interface using an additional continuity equation (Rhee et al., 2005). Rigid lid models impose a boundary at the top of the flow, and model the air-water interface using that boundary as a symmetry plane. Since the secondary circulation in a bend is a direct result of the superelevation, the rigid lid assumption must be used with caution. In particular, the rigid lid assumption can fail to capture flow separation at the inner bank (Ramamurthy et al., 2013). However, rigid lid simulations provide good agreement with experiment for bends with low Froude numbers and are generally agreed to be valid for flows with $Fr < 0.5$ (Paik and Sotiropoulos, 2005).

1.4.4 Comparing flat bed flows to those with bathymetry

Many of the studies cited in sections 1.4.1 and 1.4.2 took place in channel bends with bathymetry. The interaction of secondary flow and bathymetry is complex and circular, driven by sediment transport and topographic steering. Though a few studies have investigated both flat and deformed beds (Kashyap et al., 2012; Zeng et al., 2008), the difference in the fundamental geometry of the problem makes direct comparison difficult. Furthermore, the wide range of bend geometries found in natural rivers makes it impossible to assume that results from a single bend with bathymetry apply to every bend with bathymetry. Therefore it is still common to use a rectangular bed as a simplification when studying open channel bends (Bali et al., 2019, 2020; Kim et al., 2020; Li and Zhang, 2022), especially in the first application of novel methods.

1.5 Jets in Straight Crossflows

While mixing in channel bends is still not fully understood, there is a large body of work studying the interactions of turbulent jets into stationary ambient water and straight crossflows. The initial concentration and momentum of the jet both disperse along the jet trajectory. The centreline of the jet trajectory can be defined using either peak concentration or peak velocity in the direction of the initial jet velocity, though these do not always coincide (Shao and Law, 2011).

Pratte and Baines (1967) showed that the trajectory (defined using the jet concentration) of a turbulent jet in an infinitely wide crossflow can be described by the formula:

$$\frac{n_{jet}}{d} = Ar\left(\frac{s}{d \cdot r}\right)^b \tag{1.14}$$

Where n_{jet} is the cross-stream distance to a given point in the jet trajectory, d is the diameter of the jet outlet, $r = u_{jet}/u_{cf}$ is the jet-to-flume velocity ratio for velocities of the jet and crossflow u_{jet} and u_{cf} respectively, s is the downstream distance from the jet nozzle, and A and b are fitted parameters.

While this equation describes the overall shape of the jet, it does not explain the details of the jet structure and mixing mechanisms at work. This is done in Iyer and Mahesh (2016), Meyer et al. (2007), and Smith and Mungal (1998), to name a few.

The typical turbulent structure of a jet in crossflow is shown in figure 1.7. The key elements of the structure are the counter-rotating vortex pair (CVP), the horseshoe vortex, and the wake vortices. The horseshoe vortex and the CVP are both steady-state structures that can be observed in mean flow fields, but the wake vortices are transient and must be identified using mathematical methods such as proper orthogonal decomposition (POD) (Meyer et al., 2007) and dynamic mode decomposition (DMD) (Iyer and Mahesh, 2016).

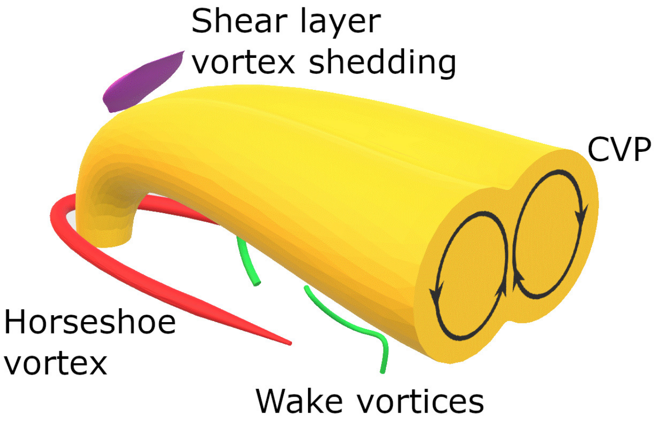

Figure 1.7: Turbulence structures of a jet in crossflow

The CVP is the main feature in the far field: it persists for up to 1000 jet diameters downstream of the jet nozzle (Pratte and Baines, 1967) and its momentum transport accounts for much of the mixing (Zhang and Yang, 2017). However, there has been little research on the CVP's interactions with other flow structures, and the research that has been done has focused on interactions between multiple jets, not on interactions between the jet and turbulence structures in the ambient flow (Li et al., 2012).

The horseshoe vortex is a structure of the ambient flow, similar to the horseshoe vortex that forms around solid obstacles in boundary layer flow. In general the jet fluid does not get entrained in this vortex, and therefore no mixing happens directly within the horseshoe vortex (Smith and Mungal, 1998). Its effect on mixing is indirect, through its interaction with the surrounding flow.

By contrast, jet fluid can be entrained within the wake vortex structures. This is observed for jet-to-crossflow velocity ratios at or above 20 (Smith and Mungal, 1998).

Figure 1.7 also shows the jet shear layer that forms on the upstream edge of the jet. This structure drives the development of a mixing layer between the jet and ambient flow. The shear layer marks the boundary between the jet and ambient flow, and comprises many transient vortices driven by the Kelvin-Helmholtz instability of the difference in velocities across the interface. The shear layer's structure can be simplified by decomposition into a few dominant modes, and their corresponding frequencies, via DMD (Iyer and Mahesh, 2016).

Though there have been no parametrical studies on jets in channel bends, there have been such studies of jets under other forces. For nonbuoyant jets in straight crossflows, Gopalan et al. (2004) focused on the influence of the jet-to-crossflow velocity ratio, r, on the structure of a jet. They found that for $r > 2$ the jet behaved as outlined above, displaying wake vortices behind the jet. For $r < 2$, a semi-cylindrical "shell" was observed behind the jet, encompassing a region of reverse flow. The horseshoe vortices and the CVP remain unchanged. The development of the shell and subsequent structure of the jet is shown in figure 1.8. The principal difference compared to the classical jet vortex structure in figure 1.7 is the jet's attachment to the wall, and the subsequent disappearance of the wake vortices. Similar results were observed by Cambonie and Aider (2014): in addition to the wall attachment and disappearance of the wake vortices, a weakening of the shear layer was observed for even lower velocity ratios of $r < 0.6$.

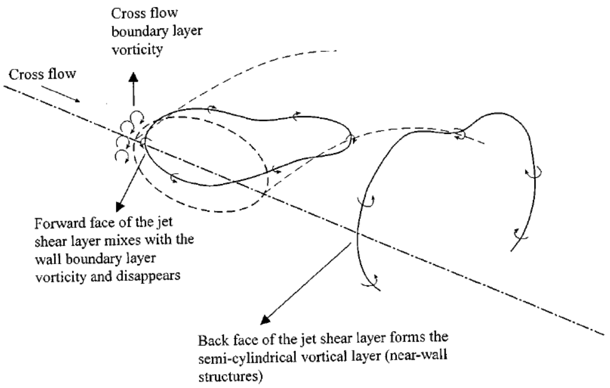

Figure 1.8: Structure of a jet in crossflow at $r < 2$ (Gopalan et al., 2004)

Jirka and Doneker (1992) identified seven length scales which together form a comprehensive classification system for submerged buoyant jets in crossflows:

$$\underbrace{\frac{Q_{jet}}{M_{jet}^{1/2}}}_{\substack{\text{discharge}\\ \text{length scale}}} \qquad \underbrace{\frac{M_{jet}^{3/4}}{J_{jet}^{1/2}}}_{\substack{\text{jet/plume}\\ \text{length scale}}} \qquad \underbrace{\frac{M_{jet}^{1/2}}{u_{cf}}}_{\substack{\text{jet/crossflow}\\ \text{length scale}}} \qquad \underbrace{\frac{J_{jet}}{u_{cf}^{3}}}_{\substack{\text{plume/crossflow}\\ \text{length scale}}}$$

$$\underbrace{\frac{M_{jet}^{2/3}}{\left(J_{jet}u_{cf}\right)^{1/3}}}_{\substack{\text{puff/thermal}\\ \text{transition}\\ \text{length scale}}} \qquad \underbrace{\frac{M_{jet}^{1/4}}{\left(-g\frac{d\rho_{\mathrm{cf}}}{dz}\right)^{1/4}}}_{\substack{\text{jet/stratification}\\ \text{length scale}}} \qquad \underbrace{\frac{J_{jet}^{1/4}}{\left(-g\frac{d\rho_{\mathrm{cf}}}{dz}\right)^{3/8}}}_{\substack{\text{plume/stratification}\\ \text{length scale}}} \tag{1.15}$$

Where Q_{jet} is the discharge of the jet, $M_{jet} = u_{jet}Q_{jet}$ is the jet's momentum flux, and $J_{jet} = Q_{jet}g\left(\rho_{cf} - \rho_{jet}\right)/\rho_{cf}$ is its buoyancy flux where g is the gravitational constant and ρ_{jet} and ρ_{cf} are, respectively, the densities of the jet and the crossflow. Using these length scales, jets are classified based on whether buoyancy or momentum dominate, whether they are in deep or shallow water, whether the plume will spread vertically or remain stratified, and whether the jet will attach to the bottom.

Jones et al. (2007) used many of the same parameters to develop a classification system for surface discharges in crossflows. For submerged jets under waves, Chang et al. (2009) provided a parametrical analysis of the behaviour of the jet, concluding that the jet behaviour is best summarized by the jet-to-wave momentum ratio.

While these studies investigated different problems than those addressed in this thesis, they do provide a framework for studying parametric behaviour of jets. Jirka and Doneker (1992) and Jones et al. (2007) in particular provide examples of binary decision trees being used to describe the qualitative behaviour of jets. No such parametrisation of jets in bends exists prior to this study.

Natural rivers tend to be much wider than they are deep, often by a factor of ten or more (Smith and Mclean, 1984). Mixing behaviour is different in such shallow channels, as the water depth limits the vertical expansion of the jet, and complete vertical mixing is achieved relatively early (Rutherford, 1994). In these situations, the formula from Seo et al. (2001) is more appropriate than eq. (1.14), as it uses the momentum ratio $m_r = (u_{jet}^2 d)/(u_{cf}^2 h)$ instead of the velocity ratio r and therefore accounts for the water depth:

$$\frac{n_{jet}}{L_d} = Am_r \left(\frac{s}{L_d \cdot m_r} \right)^b \tag{1.16}$$

Where L_d is the characteristic length scale, taken in Seo et al. (2001) to be the distance between diffuser ports.

1.6 A note on the term “vortex”

Though section 1.2 outlined some ways to identify vortices mathematically based on rotating flow, the term “vortex” is not commonly applied to all rotating flow structures, even when they meet the mathematical definitions given. In particular, Jeong and Hussain (1995) defined vortex dynamics as the study of the production and interaction of turbulent coherent structures. It is thus often implied that the term “vortex” should be restricted to transient turbulent structures. Since secondary flow in river bends is driven by mean flow phenomena, much of the early work on bend-driven secondary flows used a mean flow approach instead of considering the circulation to be made up of coherent structures (Prandtl, 1952). However, with recent developments in the study of secondary flows, it has often become convenient to define secondary circulation in terms of coherent structures (Blanckaert and de Vriend, 2005), and in some cases it has been shown that mean secondary flow is directly related to the distribution of coherent structures (Kawahara et al., 2011; Pinelli et al., 2010; Uhlmann et al., 2010, 2007; Vanderwel et al., 2019). The definition of what constitutes a vortex now has as much to do with history as with the turbulent structure of the velocity field. For instance, the horseshoe vortex and CVP of a transverse jet are always referred to as vortices despite being mostly stationary, and the outer bank cell (OBC) in a river bend is almost never referred to as a vortex, despite being transient and turbulence-driven (Blanckaert and Graf, 2001). Since this thesis deals entirely with the interactions of transverse jets and bend-driven secondary flow, it is impossible to respect both these historical conventions while also applying equivalent treatment to all coherent structures. Therefore the language of vortex dynamics is often applied to bend-driven secondary flows throughout.

1.7 Mixing in Rivers

Mixing in natural rivers is usually far more complex than in the above case, which represents a jet into an idealized straight channel. In the more general case, mixing in rivers is usually quantified using the advection-diffusion equation (Rutherford, 1994), though this approach does not directly account for the properties of the jet. Applying the advection-diffusion equation requires known diffusion coefficients and velocity fields. The equation calculates the concentration of effluent at every point in the bend:

$$\frac{\partial}{\partial t}(hC) + \frac{\partial}{\partial x_i}(hu_iC) = \frac{\partial}{\partial x_i}\left(hD_i\frac{\partial C}{\partial x_i}\right) \qquad \text{for } i = s, n, z \tag{1.17}$$

Where C is the concentration of the tracer and D_i is the diffusion coefficient in direction i.

This approach divides the mixing analysis into directional components. In the coordinate system presented, these are the streamwise, cross stream, and vertical components as used in previous sections. In shallow channels, where vertical mixing happens relatively quickly, the streamwise and cross stream components in the advection diffusion equation take on greater importance. In the case of a steady pollutant source, mixing in the streamwise direction is also less important. Therefore many studies on mixing in shallow open channels focus on determining the transverse mixing coefficient.

The hydrodynamics of river bends have a large impact on the mixing behaviour of effluent in the river, but mixing in river bends is still difficult to predict and doing so relies on many simplifications. This is in part because of the complex nature of the problem and the many parameters involved, which make measurements highly dependent on the specific location and situation of an individual study.

Early studies on mixing in rivers suggested increasing the diffusion coefficients uniformly in river bends and meandering river reaches (Fischer, 1969). For the transverse mixing coefficient:

$$D_n = \frac{U^2h^3}{\kappa^5R^2u_*}I \tag{1.18}$$

Where U is the average streamwise velocity in the channel, R is the radius of curvature of the channel bend, and I depends on the Darcy-Weisbach friction factor and the value of κ being used. Other studies have proposed similar formulae of the following general form, with possible variations (Jeon et al., 2007):

$$\frac{D_n}{hu_*} = c_1 \left(\frac{U}{u_*}\right)^{c_2} \left(\frac{B}{h}\right)^{c_3} \left(\frac{h}{R}\right)^{c_4} (S_n)^{c_5} \tag{1.19}$$

Where S_n is the sinuosity of the channel, B is the channel width, and c_1, c_2, c_3, and c_4 are model-specific constants.

Recently there have been many explorations of alternative methods to predict transverse mixing in rivers. Azamathulla and Ahmad (2012) used gene-expression programming to develop an empirical formula for the transverse mixing coefficient in straight channels given the channel width, depth, average flow velocity, and shear velocity. Huai et al. (2018) later used a similar technique, genetic programming based modelling, to include the effects of sinuosity and develop a model based on mixing results from several studies. Aghababaei et al. (2017) also predicted mixing coefficients using genetic programming based symbolic regression, and included the effects of the Froude number, $Fr = U/\sqrt{gh}$, into the analysis. Zahiri and Nezaratian (2020) also predicted transverse mixing coefficients using a variety of machine learning techniques including model trees, multivariate adaptive regression splines, genetic algorithms, and particle swarm optimization.

Uniformly increasing the diffusion coefficients is a simple way to account for increased advection and turbulent diffusion driven by the secondary circulation in river bends, but it does not account for nonuniform mixing characteristics. Since the effects of secondary circulation are highly directional and location dependent, a new method is needed to capture these details. Fischer (1978) developed an extension of eq. (1.17) using a diffusion tensor:

$$\frac{\partial}{\partial t}\langle C\rangle + \langle u_i\rangle \frac{\partial \langle C\rangle}{\partial x_i} = \frac{\partial}{\partial x_i}\left(D_{ij}\frac{\partial \langle C\rangle}{\partial x_j}\right) \qquad \text{for } i, j = s, n \tag{1.20}$$

Where $\langle\cdot\rangle$ indicates depth averaged quantities and D_{ij} are the components of the diffusion tensor, which can be found using the velocity field and the vertical diffusion coefficient D_z:

$$D_{ij} = -\frac{1}{h}\int_0^h (u_i - \langle u_i \rangle) \int_0^z \frac{1}{D_z} \int_0^z (u_j - \langle u_j \rangle) dz dz dz \qquad \text{for } i, j = s, n \tag{1.21}$$

These equations are derived by taking the depth average of eq. (1.17) after neglecting the vertical advection and horizontal diffusion terms. This simplification is justified when the tracer is sufficiently vertically mixed and the horizontal velocities are comparatively large.

Equations (1.20) and (1.21) provide a method of determining and applying spatially varying mixing coefficients using a known velocity field without having to track concentration explicitly. This can be done with a great degree of spatial resolution, as shown by Lee and Seo (2012) and Seo et al. (2008).

A more direct method of measuring diffusion coefficients is by concentration measurements in tracer tests. This has the advantage of directly incorporating the effects of secondary circulation and other complicating factors such as ice cover (Zhang and Zhu, 2011). Boxall and Guymer (2003) used this method to find large longitudinal variations in the transverse mixing coefficient likely due to the changing geometry and subsequent development of secondary circulation. While concentration measurements do not directly quantify the influence of secondary currents, the degree of mixing can still be related to the strength of the secondary circulation after taking measurements of both concentration and velocity (Moncho-Esteve et al., 2017).

Concentration measurements can also be used in combination with velocity field information to calculate diffusion coefficients. Pilechi et al. (2016) demonstrated an efficient way to accomplish this, by calibrating the diffusion coefficients to match the solution of the advection-diffusion equation to the measured concentration fields.

Large scale measurements or simulations of natural rivers always present challenges, but there are some particular challenges to the study of mixing in rivers. Measurements in natural rivers must cover an extensive area to capture the entire mixing region, and this is often not practical. In some cases, when the location of the plume is not known beforehand, it can be difficult to narrow down the measurement area (Pilechi et al., 2014). Given that the plume location is often only known after measurement, this can present logistical problems for full scale measurements.

Even when direct concentration measurements are not a problem, there are still difficulties. Mixing within river bends is highly dependent on secondary circulation, which is a definitively three dimensional process. Therefore all three velocity components are required over the entire 3D mixing region. This is especially limiting for numerical modelling: 3D models are much more computationally expensive than their 2D and 1D counterparts.

There have been various attempts to recreate river mixing using 2D and 1D simulated velocity fields: Fischer (1972) developed a 1D Lagrangian model capable of predicting mixing in a lagoon, and Park and Seo (2018) used a similar model to predict 2D mixing in rivers, including inside of bends. The Park and Seo (2018) model is an especially interesting example, as the effects of secondary circulation were simulated using only 2D velocity fields. The depth averaged velocity field for the full domain was simulated, and then extended to 3D at every point by assuming the streamwise velocity followed the log law, and the transverse velocity profile followed the linear distribution put forward by Odgaard (1986). Though the results presented were promising, they rely on simplistic models of flow within a bend, and do not take convection from vertical velocity into account, leaving the details of secondary circulation unaccounted for. By contrast, the benchmark results for mixing in river bends must always take the full picture of secondary circulation into account.

1.8 Artificial Intelligence Methods and Applications

In order to interpret measured and simulated velocity and concentration fields, this project will make use of artificial neural networks (ANNs) and fuzzy logic. These methods fall under the umbrella of machine learning, which is beginning to be applied to modelling flow in river bends.

ANNs are a method of machine learning that let a computer develop a model from a dataset (Hill et al., 1994). Typically, these models are comprised of many nodes arranged in layers: an input layer, several hidden layers, and an output layer. Each node takes on a value by calculating a weighted sum of the nodes in the previous layer, and the model is calibrated by adjusting the weights of each node until the desired output can be calculated from given input. This method is far more flexible than developing empirical equations, and does not require user input beyond basics such as the number of nodes and layers.

Fuzzy logic is a mathematical method of applying set theory to conditions that are best described by degrees of truth instead of binary true/false assertions. It becomes a powerful tool in machine learning when it is applied though fuzzy inference system modelling, which applies if-then rules to map input variables onto output. These types of models are well suited for systems which, like mixing in river bends, have complex interactions between many parameters (Bolotin, 1999; Zadeh, 1965). Combining fuzzy logic with trainable neural networks results in adaptive neuro-fuzzy inference systems (ANFISs). These systems are similar in structure to ANNs but also contain a fuzzification layer, which classifies input data into categories based on fuzzy membership functions.

ANNs have recently been applied to predicting flow in bends by Ajeel Fenjan et al. (2016) and Gholami et al. (2015a,b, 2016a,b). These researchers conducted a series of studies on machine learning-based predictions of velocity in bends. They found that ANNs trained on experimental data for a given flow condition in a bend outperformed a RANS simulation with $k - \epsilon$ turbulence closure in predicting velocity (Ajeel Fenjan et al., 2016; Gholami et al., 2015a), water surface elevation (Gholami et al., 2015a), and pressure (Ajeel Fenjan et al., 2016) at given input coordinates for the same flow in the same bend. They also applied ANNs in combination with decision trees, another form of artificial intelligence, to include the effects of different flow rates (Gholami et al., 2016a,b). Gholami et al. (2020) compared two different machine learning models, each alone and coupled with classification decision trees, and showed that prior classification improved the performance of both models. A separate model was developed using gene expression programming, which was built to include the effect of flow rate intrinsically (Gholami et al., 2015b).

Machine learning has also been used in predicting mixing coefficients in natural channels, through genetic based programming as discussed in Section 1.7

1.9 Summary

Though much work has been done in analysing and parametrising the structure of secondary circulation in bends, the mechanisms of mixing in river bends are still largely unstudied. Complete quantification of mixing in river bends still requires full a priori knowledge of diffusion coefficients and velocity fields everywhere in the bend. Without this knowledge, one can only speak to large-scale trends, as Fischer (1969) did.

The lack of a parametric model to directly quantify mixing in river bends means that predicting such mixing must be done either via oversimplified models or extremely intensive calculations. Mixing models based on complete knowledge of velocity fields and diffusion coefficients can be very reliable, depending on the method used to calculate the coefficients, but the amount of information input they require indicates another shortcoming: it is currently impossible to separate the important input from the inessential. In order to make this possible, a complete analysis of the specific mixing mechanisms at work, and the specific parameters that affect them, is necessary.

Chapter 2

Objectives, Novelty, and Scope

2.1 Thesis outline and novelty

The core chapters of this thesis, the publication status of each chapter, and their novel elements, are outlined below:

Chapter 4: Trajectory of a jet in crossflow in a channel bend

Published in Environmental Fluid Mechanics, 2018.

Authors: Schreiner, H. K., Rennie, C. D., and Mohammadian, A.

DOI: 10.1007/s10652-018-9594-8

This chapter introduces a new formulation of problem of jet mixing in a river bend. In it, the jet in the channel bend is shown to not follow the known equation for a jet trajectory in a straight crossflow. A modification to the equation is proposed to account for the difference, using the position of the centre of the secondary circulation cell. The position of the centre of the secondary circulation cell is thus demonstrated to be a key parameter in predicting the jet's trajectory in the bend.

Chapter 5: Insights into secondary flow structure from clusters of instantaneous vortices

Published in Environmental Fluid Mechanics, 2023.

Authors: Schreiner, H. K., Rennie, C. D., and Mohammadian, A.

DOI: 10.1007/s10652-022-09907-9

In this chapter, a novel method for distinguishing between overlapping sub-cells of secondary circulation is proposed, using clusters of instantaneous vortices. The method is demonstrated on a single flow condition in a bend without a jet, showing the simultaneous existence of many sub-cells. Of particular importance are the centre cell and the inner bank cell, which exhibit different circulation development and retention patterns.

Chapter 6: Effect of a nonbuoyant submerged transverse jet on bend secondary circulation

Ready for submission to Journal of Hydro-Environment Research.

Authors: Schreiner, H. K., Rennie, C. D., and Mohammadian, A.

This chapter is the first to look at a non-buoyant jet's effect on bend secondary currents. The addition of the jet disrupts the formation of an outer bank cell, and shifts the strength of the secondary circulation between the centre and inner bank cells.

Chapter 7: Machine Learning and parametrisation of multi-cell structures of secondary circulation in a tight open channel bend using LES

In preparation for submission to Engineering Applications of Computational Fluid Mechanics.

Authors: Schreiner, H. K., Mohammadian, A., and Rennie, C. D.

In this chapter, machine learning models are developed which demonstrate the effect of Froude number and aspect ratio on the distribution of secondary circulation between the sub-cells, and their development at different positions in the bend. By focusing on predicting the circulation of an entire sub-cell instead of individual velocity components at a given location, as previous bend flow models did, this chapter gives insight into the drivers of the coherent structures within the bend.

Chapter 8: Parametrisation of jet effects on secondary circulation and resulting effluent distribution

In preparation.

This chapter extends the machine learning models of Chapter 7 to cases with the jet, therefore looking at the interactions of the jet vortices and the secondary circulation structures in detail for the first time. The models are then used to investigate the effect of individual jet and crossflow parameters on the vortex interactions. Furthermore, the resulting effluent mixing is investigated using regression models to predict characteristics of the concentration distribution at the 90° cross section.

Chapter 9: Note on clustering instantaneous vortices

This chapter does not stand on its own, but discusses variations to the methods for clustering instantaneous vortices used in the previous four chapters. This chapter puts special emphasis on the instantaneous vortex clustering method that is one of the core novel components of this thesis. Variations to the methods between chapters, reasons for alterations, and possible future extensions are discussed.

2.2 Objectives

The overall objective of this project is to study in detail, via experiment and simulation, the mechanisms whereby effluents mix with ambient flow in river bends, and to identify the parameters with the most influence on mixing. This can be broken down into several smaller objectives concerning the methodology involved as well as the understanding of the physics involved. These objectives are outlined below. The first four objectives are methodological objectives, which contribute toward the final two objectives.

Objective 1: Conduct a parametric assessment in a large scale physical model

This objective is addressed in Chapter 4. Parametric analysis of the dye tests and acoustic Doppler velocimeter (ADV) measurements in the large bend flume serve to identify the most important parameters for mixing of an effluent jet in a channel bend. These results inform the more detailed parametric analysis based in simulation and validated with particle image velocimetry (PIV) in Chapter 8.

Objective 2: Conduct simulations in OpenFOAM

LES models in OpenFOAM are presented in Chapters 5 through 8.

Objective 3: Validate simulations with PIV experiments in small bend flume

PIV data is used as validation for LES results, in Chapters 5 through 8.

Objective 4: Develop a consistent method for quantifying secondary circulation

The clustering method for distinguishing sub-cells of secondary circulation is developed in Chapter 5. It serves to quantify changes in secondary circulation, whether the changes stem from changes in channel flow (as in Chapters 5 and 7) or from the addition of a jet.

Objective 5: Use machine learning tools to parametrise the affects on secondary circulation

Chapter 6 examines the effect of a submerged jet on the secondary circulation in a single channel flow condition. Chapter 7 examines the effect of channel flow conditions on the secondary circulation using the clustering method to examine effects on individual sub-cells and machine learning models to predict the circulation behaviour. A complete parametrization of secondary flow effects from both channel and jet flow conditions using machine learning is presented in Chapter 8.

Objective 6: Determine the resulting effect on the effluent distribution

The effluent distributions for two jets in a single flow condition are presented in Chapter 6. A more complete parametrisation, including the effect of several channel flow parameters on the effluent distribution at a single location, is addressed in Chapter 8.

2.3 Scope

Operational outfalls in rivers are much more varied in bend geometry and outfall positions than can possibly be covered in a single thesis. It is far beyond the scope of this project to study every possible situation; rather, this project aims to reproduce the important mixing mechanisms using conditions simple enough to allow for a straightforward analysis, with the aim of developing the tools necessary for studying other geometries, scales, and flow conditions with consistency. This project is therefore limited to the study of one channel bend geometry, with a flat bed and a single radius of curvature and bend angle. It will also only investigate one position for the jet outlet, and only consider non-buoyant effluents.

Chapter 3

Methods

A wide range of experimental, numerical, and analysis methods are employed throughout this thesis, including dye tests, ADV measurements, PIV measurements, LES numerical modelling in OpenFOAM, and vortex identification and clustering. Each subsequent chapter contains a section detailing the methods employed in the chapter. This section contains descriptions of methods either too specific to be laid out in detail in their corresponding chapter, or else too broad to be contained within a single chapter. This chapter aims to provide those necessary details without repeating information that can be found in the methods sections of other chapters.

The experiments took place in two different flumes with the same bend geometry at different scales. Both flumes have a long straight entrance section, a single 135° bend with a radius of curvature of 1.5 times the channel width (measured from the channel centreline), and then a straight exit section. The dye and ADV tests took place in the large bend flume, while PIV measurements took place in the small bend flume. Figure 3.1 shows a schematic of both flumes, with dimensions for each. The geometry of the simulations is a representation of the small bend flume.

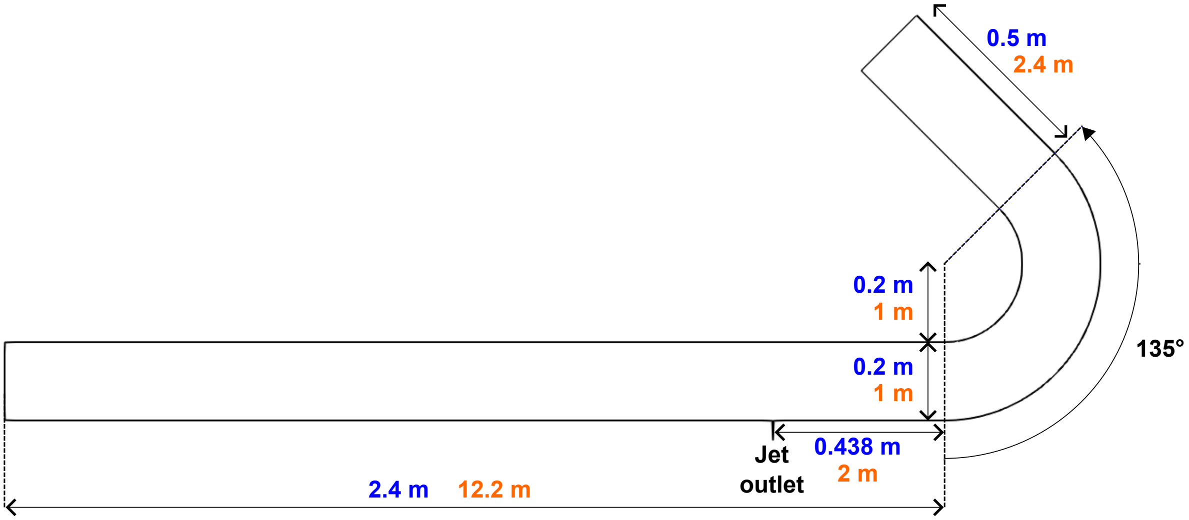

Figure 3.1: Schematic for both bend flumes, including dimensions for the small flume in blue and for the large flume in orange

3.1 Scaling

The jet and channel bend combination studied in this thesis is meant to be a representation of an effluent jet entering a river upstream of a bend; therefore it is important to scale the system in such a way as to preserve the relative scales of each part of the system. Scaling down a jet and channel bend system can be broken down into two problems: scaling the channel flow, and scaling the jet so as to maintain the relative size and strength of the two. Each problem requires a careful analysis of dimensionless parameters. Conditions in each flume should be chosen to have similar scaling parameter values to each other and to typical full scale situations.

The three most important dimensionless parameters for open channel flow in a bend are the Froude number, the aspect ratio, and the relative radius of curvature, R/B. The Froude number is the primary parameter for scaling, but ideally all three would be kept the same at every scale. The width-to-depth ratios of rivers are usually between 10 to 100, but Yalin (1971) suggests a minimum width-to-depth ratio of 5 for models of rivers.

Unfortunately it is not possible to keep the same aspect ratio in the small flume as in the large flume and in natural rivers. The flow for PIV must be deep enough to have a substantial vertical space between the regions close to the bottom and the water surface, as both may be covered by reflections and therefore not measurable. The ideal flow depths in the small bend flume are between 6 and 10 cm deep; by contrast, maintaining the minimum width-to-depth ratio of 5 would require a flow depth of 4 cm in the small flume. By extending the simulated flow depths to include values from 4 to 10 cm, and testing flow conditions experimentally in the small flume with depths of 6 and 10 cm, we can meet both requirements for at least some of the flow conditions.

The practice of scaling horizontal and vertical measurements by different fractions (i.e. to get a deeper water depth as above) is known as *distorted scaling*. Fischer and Holley (1971) caution against using distorted scaling in mixing models because it changes the relative strength of horizontal and vertical mixing. This problem can be mitigated if it can be shown that the effluent is vertically mixed before the start of the bend. Dye tests in the small flume have shown that this is not entirely true for the greatest flow depths: while the dye reaches the surface and the bed before the start of the bend, it is not uniformly mixed vertically until after the bend has begun. Unfortunately the need for PIV measurements means that we cannot operate entirely at depths where vertical mixing is guaranteed before the bend. The assumption of complete vertical mixing at all times is an important simplifying assumption for many river mixing problems. However, the assumption is unlikely to hold true at every point of a bend, where secondary circulation is constantly working to overturn the concentration distribution profile. Even in the large bend flume experiments which had a vertical scale more similar to natural rivers and which showed complete vertical mixing before the start of the bend in every case, the concentration distribution in the bend itself was not fully vertically mixed due to the influence of the secondary circulation.

Flow rates are chosen to maintain Froude numbers from 0.045 to 0.22. The range of Froude numbers chosen here is within the range studied by Farhadi et al. (2018), who found that an increase in Froude number caused an expansion of the main secondary circulation cell, and pushed the outer bank cell toward the boundary. This range is on the low end of Froude numbers found in natural rivers, however Wei et al. (2016) found that for larger Froude numbers the secondary circulation in the bend was not significantly affected by changes in Froude number.

In order to scale the jet relative to the flume, one must first decide which jet parameters to use. One easy choice is m_r, the momentum ratio from equation 1.16 which is more thoroughly described in Chapters 1 and 4. This will be the primary scaling parameter. It is also important to consider the relative size of the jet nozzle in comparison with the channel depth and width, which can be summarised in the dimensionless parameters d/h and d/B respectively. These two values will scale differently because of the distorted scaling explained above. Typical outfalls into rivers have $d/h \approx 1/10$ (Grace, 2009), though Rajaratnam and Langat (1995) state that for maximum dilution, outfalls should be designed with $d/h < 1/20$. Therefore a jet outlet of inner diameter 4.76 mm will be used. In the small flume, this value satisfies the stated realistic scale for the h=5 cm conditions (which are the most representative of realistic rivers), having a ratio of $d/h \approx 0.1$. It also satisfies Rajaratnam and Langat's recommended scale for the h=10 cm conditions (with $d/h \approx 0.05$), and is a standard imperial size for valves and tubing. The disadvantage of this size jet outlet is that it is large relative to the channel width. For the sake of comparison with a smaller jet outlet, in Chapter 6 a second jet condition is also simulated which uses a jet dimension of 2.38 mm and the same jet flow rate (which therefore has a velocity ratio of 8.7 and a momentum ratio of 3.0) .

There is a wide range of velocities in effluent jets; studies on such jets in crossflows use velocity ratios ($r = u_{jet}/u_{cf}$) anywhere from 0.5 to 30 (Zhang and Yang, 2017), corresponding to a momentum ratio between 0.025 and 90, assuming a diameter-to-depth ratio of 1/10. To compromise for jet diameter being relatively large compared to the channel width, we kept this investigation to the lower end of the momentum ratio range in order to prevent the jet from impinging on the inner bank too quickly.

Table 3.1 shows the flow conditions used in the large flume dye tests. These conditions are chosen to have the same range of Fr and m_r as previously discussed, and have a water depth of either

15 or 20 cm, which gives a more realistic aspect ratio for natural rivers than the depths which are feasible in the small flume. The jet diameter is kept constant between the two scales, and therefore the large flume experiments satisfy Rajaratnam and Langat's recommendation for jet-to-water depth ratio, with $d/h \approx$ 0.024–0.03. The conditions with the higher flow rate have ADV measurements in addition to dye tests, and corresponding velocity measurements without the jet are also taken for those flow conditions

Table 3.1: Flow conditions for tests in the large flume

Q_{cf} (m^3/s)	h (cm)	Q_{jet} (mL/s)	Fr	m_r
0.017	0.2	3.4	0.061	0.104
0.017	0.2	6.8	0.061	0.422
0.017	0.15	3.4	0.093	0.0774
0.017	0.15	6.8	0.093	0.312
0.026	0.2	3.4	0.094	0.0464
0.026	0.2	6.8	0.094	0.187
0.026	0.15	3.4	0.144	0.0346
0.026	0.15	6.8	0.144	0.138

Table 3.2 shows the exact values of h and m_r used in the small flume scaled investigation, the flow rates required for each combination, and the resulting Froude number. Using seven water depths and five momentum ratios results in 35 total combinations, all of which were investigated with and without the jet running. Three flow conditions, highlighted in blue italics in table 3.2, are studied with PIV in order to be used to validate the OpenFOAM simulations. One of these conditions, shown in bold, has been selected to be studied in the greatest amount of detail. The flow conditions are referred to henceforth using their water depth, the flow rate of the crossflow, and the flow rate of the jet rounded to the nearest mL; for instance, the run in bold in table 3.2 has name h6Q693j2.

Table 3.2: Flow conditions for tests in the small flume

m_r	h	4 cm	5 cm	6 cm	7 cm	8 cm	9 cm	10 cm
0.075	Q_{jet}	1.58	1.58	*1.58*	1.58	1.58	1.58	1.58
	Q_{cf}	894	1000	*1095*	1183	1265	1342	1414
	Fr	0.178	0.143	*0.119*	0.102	0.089	0.079	0.071
0.1	Q_{jet}	2.23	2.23	2.23	2.23	2.23	2.23	2.23
	Q_{cf}	1095	1224	1342	1449	1549	1643	1732
	Fr	0.219	0.175	0.146	0.125	0.109	0.097	0.087
0.15	Q_{jet}	2.23	2.23	2.23	2.23	2.23	2.23	2.23
	Q_{cf}	894	1000	1095	1183	1265	1342	1414
	Fr	0.178	0.143	0.119	0.102	0.089	0.079	0.071
0.25	Q_{jet}	2.23	2.23	2.23	2.23	2.23	2.23	*2.23*
	Q_{cf}	693	775	848	917	980	1039	*1095*
	Fr	0.138	0.111	0.092	0.079	0.069	0.061	*0.055*
0.375	Q_{jet}	2.23	2.23	***2.23***	2.23	2.23	2.23	2.23
	Q_{cf}	566	632	***693***	748	800	849	894
	Fr	0.113	0.09	***0.075***	0.065	0.056	0.050	0.045

3.2 Sampling Time

The velocity data in the large flume experiments, used in Chapter 4, were taken for a sampling length of 2 minutes. The sampling length was established to be sufficiently long by means of a running mean test over 5 minutes displayed in figure 4.3. This test was taken at the 90 degree cross section 80 cm from the outer bank, since preliminary tests had suggested that that location had a longer convergence time than elsewhere in the bend.

As measures of the sufficiency of sample length in the small flume, both a moving average and autocorrelation of velocity components were used, as defined in the equations:

$$\text{moving average } \bar{x}_j = \sum_{t=1}^{j} x_t \tag{3.1}$$

$$\text{autocorrelation } r_j = \frac{1}{Nc_0} \sum_{t=1}^{N-j} (x_t - \bar{x})(x_{t+j} - \bar{x}) \tag{3.2}$$

for a time series x_t with variance c_0, mean $\bar{x}$, and total N samples. The moving average and autocorrelation are calculated for each time lag, represented by j. The samples are considered sufficiently long when they include enough time lags for the autocorrelation function to cross zero or the moving average curve to appear to flatten out.

The LES of the small scale bend flow was allowed to develop its flow for 90 s before taking any results, and was subsequently run for 100 s of sampling time, and saved velocity data every half second. Figure 3.2 shows an autocorrelation function as well as a running mean of each velocity component from the simulated data, not including the development time. The data are taken from several locations in the 90 degree cross section of the h6Q693 condition in order to include the same location which was believed to have the longest convergence time in the large flume. The autocorrelation functions of all the observed points cross zero before 80 time lags (or 40 seconds), and the running mean shows velocity convergence before 100 time lags. Therefore a sampling time of 100 s is deemed to be very conservative.

Note that frequently, a stricter requirement of the autocorrelation function is required of LES data to ensure a sufficiently long LES time sample: the autocorrelation function must not only cross zero, but remain flat afterwards. This is based in the assumption that the turbulence is entirely random (Burchard, 2008); autocorrelation functions of flows that include coherent structures behave differently, and take longer to converge (Fang et al., 2017). The autocorrelation functions in figure 3.2 show slower convergence for the streamwise and cross-stream velocity components, indicating large coherent structures in the horizontal plane. These are likely connected to flow separation at the inner bank. In order to ensure the LES sample is long enough, we must compare the sample length to the time scale of the coherent structures. The average time scale can be calculated as the integral of the autocorrelation function from the y-axis to the first x-axis zero, calculated as 8.8 s for the slowest-converging point. The longest time scale of the coherent structures can be read first zero of the autocorrelation function, which is 31 s. Therefore 100 s is sufficient time to capture several coherent structures.

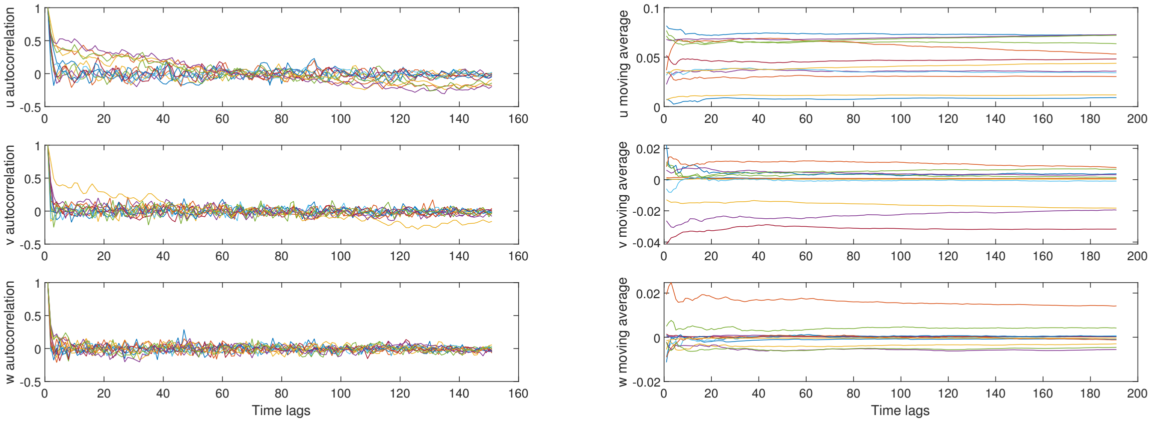

Figure 3.2: Autocorrelation and moving average of simulated velocity components at several points in the 90° cross section

Figure 3.3 shows the same autocorrelation and moving average quantities at the 90° cross section for the h6Q693 flow condition in the small flume, measured with PIV. The convergence time is visibly much smaller than the simulated convergence time by both measures. This is not to say that the large structures that increase the convergence time in the simulations are not present in the experiment; it may be that they are simply not in the field of view. Specifically, the edges of the cross sections are not covered in the PIV measurements because of interference with reflections off the flume walls. Since the coherent structures in question are specific to the area close to the inner bank, they might be covered by wall reflections and therefore not detectable within the PIV field of view. Therefore, and in order to keep the comparisons between LES and PIV most directly comparable, we take the same conservative sampling time of 100 s as for the simulation.

3.3 Numerical Methods

The details of the LES methods are presented in subsequent chapters where applicable, but here a thorough background of the dynamic k equation turbulence model is presented. For the complete

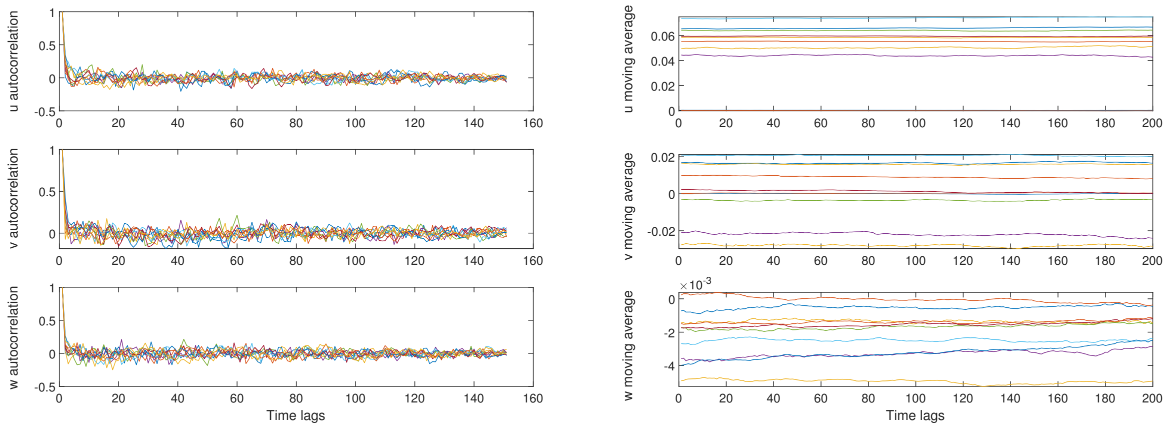

Figure 3.3: Autocorrelation and moving average of measured velocity components in the small flume at several points in the 90° cross section

implementation of the LES work in OpenFOAM, see Appendix E. For details on the choice of treatment for the air-water interface, see Appendix D.

Blanckaert and Graf (2004) showed experimentally that kinetic energy is transferred from turbulence to mean flow in the OBC. The OBC also gains circulation through the centrifugal force term, but the interaction between the OBC formation mechanisms is complex and neither mechanism can be ignored. Modelling the OBC development thus requires a turbulence closure model with the possibility of energy moving from turbulence to mean flow, counter to the direction assumed by many turbulence closure models.

Dynamic models, first proposed by Germano et al. (1991), are a category of LES subgrid scale models that calculate model coefficients based on local flow parameters. If the coefficients are calculated to be negative, energy can flow from subgrid scales into larger scales of motion, simulating the effect known as *backscatter*. This effect is only modelled to occur in regions with negative coefficients, such as the outer bank cell location; in other regions, the energy cascade is simulated as usual, though with better-tuned coefficients.

The most completely implemented dynamic model in OpenFOAM is the dynamic k equation model first proposed by Kim and Menon (1995). It is a dynamic version of the model developed by

Yoshizawa (1986), and it does not assume local equilibrium of subgrid scale energy production and dissipation as the Samgorinsky model does, but instead applies the following transport equation for k_{SGS}:

$$\frac{\partial k_{SGS}}{\partial t} + \hat{u}_i \frac{\partial k_{SGS}}{\partial x_i} = -\tau_{ij} \frac{\partial \hat{u}_i}{\partial x_j} - c_\epsilon \frac{k_{SGS}^{1.5}}{\Delta} + \frac{\partial}{\partial x_i} \left(\nu_T \frac{\partial k_{SGS}}{\partial x_i} \right) \tag{3.3}$$

where τ_{ij} are the subgrid stresses and ν_T is the SGS eddy viscosity:

$$\tau_{ij} = -\nu_T \left(\frac{\partial \hat{u}_i}{\partial x_j} + \frac{\partial \hat{u}_j}{\partial x_i} \right) + \frac{2}{3} \delta_{ij} k_{SGS} \tag{3.4}$$

and

$$\nu_T = c_\nu k_{SGS}^{0.5} \Delta \tag{3.5}$$

and the model coefficients c_ν and c_ϵ are calculated based on local flow. In particular, c_ϵ defines the rate of turbulence dissipation, and is negative in regions where backscatter occurs.

As a demonstration of the advantage of using the dynamic k equation to model the outer bank cell, consider the comparison in figure 3.4 of the secondary circulation from the dynamic k equation and Smagorinsky models on the same mesh, as well as Smagorinsky on a mesh refined by a factor of two in every direction throughout the bend. The dynamic k equation and refined Smagorinsky simulations show very similar results in terms of the sub-cells that develop and their positions, especially the outer bank cell. The unrefined Smagorinsky model shows a comparatively underdeveloped outer bank cell, which also disrupts the placement of the other sub-cells. From this example one can draw the following conclusion: On a sufficiently refined mesh where the energy transfer between turbulent scales and mean flow can be explicitly modelled, the outer bank cell will appear in a Smagorinsky model. By switching to the dynamic k equation, this transfer is modelled indirectly in the SGS, but with comparable results to the refined Smagorinsky model. This loosens

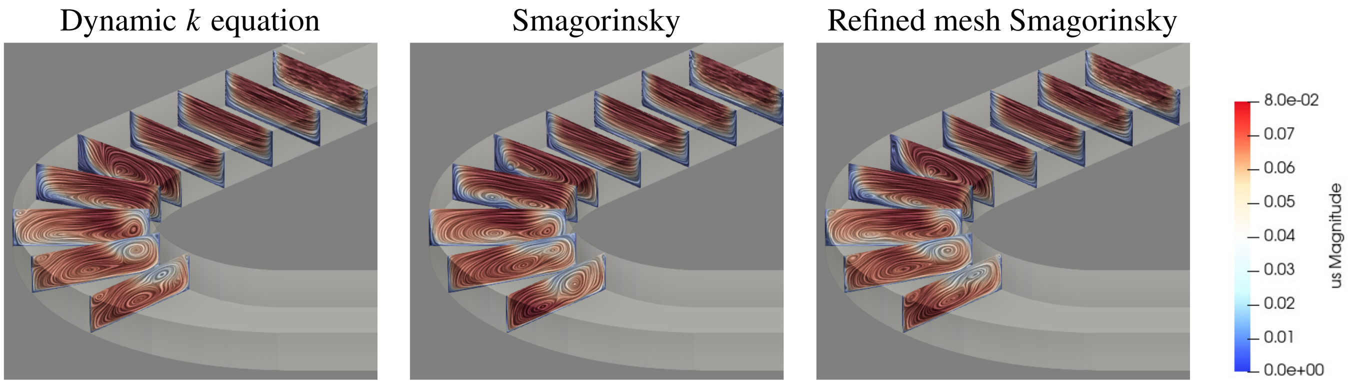
Dynamic *k* equation

Smagorinsky

Refined mesh Smagorinsky

Figure 3.4: Comparison of h6Q693 case with dynamic *k* equation and Smagorinsky subgrid scale modelling

the grid resolution requirements of the simulation, allowing the use of far fewer computational resources.

3.4 Experimental Methods

The small bend flume in the PIV room of the hydraulics lab has a self-contained recirculating water system, separate from the rest of the hydraulics lab, consisting of an inlet tank, an outlet tank, and a pump connecting the two. It is therefore able to maintain the standards of water quality necessary for PIV. The outlet tank is divided into two sections separated by a v-notch weir, allowing the flow rate to be measured using the water height above the weir and a calibration curve. The depth of water in the flume is controlled with an end gate, and the flow rate is controlled using a valve on the end of the pump hose. The flow rate of the jet is driven with a constant head tank placed above the flume, and controlled by a valve.

The PIV experiments used a LaVision Flowmaster system run by DaVis 10.2.1. The field of view is at the 90° cross section. Measurements are taken at a frequency of 2 Hz over 100 s, in keeping with the findings on sufficient sampling time, as outlined in section 3.2. While much faster sampling is possible for short times with the current system, the required length of sample was more feasible to achieve with a low frequency to limit the amount of data being written to disk during sampling.

The water for PIV was seeded with 10 µm diameter hollow glass spheres, using a concentration of approximately 1 tsp of seeding particle slurry in the small flume's self-contained reservoir.

The calibration used a custom 10 cm by 20 cm 3D printed calibration plate, with parameters defined through DaVis's user-defined calibration plate options. The proprietary polynomial calibration algorithm that DaVis 10 uses was found to account for the distortion from the curved wall without needing any optical modifications.

The time difference between the images of the particles (i.e. the frames of a single measurement, captured as two separate images in dual frame mode) varies within the range of 4000 to 6000 μs, with the precise value set to keep the particle movement between frames within the ideal range, as outlined in Section 5.4 of Appendix C. The interrogation window is 64 by 64 pixels, with an overlap of 75% between windows, giving a final spatial resolution of approximately 1.2 mm. Because of the highly reflective nature of the seeding particles and the optics of the cameras, each particle appears larger in the PIV images than spatial resolution alone would suggest, with most seeding particles appearing to take up between 3 to 5 pixels. This is slightly bigger than the optimal size of 2 to 3 pixels (Michaelis et al., 2016), and thus sufficient to avoid peak-locking errors.

Further details of the PIV methods can be found in Appendices A, B and C.

Chapter 4

Trajectory of a jet in crossflow in a channel bend

Abstract

Mixing in rivers is an important issue with many applications in water quality and water resource management. Mixing of effluents with ambient river water is especially important, particularly in river bends, where secondary circulation complicates the mixing process. By comparing measured trajectories from dye tests to velocimetry data measured with an acoustic Doppler velocimeter, this paper models the trajectory of a jet in an open channel bend using a modified formula for a jet trajectory in a straight crossflow. The original formula is shown to be insufficient for modeling the trajectory in the bend. Modifications are proposed using the position of the centre of the main secondary circulation cell to account for the bend effects. In the absence of secondary circulation, the modified formula reduces to the original formula. Once the secondary circulation has developed, the proposed formula is shown to have better residuals, lower root mean squared error, and higher R^2 than the original formula.

4.1 Introduction

Natural water systems are used as drinking water sources and for recreation, and protecting them from pollution is important for public health and environmental preservation. Water systems are also used in the disposal of treated wastewater and industrial effluent, typically injected into the river in the form of a jet, either from the channel margin or via a diffuser pipe placed along the river bed. If the effluents are not managed correctly there can be many consequences for water systems, including toxic algae blooms and harmful effects on fish species. As the human population grows and becomes more concentrated in urban centres, and the need for industry and wastewater treatment facilities grows correspondingly, it is increasingly important to build outfalls in a sustainable way in order to protect water systems. This is accomplished through developing and applying environmental regulations around how and when effluent can be put into rivers, lakes, and seas. Environmental regulations on effluent in rivers usually include a minimum dilution requirement that the effluent must meet before reaching a given distance from the outfall. In order to determine whether a proposed outfall will meet the dilution requirement, it is important to be able to model how the effluent mixes with the ambient river water. River mixing takes place via several mechanisms including molecular and turbulent diffusion and advection (Fischer, 1969), and can be difficult to model especially in river bends where the secondary circulation complicates the turbulence and advection. This paper presents a new method of predicting mixing in river bends, using the approach of predicting the trajectory of a jet in a crossflow, with modifications to account for the secondary circulation in the bend.

There have been many other studies on jets into crossflows (Ben Meftah et al., 2017; Iyer and Mahesh, 2016; Malcangio and Mossa, 2016; Smith and Mungal, 1998; Wit et al., 2014), most of which have focused on near field turbulence structures. Pratte and Baines (1967) studied the trajectories of jets in crossflows for downstream distances up to 1400 times the jet diameter, and developed the formula:

$$\frac{n_{jet}}{d} = A \cdot r \left(\frac{s}{d \cdot r} \right)^b \tag{4.1}$$

where n_{jet} is the cross-stream distance to a defined point in the jet plume (jet centreline, jet bottom, or jet top), d is the diameter of the jet, A and b are fitted parameters, s is the downstream distance from the jet, and r is the ratio of jet velocity to crossflow velocity, $r = u_{jet}/u_{cf}$ where u_{jet} is the jet velocity and u_{cf} is the velocity of the crossflow.

Equation (4.1) was developed for a jet into an infinitely wide crossflow. The experiments presented in this paper take place in a shallow flume, where the jet is limited by the surface and the bed. Seo et al. Seo et al. (2001) showed that for tee diffusers into shallow crossflows, the plume after surfacing followed the path described by:

$$\frac{n_{jet}}{L_d} = A \cdot m_r \left(\frac{s}{L_d \cdot m_r} \right)^b \tag{4.2}$$

where A and b are again fitted parameters, L_d is the distance between diffuser ports, and m_r is the ratio of jet momentum to crossflow momentum, $m_r = (u_{jet}^2 B_{diff})/(u_{cf}^2 h)$ where h is the depth of water in the flume and B_{diff} is width of an equivalent slot diffuser, which in the limiting case of a tee diffuser with one round outlet is simply the diameter of the nozzle, d. This paper explores the applicability of (4.2) in crossflows going around a channel bend. Since L_d is not well defined in the case of only one jet nozzle, n_{jet} and s will be normalized using d instead, following the convention for single outlet jets (Malcangio and Mossa, 2016; Pratte and Baines, 1967; Smith and Mungal, 1998).

The above studies of jets in crossflows used straight crossflows that flowed in only one direction, denoted as the s-direction. Many open channel flows are more complex, developing secondary circulation which adds cross stream and vertical components (n- and z- components, respectively) to the flow. Secondary circulation can be induced in straight channels under certain circumstances (Nezu and Nakagawa, 1993). It is also a defining characteristic of flow in bends (Booij, 2003; Booij

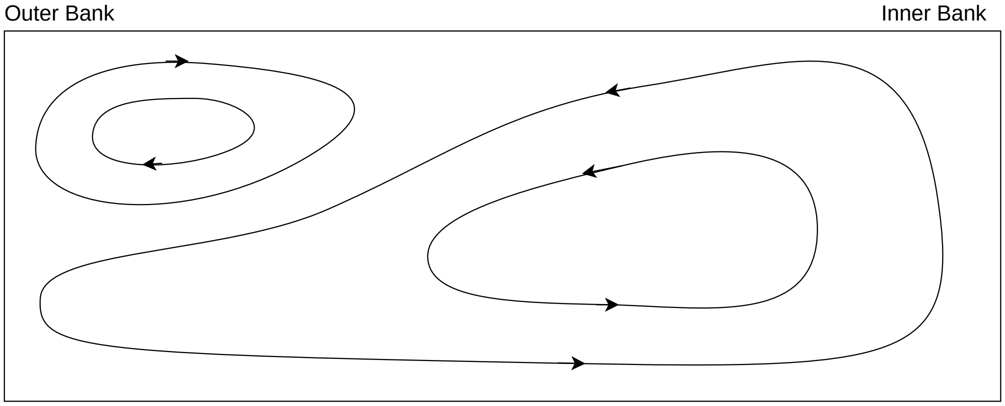

Figure 4.1: Circulation cells in a typical bend

and Tukker, 1996; Muto, 1997; Shiono and Muto, 1998). The secondary circulation changes the way contaminants mix via advection and turbulent diffusion (Fischer, 1969).

There is one principal cell of secondary circulation in river bends, bringing the water at the surface toward the outer bank and the water at the bed toward the inner bank. This is the centre cell. The centre cell is not the only cell that can develop in river bends, but it is certainly the most consistently seen and has the strongest circulation. In addition to the centre cell, there is often a cell circulating in the opposite direction near the surface at the outer bank, driven by turbulent anisotropy. The outer bank cell has not been observed as extensively as the centre cell, as its small size and velocities and its intermittent behaviour make it difficult to resolve (Blanckaert and Graf, 2001). The cells are shown in fig. 4.1.

In high curvature bends, it is possible to have even more complex patterns of circulation cells. Kashyap et al. (2012) showed two ways in which the centre cell can split, with one sub-cell that splits off at the inner bank and one at the outer bank. When the main cell splits, all the sub-cells rotate in the same direction, though their individual contribution to total circulation varies for each cell and for location through the bend. The structure of secondary circulation depends largely on the aspect ratio of the flow. The paths that each cell follows through the bend were studied by Kashyap et al. (2012), but to the authors' knowledge, there is no definitive method of predicting the path or presence of any circulation cell.

In a straight open channel the maximum velocity in a given cross section is found near the surface in the centre of the channel. This is not so in channel bends: the maximum velocity core starts close to the inner bank before moving outward through the bend, eventually reaching the outer bank after the bend. The maximum velocity also moves down and does not occur at the surface in the bend (Blanckaert and Graf, 2004). The shift toward the inner bank at the beginning of a bend was first thought to only be an effect of previous bends, but de Vriend and Geldof (1983) showed that is not the case, and that non-uniformity of flow in the bend and the redistribution of streamwise momentum are likely factors in causing the shift.

For weakly curved bends, the strength of the secondary circulation is linearly proportional to the curvature of the bend, h/R where R is the channel's radius of curvature (Rosovskii, 1961). For bends of strong curvature, the secondary circulation changes the vertical velocity profile and thus disrupts the driving mechanisms behind the secondary circulation, leading to saturation of the secondary circulation strength (Blanckaert, 2009). A more accurate model of secondary flow was developed by Blanckaert (2010) and Blanckaert (2003), and was later experimentally verified (Ottevanger et al., 2012; Wei et al., 2016).

There are many difficulties in the study of mixing in river bends. For instance, channel geometry has a strong influence on mixing, making it difficult to apply the results of one experiment to a different channel with different geometry. There are also several mixing mechanisms at work, including molecular and turbulent diffusion and advection from secondary circulation. Concentration fields can be predicted using the advection-diffusion equation (Rutherford, 1994):

$$\frac{\partial}{\partial t}(h\langle C\rangle) + \frac{\partial}{\partial s}(hu_s\langle C\rangle) + \frac{\partial}{\partial n}(hu_n\langle C\rangle) = \frac{\partial}{\partial s}\left(hD_s\frac{\partial\langle C\rangle}{\partial s}\right) + \frac{\partial}{\partial n}\left(hD_n\frac{\partial\langle C\rangle}{\partial n}\right) \tag{4.3}$$

Where $\langle C\rangle$ is the depth averaged concentration, t is time, u_s is the streamwise velocity, u_n is the cross stream velocity, h is the water depth, and D_s and D_n are the dispersion coefficients in the streamwise and cross stream directions, respectively. To account for the secondary currents in bends, which increase mixing via advection and turbulent diffusion, the transverse mixing coefficient can be increased (Rutherford, 1994). It has been shown that $\log{(D_n/hu_*)} \propto \log{(u_s B/u_* R)}$, though there is disagreement on the coefficients of proportionality (Seo et al., 2016; Yotsukura and Sayre, 1976).

Because of the structure of flow in river bends, advection and turbulent diffusion both depend on the location within the bend. Uniformly increasing the dispersion coefficients to account for the sinuosity in rivers does not account for this spatial variation. The spatial variation of the dispersion coefficients can be mapped out in detail using tracer tests, or can be calculated from measured or simulated velocity fields (Carr and Rehmann, 2007; Lee and Seo, 2012). Concentration fields in rivers have been measured directly (Dow et al., 2009; Pilechi et al., 2014; Zhang and Zhu, 2011), though it can be difficult, as the distance from the outfall to a fully mixed condition is often very large. This means a large measurement area for the experiment and also a large amount of tracer that needs to be injected.

The goal of this paper is to model the mixing in a single channel bend using the trajectory of a jet in a crossflow. The model is developed using data of transverse dispersion of a cross-flow effluent jet in a laboratory channel bend flume. The jet trajectory was traced using dye and velocity measurements were obtained at sections along the trajectory. The entire experiment takes place within 950 jet diameters downstream of the jet, putting it within the range where (4.1) was developed. Using (4.2) instead of (4.3) allows for the jet parameters to be taken into account easily, which in turn sets the stage for parametrical studies on how jet and channel conditions affect mixing in river bends.

In this paper, the methods for the dye tests and the velocimetry measurements will be detailed. The results from the dye tests will then be presented, and the dye test results will be compared to the jet trajectory predicted using (4.2). The velocimetry results will then be discussed, with special attention to the centre of the main circulation cell. A modified formula will be suggested using the cell centre to account for secondary circulation. The predicted results using this formula will be compared to the dye test results, and it will be shown that this formula gives more accurate predictions than the formula for jet trajectories in a straight crossflow, (4.2).

4.2 Experimental Methods

The flume used in these experiments is 1 m wide with a rectangular bed, and consists of a 12.2 m straight approach, a 135° bend of radius 1.5 m measured from the channel centre, and a 2.4 m straight exit. Details of the flume setup can be found in Jamieson et al. (2010) and Post (2007). The jet was placed in the flume at 10 m from the flume entrance, where the flow is fully developed but the effects of the bend have not yet started. The jet nozzle was a submerged tube that was horizontal, perpendicular to the flow, 3 cm long, and 5 cm from the floor of the flume with inner diameter 4.8 mm. It was controlled by a peristaltic pump.

For the dye tests, the jet was infused with a blue dye mixture (a 10% solution of Regal blue food dye, containing FD&C Blue No. 1), and the distance from the bank with the jet to the furthest point across the flume with a visible concentration of dye at any instant (transition point distance (TPD), shown in Fig. 4.2) was measured every 15° throughout the bend. Figure 4.2 also shows the opposite wall contact point, θ, the first angle where the dye reached the opposite bank. The dye tests were conducted for trials with different jet locations (inside or outside bank), different jet temperatures, flume flow rates Q_{cf}, flume depths h, and jet speeds u_{jet}. Parameters for each trial are shown in Table 4.1. The characteristic length, l_m, is the length separating the near and far fields. It is defined as: $\sqrt{\frac{\pi}{4}}rd$ (Hodgson et al., 1999). From Table 4.1, it is clear that this division takes place between 4 and 19 mm downstream of the jet nozzle, which is a long way before the start of the bend 2 m downstream of the nozzle. Therefore the experiments presented in this paper are definitively in the far field.

The parameters shown in the dye tests to influence mixing throughout the bend (h and u_{jet}; see below) and the angles where the bend effects were most apparent in the dye test data (45°, 67.5°,

Table 4.1: Summary of dye test trials

Run name	Bank with outfall (**o**uter/**i**nner)	Dye solution temperature (°C)	Flume temperature (°C)	Buoyancy difference (%)	Flume flow rate (m^3/s)	Flume water depth (cm)	Flume Reynolds number	Jet speed at nozzle (m/s)	Jet speed to flume speed ratio, r	Characteristic length, l_m (mm)	Jet to flume momentum ratio, m_r
RTQ1h2j1	o	-	-	0	0.0175	20.4	17543	0.181	2.10	8.94	0.104
RTQ1h2j2	o	-	-	0	0.0175	20.4	17543	0.364	4.24	18.2	0.422
RTQ1h1j1	o	-	-	0	0.0175	15.3	17543	0.180	1.57	6.68	0.0774
RTQ1h1j2	o	-	-	0	0.0175	15.3	17543	0.362	3.15	13.4	0.312
RTQ2h2j1	o	-	-	0	0.0262	20.4	26208	0.180	1.40	5.97	0.0464
RTQ2h2j2	o	-	-	0	0.0262	20.4	26208	0.362	2.82	12.0	0.187
RTQ2h1j1	o	-	-	0	0.0262	15.2	26208	0.180	1.05	4.45	0.0346
RTQ2h1j2	o	-	-	0	0.0262	15.2	26208	0.361	2.09	8.91	0.138
HOTQ1h2j1	o	34.7	21	0.39	0.0170	20.7	17038	0.180	2.19	9.33	0.111
HOTQ1h2j2	o	34.7	21	0.39	0.0170	20.4	17038	0.362	4.34	18.4	0.442
HOTQ1h1j1	o	34.7	21	0.39	0.0170	15.3	17038	0.180	1.62	6.89	0.0824
HOTQ1h1j2	o	34.7	21	0.39	0.0170	15.3	17038	0.364	3.27	13.9	0.335
HOTQ2h2j1	o	31.8	21	0.29	0.0262	20.4	26208	0.181	1.41	5.99	0.0466
HOTQ2h2j2	o	31.8	21	0.29	0.0262	20.4	26208	0.363	2.82	12.0	0.188
HOTQ2h1j1	o	31.8	21	0.29	0.0262	15.2	26208	0.181	1.05	4.46	0.0347
HOTQ2h1j2	o	31.8	21	0.29	0.0262	15.2	26208	0.362	2.10	8.93	0.139
COLDQ1h2j1	o	6	21	-0.20	0.0168	20.4	16788	0.180	2.19	9.32	0.113
COLDQ1h2j2	o	6	21	-0.20	0.0168	20.4	16788	0.363	4.41	18.8	0.458
COLDQ1h1j1	o	5.5	21	-0.20	0.0168	15.2	16788	0.181	1.64	6.96	0.0846
COLDQ1h1j2	o	5.5	21	-0.20	0.0168	15.2	16788	0.363	3.28	14.0	0.341
COLDQ2h2j1	o	6	21	-0.20	0.0262	20.3	26208	0.180	1.40	5.95	0.0462
COLDQ2h2j2	o	6	21	-0.20	0.0262	20.3	26208	0.362	2.81	11.9	0.186
COLDQ2h1j1	o	6	21	-0.20	0.0262	15.2	26208	0.181	1.05	4.46	0.0347
COLDQ2h1j2	o	6	21	-0.20	0.0262	15.2	26208	0.362	2.10	8.94	0.140
INQ1h2j1	i	-	-	0	0.0168	20.3	16788	0.180	2.18	9.27	0.112
INQ1h2j2	i	-	-	0	0.0175	20.3	17543	0.359	4.16	17.7	0.408
INQ1h1j1	i	-	-	0	0.0175	15.2	17543	0.180	1.56	6.64	0.0772
INQ1h1j2	i	-	-	0	0.0175	15.2	17543	0.364	3.15	13.4	0.313
INQ2h2j1	i	-	-	0	0.0265	20.4	26533	0.180	1.38	5.89	0.045
INQ2h2j2	i	-	-	0	0.0265	20.4	26533	0.363	2.79	11.9	0.183
INQ2h1j1	i	-	-	0	0.0265	15.4	26533	0.181	1.05	4.46	0.0343
INQ2h1j2	i	-	-	0	0.0265	15.4	26533	0.364	2.11	8.96	0.139

Temperature was not measured for trials where the dye solution was at room temperature

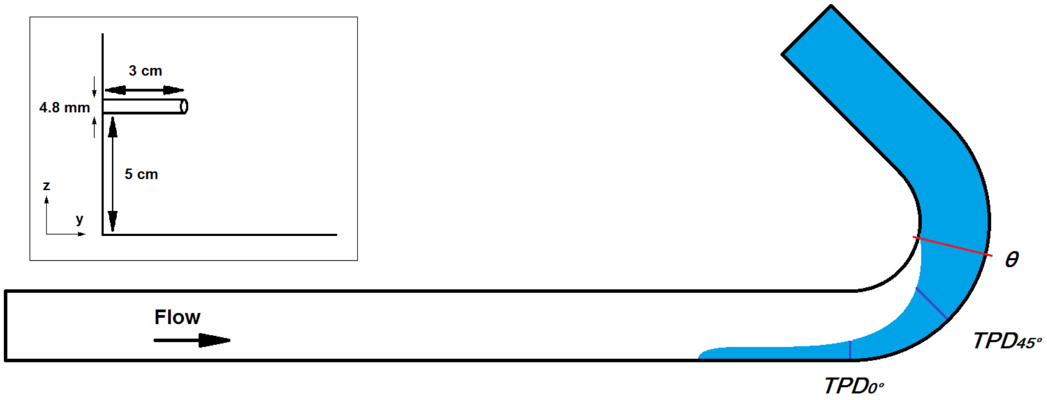

Figure 4.2: Schematic of jet and flume during dye test, showing definition of transition point distance, TPD, and opposite wall contact angle, θ

Table 4.2: Summary of ADV test trials

Run name	Water Surface Level (cm)	Jet Speed (m/s)
Q2h1j1	15	0.18
Q2h1j2	15	0.36
Q2h2j1	20	0.18
Q2h2h2	20	0.36

90°, and 0° to get the initial conditions) were examined more closely by collecting velocity data using a profiling ADV. A summary of the trial conditions for ADV tests is shown in Table 4.2. A cross section of ADV data was taken at each angle of interest using a Vectrino II profiler. Each measurement consisted of a 2.5 cm profile divided into 25 bins each of height 1.02 mm, with a 25 Hz sampling frequency for a period of two minutes. The adaptive ping algorithm was used to avoid weak spots (Nortek, 2012). The entire profile was used for mean velocity measurements, but only the centre 4 bins around the profiler's "sweet spot" were used to calculate turbulence statistics, as Brand et al. (2016) suggest is most reliable. The turbulence statistics were calculated using filtered data. The filtering methods are outlined in Jamieson et al. (2010).

ADV profiles were taken every 10 cm across the channel. The Vectrino profiler cannot measure right up to the surface of the water since the probe head must be submerged in order to take measurements. For the trials with h = 15 cm, each profile consisted of four 2.5 cm measurements, taken from 0.5 cm to 9.5 cm above the flume floor, with approximately 3 mm of overlap between each measurement. For the trials with h = 20 cm, there were 5 measurements per profile, starting at 1 cm above the flume floor and going up to 13.9 cm above the flume floor, with no overlap between measurements.

4.3 Results

In order to ensure that 2 minutes is sufficiently long to get an accurate measurement of mean velocity, one profile was taken over 5 minutes. The profile for the comparison was taken at 90°, 80 cm from the outer bank. This point was judged to be one of the more difficult points in the bend to measure, based on previous measurements, due to the presence of large turbulent coherent structures. The running mean of each velocity component, defined as the mean velocity from the beginning of the measurement to the given time, is shown in Fig. 4.3 for a representative point in the centre of the profile. It is clear that the running mean has reached an approximate equilibrium after 120 seconds, therefore it was judged that 2 minutes was a sufficient measurement time.

One profile was taken at 10 m from the flume entrance to determine whether the flow was fully developed. The streamwise velocity profiles for the h = 15 cm and h = 20 cm conditions are shown in Fig. 4.4. For both profiles, the flow clearly follows the log law for the extent of the measured profile, justifying the assumption that the flow is fully developed by the 10 m mark.

4.3.1 Dye Test Results

Figure 4.5 shows a comparison between the two jet locations used in the dye tests. It is easily seen that the outer bank jet location leads to faster mixing than the inner bank location, as predicted by

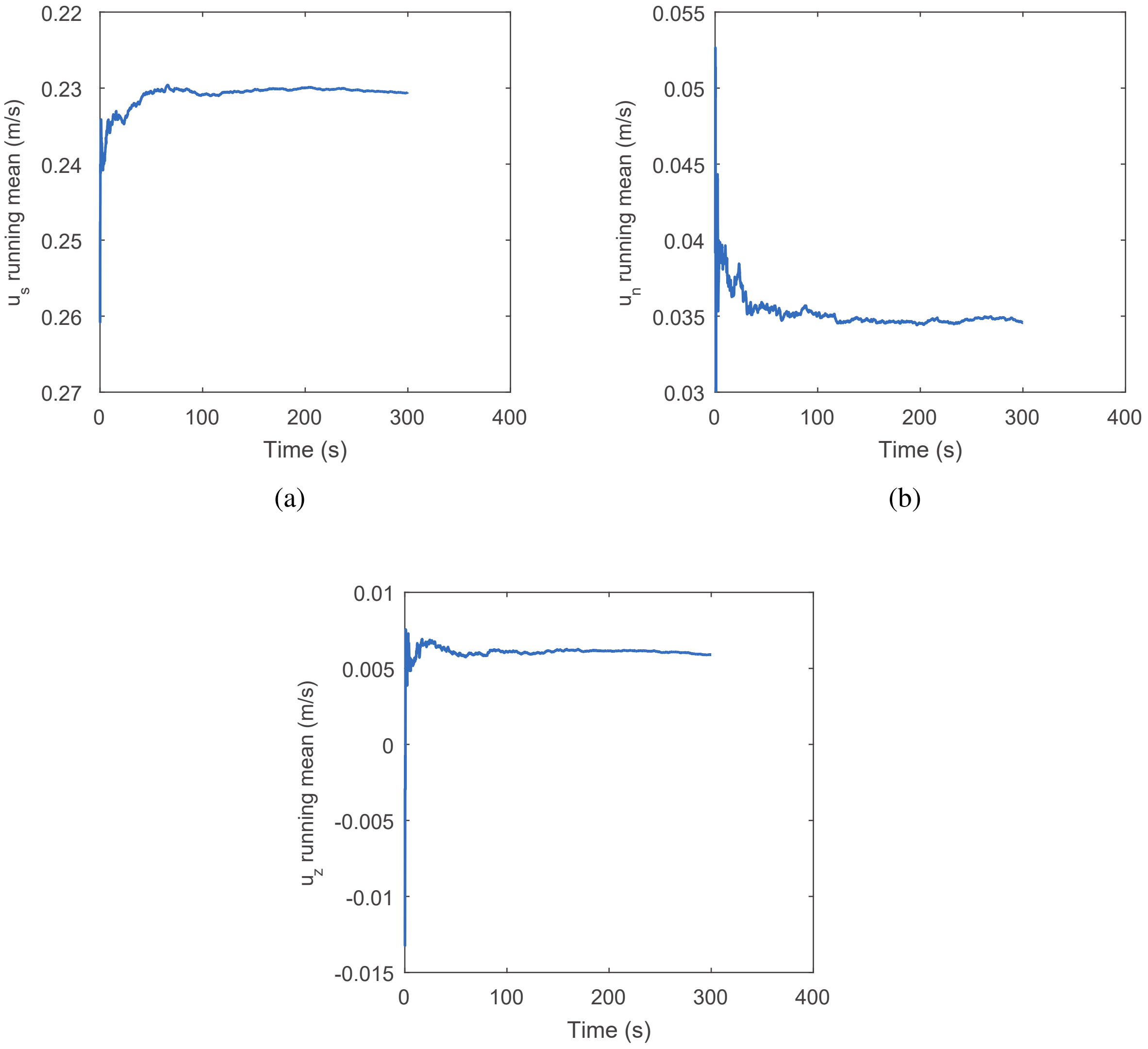

(a)

(b)

(c)

Figure 4.3: Running mean of velocity components over 5 minute measurement, shown for one point in the centre of a profile taken at 90°, 80 cm from outer bank

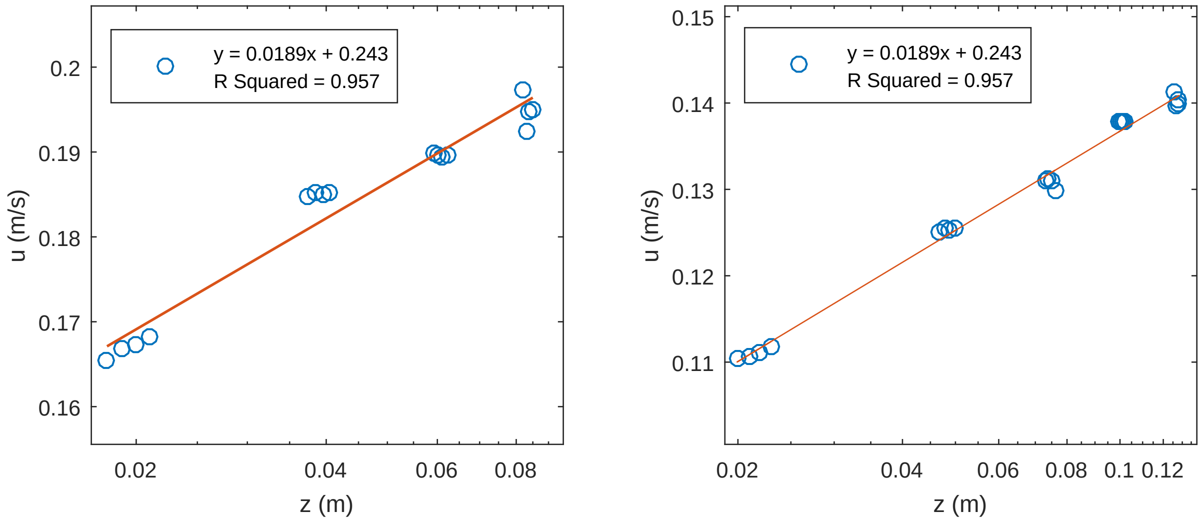

(a) (b)

Figure 4.4: Velocity profiles at 10 m from flume entrance for (a) h = 15 cm and (b) h = 20 cm

previous studies (Moncho-Esteve et al., 2017). In all the trials using the jet on the outer bank, the dye reached the opposite bank at or before 90°, while the dye from the inner bank jet never reached the opposite bank in any trial, even up to the end of the bend. Since the results from the two jet locations were not directly comparable, and there were more trials with the jet on the outer bank, the analysis will focus exclusively on the outer bank jet location.

A linear least-squares regression was applied to the dye test data, using the remaining parameters T, Q_{cf}, h, and u_{jet} to predict the opposite wall contact angle. The fitted equation and p-values for each coefficient are shown in Table 4.3. The p-value indicates the probability that the parameter in question has no influence on the contact angle θ. A small, or significant, p-value (< 0.05) indicates that it is unlikely, given the observed data, that θ is not influenced by the given parameter, and one can therefore assume that the given parameter affects the degree of mixing. While the p-values for h and u_{jet} are clearly significant, as expected based on (4.2) and the definition of m_r, those for T and Q_{cf} are not.

The temperature variation of the jet in the dye tests led to a buoyancy difference (defined as $(\rho_{cf} - \rho_{jet})/\rho_{cf}$ where ρ_{cf} is the density of the water in the flume and ρ_{jet} is the density of the jet)

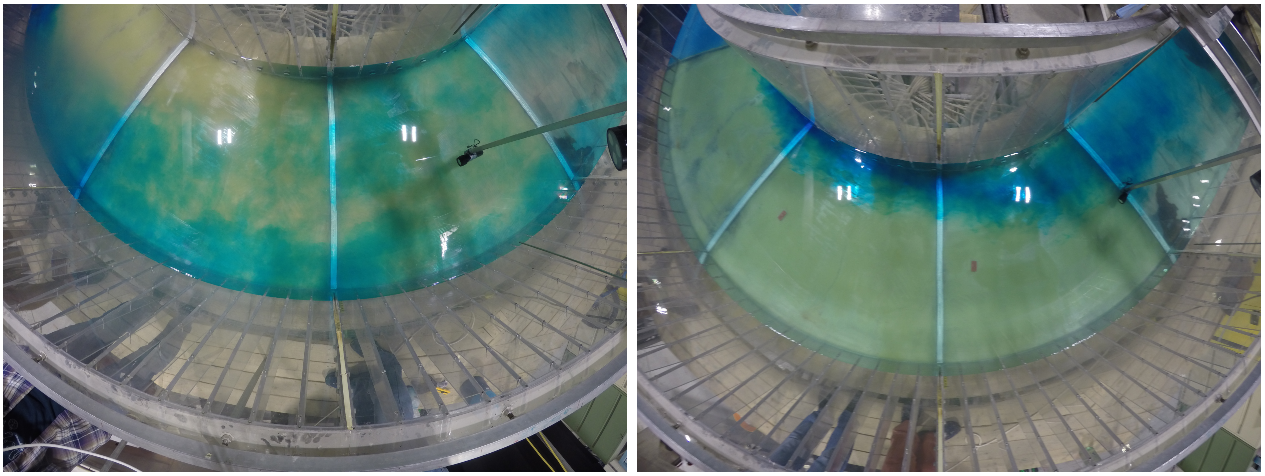

(a) (b)

Figure 4.5: Comparison of (a) outer bank jet in trial RTQ1h2j1 and (b) inner bank jet in trial INQ1h2j1. Tape lines show 45°, 90°, and 135° angles

Table 4.3: Results from opposite wall contact point regression

$$\theta = 132^\circ + 0.22T - 135Q_{cf} - 2.2h - 49u_{jet}$$

Parameter	Coefficient	P-value
T	0.22 °/°C	0.092
Q_{cf}	-135 °s/m^3	0.66
h	-2.2 °/cm	0.00071
u_{jet}	-49 °s/m	0.0050

of less than half a percent, as seen in Table 4.1. This is the largest buoyancy difference possible with this particular experimental setup, as adding substances such as salt or alcohol to the dye mixture risked contaminating the flume's reservoir. At the buoyancy difference studied, there was no observed difference in the behaviour of the jet plume at different temperatures: the plume had reached the surface and the bed before the bend entrance in every trial. Since no argument for temperature dependence based on plume behaviour or statistical significance can be made, temperature was not included in any further analysis; trials at different temperatures but otherwise identical conditions were considered to be replicates, which subsequently allowed for more robust statistical analysis.

Since Q_{cf} is directly proportional to the speed of water in the flume, Q_{cf} is also proportional to m_r, so one would expect Q_{cf} to be a good predictor of mixing if (4.2) holds in the bend. In order to examine the effects of Q_{cf} more closely, consider the linear regressions for TPD done for each angle independently. The regression results are shown for angles 0°, 45°, and 60° in Table 4.4. They show that initially Q_{cf} is a good predictor of mixing, and this holds up until 45°. However, at 60° and after, Q_{cf} no longer has a significant effect on the transition point distance. Therefore the angles investigated in the ADV tests were chosen to focus on the region where Q_{cf} transitions from significant to non-significant: 45° to 90°. By 90° the dye had already reached the opposite bank in all trials with jets on the outer bank, so there were no meaningful mixing data to compare to, and therefore no ADV data were taken after 90°.

Figure 4.6 show the raw TPD values plotted against the downstream distance s/d for flow conditions that were investigated both with dye and ADV tests, along with a pchip interpolation done with MATLAB. The figure shows that at the beginning of the bend higher m_r values correspond to higher TPD, but later in the bend this trend decreases and TPD seems to be more strongly related to flow depth h. This is consistent with the previous regression results for the significance of Q_{cf} and h.

Table 4.4: Results from transition point distance regression

(a) 0°

$$TPD = 11cm - 420Q_{cf} + 0.86h + 28u_{jet}$$

Parameter	Coefficient	P-value
Q_{cf}	-420 cm·s/m^3	0.0028
h	0.86	0.00076
u_{jet}	28 cm·s/m	0.00017

(b) 45°

$$TPD = 35cm - 385Q_{cf} + 1.5h + 27u_{jet}$$

Parameter	Coefficient	P-value
Q_{cf}	-385 cm·s/m^3	0.011
h	1.5	2.4×10^{-6}
u_{jet}	27 cm·s/m	9.3×10^{-4}

(c) 60°

$$TPD = 37cm - 56Q_{cf} + 1.8h + 20u_{jet}$$

Parameter	Coefficient	P-value
Q_{cf}	-56 cm·s/m^3	0.75
h	1.8	1.2×10^{-5}
u_{jet}	20 cm·s/m	0.033

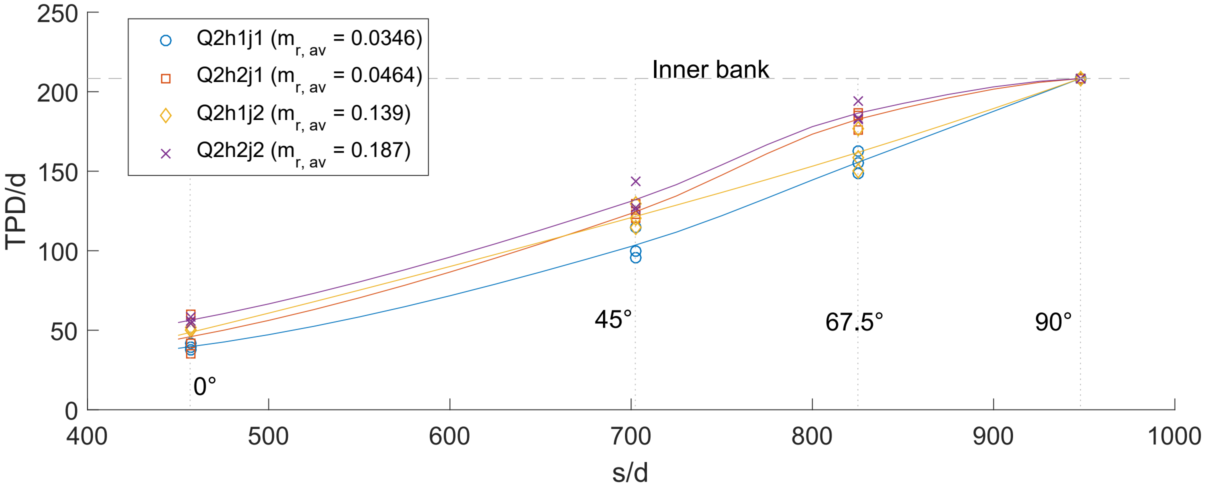

Figure 4.6: TPD vs. downstream distance s/d for various flow conditions

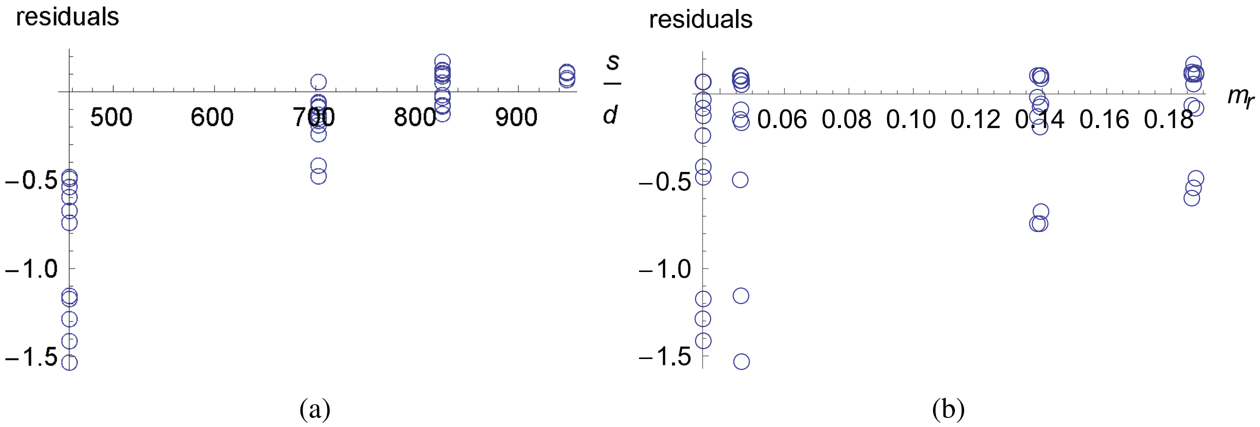

Figure 4.7: Residuals from the fit in (4.4), calculated using (4.5), vs (a) s/d and (b) m_r

4.3.2 Insufficiency of straight crossflow equation

The transition point distance as measured in the dye tests can be interpreted as the outermost edge of the jet plume, which can be modelled using (4.2). The best fit for this model, found using the Levenberg-Marquardt method (Weisstein, accessed July 2017) is given by:

$$\frac{TPD}{d} = 0.15 m_r \left(\frac{s}{d \cdot m_r} \right)^{1.0} \tag{4.4}$$

Here, s is defined as the downstream distance from the jet to the cross section in question, measured along the channel centreline to ensure consistent handling of the bend curvature. The value for b, 1.0, is much larger than the previously reported value of 0.55 (Seo et al., 2001). This model has a root mean squared error (RMSE) of 13 cm and an R^2 value of 0.95. The residuals are defined as

$$\text{residual} = \frac{TPD_{\text{measured}} - TPD_{\text{predicted}}}{TPD_{\text{measured}}} \tag{4.5}$$

and are plotted in fig. 4.7 as a function of s and m_r. It is clear from these plots that the residuals are dependent on both independent variables. Therefore this model does not properly account for mixing in the bend.

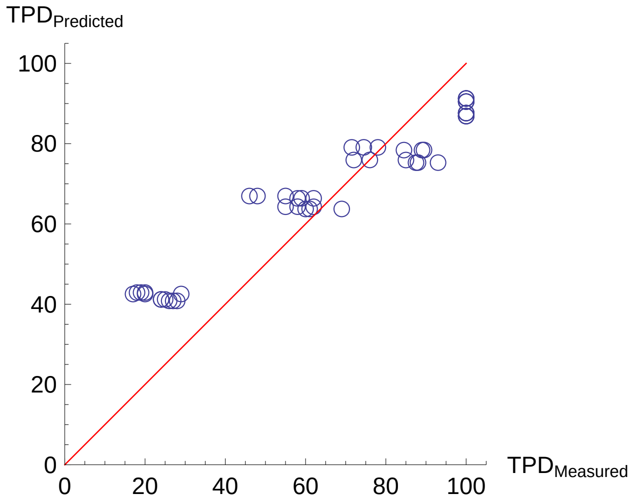

Figure 4.8: Measured vs predicted TPD using (4.4)

As further proof of the insufficiency of (4.4), a comparison of measured TPD values and TPD values predicted by (4.4) is shown in Fig. 4.8.

Taking only the data at 0°, the fit to (4.2) is much better:

$$\frac{TPD}{d} = 74m_r\left(\frac{1}{m_r}\right)^{0.83} \tag{4.6}$$

which has RMSE of 3.0 cm, a b-value closer to the value of 0.55 reported in Seo et al. (2001), and no obvious trends in the residuals (Fig. 4.9). Note that (4.6) is fit using all the dye test runs, not just the ones with corresponding ADV runs, which was the case for (4.4). Therefore, (4.2) is applicable at the beginning of the bend, but not throughout the bend. This is consistent with the previous result that Q (and therefore m_r) is a good predictor of transition point distance at the beginning of the bend but not throughout the bend.

4.3.3 ADV results and centre cell position

Figure 4.10 shows the secondary circulation at every angle of the bend for each flow condition, with the transition point distance for the given flow condition shown in blue shading for comparison.

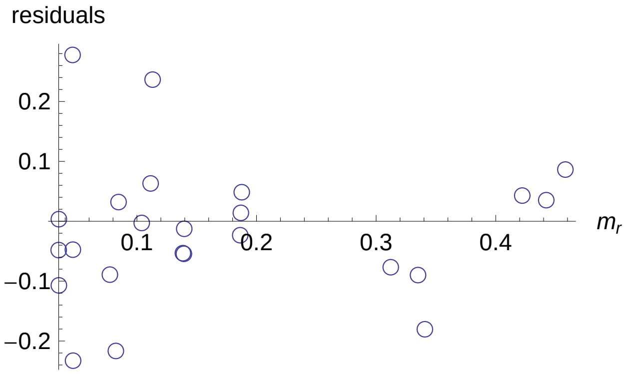

Figure 4.9: Residuals from (4.6) vs. m_r

Since TPD was not measured directly at 67.5°, it is taken as the linear interpolation of TPD between 60° and 75°. It appears that the transition point distance moves across the channel with the secondary circulation cell. In order to show this trend mathematically, consider the parameter cc, which represents the position of the cell centre and is defined in Fig. 4.11. For this study, cc was taken from the secondary circulation streamlines from the ADV measurements. For a more detailed exploration of the centre cell path in this channel, see Kashyap et al. (2012).

Figure 4.12 shows the residuals from the fit in (4.4) as a function of the centre cell position, cc. At zero degrees, the cell centre is taken to be at the outer bank, since the cell has not developed yet but does develop from the outside of the channel. The trend in this plot indicates that cc may be an appropriate variable for accounting for the effects of the bend.

Thus we are motivated to develop a new equation using the cell centre position to account for the effects of the bend on the transverse spread of the plume. The equation must reduce to (4.2) for $cc = 0$, and must allow for the influence of m_r to decrease as cc increases, as the dye test results indicate. The following form meets both these requirements:

$$\frac{TPD}{d} = m_r \left(A \frac{(1-cc)}{m_r} \frac{s}{d} \right)^{(b+f*cc)} \tag{4.7}$$

where A, b and f are fitted parameters. The best fit for this equation, using the data from Q2h2j1, Q2h2j2, and Q2h1j1 is given by:

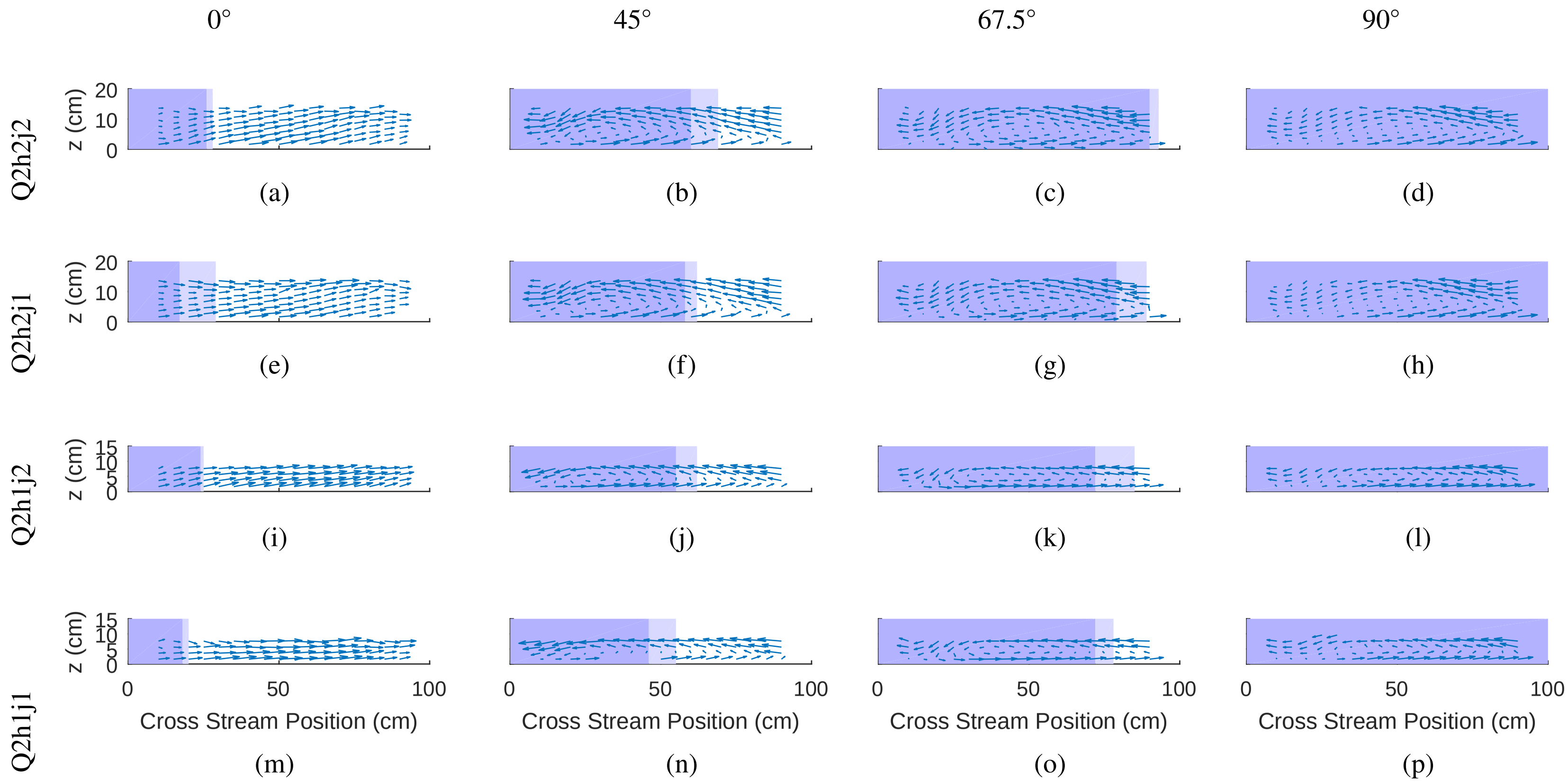

Figure 4.10: Secondary circulation streamlines and minimum and maximum measured TPD (blue shading) for Q2h2j2 (a, b, c, and d), Q2h2j1 (e, f, g, and h), Q2h1j2 (i, j, k, and l), and Q2h1j1 (m, n, o, and p) at 0° (a, e, i, and m), 45° (b, f, j, and n), 67.5° (c, g, k, and o) and 90° (d, h, l, and p). The outer bank is at 0 cm, and inner bank at 100 cm

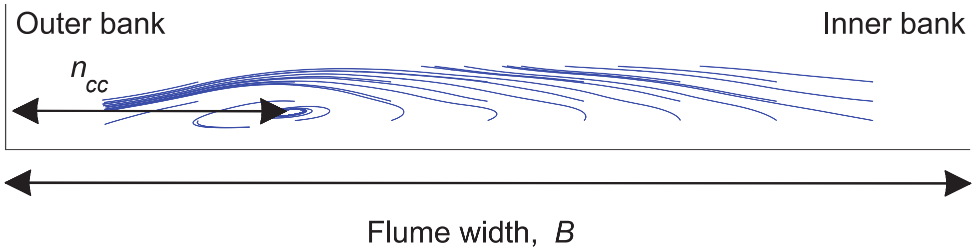

Figure 4.11: Definition of cell centre (shown for Q2h1j1 at 45°): $cc = n_{cc}/B$

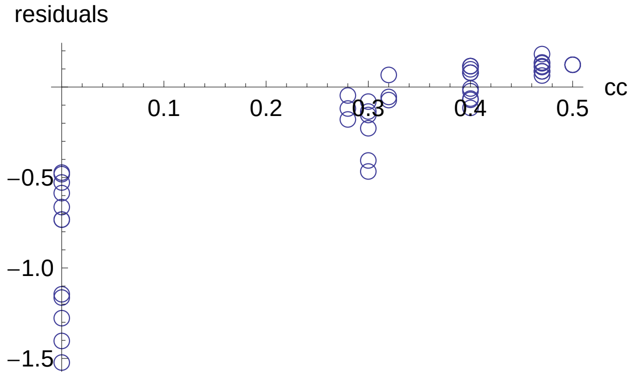

Figure 4.12: Residuals of the fit in (4.4) vs cell centre position, cc

$$\frac{TPD}{d} = m_r \left(0.38 \frac{(1-cc)}{m_r} \frac{s}{d}\right)^{(0.83+0.39cc)} \tag{4.8}$$

At the 0° cross section (where $s = 2.12$ m and $cc = 0$), this equation reduces to:

$$\frac{TPD}{d} = 72 m_r \left(\frac{1}{m_r}\right)^{0.83} \tag{4.9}$$

All the fitted parameters in (4.9) are within one standard error of the fitted parameters in (4.6). The RMSE of the fit in (4.8) is 4.6 cm, the R^2 value is 0.97, and there are no visible trends in the residuals in m_r, cc, or s/d (Fig. 4.13). As a validation of (4.8), the fit is also successful at predicting the results from flow condition Q2h1j2, with RMSE 5.0 cm and no trends in the residuals (also shown in Fig. 4.13).

Figure 4.14 compares measured TPD to TPD predicted using (4.8). Comparing Fig. 4.14 to Fig. 4.8 shows that (4.8) is a much more accurate model than (4.4).

The cell structure must be independent of the jet speed u_{jet} in order for cc to be used to predict mixing at different jet speeds. In order to show this independence, the mean cross stream and vertical velocity fields for Q2h2j1 and Q2h2j2 were compared to each other and to the velocity fields of a trial without the jet, Q2h2j0, using pairwise correlation coefficients. Q2h1j1, Q2h1j2, and Q2h1j0 were similarly compared. The correlation coefficients from all the comparisons are shown in Table 4.5. They show strong correlation ($corr > 0.85$) between all trials with different jet speeds, for both velocity components, at angles where the secondary circulation cell is present. The correlation for vertical velocity at 0° is the only situation where weak correlation is observed. It is therefore determined that the presence and speed of the jet does not influence the structure of the circulation cell.

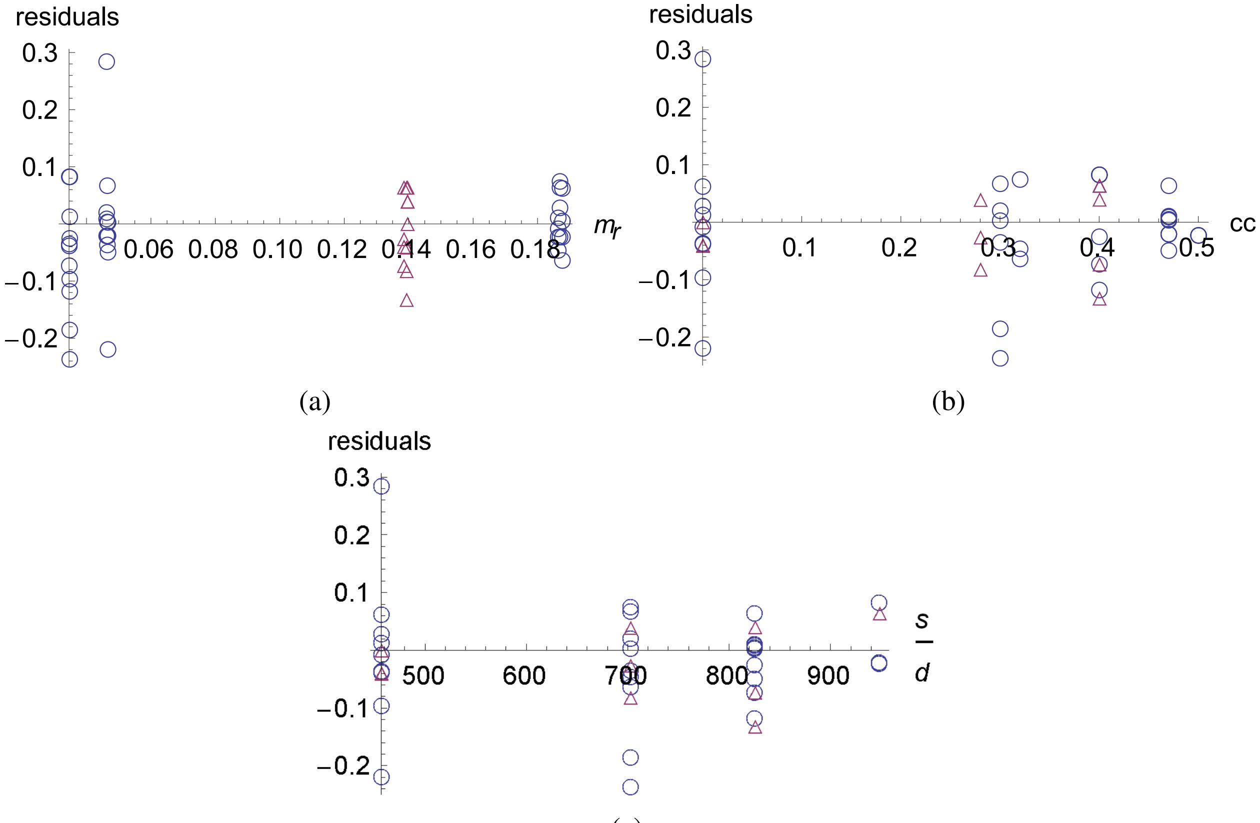

(a)

(b)

(c)

Figure 4.13: Residuals from the fit in (4.8) vs (a) m_r, (b) cc and (c) s/d. The data used for fitting are shown as blue circles, and the data from Q2h1j2 are shown as purple triangles

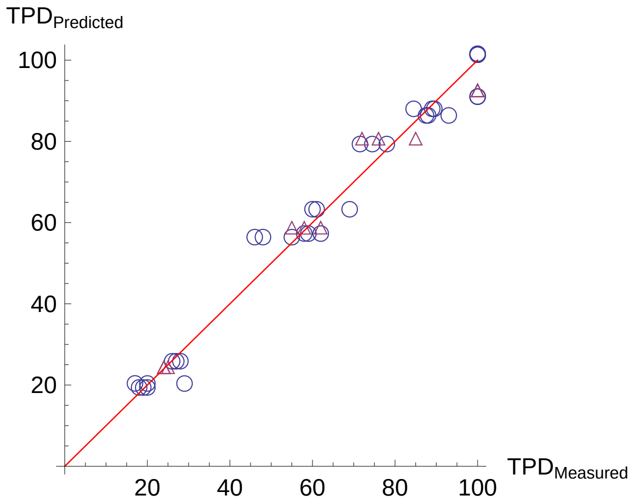

Figure 4.14: Measured vs predicted TPD using (4.8) with the runs used for fitting shown as blue circles and Q2h1h2 shown as purple triangles

Table 4.5: Comparison of secondary circulation at different jet speeds

Velocity component	Trials	$corr_{0°}$	$corr_{45°}$	$corr_{67.5°}$	$corr_{90°}$
u_n	Q2h1j0, Q2h1j1	0.92	0.98	0.99	0.99
u_z	Q2h1j0, Q2h1j1	0.52	0.94	0.97	0.91
u_n	Q2h1j0, Q2h1j2	0.95	0.99	0.99	0.99
u_z	Q2h1j0, Q2h1j2	0.67	0.95	0.94	0.93
u_n	Q2h1j1, Q2h1j2	0.95	0.98	0.99	0.99
u_z	Q2h1j1, Q2h1j2	0.60	0.93	0.91	0.88
u_n	Q2h2j0, Q2h2j1	0.94	0.99	0.98	0.99
u_z	Q2h2j0, Q2h2j1	0.58	0.92	0.96	0.91
u_n	Q2h2j0, Q2h2j2	0.94	0.99	0.99	0.99
u_z	Q2h2j0, Q2h2j2	0.67	0.92	0.96	0.89
u_n	Q2h2j1, Q2h2j2	0.94	0.99	0.98	0.99
u_z	Q2h2j1, Q2h2j2	0.65	0.92	0.95	0.90

4.4 Discussion

While (4.7) is successful at predicting the results of this experiment, it also has some limitations. Perhaps the most obvious limitation is its reliance on the position of the cell centre. There is no analytical model for predicting the position of the cell centre, so cc must be found through other means, which may be time consuming, labour intensive, or computationally demanding. Using the cell centre as an independent variable is also problematic, since it is definitely not independent of the other variables, m_r and s: s defines the downstream distance, which also defines the position within the bend and therefore the development stage of the centre cell, and m_r is defined in part by h, while h/R has been shown to affect the centre cell (Blanckaert, 2010; Blanckaert, 2003; Rosovskii, 1961). However, without a specific model relating aspect ratio and bend angle to centre cell position, the variables cannot be disentangled.

This experiment was done in a flume with a rectangular bed, and therefore did not account for the effects of topographic steering on the position of the centre cell. In channels with fully developed bathymetry, the flow through the channel is redirected into the thalweg, the deepest part of the channel (Blanckaert, 2010; Constantinescu et al., 2013b; Dietrich and Smith, 1983). The centre of the secondary circulation cell is therefore often assumed to follow the thalweg. Since natural river bends have developed bathymetry, this means that (4.7) can be applied in the field to model mixing from proposed outfalls in developed river bends.

In the dye test regression analysis, the result that Q_{cf} is not significant later in the bend is interpreted to mean that m_r in (4.2) becomes less important later in the bend. Since h and u_{jet} also affect m_r, some clarification is needed as to why they remain significant throughout the bend. It has already been stated that h has an effect on the secondary circulation, so as predictive ability shifts from m_r at the beginning of the bend to cc later, h remains an important parameter. The jet speed, like Q_{cf}, only affects m_r and not cc. One would therefore expect the p-values for both Q_{cf} and u_{jet} to increase after 45°. Table 4.4 shows that that is indeed the case, but the p-value for u_{jet} remains under the 0.05 threshold of significance. This supports the conclusion that the influence of m_r diminishes later in the bend, but does remain in part, as reflected in (4.8).

The value found for b in this paper, 0.83, is substantially larger than that reported in Seo Seo et al. (2001), 0.55. This is likely due to the bend effects that have already started at the 0° cross section. Though the secondary circulation has yet to develop at this cross section, the high velocity core has already moved toward the inner bank. Figure 4.10 shows that the flow is definitely still directed toward the inner bank at this point in the bend. Faster mixing due to advection may account for the higher value of b.

Equation (4.7) may be applicable in other geometries, but further testing is required to verify the fit parameters. In addition, different geometries will require a carefully set up coordinate system, especially for the cross-stream coordinate. The geometry of the experiments described in this paper was uniquely simple, as the jet and the centre cell both originated at the outer bank, which was therefore defined as the zero coordinate.

4.5 Conclusions

The complex nature of flow in river bends makes it difficult to model the flow, and therefore also difficult to model mixing in bends. Current methods require intensive computations using mixing coefficients that must be collected experimentally.

The experiments presented in this paper show that the methods for predicting jet trajectories in a straight crossflow are insufficient for modelling jet trajectories in channel bends. In particular, the formula from Seo et al. (2001) is not able to account for the bend effects in its original form. Modifications to the formula are proposed, which make it much more successful at predicting TPD. The success of this formula is shown by its improved RMSE and R^2, the lack of trends in its residuals, and its success at predicting the results from Q2h1j2, which were not used in fitting the model. Using this formula does not predict contaminant concentration at every point in the channel, as is predicted using mixing coefficients, but does give predictions for the maximum extent the contaminant reaches across the channel.

The modified formula could be used, along with the assumption that the secondary circulation cell follows the channel thalweg, to predict the extent of mixing in natural channels with fully developed bathymetry. For more accurate predictions, or for predictions in a channel with a flat bed, a more precise model for the position of the cell centre would be required. Further research is required to develop such a model, as well as to confirm the results of this study in different bend and jet geometries.

Chapter 5

Insights into secondary flow structure from clusters of instantaneous vortices

Abstract

A method is introduced to cluster instantaneous vortices using a density-based spatial clustering technique to better distinguish overlapping secondary circulation from different mechanisms. Applying the method to large eddy simulation results of a tight open channel bend, two secondary circulation sub-cells are distinguished: the inner bank cell and the centre cell. The identification of these structures using instantaneous vortices shows a connection between channel bend mean secondary flow and instantaneous coherent structures, which is further solidified by the agreement of mean bend circulation and circulation calculated using instantaneous vortices. The inner bank sub-cell exhibits high maximum circulation early in the bend followed by a rapid decline, a pattern which is characteristic of tight bends. The centre sub-cell exhibits slower development and retains its circulation longer, which is characteristic of milder bends. The locations of the sub-cells within the channel cross section lead to

different opportunities for vorticity generation in each sub-cell, which explains their different development patterns.

5.1 Introduction

Secondary currents in channels are motions in the plane normal to the streamwise direction. They are generally divided, after Prandtl (1952), into secondary currents of the first and second kinds, driven by centrifugal forces in curved channels and anisotropic turbulent fluctuations respectively. Turbulence driven secondary flows can form in various cases such as channel corners (Nikitin et al., 2021) and over variations in surface texture (Barros and Christensen, 2014), whereas centrifugal force-driven secondary circulation is characteristic of channel bends. Though the velocities of secondary currents are small compared to the streamwise velocity, they distort mean flow profiles and affect momentum distributions, shear stress on boundaries, and transport processes within the flow fields (Blanckaert and Graf, 2004).

The small velocities of secondary circulation cells make them comparatively difficult to measure. Only recently have more precise measurement of instantaneous velocities allowed our understanding of secondary flows to expand beyond the mean flow. Biringen (1993) presented a single instantaneous snapshot of vortices in a duct corner, but did not draw connections to the mean secondary flow. Uhlmann et al. (2007) found instantaneous structures analogous to the mean flow in marginally turbulent duct flow using a direct numerical simulation. Pinelli et al. (2010) found that at higher Reynolds numbers the coherent structures were more varied but mean flow could still be directly related to the distribution of coherent structures. Uhlmann et al. (2010) confirmed theoretically that mean secondary flow could be generated by coherent structures. Vanderwel et al. (2019) investigated roughness-driven secondary flows using instantaneous vortices and proper orthogonal decomposition, confirming that the mean secondary motions stemmed from instantaneous structures.

The above mentioned studies all investigated secondary flow of the second kind, mostly in corners of ducts (Pinelli et al., 2010; Uhlmann et al., 2010, 2007) where a single corner holds two rotating cells, one in each direction. This study applies the same principle to bend flow, with an added challenge of distinguishing overlapping structures rotating in the same direction. There is already an indication that secondary flow of the first kind manifests as coherent structures in instantaneous data: Blanckaert and de Vriend (2005) found coherent fluctuations, termed "bulk oscillation", in velocity data across a channel bend.

In open channel bends, secondary circulation is directed toward the outer bank at the top and the inner bank at the bed (Thomson, 1877). A counter-rotating, turbulence-driven cell at the top corner of the outer bank was first observed in a river bend by Thorne et al. (1985), and its development in a sharp bend was recently characterized by Li and Zhang (2022). The outer bank cell is known to depend on outer bank roughness, and the size of the outer bank cell will affect the placement of other circulation cells (Hersberger et al., 2016). The structure of secondary circulation depends on the curvature of the bend: Kashyap et al. (2012) found steeper circulation rise, higher maximum circulation, and faster and sooner decline of circulation in sharp bends. Wei et al. (2016) also found that the circulation magnitude was maximized in sharper bends. Kashyap et al. (2012) found an additional cell at the inner bank contributing to the same direction of secondary circulation in tight bends, and Blanckaert (2015) found a similar structure at the inner bank in a tight bend though not distinct enough to be classified as a separate circulation cell. The structure was found within a separation zone at the inner bank, and thus is assumed to be connected to flow separation.

The acknowledgement that the inner bank circulation is a distinct structure even when its mean streamlines are not separate raises the questions: Can circulating structures be distinguished without relying on mean streamlines? What might such a distinction reveal about the structures' development? And could the structure in the separation zone of tight bends be the cause of the qualitative differences Kashyap et al. (2012) found in circulation development based on channel bend

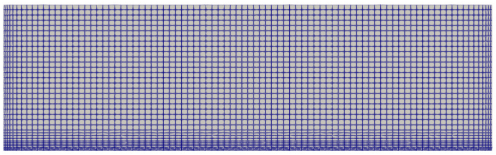

Figure 5.1: Cross section of mesh of rectangular 20 cm wide by 6 cm deep channel

radius? Herein we explore these questions using a new technique to identify secondary circulation using instantaneous coherent structures.

5.2 Methods

LES in this study were done in OpenFOAM using the pisoFoam solver with Kim and Menon's (1995) dynamic k equation subgrid scale turbulence model. The walls of the flume were modelled as no slip boundaries and the air-water interface as a symmetry plane. The inlet was modelled using the mapped inlet boundary condition, which initializes the upstream boundary with a straight inlet section with periodic upstream and downstream boundaries, and has been found to produce natural turbulent fluctuations (Montorfano et al., 2013). The flow rate was set to 690 mL/s at a depth of 6 cm. The flow domain was a 20 cm wide channel with a 2.4 m long straight inlet followed by a 135° bend of radius 30 cm and a 50 cm straight outlet. The simulations were done on a mesh of approximately 4.5 million cells ($1440 \times 88 \times 36$ cells in the streamwise, cross stream, and vertical directions respectively). The grid was refined at the wall boundaries, resulting in a y+ value below 5 everywhere along the walls. A sample cross section of the channel is shown in Figure 5.1. The time interval for each calculation was 0.001 s, and data were saved every 0.5 s of simulated time for a total length of 190 s, the first 90 s of which were for flow development and the remaining 100 s for analysis using mean flow and instantaneous snapshots.

The experiments were done in a flume with the same geometry and flow conditions as the simulations. A stereo particle image velocimetry measurement for validation was taken at the 90° cross section, illuminated by the laser from below. Distortion from the curved flume walls was corrected using LaVision's polynomial calibration to within a fit error of less than 0.01 pixels, with a scale factor of 14.27 pixels/mm. The sampling frequency and sample length were set to 2 Hz and 100 s to match the simulation.

In cases where the mean flow streamlines of two cells seem to merge, circulation calculations based on mean flow will attribute all calculated circulation to the stronger cell. It is therefore necessary to introduce a definition of circulation strength which will not misallocate the circulation of a weak cell into that of a stronger cell. Herein we consider identifying all vortices in each instantaneous time step, rather than a long-term time averaged flow field. This way, even weak or transient vortices will be identified separately. The vortex identification is done with the procedures outlined by Graftieaux et al. (2001) which supply not only the location of the vortex centre, but also its area and circulation strength. The vortex identification method is based on two parameters, Γ_1 and Γ_2, defined as:

$$\Gamma_1(O) = \frac{1}{S}\int_{M\in S} \sin(\phi_M)dS \qquad \Gamma_2(O) = \frac{1}{S}\int_{M\in S} \frac{\overrightarrow{OM} \wedge (\vec{u}_M - \tilde{u}_O)}{||\overrightarrow{OM}|| \cdot ||\vec{u}_M - \tilde{u}_O||}dS \tag{5.1}$$

Where S is an area around any point O, ϕ_M is the angle between the velocity vector ($\vec{u}_M$) at point M and the vector between O and M ($\overrightarrow{OM}$), and $\tilde{u}_O$ is the convection velocity $(1/S)\int_S \vec{u}dS$ around O. Vortices are identified as local maxima of Γ_1 which are then associated with an area of rotation-dominated flow, where $|\Gamma_2| > 2/\pi$.

Once all instantaneous vortices are identified, the vortex centres are assigned to the circulation cell they represent using MATLAB's (2021) density-based spatial clustering of applications with noise (DBSCAN) algorithm. The exact process is as follows:

1. For each individual time step, apply the algorithm from Graftieaux et al. (2001) to find the centre, size, and circulation of each instantaneous vortex from all time steps.

2. Separate the vortices into positively and negatively rotating to allow the DBSCAN algorithm to work on position alone without mixing cells in opposite directions.

3. Apply the DBSCAN algorithm on the instantaneous vortex locations

The DBSCAN algorithm works by grouping points into clusters when they are within a radius of ε to a sufficient number (M_{pt} or more) of other points. While there are many different clustering methods, DBSCAN is advantageous in this situation because of its ability to identify oddly shaped clusters, and its robustness in noisy datasets. In this paper, since different cross sections contained vastly different numbers of instantaneous vortices, M_{pt} is set to 1/30th of the total number of points being clustered at a time in order not to bias the algorithm against detecting clusters in cross sections with fewer overall instantaneous vortices. The parameter ε was kept at a constant value of 0.1 in normalized coordinates $(n/B, z/h)$ for cross stream coordinate n, channel width B, vertical coordinate z, and water depth h. Using scaled coordinates avoids having the clusters artificially bisected, as clustering algorithms tend to do in domains with unequal aspect ratios.

The clustering analysis identifies instantaneous vortices as instances of a larger pattern of coherent structures. The time-averaged circulation strength of each structure can be found using the sum of the circulation of all instantaneous vortices which are part of the cluster, averaged over the number of time steps. The centre of the cluster can be defined as the circulation-weighted mean position of the centres of the instantaneous vortices belonging to the cluster. The development of each cell can be tracked through a larger domain by repeating the analysis on cross sections close enough together to consistently identify the same clusters.

As a demonstration of the application of the clustering method to an established secondary flow problem, consider the secondary circulation generated by alternating rough and smooth streamwise-oriented strips studied by Stroh et al. (2020). The pattern and even the direction of the secondary circulation changes as the height of the smooth strip is raised from the bottom (0 case) to the middle (k_s case) and then to the top ($2k_s$ case) of the rough strips. A clustering analysis

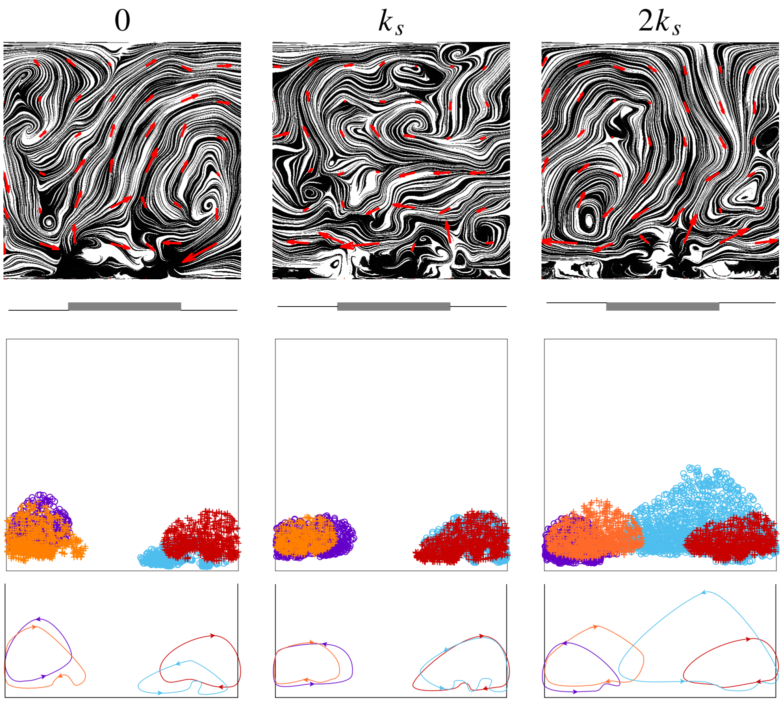

Figure 5.2: Circulation produced by roughness: Mean flow (top), clusters of instantaneous vortices (middle), and cluster outlines (bottom)

of a subset of instantaneous data from Stroh et al. (2020) is shown in Figure 5.2, with mean flow streamline visualization using surface line integral convolution based on Shamlo (2005). Since the vortices are highly concentrated at the bottom, the logarithm of the vertical coordinate is used for the purposes of clustering. ε is set to 0.1 in scaled coordinates and M_{pt} to 1/15th of the vortices being clustered at a time. Also shown in Figure 5.2 is a summary of the cluster outline and direction delineating the edge of the cluster of vortex centres. The structures representing both directions of secondary flow are present in each case. In the $2k_s$ case, the top-inward clusters dominate at the top of the flow, and in the 0 case the top-outward clusters dominate at the top, though the top-inward clusters protrude at the bottom in two places each. These patterns are consistent with those found in the mean flow in each case. The cluster patterns of the two extreme cases suggest that in the k_s case the same clusters should exist, and should be approximately equal in size. This is the case, and in fact the outlines of the clusters overlap very closely. Because of the near-exact overlap, no single

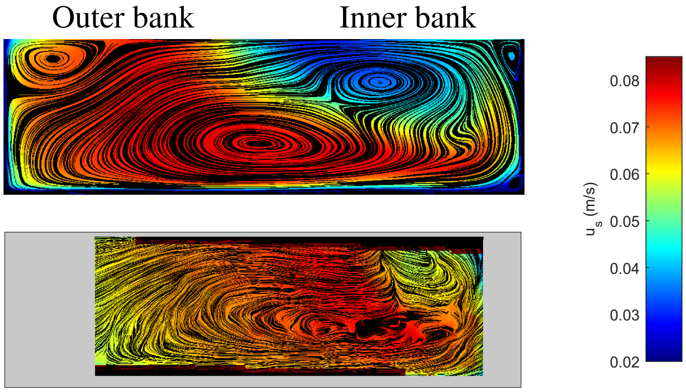

Figure 5.3: Comparison of LES (top) and PIV (bottom) mean velocities at 90 degrees

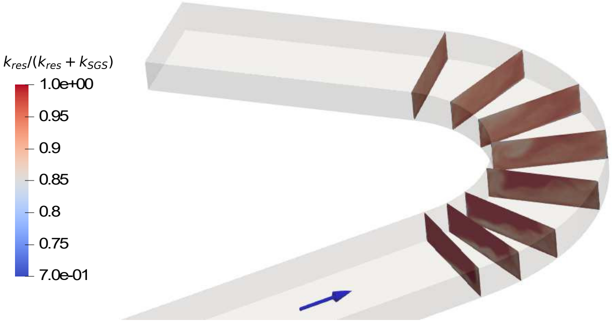

Figure 5.4: Estimate of resolved turbulent kinetic energy

direction of circulation dominates. The circulation in this case depends not on the cluster sizes, but on distributions within the clusters. We can infer that in the k_s case, the mean flow will show smaller cells of circulation in both directions.

5.3 Results

A comparison of the LES results and PIV results for the same flow rate at the 90° cross section is shown in Figure 6.4 for validation, showing a distinct two-cell structure, and agreement on the horizontal location of both cells.

An estimate of the proportion turbulent kinetic energy resolved by the LES, calculated as $k_{resolved}/(k_{resolved} + k_{sgs})$ where $k_{resolved}$ is the turbulent kinetic energy resolved directly from the

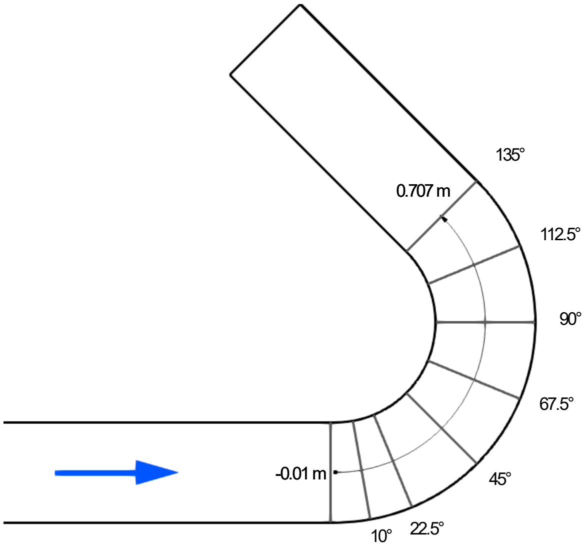

Figure 5.5: Planform view of bend with cross section locations

simulated velocity fluctuations and k_{sgs} is the subgrid scale turbulent kinetic energy, is shown in Figure 5.4. Over 80% of the turbulent kinetic energy is resolved throughout the domain.

The LES results are presented for the bend eight cross sections identified in Figure 5.5. The mean flow streamlines and streamwise velocity u_s are shown in Figure 5.6, along with the locations and strengths of each mean flow vortex as detected by the same algorithm used for detecting the instantaneous vortices. At the 22.5° cross section, there is disagreement on the position of the centre of one cell, indicated by a dotted line connecting both possible centres.

The most often-detected cells are shown as the red circle, blue square, and pink triangle; the inner bank cell (IBC), centre cell (CC), and OBC respectively, taking their names from their positions at the bend apex. The CC and IBC have negative circulation, indicating top-outward, bottom-inward flow. The IBC and CC both move toward the inner bank as the channel progresses, in keeping with previous observations of bend-induced secondary flow. Both can safely be assumed to be bend-induced secondary flow. When the IBC reaches the inner bank, it moves up and sits above the CC. In the last three cross sections the IBC placement deforms the CC, which splits into two regions. In two of those cross sections there are no detected vortices in one CC region, leaving its circulation unaccounted for. At 112.5° the larger vortices from earlier in the bend give way to

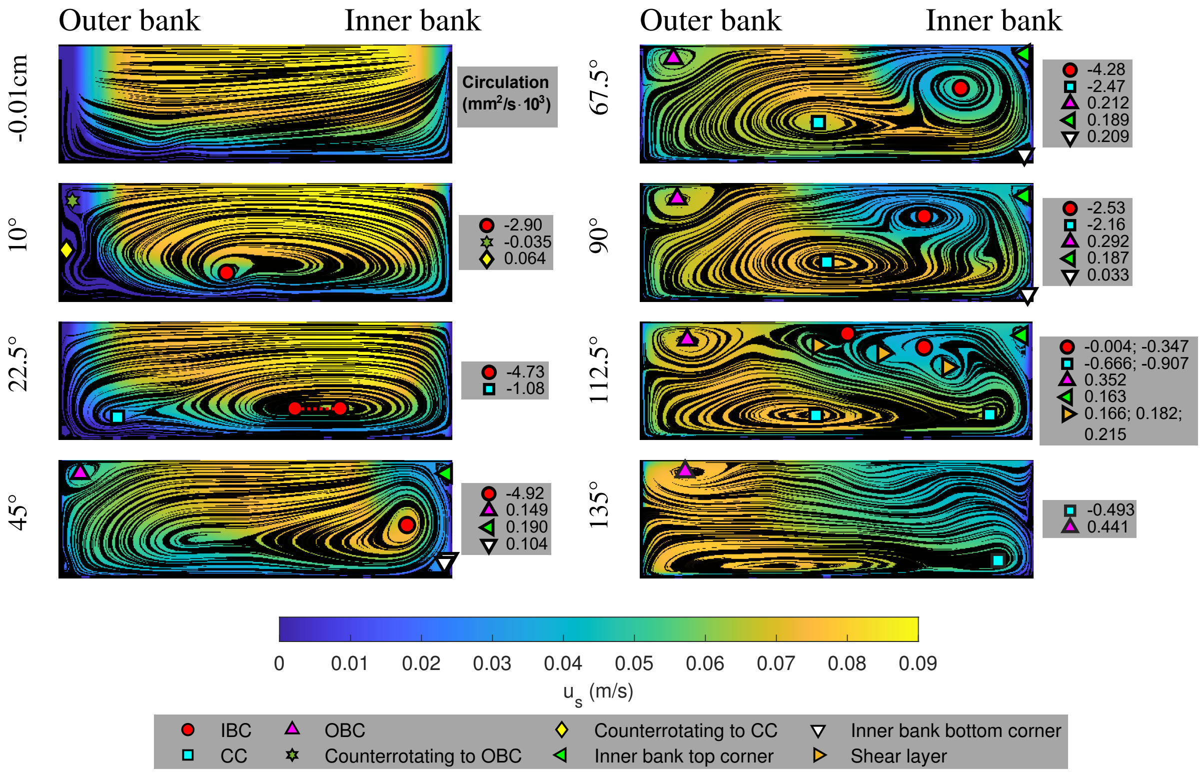

Figure 5.6: Mean flow and circulation cells detected using vortex identification on mean flow

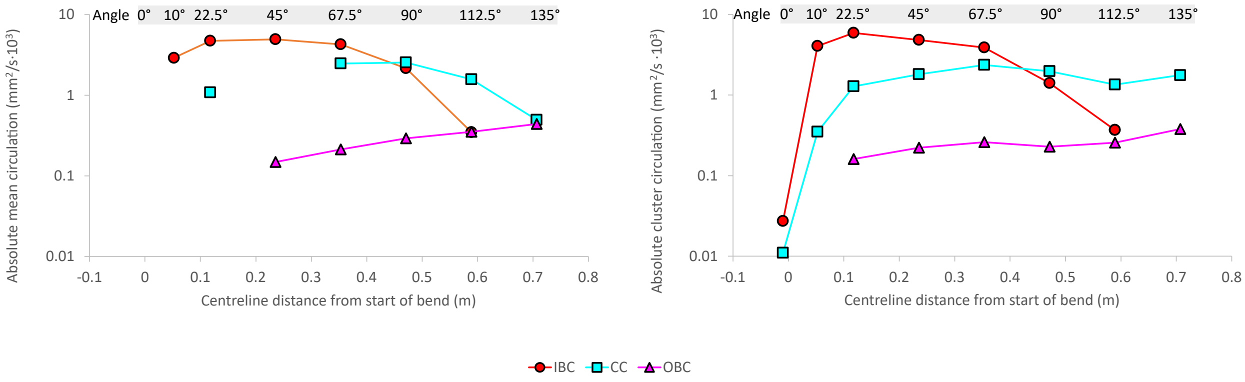

Figure 5.7: Absolute circulation development of three cells using mean flow (left) and clustering (right)

smaller, more fragmented structures. The regions occupied by the CC and the IBC each contain two smaller vortices, which are assumed to each be smaller contributions to the larger cell.

A summary of the three primary cells' development as a function of downstream distance is shown in Figure 5.7. Since the CC is not detected in every cross section, its development is not well-captured. In the 90° and 135° cross sections, only one of its contributing vortices is detected, and the circulation values are likely underestimated. Therefore only three of the eight cross sections give a reliable value for the CC circulation (22.5°, 67.5°, and 112.5°).

Clustering results are shown in Figure 5.8. The IBC, CC, and OBC are all detected earlier than in mean flow. In the case of the CC, it develops at the outer bank along with a counter-rotating cell shown in yellow. When the CC splits under deformation from the IBC, the total CC circulation is taken as the sum of both clusters (blue squares and purple triangles).

The cell circulation development as defined with clusters is also summarized in Figure 5.7, and the cell locations in Figure 5.9. All three clusters show much more detail in their development stages than the analogous summary using mean flow. The CC strength is also shown to persist farther than in the mean flow analysis, suggesting that the CC decrease in the mean flow analysis is due to missed circulation in the last cross section.

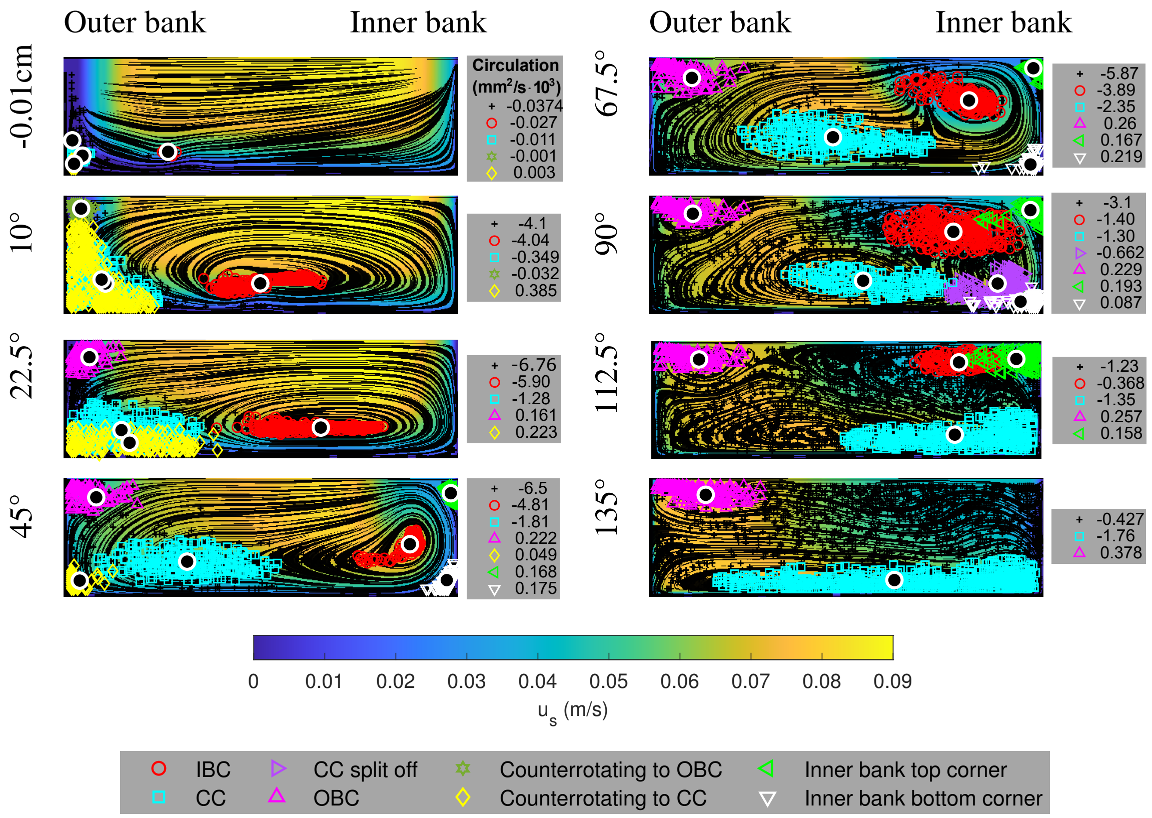

Figure 5.8: Cells detected using clusters of instantaneous vortices

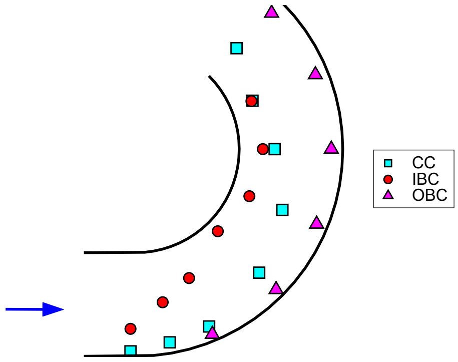

Figure 5.9: Planform view of cell locations as defined by clustering instantaneous vortices

5.4 Discussion

The results presented above show that weak and transient cells are identifiable through clustering more reliably than in mean flow. Clustering is able to detect every cell at least one cross section ahead of when the cell first appears in mean flow. Where instantaneous vortices rotating in opposite directions are found at the same location at different times, for instance in the early development of the CC, the rotation averages out and vanishes in mean flow analysis, but is detectable using clusters.

The vortex identification algorithm presented by Graftieaux et al. (2001) explicitly assigns both a centre and an area to the vortex. The fact that the centre and area are determined independently leads to an occasional artifact where the same vortex area is assigned two centres, as in the 22.5° cross section in Figure 5.6, leaving the "true" centre of the vortex undefined. Note that this artifact is only visible in the 22.5° cross section; in other cross sections where multiple centres are shown for the same cell, they correspond to different vortex areas. By using clusters to define cells, the centres are taken as weighted averages of the instantaneous vortex centres, thus the centre is still well-defined. The artifact does not stem from any particular calculation in the Graftieaux et al. (2001) algorithm, rather it comes from determining both the centre and boundary of the vortices in question, which inherently has some low probability of mismatch. Since both quantities are needed to do the full cell circulation analysis, and meaningful results are still achieved upon averaging by cluster, we can accept the occasional artifact. Furthermore, the Graftieaux et al. (2001) algorithm has distinct advantages in application to secondary flow structures, in its design to identify large-scale rotation while ignoring overlaying small scale turbulent fluctuations.

Kashyap et al. (2012) and Blanckaert (2015) only detected an IBC at later cross sections within the separation zone, thus it was reasonable to assume that it was a feature of the separation zone. With clustering, more consistent cell detection challenges this assumption. A closer examination of Figure 5.8 shows the separation zone starting at 45°, distinguishable as an area of low streamwise velocity at the inner bank. It is clear that the IBC exists before the separation zone; in fact the separation zone forms around the IBC between the 22.5° and 45° cross sections. From Figure 5.7, this is the same location where the IBC circulation strength begins to decrease. Therefore, though the IBC does overlap with the flow separation zone after it forms, it does not gain its circulation from that zone. Rather the separation zone formation may cause the IBC to lose circulation strength. After its decline in strength, the IBC and CC's strengths become more evenly matched. Given the difficulty in distinguishing vortices of very different strengths using mean streamlines, this is likely the reason that the IBC is only detected after the formation of the flow separation zone in previous studies.

If the IBC does not originate from the flow separation zone, the question of what distinguishes the IBC remains. Since both the IBC and the CC originate closer to the outer bank and then move toward the inner bank, it is possible that both are generated by the same mechanism, namely the combination of centripetal force and pressure gradient that drives bend-induced secondary currents. The IBC forms at the outer bank before the start of the bend and is transported by inner-bank-directed secondary motion, moving it away from the outer bank. The continued generation of circulation at the outer bank later in the channel would then generate the CC. Thus both cells are products of the same bend-driven circulation generation mechanism, and their distinction may only be a result of the circulation generation through bend forces being spread over a large area. If this pattern continues, then longer bends may show even more than the two circulation cells, as more circulation is generated at the outer bank after the CC has moved toward the channel centre.

Figure 5.10 shows the total circulation (the integral of mean flow vorticity in each cross section) compared to the sum of circulations of vortices detected in the mean flow and of all instantaneous vortices. It is clear from the figure that the sum of mean flow vortices does not represent the development of circulation in the channel well, whereas instantaneous vortices give a more accurate view of the total circulation trends.

Using clustering, the following conclusions about the flow field become apparent: That there are two separate circulation cells consistently detected before the development of the separation zone

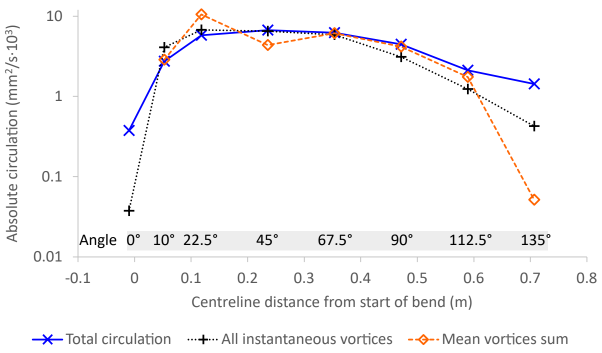

Figure 5.10: Absolute total circulation development throughout the bend

(other than the OBC); that separation zone forms as the IBC begins to lose strength; and that the CC retains its strength for longer. Since the IBC is known to be present specifically in tight bends, this suggests that different circulation development patterns exist for different bend radii. In tight bends where the IBC dominates, circulation will develop quickly, decline quickly after reaching a maximum, and then plateau once the IBC has decreased sufficiently for the CC to dominate. In mildly curved bends, where the CC dominates, the circulation will reach a plateau much sooner, and the maximum circulation in the channel will be closer to the level of the plateau, as shown by Kashyap et al. (2012).

To understand the cause of the later differences in CC and IBC behaviour, let us consider the conceptual model of vorticity production put forward by Morton (1984) and extended to three dimensions by Lyman (1990). In this model, vorticity is only produced via tangential acceleration of fluid and normal pressure gradients at wall boundaries. Importantly, the wall shear layer in this model does not produce vorticity but only transports vorticity created at the wall itself. Terrington et al. (2021) argued that this model is mathematically equivalent to the more classical interpretation of shear layers producing vorticity, and is useful for its conceptual advantages. One consequence of the interpretation is that vorticity cannot diffuse through walls, rather the wall must produce vorticity of the opposite sign via tangential fluid acceleration or pressure gradients in the opposite direction of those that produced the original vorticity. In the case of bend flow, neither fluid acceleration nor the pressure gradient is likely to switch signs partway through a bend. The CC is spread across the channel bottom, surrounded on three sides by walls; it will have little opportunity for vorticity negation or diffusion, and therefore its circulation will persist.

The experiments and simulations presented in this study take place in a scaled down channel bend, meant to represent real-world river bend systems. The scaling is based on the Froude number, which has the most established connection to bend-induced secondary flow (Leeder and Bridges, 1975). Scaling this way does reduce the Reynolds number, which in the case presented in this study is 3500, in the range of weakly turbulent flow. The comparatively low Reynolds number may affect the formation of secondary circulation cells, specifically turbulence-driven corner cells. These cells do clearly form in the given flow condition, though in a scaled-up geometry they may be correspondingly stronger.

Further, the width:depth aspect ratio (approximately 3:1) was relatively small compared to real rivers, which likely increased the bend induced secondary circulation (Kashyap et al., 2012). Though the aspect ratio of the flow in this study is smaller than in most channel bend flow studies, Kashyap et al. (2012) found that the cell structure and circulation development are more dependent on bend radius than aspect ratio. Similarly, Blanckaert (2009) found that changing the depth of flow in a tight bend only weakly changed the secondary flow strength, though it did change the recovery time to return to straight channel flow after the bend. The results of this study should thus be transferable to channel bends with other aspect ratios. This is backed up by the fact that the qualitative results of flow separation and an inner bank cell in a tight bend, as well as the circulation development pattern in tight bends, are perfectly in line with what previous studies have seen.

5.5 Conclusions

Clustering instantaneous vortices has been shown above to be more consistent than mean flow vortex detection as a method for finding secondary circulation cells, especially when those cells are developing or overlap with other cells. The clustering analysis gives a smoother picture of the cell development and dissipation, and gives a better account of the total circulation. The IBC's interaction with flow separation zone is associated with a much faster decline in circulation, whereas the CC's position at the bottom of the flow allows it to retain its circulation much longer. This analysis provides a mechanism for previously-seen differences in circulation development in mild bends (which show CC-like development) and sharp bends (which are IBC-dominated). These mechanisms are not new: evidence of the IBC interaction with the separation zone and differences between mild bends and tight bends have been shown repeatedly in previous studies (Blanckaert, 2015; Kashyap et al., 2012), but the clustering analysis gives new clarity to the mechanisms at work.

Chapter 6

Effect of a nonbuoyant submerged transverse jet on bend secondary circulation

Abstract

The system of an effluent jet discharged upstream of a sharp open channel bend is investigated using large eddy simulations and particle image velocimetry. Without the jet, three distinct sub-cells of secondary circulation are distinguished by clustering instantaneous vortices: one at the inner bank, which is a characteristic of sharp bends; one in the center; and a counter-rotating outer bank cell. Upon addition of a nonbuoyant submerged transverse jet, the outer bank cell vanishes for a low momentum jet and is driven earlier in the bend for a high momentum jet, the bend's circulation strength is redistributed from the inner bank cell to the center cell, and the development locations of the secondary circulation cells are shifted toward the inner bank. The inner bank cell develops later, and its development region is constrained to be closer to the inner bank. The center cell develops earlier in the bend, and its development region encompasses the jet vortices. The momentum of the jet influences the distribution of effluent, both by

increasing mixing with higher momentum and by advection through the jet-affected secondary circulation.

6.1 Introduction

All over the world, liquid wastes are often disposed of by discharging them into river systems, many of which contain channel bends. If not managed and diluted properly, high effluent concentrations downstream can lead to harmful effects not only for the river ecosystem but also for nearby infrastructure and human populations. It is therefore necessary to understand not only the mechanics at play in river bends and in jets in crossflows, but also the interactions between those two systems. Though river bends and effluent mixing in jets have individually been the subject of much research (Hajibehzad et al., 2022; Peng et al., 2022), there is a marked scarcity of research on jet-bend interactions.

In river bends, the water flows toward the outer bank near the surface and the inner bank near the bed, as shown schematically in blue in figure 6.1. There is also often a counter-rotating cell in the upper corner of the outer bank (magenta, figure 6.1), first detected in a river bend by Bathurst et al. (1977) and driven by turbulent anisotropy (Blanckaert and Graf, 2004). In tight bends, there may also be a cell at the inner bank (red, figure 6.1).

With recent advances in data resolution, multiple secondary circulation cells have been discerned in bend flow both experimentally (Bai et al., 2019; Constantinescu et al., 2013a) and in simulation (Constantinescu et al., 2013a,c; Kashyap et al., 2012; van Balen et al., 2010). Specifically, tight bends tend to exhibit a distinct circulation sub-cell at the inner bank (Blanckaert, 2015; Blanckaert et al., 2013; Kashyap et al., 2012). Though this structure has been assumed to be caused by inner bank flow separation, Schreiner et al. (2023) used instantaneous vortex clustering to show that the inner bank cell developed before the flow separation zone.

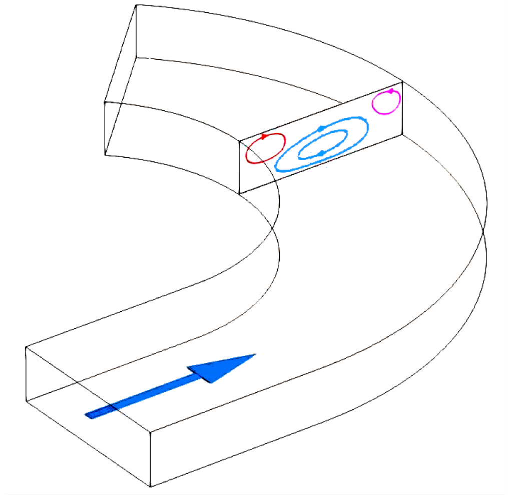

Figure 6.1: Secondary flow in a channel bend

Many studies of mixing in rivers focus on passive tracer mixing; the velocity fields and mixing coefficients are assumed to depend only on the properties of the river flow. However, many effluents are discharged into rivers by means of submerged jets or diffusers composed of an array of submerged jets. To understand how submerged jets interact with a bend crossflow, one must first understand how they interact with straight crossflows. Figure 6.2 shows the vortical structure of a typical submerged jet in a crossflow: the crossflow bends the core of the jet downstream, and induces a CVP. Stretching between the CVP and the wall are transient wake vortices. On the side of the CVP away from the wall, a shear layer between the jet and the crossflow causes vortex shedding. A horseshoe vortex wraps around the upstream side of the jet. Since the jet in this study is upstream of the channel bend, the CVP is the most relevant jet vortex; it is particularly persistent and can be detected more than 1000 jet diameters downstream of the jet outlet (Pratte and Baines, 1967), and accounts for most of the effluent advection in the far field (Zhang and Yang, 2017). While jets in crossflows are usually characterized by the ratio of the initial jet velocity in the outlet to the velocity of the crossflow, this is most useful when the crossflow is sufficiently deep that its edges are not near the jet. In shallow crossflows, jets may be characterized instead by the momentum ratio (Seo et al., 2001), defined as $m_r = (u_{jet}^2 d)/(u_{cf}^2 h)$ for u_{jet} jet velocity, u_{cf} cross flow velocity, h

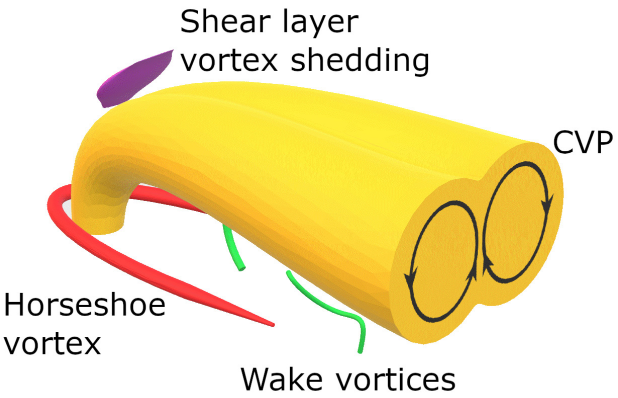

Figure 6.2: Vortex structure of jet in crossflow

cross flow depth, and *d* characteristic jet dimension in the streamwise direction. Schreiner et al. (2018) showed that the trajectory of the jet in a channel bend could be characterized using the momentum ratio of the jet and the position of the bend secondary circulation. The effluent transport could not be adequately predicted without accounting for the secondary circulation. Wang et al. (2022a,b) presented a preliminary assessment of the influence of negatively buoyant jets on bend flow circulation. However, the underlying mechanisms by which the jet interacts with the secondary circulation have yet to be studied in detail.

Though very little research has directly investigated the impact of effluent jets on the secondary circulation in bends, or the resulting mixing patterns, some studies have used jets of fluid to modify the secondary circulation and subsequent scour in river bends (Abduo et al., 2021; Chamani et al., 2011; Dugué et al., 2015; Tamoradi et al., 2019). The results of these studies indicate that in situations where effluents are discharged into river bends by means of submerged jets, one cannot assume that the secondary flow is not affected.

This study aims to map out the specific interaction mechanisms between the jet and bend turbulence structures simulated using LES and supported with PIV measurements, and to predict the effluent concentration field that results from the interaction.

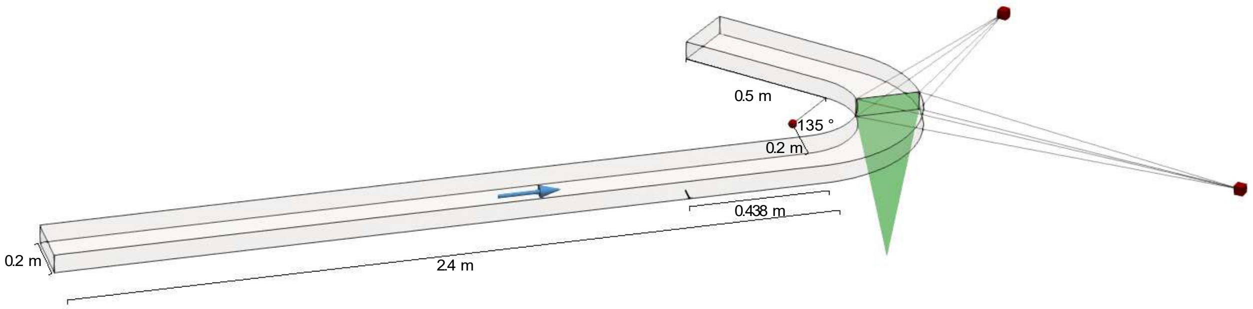

Figure 6.3: Experimental setup schematic including flume, measurement plane, and camera locations (red boxes). Flow enters from the left. The flume is 20 cm wide and the bend is 135 degrees with radius of curvature 30 cm at the channel centerline

6.2 Methods

This paper uses data from stereo PIV experiments in a flume with a 135° bend, and LES on a model of the same flume. The flume, shown schematically in figure 6.3, has a width of $B = 20$ cm and has a 135 degree bend of radius 30 cm to the channel centerline. The flow rate was 690 mL/s with a depth, h, of 6 cm, giving a Froude number of 0.075, within the range where bend secondary circulation was studied by Farhadi et al. (2018). The aspect ratio in the given flow condition is uncommon in natural rivers but possible in man made channels, and has been widely studied in laboratories Blanckaert and de Vriend (2005), Blanckaert and Graf (2001), and Gholami et al. (2020), since it is difficult to get detailed velocity measurements in either shallower lab-scale flows or full-scale natural rivers (Pilechi et al., 2014).

The jet outlet was $d = 4.8$ mm across, giving a depth to jet dimension ratio of 12.5 to represent a typical river outfall with a ratio of approximately 10 (Grace, 2009). The jet outlet was placed at the outer bank 43.8 cm before the start of the bend, where the flow is fully developed but not yet affected by bend circulation, at an elevation of 3 cm. The end of the jet outlet was flush with the side of the flume. When the jet was flowing, it had a discharge of 2.2 mL/s, resulting in a jet to flume velocity ratio of 2.14. This ratio is already well-characterized in straight crossflows (Cambonie and Aider, 2014; Iyer and Mahesh, 2016; Milani et al., 2020), though a much wider range of velocity

Table 6.1: Jet scaling parameters for two focus cases

	Low m_r jet	**High m_r jet**	**Expected range**
$\boldsymbol{m_r}$	0.375	2.99	0.025 - 90
$\boldsymbol{Re_{jet}}$	584	1167	>2000
$\boldsymbol{d/h}$	0.07	0.039	0.1
$\boldsymbol{d/B}$	0.02	0.01	0.001 - 0.01
$\boldsymbol{h/B}$	0.3	0.3	0.01 - 0.1

ratios is commonly studied, with Zhang and Yang (2017) citing examples in water systems ranging from $r = 0.5$ to 30. The jet to flume momentum ratio was 0.375.

In addition to this jet, which was studied in both experiment and LES, a second jet condition was studied in LES with the same jet flow rate but a smaller jet outlet. This resulted in a jet-to-flume momentum ratio of 2.99. This jet condition is not meant to be representative of a real-life effluent and river system, but is rather investigated here as an exaggerated comparison with the low m_r jet in order to distinguish between different jet effects.

A summary of the flow parameters is presented in table 6.1. The relatively large depth-to-width ratio is expected to result in relatively stronger secondary circulation in the channel, and relatively larger cross-stream distance covered by the jet, compared to in natural rivers. We can compensate for the expected larger cross-stream extent of the jet by only considering jets with m_r at the low end of the expected range, which will further decrease the relative strength of the jet compared to the secondary circulation. Since it is often currently assumed that outfalls will have no effect on secondary circulation patterns in a river, the increased relative strength of secondary circulation and the decreased relative strength of the jet are judged to be conservative choices to test this assumption. As shown in table 6.1, the m_r scaling does reduce the jet Reynolds number, $Re_{jet} = u_{jet} \cdot d/\nu$ where u_{jet} is the average jet velocity and ν is the kinematic viscosity of water, to outside of the expected range, but this cannot be increased without risk of the jet impinging on the inner bank.

The PIV data were collected from the 90 degree cross section, which is shown along with camera placement in figure 6.3. Scheimfplug adapters on the camera lenses ensured that the entire field of view was in focus, and the distortion from the flume walls was corrected using LaVision's polynomial calibration with a custom designed 20 cm by 10 cm calibration plate. The calibration had a fit error of less than 0.01 pixels and a scale factor of 14.27 pixels/mm. The laser plane entered the field of view from below the table. Measurements were taken every 0.5 s over a time period of 100 s, which was found in both simulation and experiment to be sufficiently long for autocorrelation function convergence. The low frequency ensures that consecutive samples are independent, thus allowing the instantaneous vortices used in the clustering algorithm to be treated as independent. The jet flow rate was controlled with a constant head tank.

The simulations took place on a mesh of approximately 4.5 million cells: 1440 cells in the streamwise direction, 88 in the cross stream, and 36 vertically. The cell resolution increased near the walls to ensure y+ was kept low; The final simulation kept y+ below 4 everywhere. Near the jet outlet, the mesh was gradually refined so that the jet outlet itself was 10 cells by 10 cells across, with a total of 4000 cells in the outlet. The jet outlet was modelled as a rectangle, with downstream dimension and cross sectional area equal to those of the round experimental jet. The simulations used the pisoFoam solver available in OpenFOAM v2006 and the dynamic k equation subgrid scale turbulence model developed by Kim and Menon (1995). The dynamic k equation model was chosen in order to better model the development of the outer bank cell, which gains energy from small scale turbulent anisotropy. The simulations were rigid lid simulations, using a flat symmetry plane boundary condition to represent the water's surface. The walls were modelled as smooth walls using a no slip boundary condition, and the outlet was modelled using the inletOutlet boundary condition. The inlet was modelled with a mapped boundary condition, which has been shown to perform well in generating realistic turbulent fluctuations (Montorfano et al., 2013). This condition maps parameters at the inlet to values taken from a downstream cross section, with velocities scaled to match the required flow rate. This allows some randomness into the inlet condition while still maintaining physically meaningful parameters. In this case the downstream cross section was 50 cm after the inlet, which was found to be sufficiently upstream of the jet to avoid jet effects in the mapped plane and sufficiently downstream on the inlet to ensure fully developed flow. The simulation with jet flow also included a scalar transport function for calculating effluent concentration at every time step using the instantaneous velocity field. The concentration inside the jet outlet was set to 1. The simulated time step was 0.001 s, and data were saved every 500 time steps for a sampling frequency of 2 Hz. All results are constructed from 200 samples, beginning after 90 s to allow the flow to develop. In total 190 seconds of flow time were simulated. The proportion of turbulent kinetic energy resolved in the simulations can be estimated as $k_{resolved}/(k_{resolved} + k_{sgs})$ where k_{sgs} is the turbulent kinetic energy calculated by the subgrid scale model. In general, LES models should resolve at least 75% to 85% of the turbulent kinetic energy (Celik et al., 2005); by the above estimate, the simulations presented in this paper resolved over 94% of the turbulent kinetic energy.

The circulation sub-cells were distinguished using the clustering methods from Schreiner et al. (2023), using DBSCAN to categorize instantaneous vortices. The vortices were detected at each time sample using the method from Graftieaux et al. (2001): The streamline topology of the flow is quantified in the parameter Γ_1, and vortex centres are found at local Γ_1 maxima. Vortex circulation is calculated by integrating vorticity over the surrounding area with rotation-dominated flow. The DBSCAN clustering algorithm assigns the instantaneous vortices to cells by clustering the vortex centre locations: if a vortex centre is within a distance of ε of M_{pt} or more vortex centres of the same cluster, then that vortex is also assigned to the given cluster. In this study, M_{pt} was set as 1/16th of the instantaneous vortices at the given cross section and ϵ was 0.149 in scaled coordinates. In the coordinate system used, the bend secondary circulation cells are negatively-rotating, and the counter-rotating corner cells are positively-rotating.

6.3 Results

Figure 6.4 shows normalized mean flow velocity and mean secondary circulation visualized using surface line integral convolution (surface LIC) based on Shamlo (2005). Both LES and PIV are

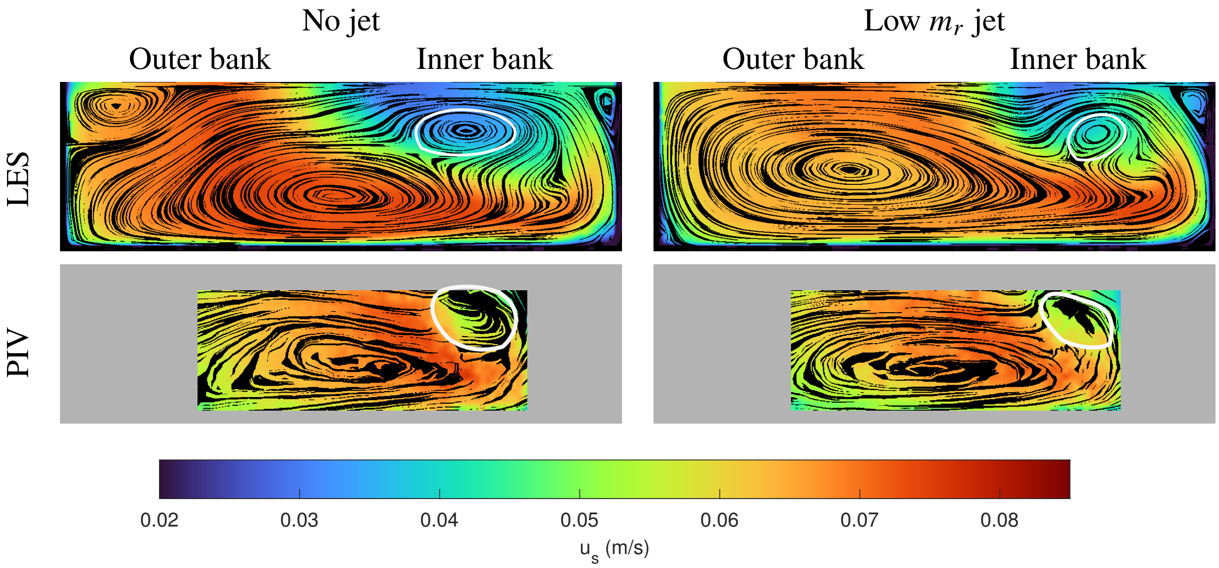

Figure 6.4: Comparison of LES and PIV secondary circulation and streamwise velocity component at the 90°cross section with no jet and with a low m_r jet. The cross section is 20 cm across and 6 cm deep. The IBC is circled in white. The field of view of the PIV is limited to eliminate reflections from the flume sides.

shown at the 90 degree cross section of the bend. In the case without the jet PIV and LES show both a centre cell and an inner bank cell, with good agreement on the horizontal position of both cells (which was shown by Schreiner et al. (2018) to be a key determinant of the mixing of the jet in the bend flow). The inner bank cell is circled in white for clarity. Though the OBC is not in the PIV field of view, its effect on the shape of the CC is clearly visible. When the low m_r jet is added, both PIV and LES show the IBC shrinking. In the LES, the OBC is observed to disappear and in the PIV the distortion of the CC shape lessens when the low m_r jet is present, indicating that the OBC shrank or disappeared.

The results of the cluster analysis for cross sections at 6, 22.5, 45, and 90 degrees as well as 1 cm before the start of the bend are shown in figure 6.5 along with surface LIC of the mean secondary flow. Without the jet, there are three principal circulation cells: One that occupies the inner bank at 90 degrees (IBC, in red circles); one that develops at the outer bank after the start of the bend and occupies the centre portion of the cross section at 90 degrees (CC, in blue squares), and the

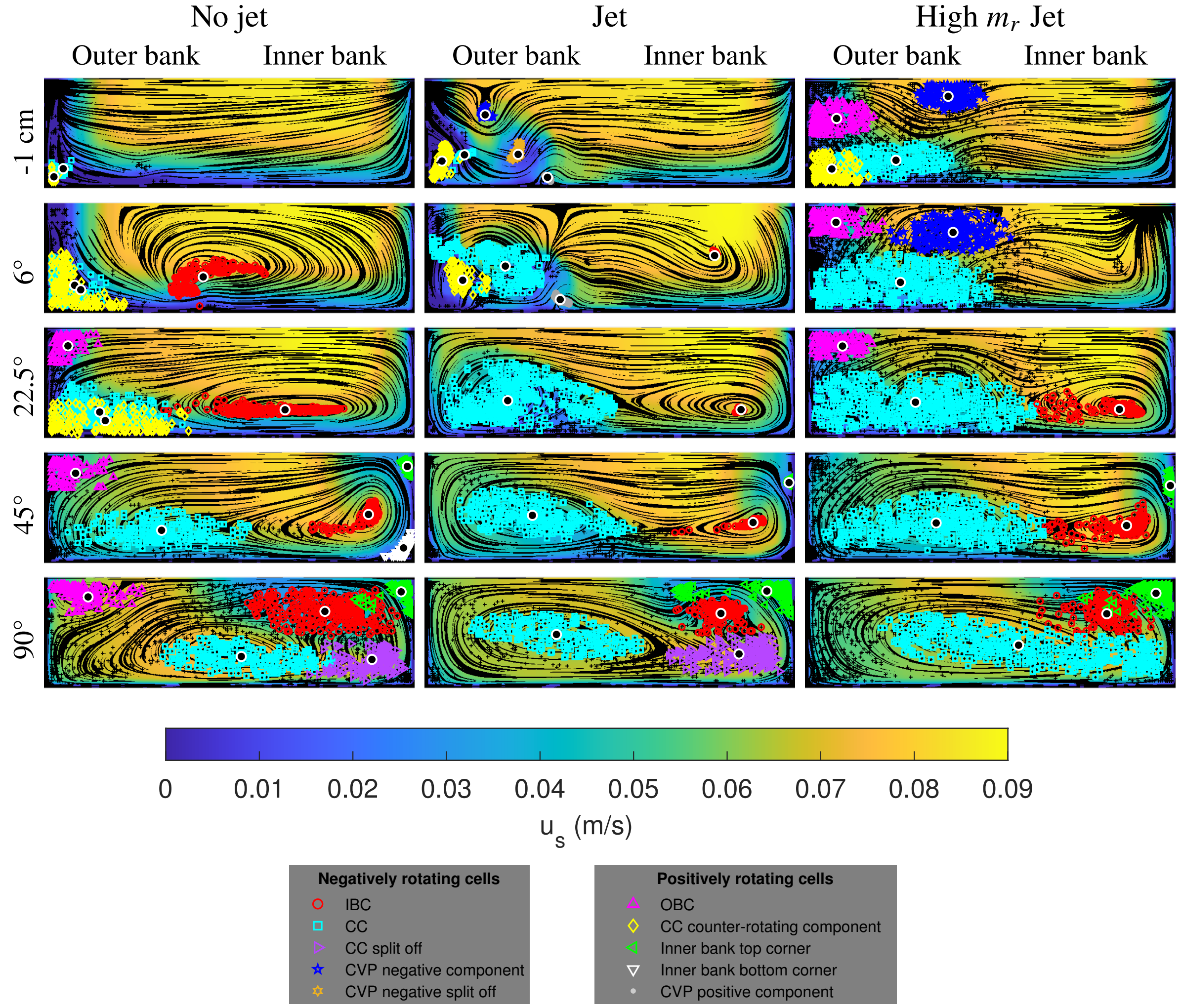

Figure 6.5: Circulation sub-cells detected using clustering for cases without a jet (left), with a low m_r jet (centre), and with a high-momentum jet (right)

outer bank cell (OBC, in pink triangles). Note that the naming convention used is based on the cells' position at 90 degrees, though they occupy different regions at different cross sections. At the 90 degree cross section, the position of the IBC distorts the shape of the CC, leading it to split into two clusters (blue squares and purple triangles).

The positive CVP vortex (shown in grey in figure 6.5) is advected into the channel bottom near the start of the bend in the low m_r jet case. This vortex disappears as the bend's negative circulation builds. In the high m_r jet case, the positive CVP component is not visible at all, as it is already much weaker than the surrounding cells at the start of the bend.

The IBC in the cases with the low m_r jet is clearly smaller than in the case without the jet. At the 6° cross section, one can see that the developing IBC circulation in the cases with the jet is limited in area and forced toward the inner bank by the presence of the jet vortices. This effect is magnified in the high m_r jet case, leading to an even weaker IBC, as is clear from the circulation development shown in figure 6.6.

The OBC is completely absent in the low m_r jet case, although it is present in some cross sections in the case with the high m_r jet. It can be concluded that the jet vortices interfere with the formation of the OBC when they are sufficiently close to the outer bank. The OBC's appearance in earlier cross sections in the high m_r jet case than the no jet case brings into question its classification: true OBCs are driven by turbulent anisotropy, and it is unclear whether that is the case for the cell seen with the high m_r jet. Rather, it is possible that this cell is composed of currents driven by the surrounding CC and negatively-rotating CVP vortex. This suggests that, although when close to the wall submerged jets at the outer bank prevent OBCs from forming, when offset from the wall submerged jets can drive similar cells where there would otherwise not be an OBC.

The circulation strengths of the principal cells throughout the bend with and without the jet are summarized in figure 6.6, along with the total time-averaged circulation in each cross section from all instantaneous vortices, clustered or unclustered. For the sake of clarity, the inner bank corner cells (white and green triangles) and the CVP cells (blue stars, orange x's, and grey dots) are

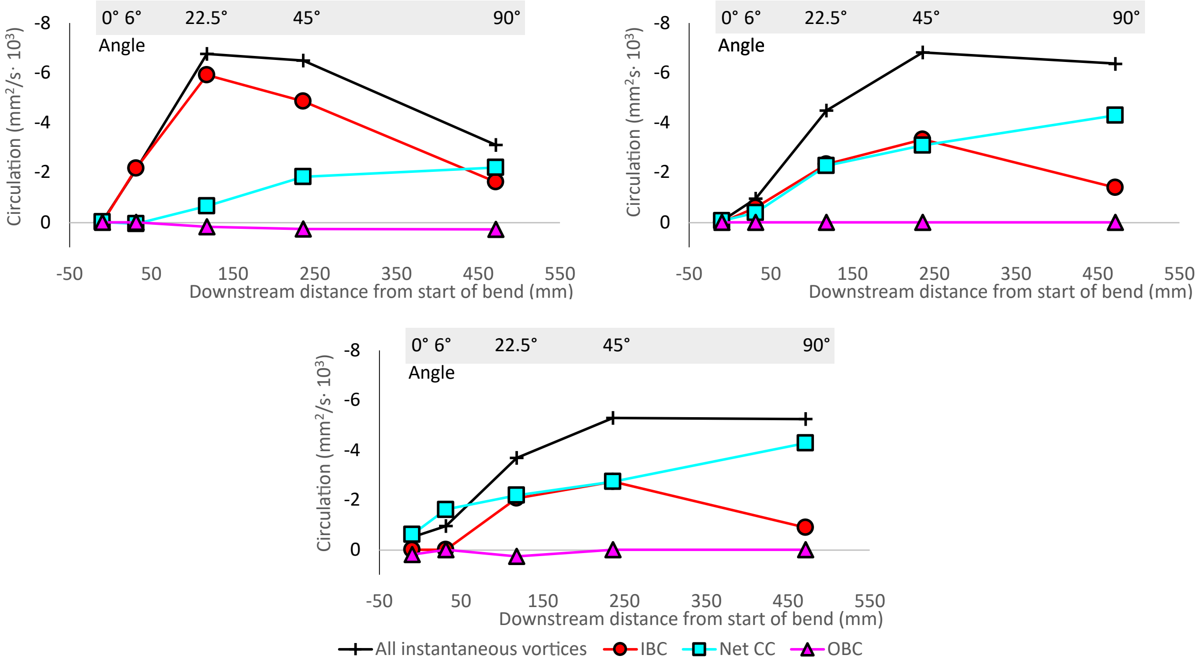

Figure 6.6: Summary of negative cell circulation strength for the no jet (left), jet (centre), and high m_r jet (right) cases at cross sections 1 cm before the start of the bend and at 6, 22.5, 45, and 90 degrees

omitted, and circulation of the CC is calculated as the net circulation of the main CC (blue squares), the counter-rotating cell that develops with the CC (yellow diamonds), and inner bank cluster that splits off from the main CC (purple right-pointing triangles). Since most of the cells are negatively rotating, the figure presents the negative of the calculated circulation. Compared to the no jet case, the circulation of the IBC is lowered and develops later in the low m_r jet case, while that of the CC is raised and develops earlier. The overall peak circulation is not much changed by the addition of the low m_r jet. The high m_r jet shows even further delay of IBC development and earlier CC development, as well as a reduction in the peak total circulation. The OBC is completely absent in the low m_r jet case, and only present in the earliest cross sections in the high m_r jet case.

Integrating along the length of the channel gives total circulation strength for each cell (table 6.2), which emphasizes the previously discussed results: while the total circulation does not exhibit much change, the circulation is redistributed from the IBC to the CC when the jet is added.

Table 6.2: Total circulation of each cell integrated along the length of the channel, peak total circulation, and percent change upon addition of jet

	No jet	**Low m_r jet**	**High m_r jet**	**Low m_r jet**	**High m_r jet**
	Integrated circulation (mm^3)			% difference	
IBC	-1.792	-1.028	-0.799	43	55
CC	-0.642	-1.313	-1.324	104	106
OBC	0.100	0	0.032	100	68
IBC+CC	-2.434	-2.430	-2.124	4	13
	Peak circulation (mm^2 × 10^3)			% difference	
Total	-7.2	-6.4	-5.5	10.7	23.9

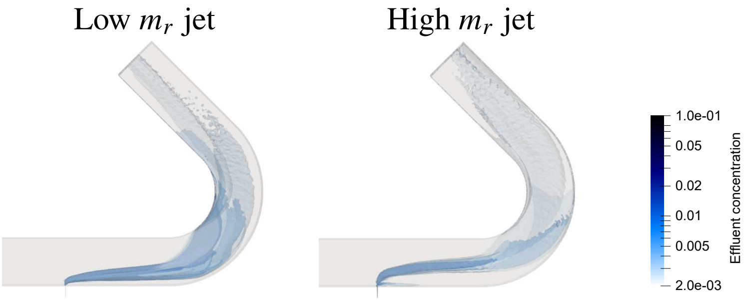
Low m_r jet

High m_r jet

Figure 6.7: Time averaged effluent concentration contours of two different jets

Figure 6.7 shows the time-averaged result of the scalar transport done concurrently with the LES simulations. The 90 degree cross section is shown in figure 6.8, showing that the IBC has much lower concentration than the surrounding regions. A similar but exaggerated effect is seen in the case with the high momentum jet.

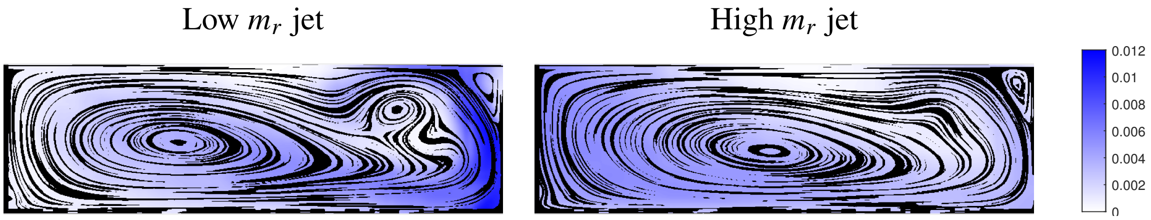
Low m_r jet

High m_r jet

Figure 6.8: Time averaged effluent volumetric concentration contours at the 90° cross section

6.4 Discussion

Two primary changes are evident with the addition of a jet: The disappearance of the OBC at some or all cross sections and the rearrangement of circulation between the IBC and CC. The OBC result suggests that the CVP vortices disrupt OBC formation if they are sufficiently close to the outer bank. This effect is localized at the outer bank, and is likely governed only by the position of the jet vortices at the given downstream location, i.e. whether the jet stays attached to the outer bank. The effect of bends on jet attachment is not yet known.

The change in circulation of the CC and IBC is best described as a redistribution of existing circulation, rather than a net change, with the IBC shrinking and developing later and the CC growing and developing earlier. This is especially true in the low m_r jet case (which is more representative of real world applications), where the CC and IBC total circulations only differ by 4%. There is a substantial decrease (24%) in the peak circulation in the case of the high m_r jet, as the two cells move apart and overlap less, but the integrated circulation is still only 13% less than the case without a jet.

The circulation changes between the no jet and jet cases start even before the beginning of the bend; it is clear from the first cross section in figure 6.5 that the CC develops in the region at the outer bank that includes the CVP, and that this region expands when increasing the strength of the jet. By contrast, the IBC is constricted toward the inner bank even at its development. Schreiner et al. (2018) found that the jet behaviour up until the start of the bend could be well accounted for using predictions based on straight crossflows alone, without accounting for any bend effects, and it is therefore possible that the redistribution of circulation between the CC and IBC is likewise independent of the total bend flow and circulation. In this case, the momentum ratio m_r would be the defining parameter to determine how far across the channel the jet reaches before the start of the bend. The extent of the jet at the very start of the bend where the IBC develops, taken as a proportion of the total channel width, may offer a simple predictive tool for quantifying the decrease in IBC strength.

In rivers, there are many geometric parameters of bends that affect the sub-cell distribution of circulation. The inner bank flow separation region, often associated with the IBC, was found by Blanckaert (2015) to grow with greater flow depth, which would imply that at aspect ratios commonly found in natural rivers, the IBC would be smaller than in this study. However, the presence of circulation structures at the inner bank in channels with aspect ratios similar to rivers has been well established (Blanckaert, 2015; Blanckaert et al., 2013; Kashyap et al., 2012), and the same jet-IBC interactions would take place, albeit to a lesser extent.

A comparison of the effluent distribution of the two jet cases, as shown in figure 6.8, shows that the cross-channel mixing occurs faster in the case with the high m_r jet, as would be expected for jets in crossflows in any other configuration. In the low m_r jet case, comparatively slow mixing is compounded by the strength of the IBC, which deflects the high effluent concentration core into the potentially sensitive area at the channel bed and the inner bank. This is in contrast to predictions made using river mixing models that don't take sub-cell structure of secondary circulation into account, which consider effluent reaching the inner bank to be a sign of full mixing. Though deflection by the IBC clearly plays a role in the position of the high concentration regions, the IBC strengths in the cases presented in this paper are changed only through the effect of the jet momentum. It is unclear whether changes in IBC strength due to bend radius, aspect ratio, or other geometric parameters would have the same effect on effluent mixing when unconnected to jet momentum.

Though this paper only considered the effect of the jet on the velocity field and the resulting effluent concentration, these effects might lead to further consequences in other areas. In particular, the simultaneous disappearance of the OBC and redistribution of circulation into the CC (which, in the absence of the OBC, lies directly next to the outer bank) may have morphological consequences yet to be considered.

6.5 Conclusions

Including a transverse jet in the channel bend brought about several distinct differences in the flow field: the IBC development was constricted at the inner bank, away from the region encompassed by the jet's CVP, and the IBC was therefore weaker and developed later. The CC developed in the region containing the CVP, and was correspondingly stronger and developed earlier. The OBC did not develop at all in the cases with the low m_r jet, and was driven earlier in the bend by the high m_r jet. The peak total circulation and integrated total circulation were not substantially changed by the low momentum jet.

The redistribution of circulation within the bend has implications for effluent transport. Specifically, the fact that the IBC developed in the region of low effluent concentration toward the inner bank resulted in the IBC recirculating low effluent concentration fluid even much later in the bend. Correspondingly, there were regions of higher effluent concentration around the IBC along the bottom and the inner bank. Other effects of circulation redistribution, such as the impact on erosion and deposition within the bend, were not directly studied here.

The changes in secondary flow structure developed at the outer bank before or shortly after the beginning of the bend, a region in which the jet behaves similarly to a jet in a straight crossflow. Now that the pattern of circulation redistribution has been identified, it may be possible to predict the amount of redistribution using the same parameters as for jets in straight crossflows.

Chapter 7

Machine Learning and parametrisation of multi-cell structures of secondary circulation in a tight open channel bend using LES

Abstract

Large eddy simulations of an open channel bend are performed at a variety of water depths and flow rates. The results at several cross sections are decomposed into sub-cells of secondary circulation using clusters of instantaneous vortices. The strength and position of the sub-cells are then modelled using decision trees, multiple linear regression, multi-layer perceptrons, and adaptive neuro-fuzzy inference systems to obtain parametric models of secondary circulation development in a channel bend. The development of individual cells and total circulation is shown for an arbitrary flow condition using the model, as well as the dependence of all the circulation output variables on the input parameters of aspect ratio and Froude number. The positions of the sub-cells (but not their circulations) are largely independent of the Froude number, and the cross-stream position of the centre cell is found to behave linearly. The model

with the best performance across all predicted variables is the ANFIS model without classification.

7.1 Introduction

Water passing through river bends flows in circulating paths that travel toward the outer bank at the top of the river and toward the inner bank at the bottom. The rotation of the water in these paths, called secondary circulation, drives all the flow-dependent processes that occur within the river bend, and therefore has effects on mixing, sediment transport, and river morphology.

In some channel bends, the secondary circulation does not go around the entire cross section of the channel at once, but is rather divided into smaller areas, or sub-cells, which each circulate separately. The most commonly observed sub-cell is the OBC, first observed in rivers by Bathurst et al. (1977). The OBC is a counter-rotating cell driven by turbulent anisotropy that occurs just beneath the surface at the outer bank. The presence of the OBC can be related to instability (de Vriend, 1981) which develops within a certain range of Dean number De, defined as (Dean, 1927, 1928):

$$De = \mathrm{Re}\sqrt{Cr} \tag{7.1}$$

Where Re is the Reynolds number and $Cr = h/R$ is the curvature ratio for bend radius of curvature R. The Dean number, like the Reynolds number, is often interpreted as a ratio of inertial forces to viscous forces in a fluid, but unlike the Reynolds number, the Dean number directly accounts for the centrifugal forces induced by channel curvature as part of the inertia.

Additionally to the OBC, some bends show the main secondary flow broken into two or more sub-cells, a phenomenon that can have further effects on the bend shape (Blanckaert et al., 2013) and bathymetry (Constantinescu et al., 2011). In tight bends, this takes the form of a sub-cell at the inner bank which is usually attributed to flow separation (Blanckaert, 2015; Leeder and Bridges, 1975). Kashyap et al. (2012) identified the inner bank cell, as well as a split-off cell at the outer bank, and traced the paths of all the sub-cells, defined by their mean centres, through a channel bend. Schreiner et al. (2023) introduced a method of defining the position of sub-cells using clustering of instantaneous vortices, which provides a method for tracking sub-cells even when their mean flow streamlines are not distinguishable.

In order to use the method for clustering instantaneous vortices, it is necessary to have data which gives snapshots of instantaneous velocity across the entire channel cross section. LES is one way to get that type of data numerically. While LES models of river bends have been very successful in modelling secondary circulation structures (Constantinescu et al., 2013a; van Balen et al., 2010, 2009), they can be computationally expensive, making it difficult to compare large numbers of flow conditions for parametrical analysis.

Machine learning is a powerful category of analysis tools capable of dissecting and characterizing even very complex and nonlinear problems; therefore it has high potential for applications to velocity in river bends. Given the computational expense of simulating each flow condition in a channel bend, machine learning has enormous potential for reducing the cost of studying bend flow. Many different machine learning techniques have been applied to predicting flow in river bends, such as gene expression programming (Gholami et al., 2015b) and artificial neural networks (Ajeel Fenjan et al., 2016; Gholami et al., 2015a) including feed-forward and cascade feed-forward neural networks and extreme learning machines (Vaghefi et al., 2020). When predicting secondary circulation at varying flow rates, many studies have found that it is useful to combine a decision tree with another model to first classify the flow into subcategories; for instance, classifying the flow into low velocity, medium velocity, or high velocity before fitting a machine learning model to each category of data. This method has been shown to yield results more accurate than standalone models without decision trees (Gholami et al., 2020, 2016a,b). Decision trees may also be built intrinsically into machine learning methods, such as with the methods used in Bali et al. (2019, 2020) to develop novel formulae for vertical and transverse velocities within a channel bend.

It is not always clear how exactly the decision trees in combined models classify cases: for instance, what is the dividing line between a high- and medium-velocity flow? By applying instantaneous vortex clustering to divide the secondary circulation into sub-cells, a clear idea of what should be classified becomes apparent: which sub-cells exist at the given cross-section. Thus the aim of this study is to combine sub-cell tracking using instantaneous vortex clustering with machine learning techniques to predict secondary circulation in a channel bend, first classifying which cells appear in a given cross section and flow condition and then predicting the circulation strength and position of each sub-cell.

7.2 Methods

All the bend flow secondary circulation data fed into the machine learning algorithm were generated using LES. The simulations were validated using PIV. The LES models took place on meshes containing between 3.4 million and 7 million cells, representing a rectangular bed channel of width 20 cm with a straight entrance section 2.4 m long followed by a single 135° bend of radius 30 cm and a straight exit section 0.5 m long, as shown in figure 7.1. The meshes divided the channel into 1440 cells in the streamwise direction and 88 cells in the cross stream direction, with a progressively finer mesh near the walls; the number of cells in the vertical direction depends on the water depth. The increased resolution near the walls kept the y+ value below 4 everywhere. The simulations used OpenFOAM's implementation of the dynamic k equation subgrid scale model first proposed by Kim and Menon (1995). This subgrid scale model was chosen in order to model the generation of the outer bank cell from small scale turbulence characteristics. The walls were modeled using a no slip boundary condition, and the air-water interface with a symmetry plane. The inlet was modelled by mapping the velocity distribution of the cross section 50 cm after the inlet back onto the inlet

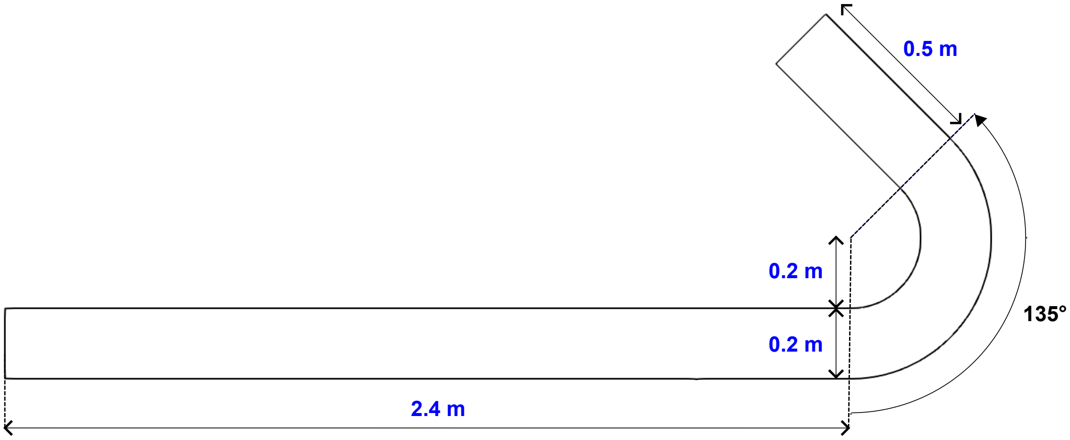

Figure 7.1: Schematic of bend geometry

plane, scaled to match the required flow rate, a method which has been shown to generate realistic turbulent fluctuations (Montorfano et al., 2013). As a verification of sufficient grid resolution, the proportion of resolved turbulent kinetic energy was estimated as $k_{resolved}/(k_{resolved}+k_{sgs})$, where k_{sgs} is the turbulent kinetic energy calculated by the dynamic k equation subgrid scale model. This quantity did not fall below 85% (the range suggested for a "good" LES model in Celik et al. (2005)) anywhere in the presented simulations. Further details on the simulation setup and the suitability of the dynamic k equation turbulence model can be found in Schreiner et al. (2023).

Validation PIV measurements were taken for three flow conditions using a LaVision Flowmaster system from a flume of the same geometry as the above described mesh. Measurements were from the 90 ° cross section using two cameras looking through the curved wall of the flume; the LaVision polynomial calibration algorithm was able to account for the distortion of the curved wall without any additional optical arrangements. The interrogation windows were set to 64 by 64 pixels, with a 75% overlap, giving a resolution of approximately 1.2 mm.

Channel bends are found in a variety of situations and applications, but most commonly in natural rivers. Rivers' width-to-depth ratios generally range from 10 to 100, ratios which can be difficult to achieve in laboratories while still enabling detailed velocity measurements. Though Yalin

(1971) recommends a minimum width-to-depth ratio of 5 in order to model river channels with minimal distortion, it is sometimes necessary to use deeper flows in laboratory scale models, and ratios around 3 are commonly seen in the laboratory experiments (Blanckaert and de Vriend, 2005; Blanckaert and Graf, 2001; Gholami et al., 2020). These ratios are representative of man-made channels rather than natural rivers. Because of the abundance of literature at these aspect ratios, it is useful to include them in a comprehensive parametric analysis of secondary circulation in channels. By further increasing the depth of flow to one half of the channel width, we can connect the rectangular-bed open channel bend model with a model of half of a square duct (where much of the literature on Dean instability is focused). This connection relies on the use of a symmetry plane to model the free surface of the water, which is generally held to be a sufficient model in open channels with low Froude numbers (Paik and Sotiropoulos, 2005). A full list of flow conditions with aspect ratios from 2 to 5 and Froude numbers from 0.045 to 0.22 is given in table 7.1. The flow conditions are defined by the water depth h and flow rate Q, and their corresponding dimensionless parameters B/h for channel width B and Froude number Fr. Each of these conditions is simulated, and five cross sections of LES data are used for the clustering and machine learning analysis: the cross section 1 cm before the start of the bend, and the cross sections at 6°, 22.5°, 45°, and 90°.

The sub-cells are distinguished using clusters of instantaneous vortices: vortices are detected at each time step using the algorithm from Graftieaux et al. (2001), and the centres of the vortices for all time steps combined are divided into clusters using DBSCAN. DBSCAN clustering was implemented in MATLAB using the method first proposed by Ester et al. (1996). A detailed description of the clustering method applied to instantaneous vortices is presented by Schreiner et al. (2023). Some adjustments to the basic method are made here in order to be able to apply the same parameters to so many cross sections of varying size and vortex density. The smallest 5% and the weakest 5% of the vortices are removed prior to clustering, as they generally appear on the edges of sub-cells and therefore applying a threshold enables better distinction between adjacent sub-cells. In order to account for a large variety in vortex density brought on by the changing size of the

Table 7.1: Flow conditions and predictor variables. Conditions with PIV measurements are in bold. Naming convention takes the water depth in cm and flow rate in mL.

Flow name	h (cm)	B/h	Q (mL/s)	Fr
h4Q566	4	5	566	0.113
h4Q693	4	5	693	0.138
h4Q894	4	5	894	0.178
h4Q1095	4	5	1095	0.219
h5Q632	5	4	632	0.090
h5Q775	5	4	775	0.110
h5Q1000	5	4	1000	0.143
h5Q1225	5	4	1225	0.175
h6Q693	6	3.33	693	0.075
h6Q1095	**6**	**3.33**	**1095**	**0.119**
h6Q849	6	3.33	849	0.092
h6Q1342	6	3.33	1342	0.146
h7Q1183	7	2.86	1183	0.102
h7Q1449	7	2.86	1449	0.125
h7Q748	7	2.86	748	0.064
h7Q916	7	2.86	916	0.079
h8Q1265	8	2.5	1265	0.089
h8Q800	8	2.5	800	0.056
h8Q1549	8	2.5	1549	0.109
h8Q980	8	2.5	980	0.069
h9Q1342	9	2.22	1342	0.079
h9Q849	9	2.22	849	0.050
h9Q1643	9	2.22	1643	0.097
h9Q1039	9	2.22	1039	0.061
h10Q1414	10	2	1414	0.071
h10Q1732	10	2	1732	0.087
h10Q1095	**10**	**2**	**1095**	**0.055**
h10Q894	10	2	894	0.045

cross sections and the changing number of vortices detected in each cross section, both clustering parameters are defined using N, the number of vortices detected in the cross section. The radius ε that defines the neighbourhood to be queried around each point is set to $3/\sqrt{\pi N}$, and the minimum number of points in the neighbourhood to define the centre point as a core cluster point, M_{pt}, is set to $\min(25, N/20)$. Using these definitions, and coordinates normalized using their ranges, both M_{pt} and the area queried around each point scale with the vortex density of the cross section. This allows the clustering step to be equally sensitive in a variety of cross section sizes and vortex densities.

In all cases, the circulation of a vortex is calculated as the integral of vorticity over the area detected as the vortex core by the method in Graftieaux et al. (2001). The circulation of a cluster is the time-averaged circulation of all contributing vortices, and the position of the cluster centre is taken as a circulation-weighted mean of the centres of all contributing vortices. The total circulation in the cross section is taken as the combined circulation of all vortices, regardless of which cluster, if any, they belong to.

Figure 7.2 shows a sample LES result, showing streamwise velocity and secondary circulation streamlines throughout the bend for the flow condition h6Q1342, as well as the coordinate system (s, n, z) representing streamwise, cross-stream, and vertical directions respectively. The division between adjacent cells of secondary circulation is not always clear; for consistent distinction of sub-cells and quantification of their circulation, it is necessary to use the instantaneous vortex clustering method. In the coordinate system presented, the main direction of secondary circulation is negative, and counter-rotating sub-cells have positive circulation. A sample cross section is shown in figure 7.3, showing the IBC (in orange squares), the CC (in red circles) and the outer bank cell (OBC, in yellow diamonds). These three cells are the most consistently seen, though others are detected in some cross sections. For instance, corner cells can develop at the inner bank (seen in figure 7.3 as green triangles), and a positively-rotating cell develops concurrently with the CC (shown in figure 7.3 as blue triangles) before disappearing in later cross sections. In later cross sections, the CC is sometimes split in two because of distortion caused by its proximity to the IBC.

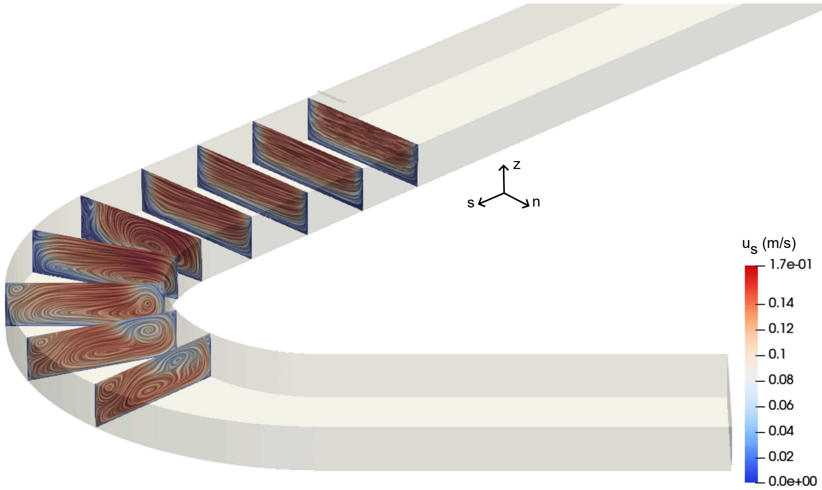

Figure 7.2: Sample LES mean flow results, shown for the h6Q1342 flow condition

The total circulation of the CC is therefore taken as the sum of the CC, its counter-rotating fellow, and the split-off cell. A full analysis of all the cells present in a single flow condition is available in Schreiner et al. (2023).

Many cross sections of many flow conditions do not contain all possible cells. In order for a circulation model to predict a circulation of zero for a cell which doesn't exist at the given input parameters, the input coordinates must correspond to a point in the model's nullspace. By first using a classification model to determine which cells exist, and only modelling the circulation for those that do, we loosen the requirements on the circulation model: the model must still predict nonzero values of circulation correctly, but the inputs corresponding to nonexistant cells do not all have to be within the model's nullspace. We can further loosen the requirements on the model by using a threshold to take extremely small circulation values, as happen when the cell is first developing, as equal to zero.

Before training the models, the circulation data are pre-processed by normalizing each variable by mapping the range of the variable to values between -1 and 1.

There are many ways to evaluate the predictive success of linear regression and machine learning models. In this study we use the R^2 value of the line of actual parameter vs predicted parameter, and

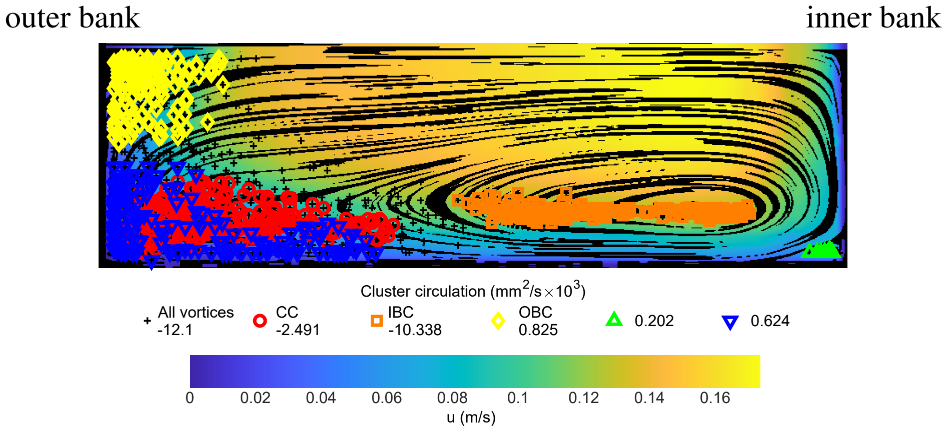

Figure 7.3: Sample clustering results of a cross section, presented for the 22.5 degree cross section of the h6Q1342 flow condition

the root mean squared error normalised root mean squared error (NRMSE), defined for a general variable, X, compared with predictions of its values, Y as:

$$\text{NRMSE} = \frac{\sqrt{\frac{1}{N}\sum_{i=1}^{N}|X_i - Y_i|^2}}{\max X - \min X} \tag{7.2}$$

This allows us to directly compare the linear regression and machine learning models using the same quantities, and allows us to quickly compare many different models at a glance.

The first regression method, used for the sake of establishing a baseline for each variable, is multiple linear regression (MLR). The second type of model is a multi-layer perceptron (MLP). These are feed-forward networks comprising an input layer, an output layer, and four inner layers. Each node in each layer contributes to the calculation of the nodes in the following layer, as shown in figure 7.4, with a fitted weight. The other machine learning method in this paper are ANFIS models. These systems are similar to non-fuzzy artificial neural networks but with an initial fuzzification layer. This layer classifies the input parameters into categories based on their values; membership in the categories is not absolute and takes values between 0 and 1, set by membership functions such as the triangular membership function shown in figure 7.5. The ANFIS systems used herein are

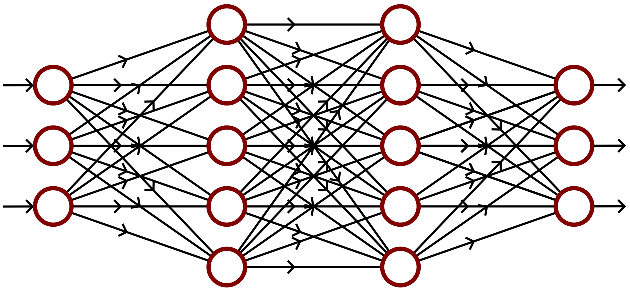

Figure 7.4: Sample structure of an artificial neural network

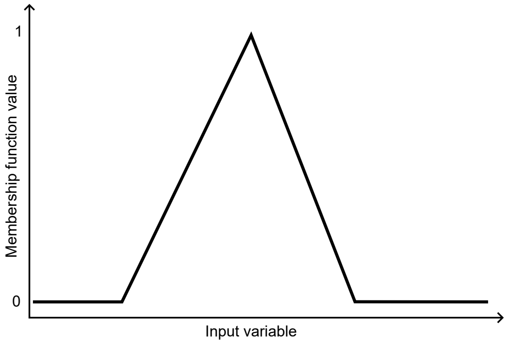

Figure 7.5: Sample structure of an ANFIS membership function

initially generated using grid partition clustering with triangular membership functions. During training, they are optimized in 10 training epochs using backpropagation to determine the parameters of the input membership functions, and least squares for output.

Each model (the multiple linear regression (MLR), the MLP, and the ANFIS) are fit in two different ways: first, to all data whether or not the cell in question is present; and second to only the cross sections which are classified using a decision tree as producing the cell in question. The classification models are binary decision trees: each decision node splits into two branches depending on the value of a single input variable.

To train machine learning models, a dataset must be partitioned into three parts: The training data, which is used to fit the model parameters in each iteration; the validation data, which is used to tune the hyperparameters of the model, and the holdout data (also called the test data), which is used to ensure that the final model developed using the training and validation data is not overfit to those datasets. For the purposes of this study, it is necessary to be able to directly compare different types of models, and the following data partition is thus adopted: the data is first divided into holdout and non-holdout data, with 14% of the data assigned randomly to be holdout data. Each model treats the partition between training and validation data differently: The MLR model and the decision trees have no need for validation data, and are therefore trained on the entire set of non-holdout data. The MLPs are fit using the first 75% of the non-holdout data for training; the remaining 25% is used for validation that is internal to the model fitting process in order to optimize model hyperparameters. ANFIS models are known to perform much better when trained on larger datasets (Akan and Keskin, 2019), and given that the size of the dataset used herein was relatively small for most machine learning applications, the ANFIS model was trained on 95% of the non-holdout data, with the remaining 5% reserved for tuning the model hyperparameters. In reducing the relative size of the ANFIS validation data, it is possible that the optimal ANFIS model was not achieved, but it was necessary to reduce the size of the validation dataset to ensure convergence on training data without sacrificing the size of the holdout data set. Though a 95%/5% split is uncommon, it is not unheard of: for example, Kazemi et al. (2023) used a 94%/6% training/validation split, with no holdout data. The additional holdout data in this ANFIS setup serves as further validation against overfitting, but does not contribute to optimizing the model. In both the multi-later perceptron (MLP) and ANFIS models, the training and validation partition was done at random.

7.3 Comparison with experiment

Figure 7.6 shows a comparison of streamlines and streamwise velocity for two flow conditions in PIV measurements and in simulation, with the CC, IBC, and OBC centre positions with markers sized proportionally to the strength of circulation. The circulation in the PIV measurements is taken as the sum of the vorticity over the cell area, which is identified as the connected area containing the same sign of vorticity, and the positions of the cells are taken as the vorticity centroid of the region.

The field of view of the PIV measurements is limited at the edges due to reflections off the walls of the flume. The circulation of the cells should not be directly compared between the simulation and experiment because of the absence of contribution in the PIV measurements beyond the field of view, and the differences in their methods of calculation. In particular, the definition of a cell from the simulation is based on the clustering method, but the definition in the PIV data is based in mean flow. This is because the centres of rotation of the OBC and IBC frequently lie outside the field of view, preventing the instantaneous vortices from being captured using the Graftieaux et al. method. However, the increase in IBC circulation, comparative consistency of CC circulation, and the increase in the size of the OBC between the h6Q1095 and h10Q1095 conditions is apparent in both simulation and experiment. In simulation, the increase in OBC size accompanies a *decrease* in OBC circulation which is not captured in experiment; this is likely because the decrease in circulation strength is countered by a greater proportion of the cell's vorticity being within the field of view, as can be seen by the change of position of the OBC between the cases.

7.4 Classification models

Once the cells and their circulations are properly defined and calculated, the first step to building a subcell circulation model is the classification model that determines which cells exist at a given input. This is accomplished with decision trees, fit to binary data of whether a given cell exists and meets the threshold minimum circulation (defined as 5% of the maximum circulation of the given cell) at the given input (giving a value of 1) or not (giving a value of 0). The fitted decision trees are presented in figures 7.7, 7.8, and 7.9 for the CC, IBC, and OBC sub-cells, respectively.

The classification models provide some insight into the development patterns of the sub-cells, with given inputs of Fr, B/h, and downstream position s. Figure 7.7 shows that the CC develops in every flow condition, but lower Froude number flows develop the CC later in the bend; likewise, figure 7.8 shows that the IBC develops in every flow condition but develops later for flows with

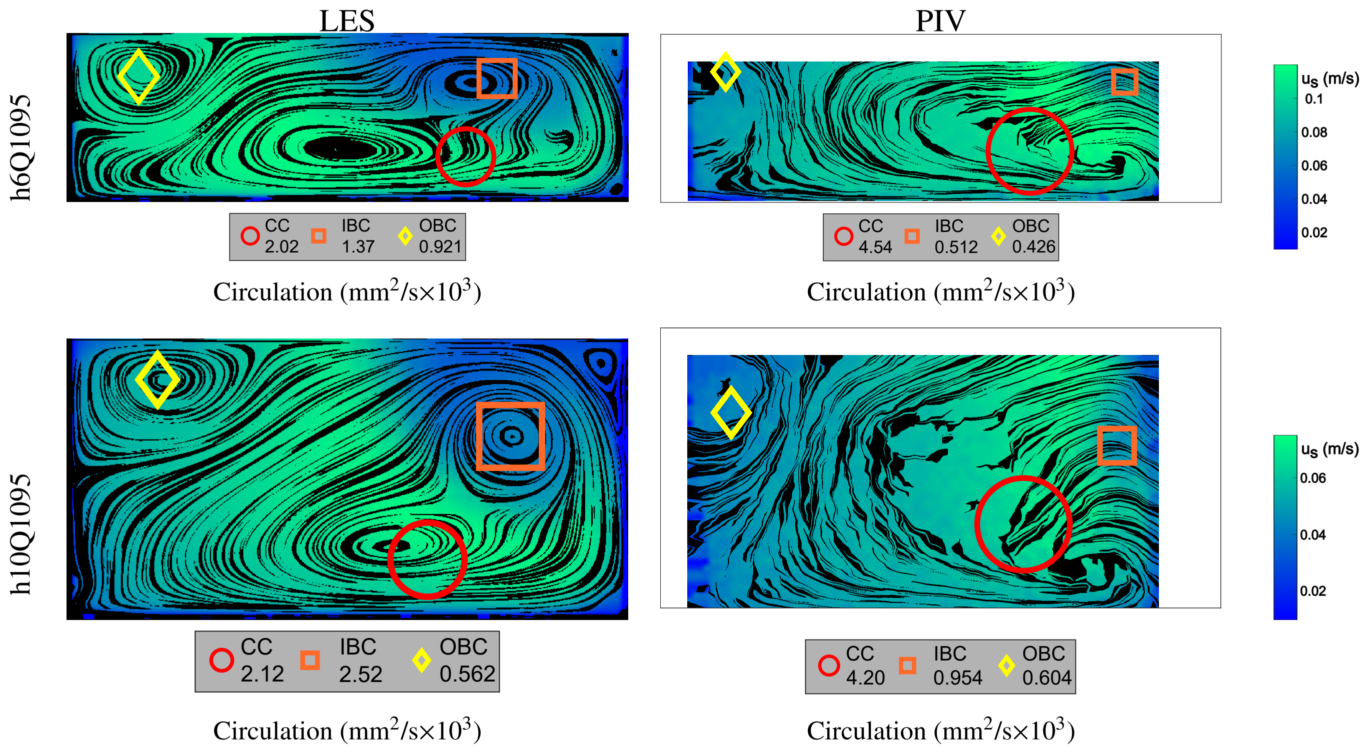

Figure 7.6: Comparison of LES and PIV for h6Q1095 (top) and h10Q1095 (bottom) flow conditions at the 90° cross section along with circulation strength of clusters in mm^2/s×10^3. The channel width is 20 cm, and the flow depth is 6 cm in the h6Q1095 case, and 1 cm in the h10Q1095 case.

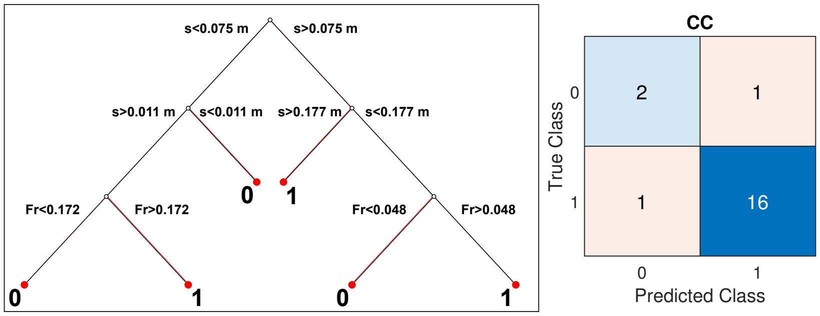

Figure 7.7: Decision tree for existence of CC showing 90% correct classification. A class of 0 indicates that the CC was not detected, while 1 indicates that the CC was detected. Each square in the confusion matrix shows the number of instances corresponding to the true class on the vertical axis and the predicted class on the horizontal axis. The blue cells indicate correctly categorized instances, and the other cells indicate incorrect classification

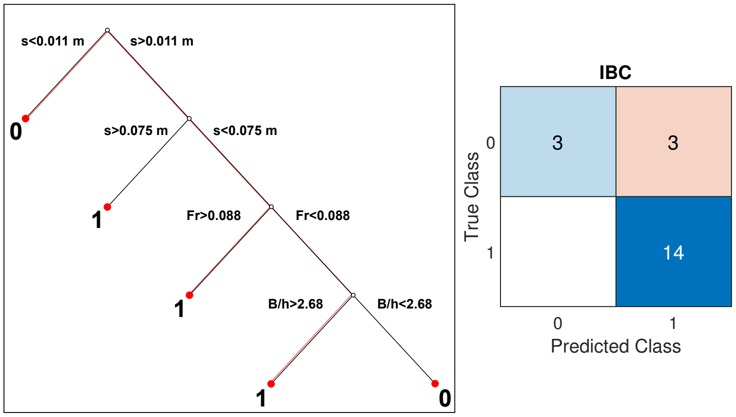

Figure 7.8: Decision tree for existence of IBC showing 85% correct classification. The blank quadrant indicates that there were no instances in that category

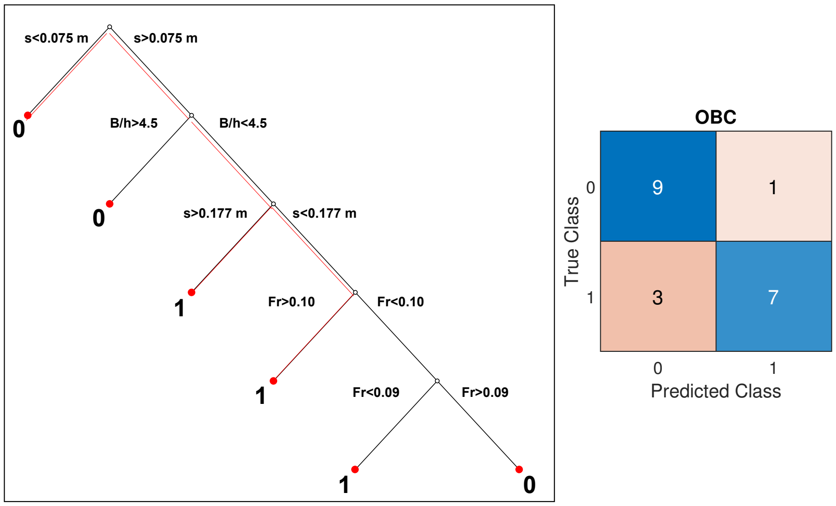

Figure 7.9: Decision tree for existence of OBC and confusion matrix showing 80% correct classification

smaller Froude numbers or width-to-depth ratios. The OBC classification is slightly different, since not all flow conditions contain an OBC at any point. This method misclassifies 20% of the holdout data, and will be revisited later.

7.5 Fitting models

The fitted models, both classification and regression models, are tested against the holdout or testing dataset. Since the existence of the total circulation is not contingent on the existence of any cell, no classification models are performed for the total circulation. Table 7.2 summarizes the R squared and NRMSE of all models applied to holdout data. Models are shown in bold if they meet a threshold for performance on holdout data slightly loosened from the thresholds on non-holdout data to an R^2 >0.8 and NRMSE< 0.125. This threshold is applied only for a convenient visual identifier, and does not hold any further significance.

Going forward, it is convenient to consider only one model for each variable to be predicted. The model choice going forward is presented in table 7.3. The chosen models are not necessarily the best performing models, but are chosen to present a variety of model types in the following sections.

As further comparison of the model results and simulation results for the holdout data, figure 7.10 is presented showing LES streamlines, clusters defining sub-cells, and cluster centres as well as the predicted cluster centres using the models from table 7.3. The circulations of the cells in simulation and in the models are presented in table 7.4.

Table 7.2: R squared and NRMSE for all models on holdout data, highlighted models have R^2 >0.8 and NRMSE<0.125

	No classification			With classification		
	MLR	MLP	ANFIS	MLR	MLP	ANFIS
Output parameter	R^2 NRMSE	R^2 NRMSE	R^2 NRMSE	R^2 NRMSE	R^2 NRMSE	R^2 NRMSE
Total circulation	0.245 0.215	**0.951** **0.063**	**0.956** **0.054**	—	—	—
CC circulation	0.524 0.175	0.746 0.130	**0.867** **0.096**	0.607 0.162	**0.823** **0.107**	0.381 0.269
IBC circulation	0.129 0.260	**0.905** **0.090**	**0.900** **0.097**	0.478 0.202	0.708 0.153	**0.881** **0.107**
OBC circulation	0.568 0.160	**0.820** **0.104**	**0.893** **0.081**	**0.829** **0.106**	**0.831** **0.103**	0.755 0.124
CC n	**0.943** **0.083**	**0.918** **0.100**	**0.992** **0.030**	**0.949** **0.073**	**0.978** **0.050**	0.850 0.221
IBC n	0.332 0.216	0.728 0.128	**0.882** **0.105**	0.242 0.222	**0.956** **0.057**	0.772 0.152
OBC n	0.728 0.134	**0.915** **0.076**	**0.913** **0.084**	**0.931** **0.067**	**0.927** **0.072**	**0.955** **0.067**
CC z	0.605 0.151	0.763 0.127	**0.826** **0.095**	0.652 0.079	0.650 0.063	0.493 0.085
IBC z	**0.897** **0.086**	**0.963** **0.064**	**0.960** **0.054**	**0.898** **0.087**	**0.996** **0.018**	**0.959** **0.057**
OBC z	**0.916** **0.097**	**0.924** **0.073**	**0.927** **0.071**	**0.869** **0.073**	**0.835** **0.094**	**0.854** **0.078**

Table 7.3: Machine learning models used for further analysis

Output parameter	Model choice
Total circulation	MLP
CC circulation	MLP+Fr-class.
IBC circulation	MLP
OBC circulation	MLR+Fr-class.
CC n	MLR+Fr-class.
IBC n	ANFIS
OBC n	MLP
CC z	ANFIS
IBC z	MLP
OBC z	MLP

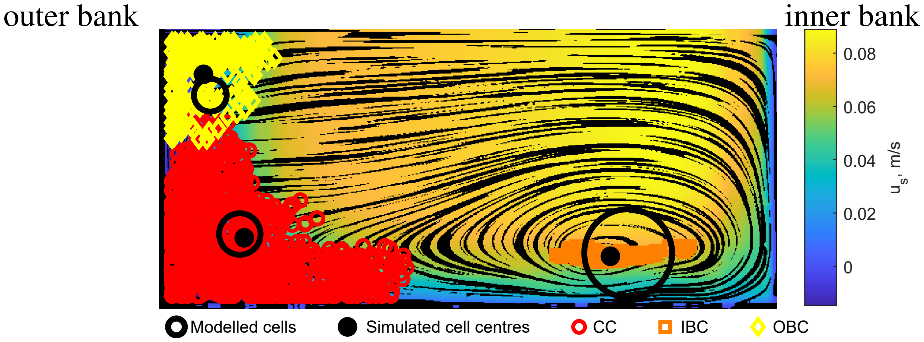

Figure 7.10: LES (coloured clusters, black dots at centroids) and machine learning-modelled (black circles) cells for sample holdout cross section (h9Q1039 flow condition at 22.5 degrees). Machine learning-modelled markers scale with circulation; circulation quantities for machine learning and LES cells are given in table 7.4.

Table 7.4: Simulated and modelled cell strengths for h9Q1039 flow condition at 22.5°

Cell strength ($mm^2/s\times10^3$)	CC	IBC	OBC
Simulated circulation	-1.02	-3.68	0.4
Modelled circulation	-0.89	-4.01	0.56

7.6 Choice of classification models

The previous section's model assessments focus either on the classification models, with confusion matrices, or the regression models, with tables of R^2 and NRMSE. Assessing the performance of both together is more complex, and is worth taking the time to focus on the changes to model performance when including a classification step.

In comparing the models without and with classification, one obvious conclusion is that the ANFIS models decrease in reliability with the addition of a decision tree. Recalling the structure of an ANFIS model, it includes a classification step using fuzzy membership functions. This classification step is not specifically directed toward classification of the presence of circulation cells (as the decision tree models are), but if the fuzzy classification results align sufficiently well with the presence of the circulation cells, then the decision tree model becomes redundant and only introduces another source of error. Another possible reason that that the classification-coupled ANFIS models did not perform well as those with no classification is that ANFIS models are known to improve with the size of the training dataset. Therefore, allowing the ANFIS model to train on all data points, including points where the cell has zero circulation, likely has an inherent benefit

In contrast to the ANFIS models, the MLP and MLR models for cell positions (especially cross stream position) often improve with the addition of classification, though the same cannot be said of circulation models. This is a result of how errors from misclassification propagate into the error metrics (i.e. R^2 an NRMSE) for the regression models: if the classification model makes an error in the existence of a cell, then the performance metrics of the combined models for cell location will not show a decrease in model performance, since the cell location is not well defined when the cell does not exist, and therefore is not well defined in both the modelled and LES data. The same error propagation is also likely occurring in the ANFIS models, but the overall decrease in performance metrics for the classification-coupled ANFIS models obscures the effect.

In principle, this could be entirely avoided if there were a way to define the location of cells when they are not present. Looking at the classification trees for both the CC and the IBC, it is clear that both will eventually develop in all studied flow conditions, and therefore when they are not present it is because they are still developing. If they could be shown to develop at a consistent location, one could use those coordinates as a default in order to have well-defined numbers for the sake of comparison. This could work in the case of the CC, which develops at the outer bank (Schreiner et al., 2023); but not necessarily in the case of the IBC or in cases with more complex bathymetry, where there may not be specific coordinates of the developing cells.

Thus it is highly important to ensure accuracy in the decision tree models to maximize the benefit to the performance of the coupled regression models. Unlike the CC and IBC, the OBC has an established body of literature on determining where it will exist, depending on the Dean number; the outer bank cell is known to appear in flows with Dean numbers within a critical range (de Vriend, 1981), something that should be easily modelled with a decision tree given the right inputs. Since all the flow conditions included in the models have the same bend geometry, the Dean number can replace the Froude number in an OBC-specific decision tree, accounting for flow inertia. If it were necessary to account for variation in both flow rate and channel curvature, it would become necessary to include both Fr and De. A decision tree using the inputs of De, B/h, and s is shown in figure 7.11, showing only a slight improvement over Fr-based classification when applied to holdout data.

The marginal improvement in classification will likely result in the same errors as before, as described above, but it is worth a demonstration of the full models built with De-classification for explicit comparison. The performance metrics of the models using De-based classification models are shown in table 7.5, which show no clear advantage of De-classification over Fr-classification, despite the marginally better classification results.

Li et al. (2017) found that Dean instability could also manifest in the splitting of the main secondary circulation cell, not unlike the split seen in the present study between the CC and IBC,

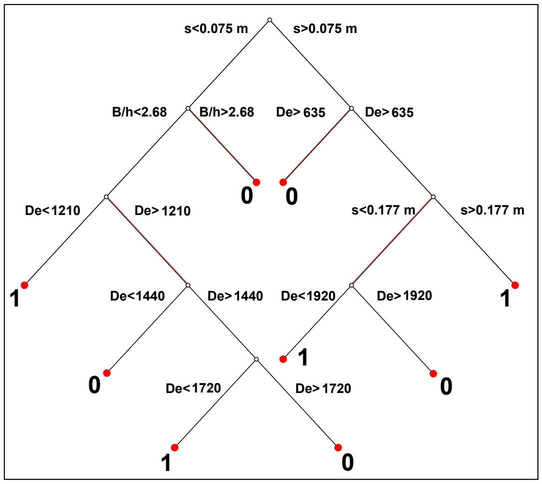

Figure 7.11: Decision tree for existence of OBC based on De

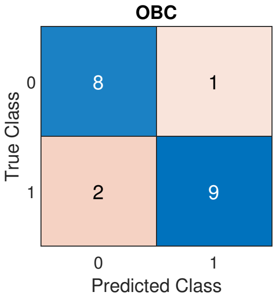

Figure 7.12: Confusion matrix for OBC classification with De on holdout data, showing 85% correct classification

though the present cells' definitions are based on instantaneous flow vortices and Li's observations were based on mean flow streamlines. This raises the possibility that the CC and IBC classification could also be done with the Dean number instead of the Froude number. However, given that the OBC has a much stronger demonstrated connection to the Dean number and yet the De-based classification only yielded a marginal improvement on the Fr-based classification and the resulting regression models did not show any improvement, it is unlikely to be beneficial to switch entirely to De-based classification for all cells. As proof, confusion matrices for De-based classification of the CC and IBC are shown in figure 7.13, showing worse classification results than Fr-classification.

Table 7.5: R squared and NRMSE for Dean classification-based OBC models on holdout data, highlighted models have R^2 > 0.8 and NRMSE< 0.125

	No classification			With Fr-classification			With De-classification		
	MLR	MLP	ANFIS	MLR	MLP	ANFIS	MLR	MLP	ANFIS
Output parameter	R^2 NRMSE	R^2 NRMSE	R^2 NRMSE	R^2 NRMSE	R^2 NRMSE	R^2 NRMSE	R^2 NRMSE	R^2 NRMSE	R^2 NRMSE
OBC circulation	0.568	**0.820**	**0.893**	**0.829**	**0.831**	0.755	0.581	**0.859**	**0.828**
	0.160	**0.104**	**0.081**	**0.106**	**0.103**	0.124	0.127	**0.083**	**0.143**
OBC n	0.728	**0.915**	**0.913**	**0.931**	**0.927**	**0.955**	0.644	**0.840**	**0.949**
	0.134	**0.076**	**0.084**	**0.067**	**0.072**	**0.067**	0.146	**0.107**	**0.076**
OBC z	**0.916**	**0.924**	**0.927**	**0.869**	**0.835**	**0.854**	**0.922**	**0.968**	**0.925**
	0.097	**0.073**	**0.071**	**0.073**	**0.094**	**0.078**	**0.091**	**0.051**	**0.089**

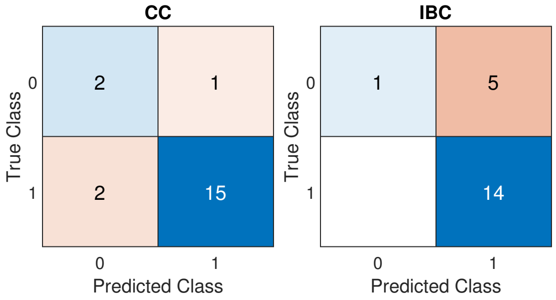

Figure 7.13: Confusion matrices for CC and IBC classification using De

7.7 Relative importance of parameters

Now that we have models that are able to predict the circulation and position of the sub-cells given input parameters, we can use them to gain information about the response of the output variables to changes in flow conditions. There are many ways to assess the relative importance of input parameters in regression models, but most are specific to a particular structure of model; for instance, the p-value of coefficients in a multiple linear regression or using metrics calculated using connection weights of neural networks, such as proposed by Garson (1991). In order to compare different types of models directly, we can instead compare the performance of the model given a complete set of input variables to the performance if a variable is removed, using to the method proposed by Kemp et al. (2007). When a variable is removed for this test, it is replaced with uniformly distributed data within the range of the input parameter. Table 7.6 compares the R^2 and NRMSE results of each modelled output variable when given the unaltered input data, and when each input variable is removed. If the removal of an input variable does not decrease the performance of the model, it suggests that the model is not sensitive to the variable, whereas a decrease of model performance upon the removal of an input variable indicates dependence on that variable. From table 7.6 it can be seen that the cell positions are largely independent of the Froude number, with the exception of the vertical position of the CC.

Table 7.6: Analysis of parameter importance by R squared and NRMSE comparison with variable omissions

		All	No Fr	No B/h	No s
Output parameter	Model	R^2 NRMSE	R^2 NRMSE	R^2 NRMSE	R^2 NRMSE
Total circulation	MLP	0.951	0.729	0.786	0.082
		0.063	0.136	0.122	0.301
CC circulation	MLP+Fr-class.	0.823	0.583	0.151	0.054
		0.078	0.204	0.184	0.314
IBC circulation	MLP	0.905	0.652	0.496	0.129
		0.090	0.180	0.227	0.328
OBC circulation	MLR+Fr-class.	0.829	0.670	0.004	0.094
		0.111	0.367	0.295	0.261
CC n	MLR+Fr-class.	0.949	0.944	0.898	0.009
		0.073	0.078	0.089	0.252
IBC n	ANFIS	0.882	0.606	0.485	0.009
		0.105	0.253	0.212	0.400
OBC n	MLP	0.915	0.859	0.096	0.355
		0.076	0.167	0.466	0.340
CC z	ANFIS	0.826	0.072	0.001	0.054
		0.095	0.226	0.272	0.228
IBC z	MLP	0.963	0.939	0.232	0.223
		0.064	0.101	0.274	0.270
OBC z	MLP	0.924	0.881	0.152	0.874
		0.073	0.100	0.440	0.097

Though it is difficult to characterise dependence on input parameters for black box models such as the MLPs and ANFIS models, it is easy to do in the case of the linear regression models. For instance, the linear regression model employed for the CC n position can explicitly show the dependence on input variables: the coefficient for Fr (normalised by the total range that Fr takes) in the regression model is -2.4×10^{-4}, with a 95% confidence interval of $(-0.0084, 0.0079)$ and the coefficient for B/h (similarly normalised) is -0.0079 with a confidence interval of $(-0.0139, -0.0019)$. Thus one can explicitly state that this model is independent of Fr and significantly dependent on B/h, though B/h has a small influence due to its small coefficient. This is borne out by the results in table 7.6.

7.8 Model responses to parameters

It is also possible to investigate the circulation responses to changes in individual variables: figures 7.14, 7.15, and 7.16 show how the circulation changes, according to the models chosen in table 7.3, with channel position, Froude number, and aspect ratio, respectively. In each case, the two variables that are not being investigated are held constant at the centre of the ranges they take in the dataset, with exact values given in the figures. This represents a flow condition that was not directly simulated, but was modelled using simulated data, as a demonstration of the models' abilities to predict properties of the flow without incurring the computational expense associated with LES.

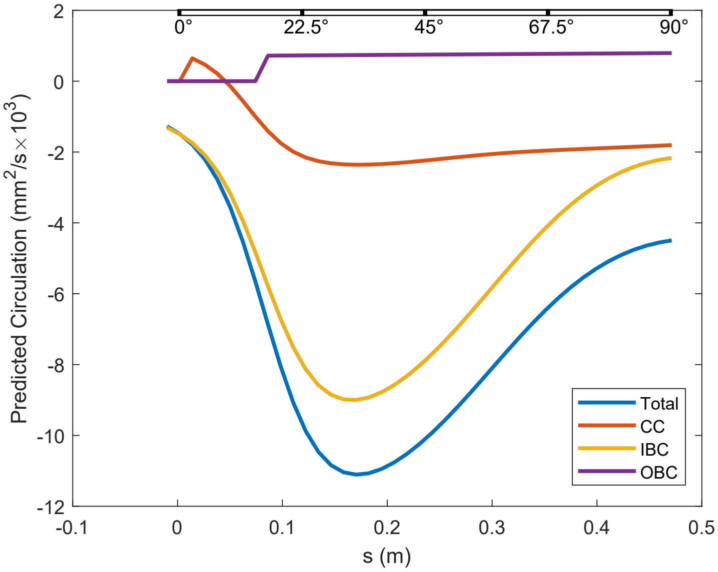

Figure 7.14: Circulation development over channel position s with $h = 5.71$ cm and $Fr = 0.1318$

Figure 7.14 shows the development through the channel of the sub-cells and total circulation. The IBC develops quickly, reaches a peak, and then drops quickly, where the CC develops more slowly and reaches a plateau. This is the same pattern established by Schreiner et al. (2023). The OBC develops later in the bend than the other cells, and stays relatively steady after development, which is also in keeping with the results from Schreiner et al. (2023). The late development and the steadiness after would not be achievable together in a single linear model; thus the OBC development also serves as a demonstration of the usefulness of classification-coupled models.

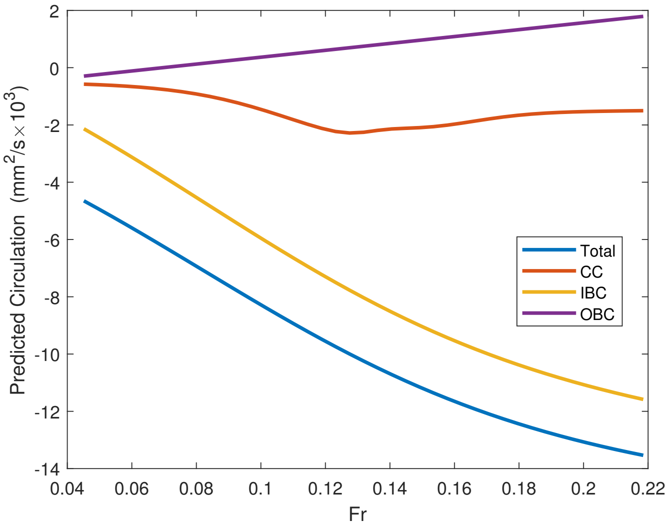

Figure 7.15: Circulation variation over Fr at 45°(s=0.23 m) with h = 5.71 cm

Figure 7.15 shows an increase in CC circulation over low Froude numbers, which does not continue after Fr reaches a value of 0.125. This is in keeping with the findings of Wei et al. (2016) that secondary circulation was not dependent on the Froude number when it was in the range $0.1 < Fr < 0.5$. However, figure 7.15 shows an increase in total circulation and in IBC circulation with increasing Froude number, which seems to indicate that Wei et al.'s results only apply to the centre region cell.

In the limit of high width-to-depth ratios, which is more representative of natural rivers, the circulation of the CC goes to nothing in the example given in figure 7.16. Since this is predicted

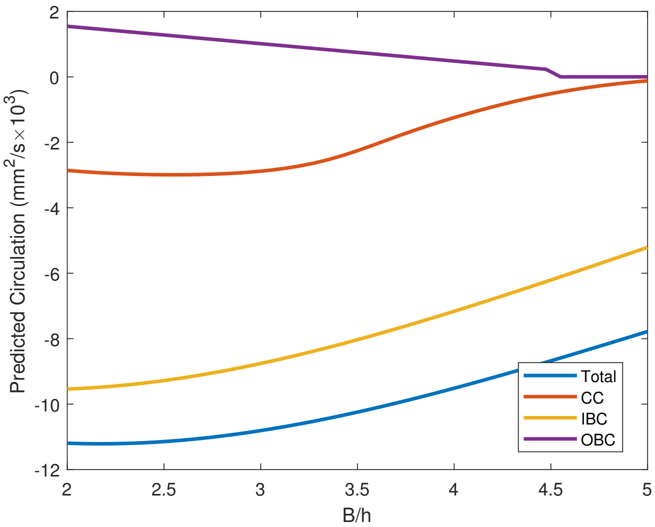

Figure 7.16: Circulation variation over B/h at 45°(s=0.23 m) with Fr = 0.1318

using a classification model, it is worth recalling that very weak circulation will be classified as non-existence, and it is therefore possible that the CC has very weak but present circulation. It is also worth noting that (Bali et al., 2020) saw a similar effect over aspect ratio in the maximum transverse velocity observed at the surface for low deflection angles where the CC would be the dominant circulation cell.

The positions of the circulation cells can be similarly predicted for arbitrary flow conditions. Figure 7.17 shows the locations of each developing cell throughout the bend flow, with the CC and IBC scaled according to their circulation strength. The figure shows discontinuities in the behaviour of both the cross stream position of the IBC and the vertical position of the CC. These stem from changes in the ANFIS membership functions which apply different rules to the cells' locations at different points in the bend: the IBC's cross stream location behaves differently after the CC develops, and the CC's vertical location shifts once it is close enough to the IBC to be deflected downward.

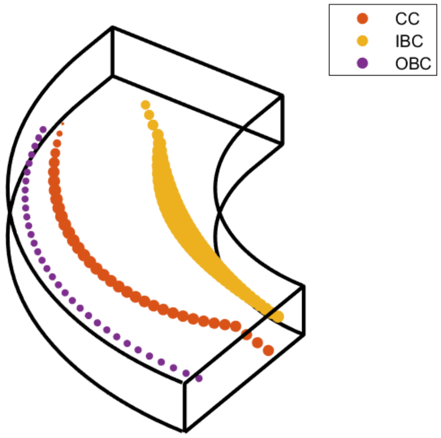

Figure 7.17: Cell positions for $Fr = 0.1318$ and $h = 5.71$ cm, with CC and IBC size proportional to circulation strength. Values of circulation strength are given in figure 7.14.

7.9 Discussion

As stated in section 7.6, the Dean number functions very similarly to the Froude number in these models, since both account for the inertia of the channel flow. Extending a similar model to other bend geometries would greatly increase the usefulness of the model, and would also require the addition of input parameters to account for the bend geometry. In such a model, both the Dean number and the Froude number could be used for predicting the behaviours of all circulation cells.

One interesting result from table 7.2 is the apparent difficulty of modelling the vertical position of the CC, which only had one model reach the given thresholds (the ANFIS model, with R^2 0.826 and NRMSE 0.095). In considering the validity of the tested models, one must also consider the distribution of the actual values of the CC vertical positions, which were very closely spaced within a total range of 3.39 cm in all simulations, translating to a non-normalized RMSE of 3.2 mm for the ANFIS model. Fifty percent of the CC instances were grouped even more closely, between 1.55 cm and 2.13 cm. Since the average vertical grid resolution of the mesh was 1.66 mm, it is possible that any attempt to better predict vertical location of the CC given the current simulation data will run into the fundamental limitation of grid resolution.

The IBC is often considered to be a result of flow separation, which is known to be a feature of tight channel bends (Leeder and Bridges, 1975), though it has not always been possible to reliably distinguish the IBC's circulation from circulation contained in the CC. The pattern of circulation development and retention, as shown in figure 7.14, differs between the cells, with the IBC developing faster, peaking higher, and decreasing in strength more quickly than the CC. Importantly, these are all features of circulation in tight bends (Kashyap et al., 2012). Therefore the distinction between the CC and IBC could illuminate the causes of circulation differences between mild and sharp bends, which show CC-like and IBC-like development patterns, respectively.

7.10 Conclusions

Machine learning models of secondary circulation have been built using LES models of flow in a channel bend. Using these models, we can establish the sensitivity of the output variables (total circulation, sub-cell circulation, and sub-cell position) to the input variables of downstream position, aspect ratio, and Froude number. The positions of the sub-cells are largely independent of the Froude number, and the cross-stream position of the CC is linear and depends only on the streamwise coordinate. The models are also shown to produce circulation development patterns for the sub-cells similar to those already established in Schreiner et al. (2023).

In general, the ANFIS model without classification was the best-performing model. Given the small size of the dataset used in this study and the simplicity of the ANFIS model used, it is also likely that even better ANFIS models could be developed for bend circulation if given a larger dataset. Given the success of models coupled with decision trees in previous studies on bend flow, it is surprising that the addition of a classification tree did not universally improve the performance of the models, but it is apparent that the potential for introducing error via misclassification outweighed the benefits of adding a classification step to the ANFIS models in particular.

Chapter 8

Parametrisation of jet effects on secondary circulation and resulting effluent distribution

Abstract

The jet and bend combined circulation cells, identified using clusters of instantaneous vortices from LES data, are modelled using decision tree classification, linear regression, and machine learning models. The effect of varying the jet strength on the sub-cell distribution is thus investigated: the effect on the circulation of each sub-cell is highly dependent on the relative strength of the jet, as different jet conditions result in different CVP positions within the bend. The most successful model for predicting the sub-cell parameters with the jet present is the ANFIS model coupled with classification.

LES data are compared with PIV velocity data and dye test effluent distribution. The effluent concentration distribution at the 90° cross section from LES is also characterised using linear regression, showing good agreement.

8.1 Comparison of simulation and experiment

Figure 8.1 shows a comparison of PIV and LES streamlines and streamwise velocity for the flow conditions h6Q1095j0, h6Q1095j1, and h6Q1095j2, along with the position and size of each circulation cell, using the same calculation methods for PIV cell circulation and position as in Chapter 7. Both the PIV and LES results show the OBC shrinking with the addition and subsequent strengthening of the jet. The CC shows an increase in circulation in the weak jet case, and a decrease again when the jet is increased; additionally, the CC shows strong distortion in the streamlines underneath the IBC in the case without the jet, which decreases as the jet is added. Note that the weighted centre position of the CC includes contribution from the high vorticity region beneath the IBC, which is why it does not align with the visual centre of the streamlines. The IBC initially increases slightly in strength with the addition of the jet, but the simulations and experiment show disagreement in the effect of the stronger jet: the simulations show a further increase in IBC strength while the experiments show a decrease, which could be in part due to the lack of data from the IBC region close to the inner wall, which is obscured with reflections.

The flow conditions h10Q1095j0 and h10Q1095j2 are similarly displayed in figure 8.2. Both the simulation and the models show a distinct IBC that is reduced when the jet is added. In the PIV, the IBC is not explicitly visible in streamlines, but its presence may be deduced from the strong u_s gradient, the sharp bend in streamlines at the top right corner, and by a region of opposite vorticity between the two cells (not shown). In both simulation and measurement, the IBC shrinks with the addition of the jet. The OBC also diminishes with the addition of a jet, though not as much as in the h6Q1095 flow rates in figure 8.1. The effect of the jet on the CC is not consistent between LES and experiment, with the LES showing a substantial increase in CC circulation, while the PIV measurements show a slight decrease.

Figure 8.3 shows a comparison of results for the h6Q693 flow conditions. Again the reduction of the OBC with the addition of the jet is visible in both experiment and simulation. However, this flow

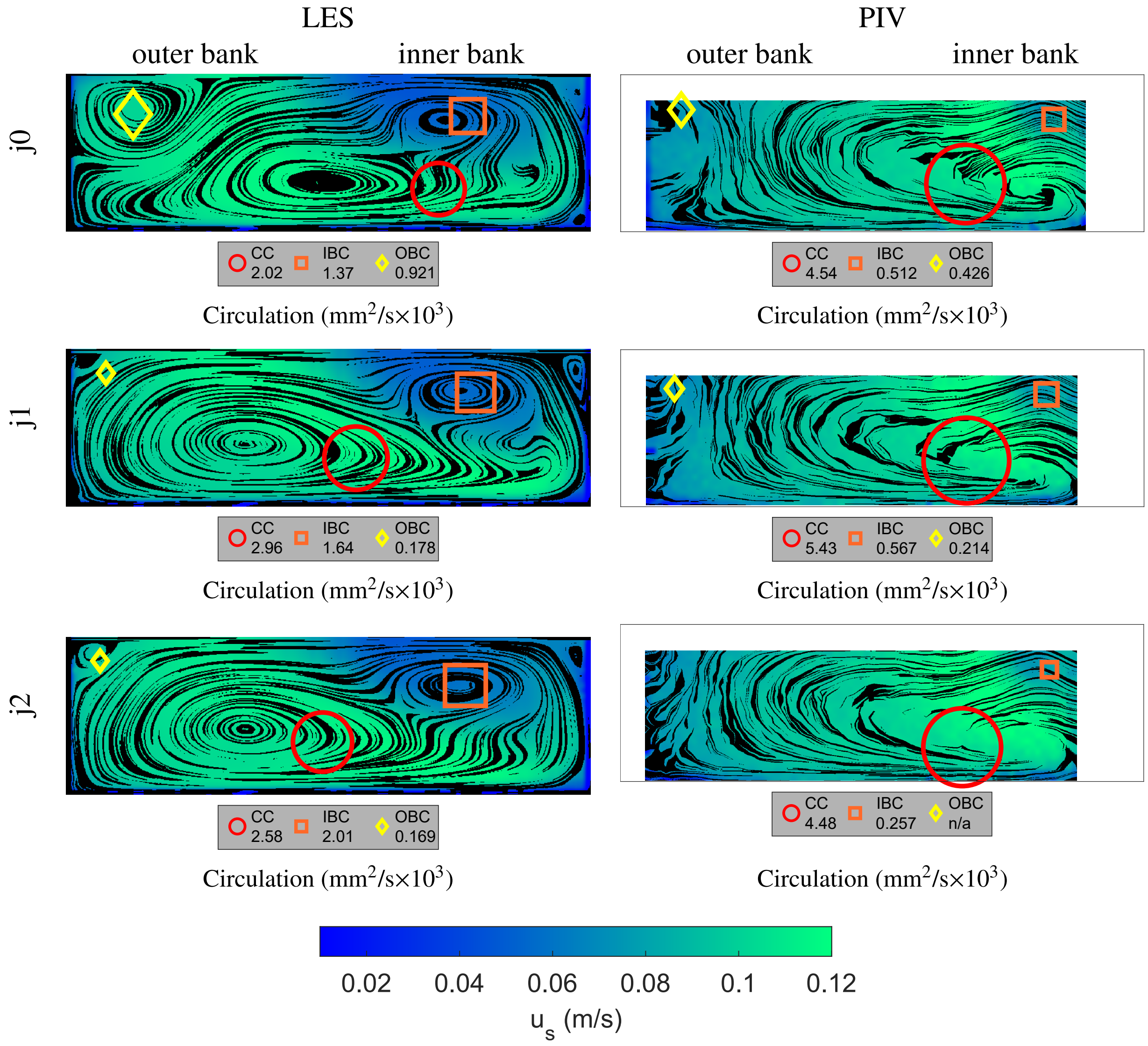

Figure 8.1: Comparison of LES and PIV for h6Q1095 flow conditions

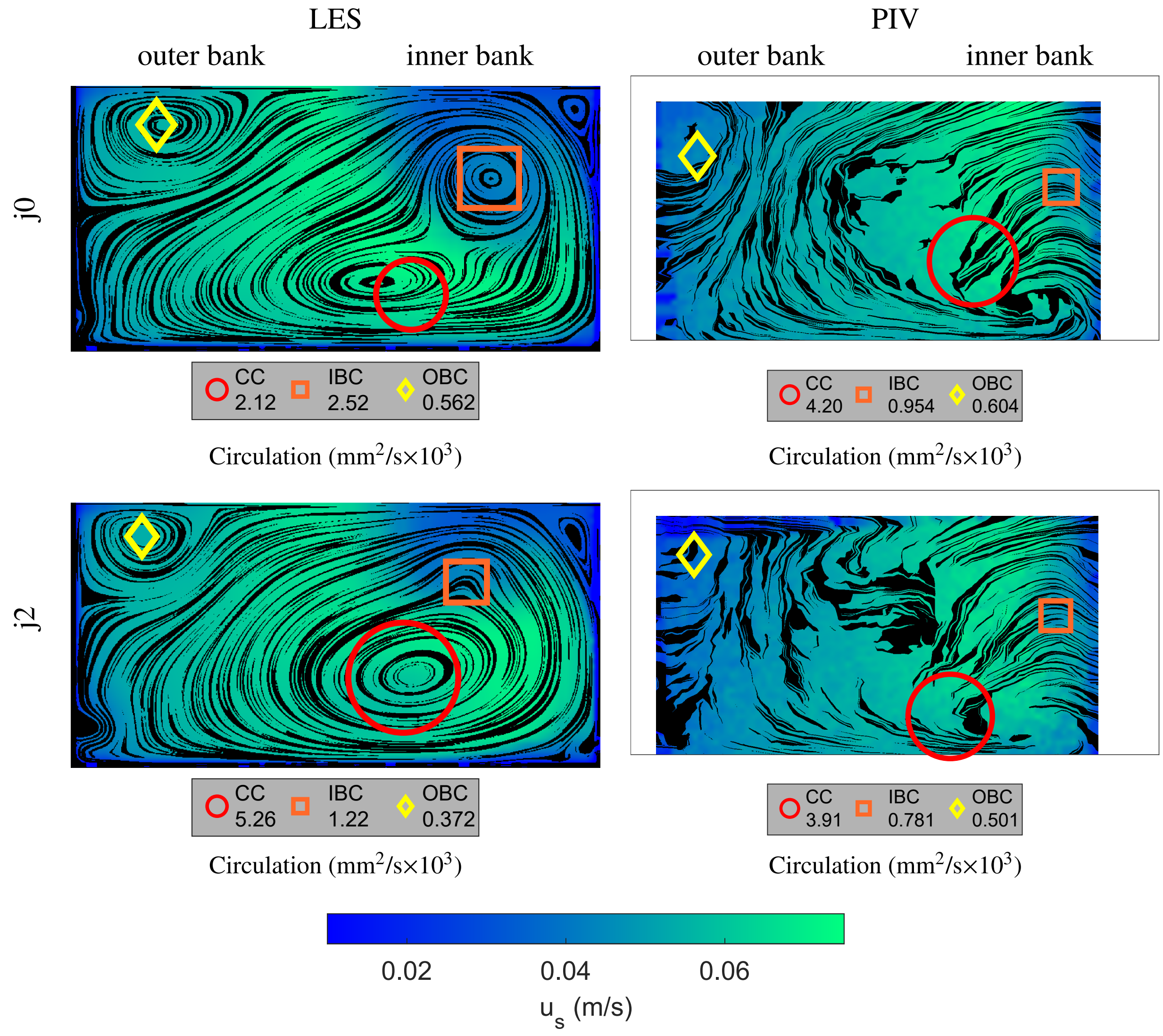

Figure 8.2: Comparison of LES and PIV for h10Q1095 flow conditions

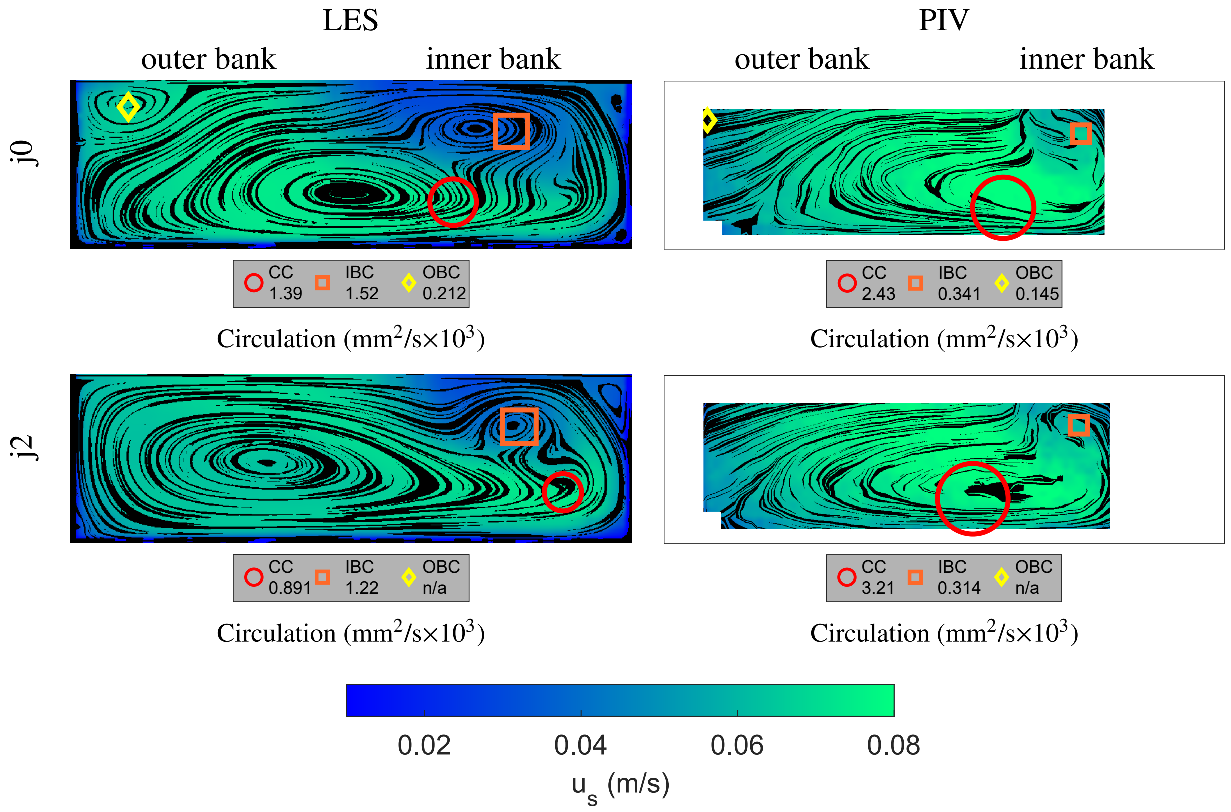

Figure 8.3: Comparison of LES and PIV for h6Q693 flow conditions

condition shows an error in the processing of the CC location in the simulation: the CC circulation is only detected at the inner bank split of the CC beneath the IBC. This is likely because the vortex density is so much greater at that location than in the rest of the CC. The IBC shows a very slight reduction in circulation with the addition of the jet in both LES and PIV, however the IBC area in the PIV measurements is not well captured because of strong reflections off the inner wall of the flume.

In general, the above comparisons between simulation and experiment show two persistent differences: The simulations tend to over-predict the IBC and under-predict the OBC. OBC underprediction is a common problem with many turbulence models, and these simulations were set up with that in mind by choosing the SGS model that produced the largest OBC, as shown in figure 3.4. The overprediction of the IBC was not expected: Ramamurthy et al. (2013) found that rigid lid models could fail to predict flow separation at the inner bank, and given the IBC's connection to flow separation one could also assume that rigid lid models would under-predict the IBC. Given the results above, this effect is not happening in these simulations, likely due to the small Froude numbers modelled (Paik and Sotiropoulos, 2005). Therefore though these simulations do show differences with experiment, the choices made in setting up the simulations likely reduce the differences as much as possible with the available computational resources.

8.2 Parametrisation of jet effect on secondary circulation

In this section, the secondary circulation in the channel bend with the jet is parametrised in exactly the same way as it is in Chapter 7 without the jet. The vortex clustering uses the same parameters to define cells. The same structure of MLP and ANFIS models are used, with and without prior decision tree classification based on the same threshold. The only difference is the inclusion of the cases with the jet, and the input variable m_r in addition to the previous input variables of Fr, B/h, and s. The cases without the jet are included with m_r=0. Out of the total 315 samples (5 cross sections from 63 LES models as shown in 3.2 and including the simulations with no jet), 285 are used for training and validation and 30 as holdout, assigned randomly. The proportions of training and validation data for each model are thus the same as in Chapter 7.

The same sub-cells (CC, IBC, and OBC) are tracked for the cases with the jet as for the cases without. The CVP component vortices are not explicitly tracked because they are not necessarily separable from the bend secondary circulation cells after secondary circulation has developed. In general, the negatively-rotating component of the CVP often connects to a developing bend circulation cell, while the positively-rotating component, being surrounded by oppositely-rotating structures, often dissipates early in the bend or before the area of interest entirely.

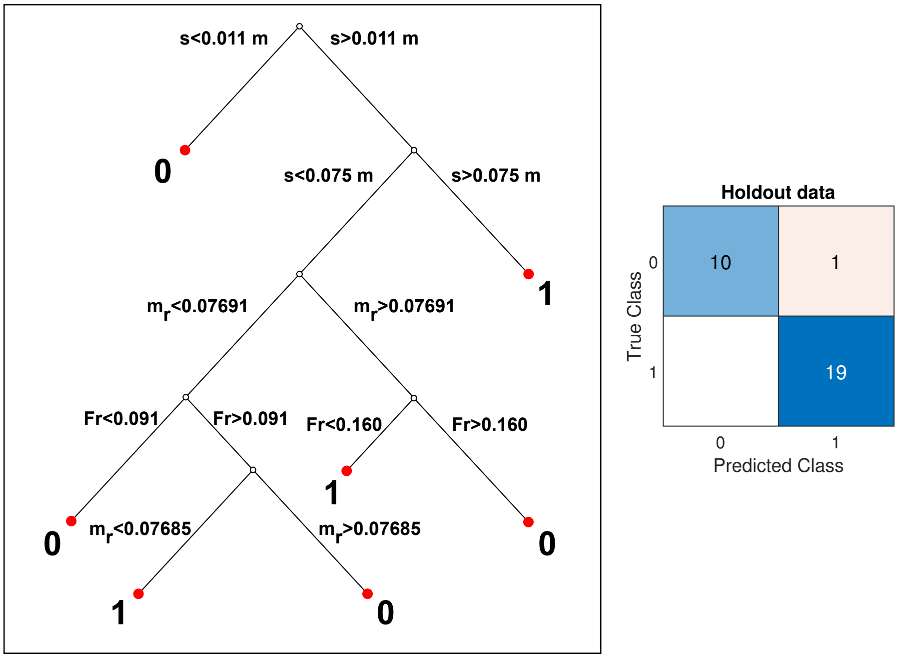

Figure 8.4: Fr-based decision tree for existence of CC with a jet and confusion matrix showing 97% on holdout data

8.2.1 Classification models

The Fr-based classification trees for the CC, IBC, and OBC and their corresponding confusion matrices are shown in figures 8.4, 8.5, and 8.6 respectively. The classification for the OBC is also redone using De instead of Fr, and the De-based classification and resulting confusion matrices are shown in figure 8.7.

The switch from Fr to De based classification in the case without the jet presented in Chapter 7 resulted in marginally better classification though not enough to result in better models, but the margin in the case with the jet is reduced to no more than a rounding error. This difference is likely due to the introduction of a new parameter, m_r, that has a much stronger effect on the presence of the outer bank cell, reducing any relative importance of either Fr or De. Note that the Fr-based OBC classification also relies on the aspect ratio but the De-based classification removes this dependency. This may reflect that in the case of a single bend geometry, the Dean number can be calculated from

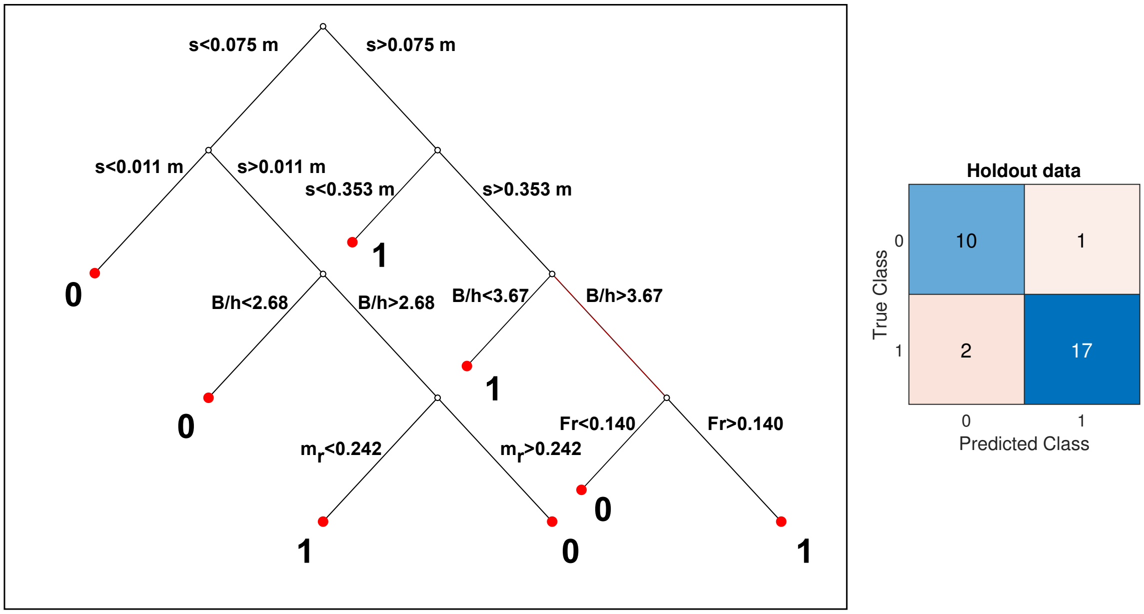

Figure 8.5: Fr-based decision tree for existence of IBC with a jet and confusion matrix showing 90% on holdout data

the Froude number and the aspect ratio: $De = \frac{gB^{2.5}}{\nu\sqrt{R}} \frac{Fr^2}{(B/h)^{2.5}}$; thus De-based classification may be more efficient, even if the results of both methods are similar. Therefore, the outer bank classification is done with the Dean number henceforth in this chapter.

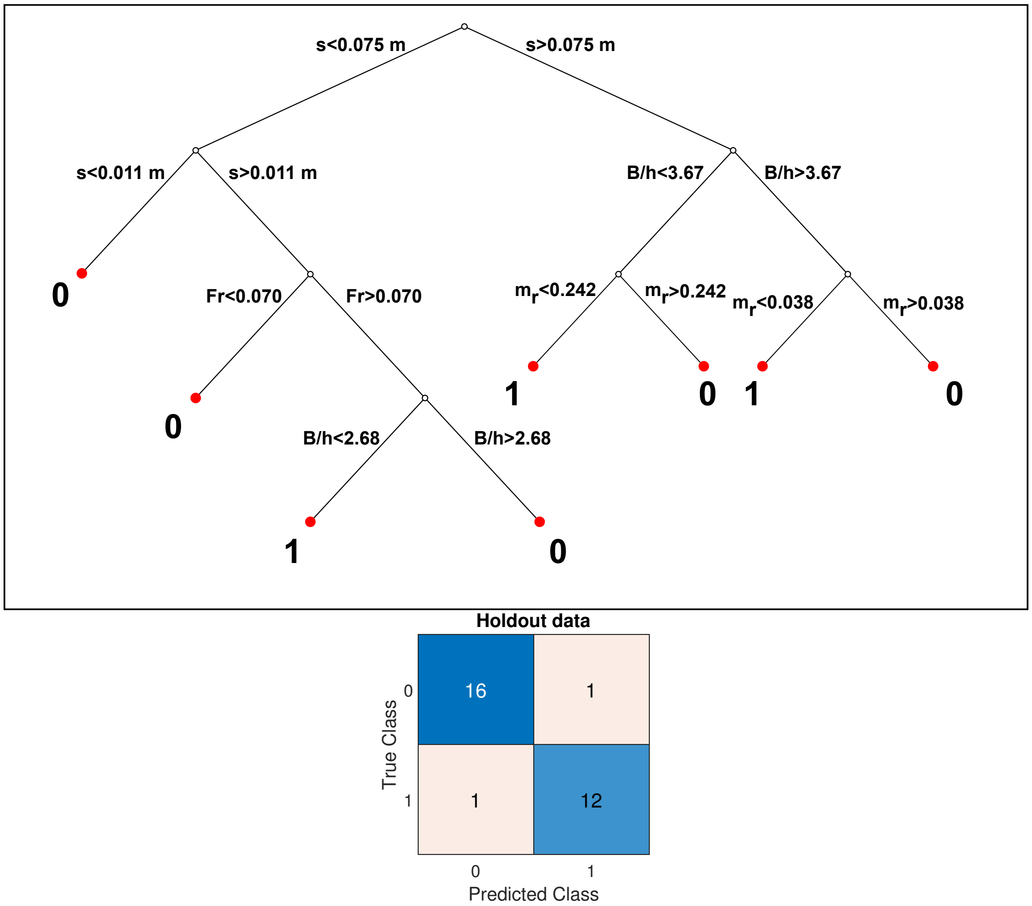

Figure 8.6: Fr-based decision tree for existence of OBC with a jet and confusion matrix showing and 93% on holdout data

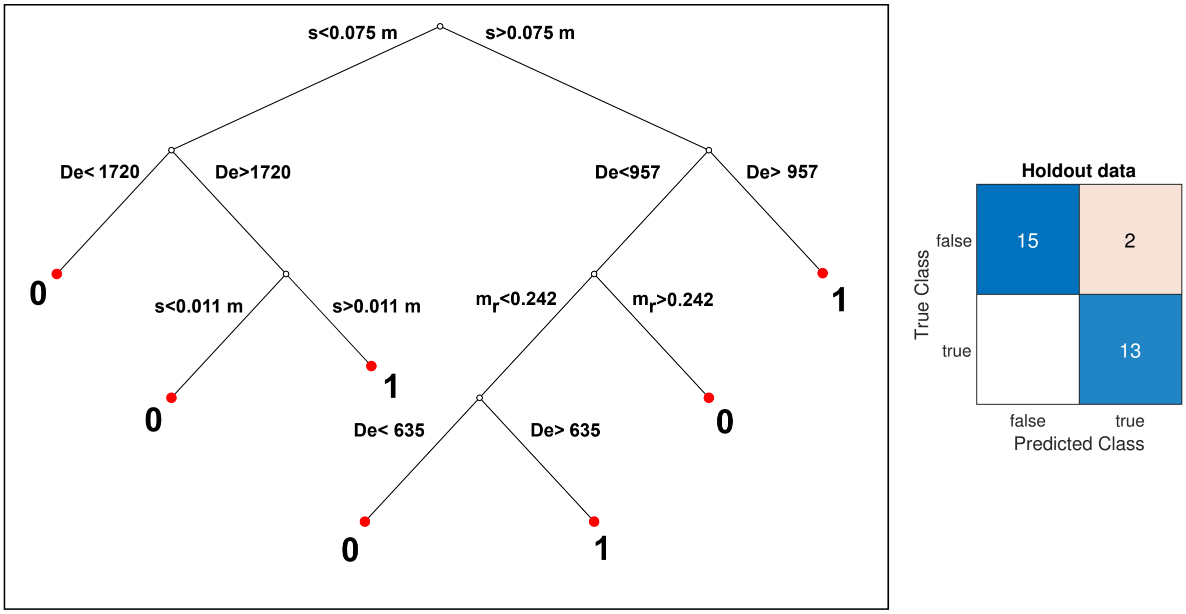

Figure 8.7: *De*-based decision tree for existence of OBC and confusion matrix showing 93% on holdout data

8.2.2 Performance comparison of all models

The performance of the regression models is assessed, as in Chapter 7, using the R^2 and the NRMSE normalised using parameter ranges. The results are presented in table 8.1 for holdout data. The model choice for analysis going forward is also presented in the table. As with the choices in chapter 7, these are not necessarily the best performing models, but are chosen to give insight into models from all categories.

It should be noted that the ANFIS models with classification presented in this section are much more consistently reliable than those in Chapter 7. Since this model has the most complex structure, it makes sense that it is the one that benefits the most from the increased size of the dataset.

Table 8.1: R squared and NRMSE on holdout data for jet models, highlighted models have $R^2 > 0.8$ and NRMSE< 0.125

	No classification			With classification			
	MLR	MLP	ANFIS	MLR	MLP	ANFIS	
Output parameter	R^2 NRMSE	R^2 NRMSE	R^2 NRMSE	R^2 NRMSE	R^2 NRMSE	R^2 NRMSE	Model choice
Total circulation	0.652	**0.920**	**0.976**	—	—	—	MLP
	0.149	**0.072**	**0.042**				
CC circulation	0.683	0.799	**0.864**	0.756	0.709	**0.912**	ANFIS
	0.144	0.113	**0.093**	0.125	0.134	**0.074**	
IBC circulation	0.383	**0.878**	**0.941**	0.653	**0.849**	**0.914**	ANFIS
	0.156	**0.082**	**0.060**	0.117	**0.075**	**0.062**	
OBC circulation	0.470	0.721	**0.918**	0.358	0.533	**0.855**	ANFIS+De-class.
	0.144	0.107	**0.057**	0.160	0.141	**0.076**	
CC n	**0.813**	**0.875**	**0.884**	**0.852**	**0.960**	**0.831**	MLR+Fr-class.
	0.106	**0.087**	**0.084**	**0.103**	**0.054**	**0.104**	
IBC n	0.437	**0.826**	**0.990**	0.191	**0.982**	**0.986**	MLP+Fr-class.
	0.234	**0.123**	**0.030**	0.196	**0.029**	**0.026**	
OBC n	0.765	**0.842**	0.463	0.757	**0.862**	**0.953**	MLP+De-class.
	0.109	**0.077**	0.211	0.087	**0.058**	**0.035**	
CC z	0.478	0.488	0.540	0.547	0.661	**0.857**	ANFIS+Fr-class.
	0.146	0.145	0.150	0.121	0.106	**0.085**	
IBC z	0.816	**0.897**	**0.974**	0.834	**0.945**	**0.992**	MLP+Fr-class.
	0.146	**0.103**	**0.052**	0.151	**0.081**	**0.028**	
OBC z	**0.889**	**0.945**	**0.897**	**0.917**	**0.950**	**0.949**	MLR+De-class.
	0.088	**0.063**	**0.081**	**0.088**	**0.061**	**0.065**	

8.2.3 Importance of flow parameters

Table 8.2 shows a comparison of the R^2 and NRMSE for models including all parameters and with individual parameters omitted. One can see from the table that each individual cell's circulation depends on all the input parameters, contrary to the results without the jet, but that the total circulation is not much affected by the inclusion of m_r or B/h.

As in Chapter 7, the models may now be applied to any flow condition with input parameters within the range of the original simulations. Figure 8.8 shows explicitly the circulation variation of each individual cell and the total circulation as a function of m_r. The other parameters are held constant at $Fr = 0.132$ ($De = 1.35$ for the outer bank cell model), $h/B = 3.5$, and $s = 0.23$ m.

Table 8.2: Analysis of parameter importance by R squared and NRMSE comparison with variable omissions for jet models. Values are not given for models that do not include the given variable

		All	No Fr	No De	No m_r	No B/h	No s
Output parameter	Model	R^2 NRMSE	R^2 NRMSE	R^2 NRMSE	R^2 NRMSE	R^2 NRMSE	R^2 NRMSE
Total circulation	MLP	0.920	0.526	—	0.882	0.950	0.118
		0.072	0.200		0.073	0.057	0.267
CC circulation	ANFIS	0.864	0.071	—	0.003	0.483	0.348
		0.093	1.244		0.702	0.431	0.225
IBC circulation	ANFIS	0.941	0.039	—	0.470	0.525	0.073
		0.060	0.721		0.249	0.244	0.250
OBC circulation	ANFIS+De-class.	0.855	—	0.108	0.326	0.002	0.053
		0.076		3.324	0.244	0.825	0.291
CC n	MLR+Fr-class.	0.852	0.809	—	0.766	0.853	0.134
		0.103	0.115		0.115	0.102	0.248
IBC n	MLP+Fr-class.	0.982	0.956	—	0.517	0.568	0.0008
		0.029	0.065		0.171	0.164	0.352
OBC n	MLP+De-class.	0.862	—	0.775	0.638	0.019	0.0005
		0.058		0.093	0.106	0.192	0.316
CC z	ANFIS+Fr-class.	0.945	0.215	—	0.0004	0.002	0.700
		0.085	0.817		0.568	0.366	0.119
IBC z	MLP+Fr-class.	0.906	0.905	—	0.939	0.585	0.492
		0.081	0.104		0.082	0.143	0.243
OBC z	MLR+De-class.	0.917	—	0.919	0.913	0.011	0.791
		0.088		0.084	0.070	0.390	0.109

When a weak jet is initially added, the CC increases in strength and the IBC decreases in strength, as seen in Chapter 6. However, when the jet strength is increased, these trends reverse, and the IBC increases in strength and the CC circulation magnitude decreases. This could indicate that the CVP is moving past the CC's development zone and into the IBC's. However, since this plot only shows the circulation at a single cross section, it is not completely clear that this represents an increase or decrease in the total strength of the cell. Rather, it could represent shifting of the cells' development earlier or later in the bend, as was also observed in Chapter 6.

There is a discontinuity in the slopes of the CC and IBC curves at momentum ratios just above zero. Mathematically, these discontinuities are likely due to the structure of the ANFIS models: when the parameters transfer from membership in one fuzzy category to another, different model structures apply. Physically, this corresponds to the discontinuous nature of turning on the jet. This demonstrates an advantage of the ANFIS models over the MLPs when accounting for cases with and without a jet in a single model: the classification step in the ANFIS models can account for the presence of the jet and apply different rules when the jet vortices are present.

The ANFIS models in this chapter benefit from the addition of a coupled decision tree, unlike the ANFIS models from Chapter 7. This is likely due to the inclusion of the jet cases, since ANFIS models are known to perform better when trained on larger training datasets (Akan and Keskin, 2019): removing all the data points without a given cell for the classification-coupled ANFIS models in Chapter 7 therefore had a negative effect on the performance of the ANFIS models due to the small size of the dataset, but the effect was mitigated with the inclusion of more data for the models including the jet.

Additionally, the outer bank cell is seen to decrease in strength consistently upon addition and subsequent strengthening of a jet. This is consistent with the observations in Chapter 6. Note that it is predicted that at high m_r values, the circulation of the OBC becomes negative, and the circulation of the CC becomes positive. Both are unphysical results, given the direction that the cells circulate. This is the type of error that should be prevented with a classification model: in the absence of classification, the model's nullspace does not perfectly map to all the cases where the cell does not exist, resulting in some conditions that should be mapped to a circulation of zero instead being mapped to nonzero numbers in error. The addition of a classification model that assigns a circulation of zero where the cell does not exist imposes a nullspace on the overall model. If the classification model works perfectly, then it should eliminate errors of this type. The fact that the error is observed in the CC circulation model, which does not include classification, is therefore not surprising; however, that the same error, however small, is seen in the OBC model indicates that the decision tree has misclassified the existence of the OBC at this point.

To differentiate between the jet's effect on the total amount of circulation in a cell and the location of each cell's circulation, figure 8.9 shows the circulation development throughout the bend

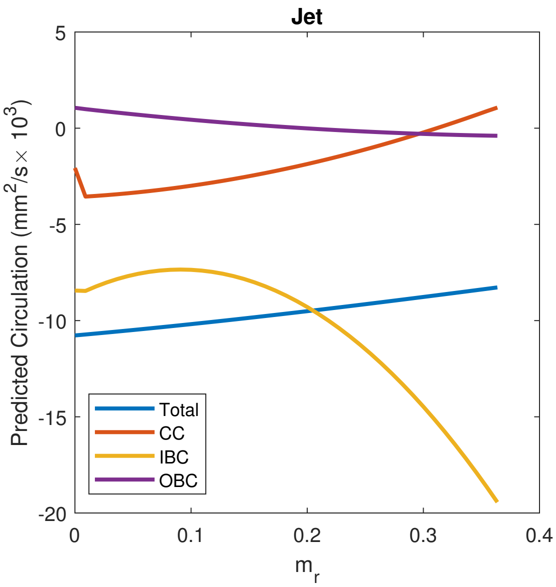

Figure 8.8: Circulation of all cells as a function of m_r with $Fr = 0.132$ ($De = 1.35$ for the outer bank cell model), $h/B = 3.5$, and $s = 0.23$ m using models chosen in table 8.1

for one case without a jet at the same flow condition as in figure 8.8, and the same case again with a jet of $m_r = 0.182$.

The OBC's development is substantially delayed by the jet. In both cases, the OBC is first present after a sudden discontinuity; in the case without a jet, this indicates the position in the bend where the classification tree turns the jet on. Before this position, the jet may be developing but has very weak circulation. In the case with the jet, the OBC is predicted to develop negative circulation; this is a similar error as was already observed in figure 8.8, and indicates that the classification tree and coupled regression model are not in agreement on the development location of the OBC.

The CC shows much quicker development with the jet present, but then declines much more rapidly than is typical of the CC, as shown in Chapter 5. The explanation for the CC's persistence put forward in Chapter 5 is that it is surrounded by walls and negatively rotating vortices which are unable to dissipate or cancel out its vorticity. Therefore, this persistence cannot be expected to be maintained if a strong positive component of the CVP is present in the bend.

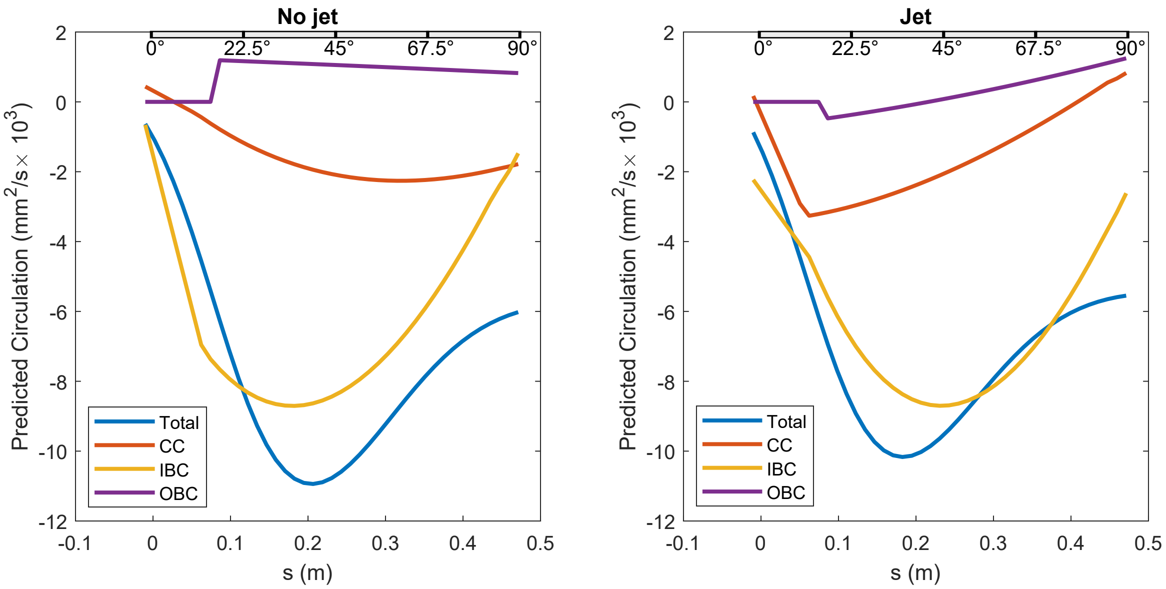

Figure 8.9: Circulation development for all cells with and without a jet with $m_r = 0.182$, at the flow condition $Fr = 0.132$ ($De = 1.35$ for the outer bank cell model) and $h/B = 3.5$ using models chosen in table 8.1

Figure 8.9 shows very little difference in the IBC's peak circulation, but a noticeable shift in its peak location to later in the bend when the jet is added. The lack of decrease in the IBC peak may be another indication that the positively-rotating component of the CVP is within the region of the CC (as stated in the previous paragraph) rather than interfering with the IBC's development region as in Chapter 6. The shift to developing later in the bend is consistent with the findings of Chapter 6. Since the IBC's peak location shifts to approximately 0.22 m with the addition of the jet, and figure 8.8 represents the circulation at the 0.23 m cross section, some of the increase in the IBC's circulation shown in figure 8.8 up to $m_r = 0.182$ can be attributed to the location shift. At this point figure 8.8 is approximately aligned with the IBC's peak, and therefore any subsequent increase in IBC circulation at greater momentum ratios must come from an increase in the total circulation of the IBC.

Figure 8.10 shows the predicted positions of the cells with and without a jet at the same conditions as figures 8.8 and 8.9. The IBC is shifted noticeably toward the inner bank and the CC toward the

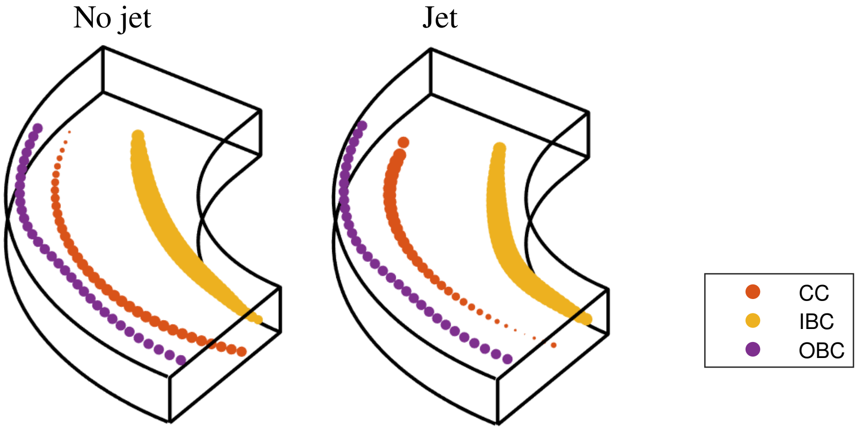

Figure 8.10: Cell location and development with (right) and without (left) a jet with $m_r = 0.182$, with $Fr = 0.132$ ($De = 1.35$ for the OBC), and $h/B = 3.5$ using models chosen in table 8.1, with point size proportional to circulation magnitude. Exact circulation is found in figure 8.9.

outer bank with the addition of the jet. The circulation location changes with the jet, with the CC's circulation shifting earlier and the IBC's later, are also noticeable.

8.3 Small flume dye tests

A series of dye tests in the small bend flume serve to validate the effluent distribution results from LES. The tests used the same 10% solution of food dye as the dye tests in Chapter 4 but took place in the small flume. Figure 8.11 shows a comparison of select simulation results with photos from equivalent dye tests. The flow rates of dye tests show fewer significant digits than the LES flow rates to reflect the measurement precision of the flume flow rate at the time. The effluent concentration is normalized using the maximum concentration, so that fluid entering at the jet boundary has a concentration of 1.

From both the photos and the simulation results, it is clear that the transverse movement of effluent is sped up when the flow rate is decreased and when the depth is increased. The 9 cm flow depth simulations show a distinct movement of effluent away from the outer bank, leaving a zone of relatively low concentration along the outer bank; the dye test photos are less clear, as the outer bank

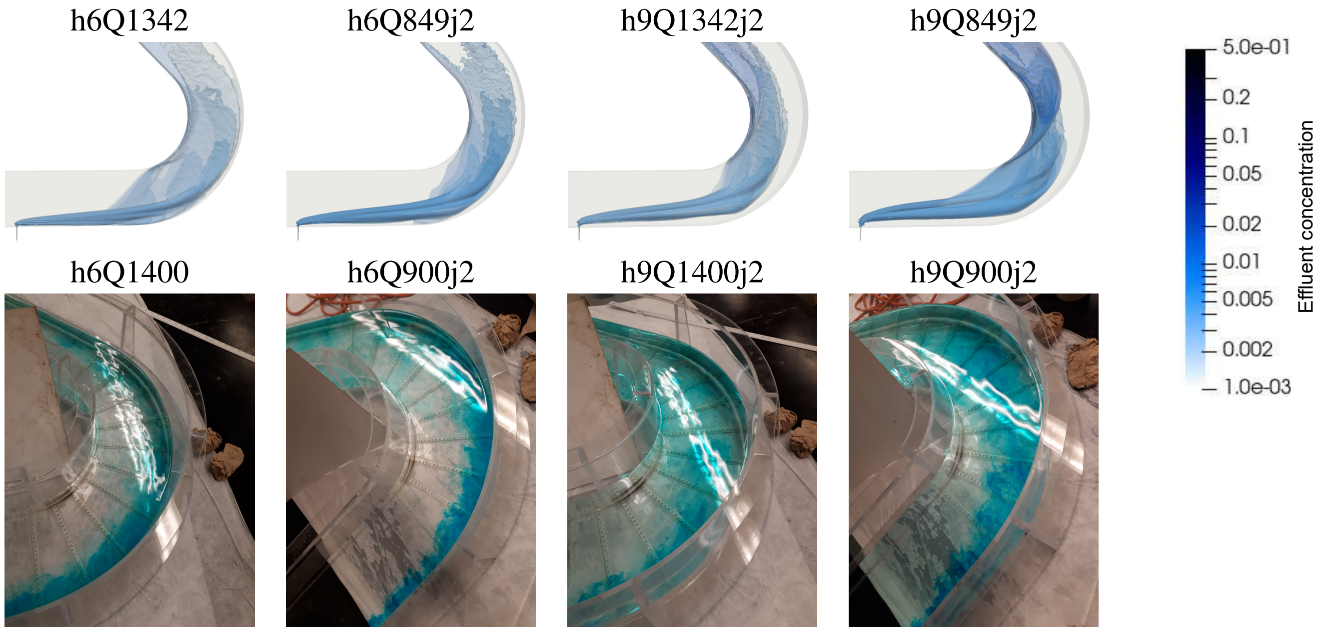

Figure 8.11: Effluent transport in LES (top) and small flume dye tests (bottom)

contains a reflection and a shadow that make the dye appear more concentrated there. In actuality, the outer bank dye concentration is much less than it initially seems in the photo. Looking at the very end of the bend after the reflection and shadow, the dye is visibly much less concentrated at the outer bank in both 9 cm depth conditions.

The difficulty with perspective and lighting for estimating dye concentration is an inherent limitation of this sort of dye test. Additionally, the images from the tests represent instantaneous dye distributions, which is limited in its usefulness considering the dominance of coherent structures in the bend. All these limitations can be addressed with laser-induced fluorescence (LIF) experiments, which should be done in the future to quantitatively assess the effluent distribution in the bend.

8.4 Parametrisation of effluent distribution

The most common framework of river mixing, as laid out in Chapter 1, is to use a constant mixing coefficient for each direction in the river. Thus effluent released at the outer bank would

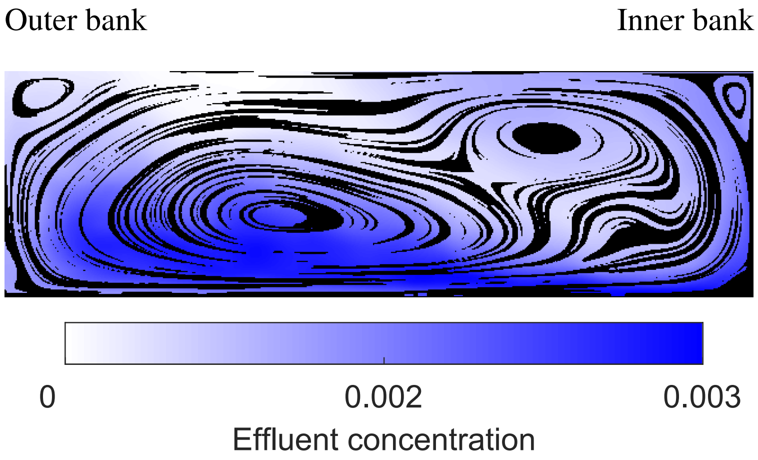

Figure 8.12: Sample effluent distribution at 90 degrees, shown for h6Q1342j2 flow condition

gradually spread toward the inner bank at a rate defined by the transverse mixing coefficient. This model relies on the underlying assumption that the flow in river bends can be approximated using parallel "streamtubes", or subdivisions of the water volume that lie parallel to each other, where individual streamlines of the bend flow lie entirely within one streamtube. The previous section's parametrisation of secondary flow shows that this is not a good approximation of how bend flow streamlines work: sub-cells do not remain parallel, and can split, or cross each other, or form at different times. What then is the resulting effect on effluent mixing in a channel bend?

A sample effluent distribution at the 90° cross section is presented in figure 8.12. This sample clearly shows the inherent relationship between the effluent distribution and the secondary circulation cells. Of particular interest is the curl of high-effluent-concentration fluid reaching around the IBC and up the inner bank wall. As a result, the depth-averaged effluent concentration at the inner bank is higher than under the IBC. This result can also be seen in all the dye test sample photos in figure 8.11.

In this section, therefore, let us leave behind previous methods of predicting mixing and instead consider the problem of directly predicting aspects of the effluent concentration distributions, taken at the 90° cross section. The particular quantities to be predicted are defined in table 8.3. The concentration at full mixing is $C_{\text{full mix}} = Q_{jet}/Q_{cf}$.

Table 8.3: Effluent distribution characteristic parameter definitions

Normalised 90th percentile	90th percentile of concentration distribution, normalised using $C_{\text{full mix}}$
Centroid n	weighted average cross stream coordinate of effluent distribution
Centroid z	weighted average vertical coordinate of effluent distribution
Normalised variance	Variance of effluent concentration distribution, normalised using $C^2_{\text{full mix}}$

Table 8.4: Linear regression models for concentration distribution parameters

	Normalized 90th percentile			Centroid n		
	Coefficient	Confidence interval		Coefficient	Confidence interval	
intercept	-0.078	-0.920	0.764	0.437	0.389	0.485
Fr	2.832	-0.443	6.106	-0.303	-0.490	-0.117
m_r	0.672	-0.115	1.458	-0.123	-0.167	-0.078
h/B	5.383	4.243	6.522	-0.300	-0.365	-0.235
	Centroid z			**Normalized variance**		
	Coefficient	Confidence interval		Coefficient	Confidence interval	
intercept	-0.029	-0.047	-0.010	-2.279	-3.373	-1.185
Fr	0.083	0.011	0.155	4.882	0.627	9.138
m_r	0.048	0.031	0.065	2.235	1.213	3.257
h/B	0.115	0.090	0.140	6.110	4.630	7.591

Figure 8.13 shows the results of a multiple linear regression model for each of the defined parameters, with the fitted model coefficients presented in table 8.4.

From the confidence intervals of the model for normalised 90th percentile, it is clear that the effects of Fr and m_r are not significant; therefore a minimal model for the normalised 90th percentile is also presented in figure 8.14 and table 8.5.

Given that the secondary circulation that drives the effluent mixing is known to be a highly nonlinear process, the resulting effluent distribution should also be expected to be nonlinear.

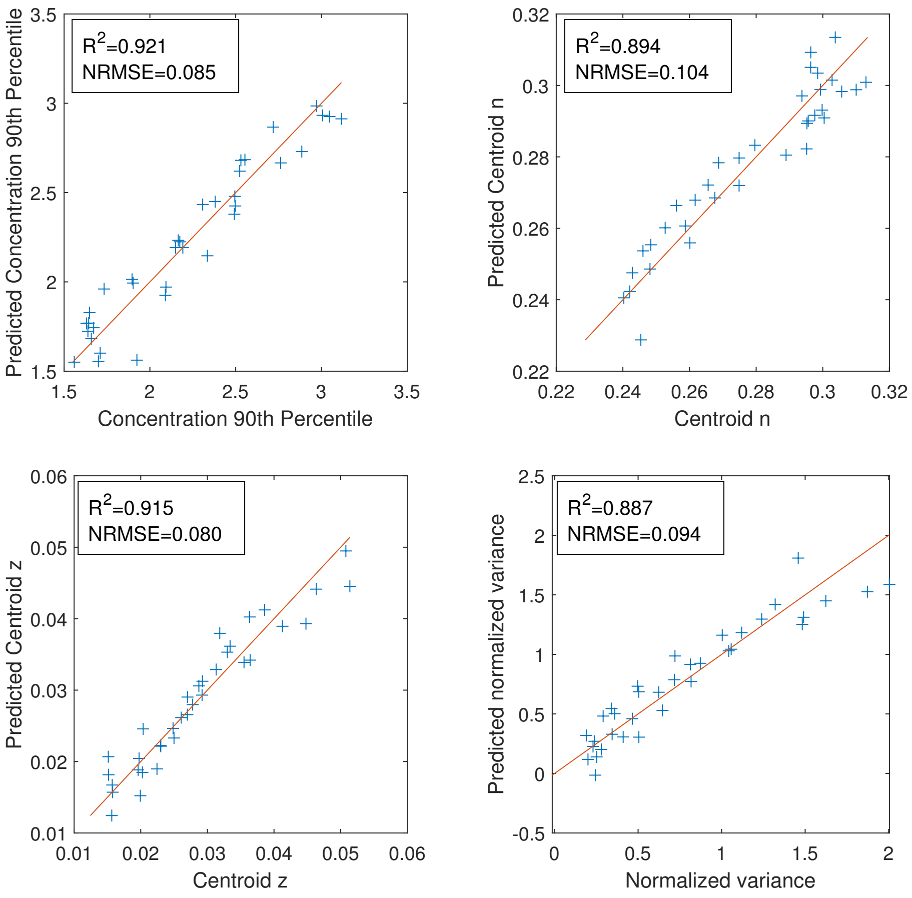

Figure 8.13: Linear regression model results compared to LES concentration distribution parameters

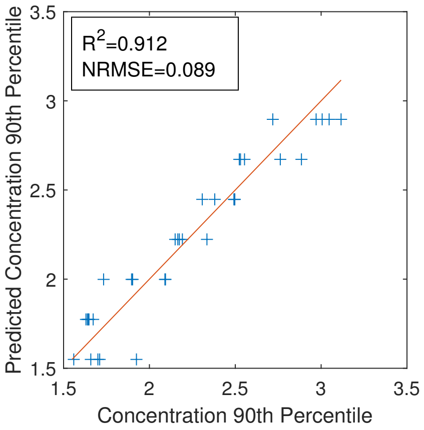

Figure 8.14: Linear regression model results for 90th concentration percentile using only aspect ratio, compared to LES effluent distribution

Table 8.5: Linear regression model for 90th percentile using only aspect ratio

	Normalized 90th percentile		
	Coefficient	Confidence interval	
intercept	0.652	0.473	0.831
h/B	4.488	3.996	4.980

Therefore the MLR models presented above are unlikely to be the best possible models to predict effluent distribution. However, given their agreement with the data as presented, and the amount of data currently available, adding more complexity to the model would risk the possibility of over-fitting, and therefore no further models are attempted here. The linearity of the effluent distributions is not expected to hold for all possible Froude numbers, aspect ratios, and momentum ratios, as it is not expected to be representative of the fundamental processes at play (which, again, are highly nonlinear). However, it is useful to acknowledge that a MLR model has some success in predicting the effluent concentration distribution over the wide range of Fr, h/B, and m_r studied here: Firstly, to counter the assumption that any model of effluent mixing that accounts for the 3D nature of the flow field must be vastly complex; and secondly, as a first approximation to narrow down the range of parameters and the physical area of interest for future studies.

8.5 Conclusion

The interactions of the jet and bend flow presented in this chapter are very complex, but the combination of cluster-based sub-cell definitions and machine learning presents a relatively simple conceptual model: the strengths of the CC and IBC change with the addition of the jet, with the direction and magnitude of the change depending on the placement of the CVP components. The OBC is consistently disrupted by the presence of the jet. The total circulation is not highly dependent on the strength of the jet. These effects are especially visible in the machine learning parametrisation, even for flow conditions that have not been explicitly simulated. The machine learning models show that the cross-stream position of the CC continues to be linear even with the addition of the jet, though the positions of all the cells have different dependencies on flow parameters when the jet is included.

The ANFIS model with classification is the most consistent model for predicting all the flow parameters; this is in contrast to the models without the jet from Chapter 7 where the ANFIS model performed best but was hindered by the addition of a classification tree. This is likely due at least in part to the larger dataset. Both ANFIS models benefit from the fuzzy classification layer's categorization of input parameters in order to apply different rules to cases with and without the jet, therefore outperforming the MLPs.

The resulting effluent distribution is highly 3D, with a tendril of high-effluent-concentration fluid reaching around the IBC, which has comparatively low effluent concentration. Despite all this complexity, basic properties of the effluent distribution can be predicted using linear regression. This is most likely connected to the linear behaviour of the cross-stream position of the CC, which was established in Chapter 4 as the key variable in predicting the jet trajectory.

The LES simulations showed some consistent differences with PIV measurements. In particular, the simulations overestimated the IBC and underestimated the size of the OBC. Both these types of errors justify the choices made during the simulation setup, which were made to maximize the simulated OBC and carried the potential to fail to produce the IBC. In addition, the sub-cell definitions provide a useful way to frame the discrepancies between simulation and experiment. Provided with enough experimental data, it might even be possible to train machine learning models such as the ones in this chapter to account for the discrepancies themselves.

Chapter 9

Note on clustering instantaneous vortices

The instantaneous vortex clustering method used herein was developed as part of the thesis for the analysis of sub-cells of secondary circulation. The method has been developed and adjusted throughout its use in this thesis, and therefore has slight differences in each implementation. Though each implementation has a thorough description in the chapter where it is used, a comprehensive comparison is provided here for the sake of discussing the differences and further possibilities for future use. The basic implementation is shown in figure 9.1. The variations between each implementation of the method have to do with the thresholds in the second step and scaling coordinates in the DBSCAN step.

The chapters in this thesis contain four separate implementations of instantaneous vortex clustering: two within Chapter 5, applying the method to secondary circulation driven by rough strips and then to bend secondary circulation with a depth of 6 cm; one in Chapter 6, applied again to bend flow with a 6 cm depth; and one in Chapter 7, applied to flow depths from 4 to 10 cm.

The first example of vortex clustering, that of secondary circulation over rough strips presented in Chapter 5, was used for demonstration because it is the simplest application of the clustering method. There is no threshold applied to the vortices, and all three sample cross sections have the same dimensions and are symmetric, with the result that positively- and negatively-rotating

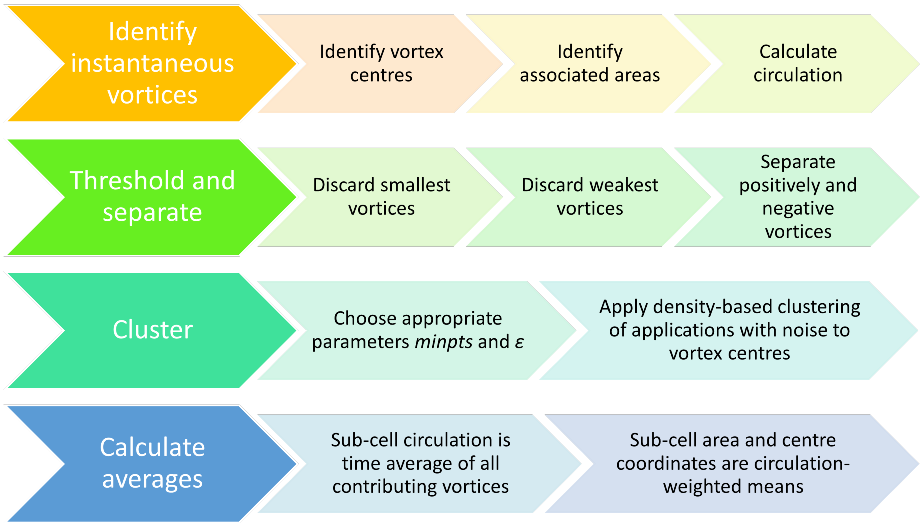

Figure 9.1: Basic method for vortex clustering algorithm

vortices are generated in approximately equal numbers. Each clustering application in this example considers only the positively- or negatively- rotating vortices, and sets the parameter M_{pt} equal to 1/15th of the vortices it considers, while ε is kept to a constant 0.1 (in normalised coordinates). The only complication to this example is the need for logarithmic scaling in the vertical direction to account for the increased vortex density closer to the rough strips.

In applying the method to secondary circulation in the channel bend, a few modifications are required. First, the unequal aspect ratio of the channel cross section makes it important to scale the coordinates even if logarithmic scaling is not required; therefore the vortex centres are normalised using their ranges before clustering. Second, the lack of symmetry in the directions of the generated vortices means that, if the method were applied in the same way as in the demonstration, it would be more capable of distinguishing between clusters of negatively rotating vortices, since they are much denser than the positively rotating vortices. Thus M_{pt} is set as a fraction of the total vortices in the cross section, not just the vortices of a single sign. Lastly, because of the complexity of the vortex distribution it is useful to apply a threshold to make the distinction between adjacent sub-cells sharper. Thus the smallest 5% and the weakest 5% of the vortices, which are generally towards the edges of the circulation sub-cells, are discarded.

The clustering method is applied as described in the previous paragraph in Chapters 5 and 6, with only slight differences in the exact values of ε and M_{pt}. However, in Chapter 7 it is necessary to adapt again in order to directly compare results from cross sections of different sizes. To this end, ε is not held constant but is scaled in proportion to $1/\sqrt{N}$ where N is the number of vortices in the cross section. Since ε is the radius of the area of interest around each point to be clustered, this scaling for ε ensures that the area is always proportionate to the vortex density, when working in scaled coordinates. Defining both cluster parameters as a function of vortex density is a convenient way to account for changes in both numbers of vortices and size of cross sections at the same time. Additionally, since this chapter processes a wider variety of cross sections, with a wide range of detected vortices, it is necessary to put a limit on the value of M_{pt}; therefore it is set to $M_{pt} = \min(25, N/20)$. The limit is in place to ensure that common clusters such as the CC and IBC do not get missed if the overall vortex density increases substantially due to vortices from other sources.

Adjusting the parameters of the clustering algorithm will affect the final calculated circulation and location of the clusters by including or excluding vortices in the clusters. Increasing the radius ε or decreasing M_{pt} will loosen the criteria for inclusion in a cluster, resulting in larger clusters and therefore including circulation contributions of more vortices. Two implementations of the clustering method, provided they find the same clusters, will calculate different circulations for each cluster but each cluster's circulation will change in the same direction. Thus it is possible to compare circulation using any clustering parameters, provided the clustering parameters and methods are consistent.

This is a bit more complicated when different implementations of the clustering algorithms detect different clusters. In some cases, loosening the criteria for cluster inclusion (i.e. increasing ε or decreasing M_{pt}) allows the inclusion of points that act as a bridge between two clusters, joining the clusters into one large cluster. In extreme cases, all points are identified as a single cluster. Obviously, this result prevents the clustering method from being of any use, since its power comes from its ability to distinguish between sub-cells. In cases when many different datasets are clustered and compared, each one may have slightly different ideal parameters, and it becomes impossible to cluster each dataset ideally without losing the comparability between the resulting clusters. In these cases, it is best to allow the clustering algorithm to detect many clusters, and then decide afterwards to join clusters together manually, rather than letting the algorithm oversimplify the clusters.

The choice of clustering parameters does allow some subjectivity in the clustering analysis. In future implementations, it may be possible to limit subjectivity by choosing the parameters according to a set method such as the OBLAOA-DBSCAN optimization algorithm proposed by Yang et al. (2022). However, if the parameters change for every set of vortices being clustered, the assumption that subsequent cluster results can be directly compared would weaken. Any implementation of parameter optimization should therefore also implement some sort of circulation normalization to be able to compare results across different clustering parameters. It is currently unclear how such normalization could occur, but if implemented it could have wider applications (e.g. comparing clustering results between different data sources, and therefore allowing comparison between simulation and experiment).

Another potential future improvement to the clustering method could be to include time data with each vortex point, allowing the coherent structures represented by the clusters to be tracked through time. It could also be possible to define the edge of the clusters either by drawing a polygon around the vortex centre points included in the cluster (thus delineating the region where the vortices are *centred*) or by including the specific area covered by a vortex as part of the data associated with each instantaneous vortex before clustering, which would allow ultimate edge of the vortex clusters to be defined. Defining the edge of each cluster's area of influence would be particularly useful, as relationships between circulation within those areas and mean flow velocity could potentially be used to reconstruct mean velocity fields from cluster-based circulation data.

Chapter 10

Conclusions and future work

10.1 Summary

This thesis establishes that the trajectory of a jet in a channel bend differs from the expected trajectory in a straight channel, and that the difference can be accounted for using the position of the secondary circulation cell. This result emphasises the importance of modelling the secondary circulation directly, rather than relying on uniform increases to mixing within bends. A method to build such a model has been presented, using clusters of instantaneous vortices to quantify and separate sub-cells, and regression and machine learning techniques to break down the effect of flow parameters on the sub-cells' circulation and position. The clustering method allows for greater resolution of circulation for developing sub-cells, which reveals connections between the sub-cell structure, the sharpness of the bend, and the generation and retention of vorticity. The machine learning models give insight into the relationship between the flow conditions and the resulting sub-cell distribution. With the addition of the jet, the sub-cell distribution changes: the outer bank cell's formation is disrupted, and the distribution of circulation between the centre cell and the inner bank cell changes (though *how* it changes depends on the strength of the jet). The resulting effluent concentration distribution in the bend has also been investigated, and shown to depend linearly on the flow condition parameters.

One interesting result within this thesis is the apparent linearity of several parameters. In particular, the position of the centre cell and the distribution of effluent concentration at individual cross sections are able to be predicted with linear regression models with surprisingly good results. Since secondary circulation in bends has previously been well-established as a nonlinear problem, this is highly unexpected. The observed linearity is not expected to be indicative of any fundamental law governing the processes, nor is it expected to extend beyond the ranges of parameters studied herein. However, linear models for secondary circulation position and effluent distribution may be useful to determine areas of interest for detailed measurements (which would be an especially valuable tool for field studies), or to interpolate between flow conditions that are modelled in detail.

10.2 Future work

Though this thesis has set out an approach to modelling jet flow in river bends, the problem is much too complex to be addressed in a single document, and as such there remains much to study about jet-bend interactions.

The work of this thesis focused on a simplified problem, limiting the channel bend geometry to a single angle and radius of curvature with a rectangular bed. Now that a method for secondary circulation decomposition into sub-cells has been established, similar investigations into more bend geometries are possible. In particular, investigating larger scale bends with aspect ratios closer to those of natural rivers will be necessary before the results in this thesis can be applied to real-world examples. Additionally, applying the clustering method to bends with bathymetry could greatly advance models of secondary flow development: developing sub-cells can be detected more easily using clusters than using mean streamlines, which would allow for more precise determination of the regions where circulation cells develop and the mechanisms that cause cell splitting. By developing the clustering method to include time and cell area information, it could then become possible to reconstruct velocity components by location, as well as velocity time series data.

Variations of the jet were also not considered in this thesis. Actual outfalls in rivers are widely varied in placement, in effluent density, and in diffuser design and angle, as well as in effluent buoyancy. A more complete study on these jet parameters would allow the kinds of models developed herein to be applied to real-world scenarios.

In the immediate future, a more detailed experimental study of the same geometry should be undertaken, using LIF to directly measure the concentration distribution of the effluent, and using Tomographic PIV to investigate the turbulent interactions of the jet and bend flows in small volumes of interest (for instance, the disruption of the OBC under the influence of the jet, or the interaction between the CC and IBC). Both are possible in the near future with equipment in the University of Ottawa's PIV room.

Appendix A

Water quality for PIV

A.1 Water Quality

In order to get pictures of sufficient quality to use for PIV, the water in the flume must be very clear and free from large particles. Large particles can interfere with PIV data processing by biasing the statistics toward the velocity of that particle over others in the interrogation window. Additionally, particles other than those designed to be used for PIV may be influenced by buoyant forces. Since the water quality restrictions for PIV are stricter than what is necessary for safe drinking water (and therefore what is supplied through city taps), it is important to take measures to monitor and control the water quality in the lab.

The tracer particles in the PIV experiments are glass spheres from LaVision that are approximately uniformly sized at around 10 microns in diameter. Regular cartridge filters usually remove particles larger than 20 microns. Smaller particles may be removed with more advanced filtration techniques; however this involves a trade off between the desired water quality and the pressure and time required to filter enough water for the small flume system. Therefore a cartridge filter is used to remove the largest particles from the tap water while filling the flume, and water quality checks (visual and with the laser at low power) are done before taking measurements.

The water tanks in the small flume's self-contained recirculating system are built out of aluminum. Though solid aluminum after exposure to air is covered in an oxide layer that prevents reaction with water, this layer can be damaged, leaving the water in direct contact with the aluminum and resulting in the following reaction:

$$2\,\mathrm{Al} + 6\,\mathrm{H_2O} \longrightarrow 2\,\mathrm{Al(OH)_3} + 3\,\mathrm{H_2} \tag{A.1}$$

This reaction results in pitting in the aluminum walls of the tanks, which further exposes the aluminum to water. The solid aluminum hydroxide particles produced in the water extend visibly from their source at the wall, but dislodge easily into the water. To prevent large clumps of aluminum hydroxide from interfering with PIV measurements, it is therefore necessary to prevent the reaction at its source by protecting the aluminum tank walls. As a temporary measure, the walls of the tanks have been covered with adhesive vinyl; this is not a long term solution, and future lab work should use a more permanent coating on the aluminum tanks.

To ensure that no large dust particles from the lab enter the field of view, and to mitigate surface waves, a filter is stretched across the inlet of the flume, as shown in figure A.1.

Figure A.1: Inlet tank for small flume with filter across inlet

A.2 Removing Bubbles

Along with solid particles in the water, bubbles in the flume water will also be visible to the PIV system. There are several mechanisms by which air may be entrained in the circulating water, which must all be controlled in order to minimize the appearance of bubbles.

Air entrainment occurs in the outlet tank immediately after the overflow from the flume gate and again after the v-notch weir. The free-fall of water over an edge plays an important role in setting (for the flume end overflow) or measuring (for the v-notch weir) a consistent flow condition in the flume. Therefore, some turbulence and air entrainment is inherently necessary at both locations where the falling water meets the still water of the tank. However, the excess turbulence can be mitigated by having the water flow through a filter bag filled with plastic pellets as shown in figure A.2. When correctly positioned, the plastic pellets slow the water down and prevent most of the air entrainment. The filter bag itself, as well as holding the pellets, collects and contains any large bubbles of air that may still form.

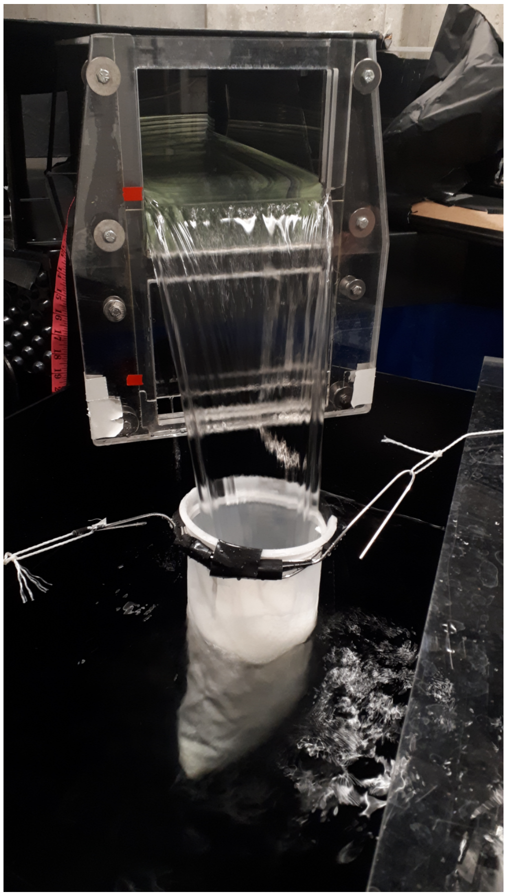

Figure A.2: Filter bag with plastic pellets catching overflow from flume outlet

Even if no additional air is entrained into the water, there may be some dissolved air in the water when it comes in from the taps. The water coming from the taps is 5-10°C in winter (City of Ottawa, n.d.), and therefore has higher air solubility than it will once it has warmed up to the ambient lab room temperature. Assuming the water is initially 10°C and the ambient lab temperature is 20°C, the air solubility will be 0.00105 mol/kg initially, and 0.00083 mol/kg after reaching thermal equilibrium (Zheng and Mao, 2019). A quick calculation yields:

$$\begin{aligned}\begin{array}{r}\text{excess air}\\ \text{concentration}\end{array} &= \frac{(0.00105-0.00083)\,\frac{\text{mol air}}{\text{kg water}} \times 1\,\frac{\text{kg water}}{\text{L air}} \times 29.0\,\frac{\text{g air}}{\text{mol air}}}{1.3\,\frac{\text{g air}}{\text{L air}}} \\ &= 0.0049\,\frac{\text{L air}}{\text{L water}}\end{aligned} \tag{A.2}$$

If the excess air takes the form of bubbles evenly distributed throughout the water, then every litre of water will contain 4.9 mL of air bubbles. At the deepest experimental water depth of 10 cm, there is 100 mL of water within a 5 mm wide cross sectional volume centred over the laser sheet, and therefore also up to 0.49 mL of air bubbles within 2.5 mm of the laser sheet centre. This translates to approximately 7 bubbles if they are 2.5 mm in radius, and many more if they are smaller; either way, this is a problem for PIV measurements.

The assumption that the excess air would take the form of uniformly distributed bubbles is an oversimplification; largely, the air would evaporate out of the water harmlessly or form bubbles attached to the tank walls and other submerged surfaces. The bubbles attached to surfaces are not harmless, as they can dislodge during the experiment and come into the field of view. It is therefore necessary to mitigate bubble formation and encourage the remaining bubbles to dislodge and surface before the beginning of the experiment.

The water coming from the taps is not necessarily saturated with air; however, if the flume is immediately run with the cold water and allowed to overflow and mix, it may become saturated. In order to minimize the air dissolved in the cold water and maximize the release of bubbles after the water warms up, the following best practices have been adopted: Firstly, to allow the water to sit for a day between filling the tanks and running the flume; and secondly, to gently brush all surfaces of the inlet and outlet tank to remove bubbles before running the flume.

Even if both tanks are completely clean of bubbles before the flume flow is started, bubbles may cover surfaces such as the flume walls and the pump, hose, valve, and inlet filter after the flume is first filled. The flume walls, pump, inlet filter, valve, and hose exterior may be gently brushed to remove bubbles after the flume flow is set up. Bubbles can be dislodged from the interior of the hose and valve by shaking the hose. The flume should be allowed to run for at least half an hour to ensure that no further bubbles appear before turning on the laser and acquisition system. A visual inspection of the water running through the flume (best performed against a dark background), as well monitoring the inlet filter for bubble accumulation, will give a ballpark idea of whether there are bubbles present. However, it should be noted that since the laser and cameras can detect much smaller bubbles than the eye can see, a clear visual inspection is not a guarantee that the water is clear enough for a PIV experiment. A water quality check with the laser at low power should always be performed before the full system is put to use.

All the above listed strategies for bubble reduction work by reducing the overall air contained in the water. There is another important factor to managing bubbles, which is to ensure that the bubbles that do form are as large as possible. Larger bubbles float to the surface faster and are easier to trap using filters. Bubbles forming on a surface will coalesce with nearby bubbles if they are within a critical distance, which increases as a function of the contact angle of the surface (Yuan et al., 2021). By choosing materials with high contact angle for areas where bubbles form, we can encourage bubble coalescence, resulting in large bubbles which are easily brushed off the surface and which float to the water surface quickly. The plastic pellets in the filter bags are polypropylene, which has a contact angle around 104°, and the tank surfaces are covered in vinyl, which has a contact angle around 90° (Mittal, 2003). In general, a contact angle of 90° is taken to be the dividing line between hydrophobic and hydrophilic surfaces, with high and low contact angles respectively. Thus the polypropylene pellets are in a suitable contact angle range to encourage bubble coalescence, but the vinyl covering on the tank walls is at the low end of the desirable contact angle range. Since the vinyl coating was intended to be a stopgap measure before a more permanent coating is installed, this effect should be taken into account when choosing a new coating for the tank walls.

Appendix B

PIV SOPs

Manufacturer:	Litron Lasers	**Model:**	NANO L100-50	**Serial Number:**	LM1975
Type:	Nd:YAG	**Max. Power:**	200 mJ	**Class**	IV
Laser Location:	STEM 0014				
Emergency Contact	Majid Mohammadian (613) 562-5800 ext.6492	**Last Update:**	March 2023		

This Standard Operating Procedure (SOP) was developed as a standard for safe practices while utilizing the laser system. This SOP shall address specific safety considerations during normal operations, emergencies, beam alignment (servicing) and any non-beam hazards that might exist. This SOP does not take the place of specific laser safety training associated with this laser system, nor the Laser Safety Training offered by the Office of Risk Management.

Periodic reviews of these procedures shall be made with the effective date noted in the header. Ask staff if they recommend changes as part of the review process.

Laser System Characteristics

Wavelength:	532 nm	**Beam Diameter:**	6.795 e^{-2}
Pulse width:	5 ns	**Rep. Rate:**	100
Required Goggle OD:	532 nm 7+		
Storage Location:	Shelf below computer in PIV room		

Operation of this system is restricted to authorized and trained users as indicated on the reverse side of the University of Ottawa Laser Emitting Device Permit. Digital copies of this permit are located with Majid Mohammadian and Mark Lapointe, and a physical copy is located in the back of the laser system user manual under the PIV monitor.

Start-Up Procedure

Setup

☐ Clean flume walls
☐ Fill tanks
☐ Add tracking particles if needed
☐ Check beam blocks:
  - All around flume, including over flume exit
  - Behind laser arm
  - On bottom of flume/above flume (depending on laser direction)
  - Anywhere with likely reflections

Notifications

PIV room

☐ Ensure everyone in PIV room has laser goggles on
☐ Turn laser sign on
☐ Lock PIV room door

Water resources lab outside PIV room

☐ Inform everyone working in lab that laser will be turned on, ensure they have laser goggles on. **No one may work on elevated platforms without laser goggles** during laser experiments
☐ Notify people to let you know before passing the curtains
☐ Draw all laser curtains including those between the water resources lab and structures lab; put notification sign on curtains
☐ Turn laser sign on
☐ Lock lab doors (including the door between the water resources lab and structures lab)
☐ Lock garage door using switch next to door.

Manufacturer:	Litron Lasers	**Model:**	NANO L100-50	**Serial Number:**	LM1975
Type:	Nd:YAG	**Max. Power:**	200 mJ	**Class**	IV
Laser Location:	STEM 0014				
Emergency Contact	Majid Mohammadian (613) 562-5800 ext.6492	**Last Update:**	March 2023		

Experiment setup

- ☐ Set flume to desired flow rate and water depth
- ☐ Turn on cameras, computer, and acquisition device
- ☐ Turn laser on:
    - Power button
    - Turn key
    - System on
    - Pump on
        - Check coolant level
    - Laser on
    - Warm up laser:
        - set both pulses to low power (15 to 25%) in DaVis
        - Press “light source on”
        - Wait 1 or 2 minutes
        - Press “light source off”
    - Shutter open
- ☐ Turn down laser power **for both pulses** using DaVis controls. Take one image with both pulses about 20% power to ensure all reflections are covered, especially reflections from water surface. If reflections are visible, rearrange beam blocks. Once no reflections are visible, turn laser power up to minimum required
- ☐ Laser should be off if it is not in use (see PIV best practices document)

Shutdown Procedure

- ☐ Turn laser off:
    - Close shutter
    - Laser off
    - System off
    - Turn key
    - Power button
- ☐ Turn off cameras and put on the lens caps
- ☐ Empty flume
- ☐ Turn off flume pump, and close valve completely
- ☐ Unplug laser if laser will be disabled for a long time

Location of Important Documents

Laser Manual:	Shelf below PIV monitor	**Safety Data Sheets:**	In laser manual
Accident Forms:	Online at: orm.uottawa.ca	**Training Documentation:**	With laser safety office

Laser Emergency Shut Down Procedure

All efforts should be made to set up a single step safe shutdown of the system so that laser operators can rapidly exit the area while ensuring that the laser hazard is minimized or non-existent.

- Close shutter
- Laser off

- System off
- Turn key
- Power button
- Unplug laser

Emergency Procedures

Evacuation map location:	In hall outside lab door
Safety shower location:	Inside lab door at end of large bend flume
Eyewash station location:	Left side of lab sink
Fire extinguisher location:	Inside both lab doors

Laser Goggle Calculation

For t_{min} hazard rule:

MPE:	95 nJ/cm^2	**Exposure Time:**	0.25 s

$$OD = \log\left(\frac{E_0}{MPE}\right) = \log\left(\frac{100\,\frac{\text{mJ}}{\text{pulse}}}{\frac{\pi}{4} * (0.6795\text{ cm})^2} \bigg/ 95\text{ nJ/cm}^2\right) = 6.46$$

Laser Training Protocol

1. Ensure trainee has completed a new user registration form and perform in-lab training;
2. Have the trainee document, in short form and in their own words, their training in the specific fields on the form;
3. Verify that the new user has attended or will attend the 3 hour Principles of Laser Safety course provided by the Office of Risk Management (ORM) at the University of Ottawa. This requirement can be fulfilled by reviewing the permit for this system, seeing a copy of the trainee’s certificate provided by ORM upon successful completion of the course, or in writing by the Laser Compliance Specialist that the training was completed;
4. Sign and have the form sent to ORM;
5. Provide these SOPs to the user and indicate all areas where they can be accessed, including written and electronic formats;
6. Communicate who is currently authorized to use the system, the lab designate and/or the principal investigator on the permit, and who to contact in case of an emergency including where the contact information can be located;
7. Demonstrate all emergency protocols associated with the laser system and all the safety features;
8. Show locations of laser goggles and all emergency equipment
9. Demonstrate laser start-up and shutdown procedure;
10. Demonstrate laser sheet alignment using fluorescent tape, and PIV software, ensuring beam blocks are in place and laser is on lowest poser possible

Laser Beam Alignment

1. Fill flume
2. Align laser arm to point laser sheet at plane of interest
3. Ensure beam blocks are in place, and put camera lens caps on
4. Keep table free of reflective and flammable materials
5. Turn laser on following above procedures, set to low power

Manufacturer:	Litron Lasers	**Model:**	NANO L100-50	**Serial Number:**	LM1975
Type:	Nd:YAG	**Max. Power:**	200 mJ	**Class**	IV
Laser Location:	STEM 0014				
Emergency Contact	Majid Mohammadian (613) 562-5800 ext.6492	**Last Update:**	March 2023		

6. Use fluorescent tape on bottom of flume to show when the laser sheet is properly aligned
7. Stop laser and close shutter before adjusting laser arm

Laser Maintenance

These steps should be followed, including by external service providers.

Required Goggle OD:	532 nm 7+
Storage Location:	Grey cabinet in PIV room

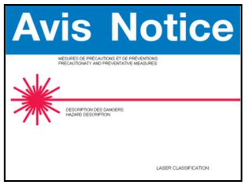

1. Post the Notice sign over the Danger sign. An example of a Notice sign is shown in the figure. Place the goggle requirements on the sign as well as the conditions of the exposed laser beam. Indicate Laser Repair In Progress
2. For replacing deionized water or flashlamps, follow procedure in Laser Systems user manual, on shelf under PIV monitor;
3. All other maintenance should be done by manufacturer and not attempted by user;
4. Remove interlock defeats, replace all enclosures and safety devices;
5. Verify normal laser operation;
6. Remove ANSI Notice sign after returning the laser to service.

Non-Beam Hazards

The corresponding standard operating procedures for non-beam hazards associated with this laser system, including required protective equipment and emergency procedures, are listed below.

PIV particles:	Dry PIV particles present inhalation hazard. Use mask when handling dry particles. Do not add dry particles directly to experiment, use pre-prepared concentrated solution of particles instead.

Only properly trained personnel shall work on high voltage systems (Electricians should be trained in CPR as a safety precaution). The "buddy" system should always be used when working on electrical systems. Note the placement of fire extinguishers and assure the laboratory staff knows how to use extinguishers and the fire alarm system.

Remember that poor housekeeping can create physical hazards. Remove any light reflective objects from the laser table (pliers and tools, pens and rulers, etc.). Keep flammable objects out of the beam path (paper, fabrics, solvents, etc.).

Appendix C

PIV manual

PARTICLE IMAGE VELOCIMETRY SYSTEM
User Manual

MOHAMMEDI YACINE AND SCHREINER KATIE

August 28, 2023

Water Resources Engineering Laboratory

Department of Civil Engineering

University of Ottawa

Contents

List of PIV documentation

This manual

- Principles of PIV
- Procedures for preparing experiments
- Beginning-to-end procedures for running basic Stereo-PIV experiments with our equipment

LaVision manuals

Hard copies under computer in PIV room
PDFs available through DaVis help menu or through LaVision online

- Detailed descriptions of all equipment and procedures
- Includes methods not yet implemented in our lab, and equipment different from ours

Laser manual

Hard copy under computer in PIV room

- Maintenance instructions, including replacing deionized water and deionization cartridges
- Specifications for our lasers, including optimal Q-switch delay and burn test results

Standard operating procedures (SOPs)

Hard copy posted on back of PIV room door
Document with Dr. Mohammadian and with Office of Risk Management

- Most up-to-date document
- Instructions for turning on and off laser
- Safety procedures
- Checklist for preparing and running experiment

Laser maintenance sheet

Hard copy posted next to PIV room computer

- Record of deionized water and cartridge replacement

1 Understanding PIV

Particle Image Velocimetry (PIV) is a non-intrusive technique for measuring fluid velocity. Light scattering particles are added to the flow. A laser beam is diverged through lens into a light sheet, illuminating seeding particles twice with a short time interval Δt. Images of the seeding particles at both times are compared statistically, giving the velocity of the particles everywhere where they are illuminated with the laser. In Stereo-PIV, two cameras at different observation angles are used to provide the third (out-of-plane) component of the flow velocity in the light sheet.

To calculate the velocity, each image must be transformed into real-world coordinates with a calibration transformation. The images are then subdivided into small interrogation windows. The average particle displacement within an interrogation window is determined by cross-correlation followed by the localization of the correlation peak. The velocity is calculated from the known time difference Δt and the measured displacement in each direction. Advanced multi-pass image deformation techniques are used for higher accuracy and spatial resolution.[1]

Figure 1: Principle of Particle Image Velocimetry method

2 Our PIV system

2.1 PIV System Components

PIV experiments require may pieces of equipment which each have an important role. It is important to know the function of each component.

PIV lasers:

The light source we use for the images is the Nano PIV system, a device with two independent lasers. This system generates the double pulse necessary for PIV experiments. The output beams are combined by dielectric polarizers and then the frequency is doubled to get the green light which is visible to the cameras.

Laser power source:

These are the two large boxes on the laser cart under the controls.

Laser controls:

Figure 2: Laser head

The laser controls are on the top of the laser cart. There is one set of controls for each laser. Every time you change use laser control, you should do the same for both lasers.

Laser arm:

The laser arm conducts the laser to the place of use. For this, a mirror assembly device is mounted inside to change the direction of the laser beam.

Figure 3: Laser arm

Sheet Optics:

The sheet optics are the combination of diverging lenses at the end of the laser arm that split the laser beam into a sheet in order to illuminate a cross sections of a fluid.

Cameras:

For stereo PIV, two cameras must be connected to the system. Each camera has two data cables, a trigger cable, and a power cable. The cameras are on adjustable mounts. They each have a lens, connected with a Schiempflug mount, with adjustable aperture and focus. They should also each have a filter that blocks all light outside of the frequency emitted by the laser. When not in use, they should always have their lens caps on. Figure 4 shows a camera with all its attachments.

The cameras need to see the laser light in order to take particle images, but too much light can damage the cameras, leaving dead pixels in images. Our cameras detect the amount of light coming in at each pixel up to an intensity of 64 000 counts. Anything above 64 000 counts is "saturated", and is reported as 64 000. If there are parts of an image being displayed as an intensity of 64 000 counts, it is possible that even more light is actually coming into the camera, and you should adjust beam blocks, change the camera aperture, or adjust the laser power to reduce the amount of light.

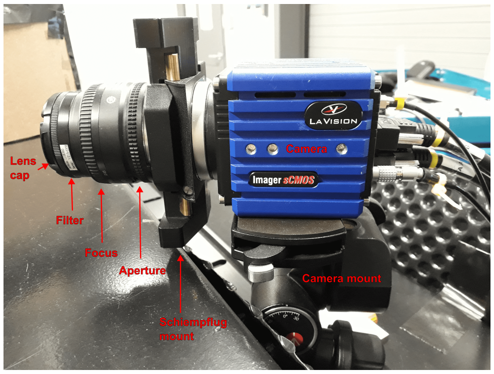

Figure 4: Camera

Camera mounts:

The cameras are equipped with two adjustable mounts: one to adjust the camera angle, using three knobs to adjust in each direction, and the Scheimpflug mount, which adjusts the relative angle of the lens and the camera acquisition plane, allowing for the field of view to be in focus from an oblique angle. Figure 5 illustrates the adjustment of the focal plane by using the Scheimpflug mount.

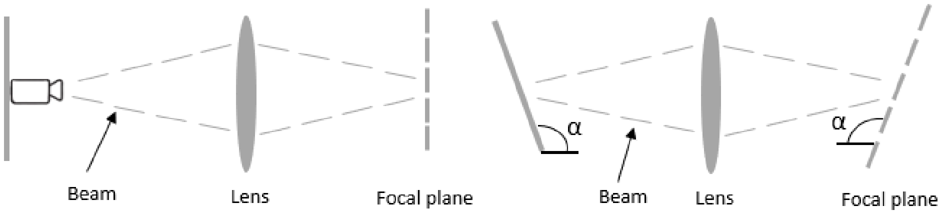

Figure 5: Adjustment of the relative angle of the acquisition plane of the camera and the lens

Calibration plates:

Calibration plates are plates with a series of dots of known size, shape, and location. By taking images of a calibration plate, DaVis can calculate an appropriate transformation between coordinates on an image (that include effects of perspective and distortion) and real-world coordinates. We have two LaVision calibration plates, but if they are not suitable for the geometry of you project you can 3D print one more suited to your experiment. In this case you will need to define the plate parameters such as the size of the dots, and the distance between dots and between planes of the plate. You can define a new plate in the same menu as you select existing plates from once you enter the calibration procedure.

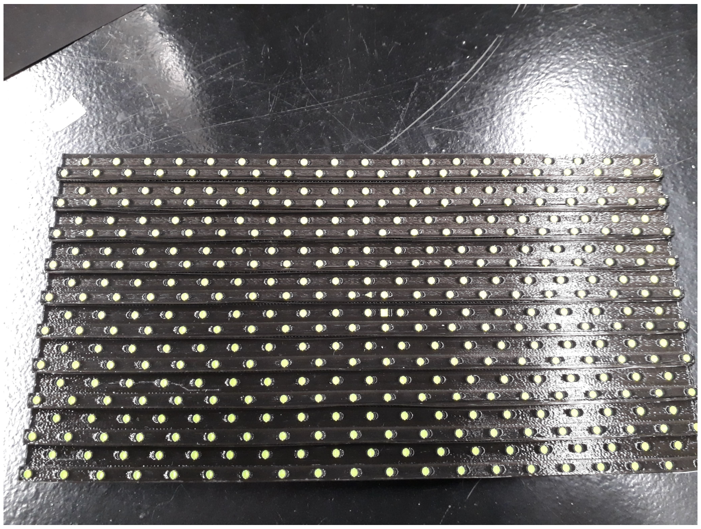

Figure 6: Calibration plate

Programmable timing unit:

The programmable timing unit (PTU X) generates trigger pulses for the cameras, lasers and other external devices under the control of DaVis software.

Figure 7: Programmable timing unit

2.2 DaVis software

The DaVis software on the PIV computer controls all the acquisition hardware, does the camera calibrations, and processes the data. It can also do some analysis of the resulting velocity fields, or it can export them for analysis in another program.

When you open DaVis, it will immediately check for connected hardware. If you need to record anything, be sure to turn on your cameras and the PTU before opening the software. If you just need to access the software without the cameras, it will give you an initial error telling you that it couldn't find the cameras or PTU. This is fine. Unlike the cameras and PTU, the laser can be turned on anytime after the software is opened without the software having to reconfigure.

Figure 8 shows the main screen of the DaVis software. You can enter old projects or create new ones. If you click on a saved image or dataset, it will bring up a visualization on the right, as the sample screenshot shows. Below the visualization you can toggle between samples and frames. The frames toggle bar is immediately below the image. In figure 8 there are four frames, corresponding to: camera 1 at time t_i (frame 0); camera 1 at time $t_i + Dt$ (frame 1, shown);

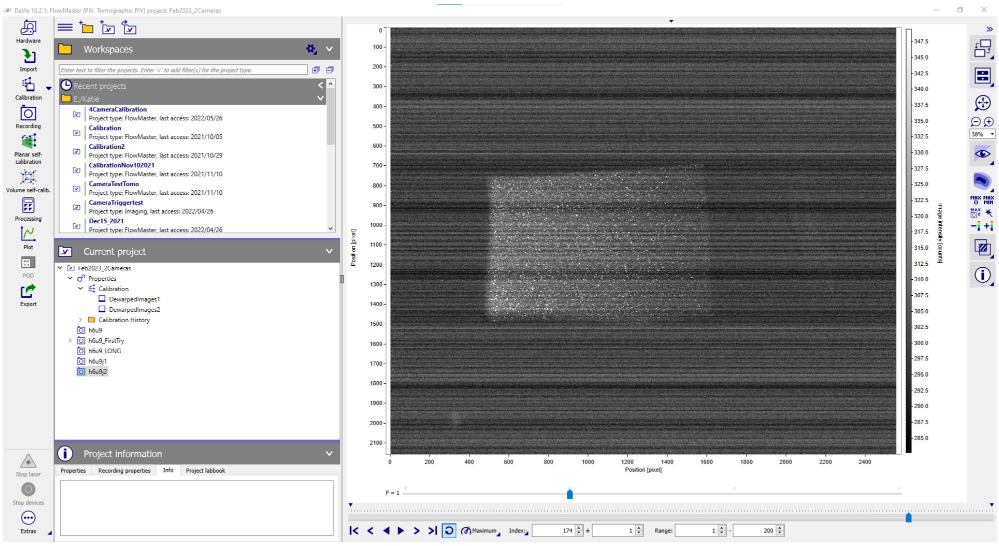

Figure 8: DaVis main screen

camera 2 at time t_i (frame 2); and camera 2 at time $t_i + Dt$ (frame 3). All four frames make up a single sample. To view other samples, use the toggle bar below the frame toggle bar.

On the very left is a series of icons for entering different interfaces, including the hardware settings, the calibration procedure, recording (for taking images for calibration and for data acquisition), self-calibration, processing, and some others not covered in detail in this manual.

2.3 Checking the hardware connections

The graphical hardware configuration (found by clicking the hardware icon on the top left of the DaVis main screen and shown in figure 9) presents the systems in a visual layout and allows you to see which cameras are connected and if they are connected to the right port. Check on the software that all the connected cameras are associated to the correct trigger. The process of controlling and associating cameras to ports is simplified by drag-and-drop hardware configuration and automatic detection of installed devices.

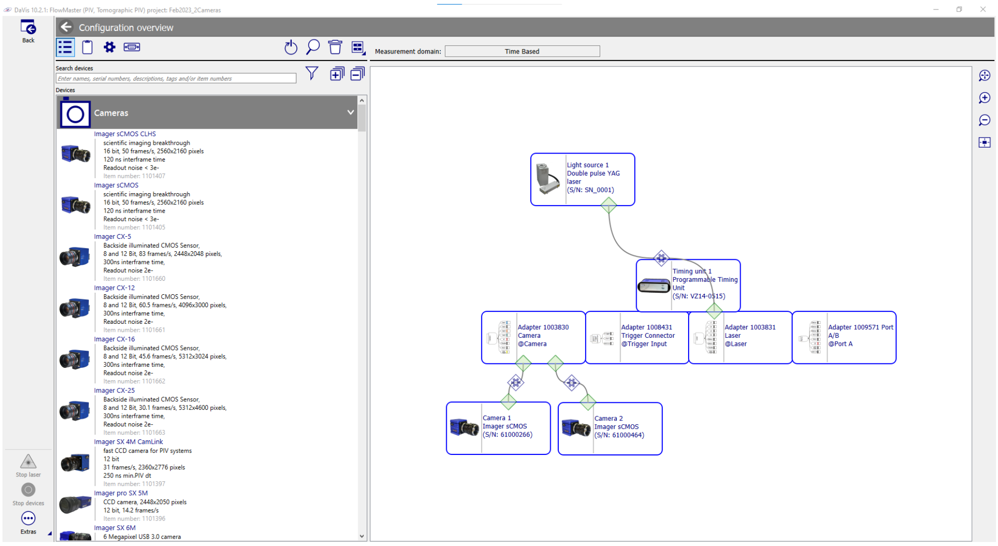

Figure 9: Hardware visual interface

DaVis assigns numbers to all connected cameras using the cameras' serial numbers. This means that "Camera 1" is not necessarily the camera connected to the first data port, or to the "camera 1" trigger on the PTU. If you have specifically plugged in the cameras in order of serial number, it will be easier to keep track of which cameras are associated with which numbers. Even if you plug everything in in order, an issue may arise if you have more cameras plugged in than you have turned on for your current experiment; for example, if all cameras are plugged in but only the first and last (in serial number order) are being used, then DaVis will number the first Camera 1 and the last Camera 2. However, the last camera (if all are plugged in in order) will be connected to the Camera 4 trigger cable of the PTU. You can fix this by going into the hardware interface and specifying that Camera 2 connects to Trigger 4, as shown in figure 10.

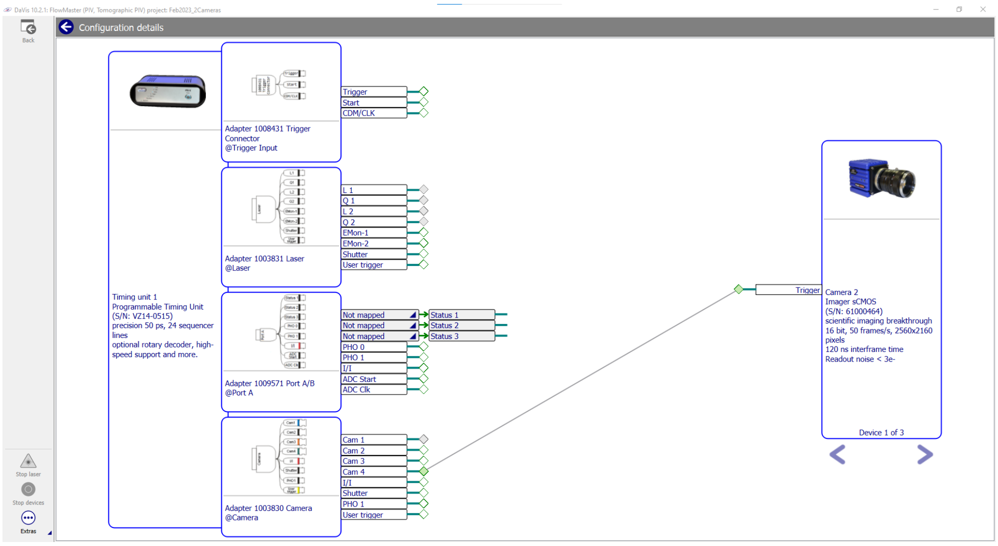

Timing unit 1
Programmable Timing Unit
(S/N: VZ14-0515)
precision 50 ps, 24 sequencer lines
optional rotary decoder, high-speed support and more.

Adapter 1008431 Trigger Connector
@Trigger Input

Adapter 1003831 Laser
@Laser

Adapter 1009571 Port A/B
@Port A

Adapter 1003830 Camera
@Camera

Camera 2
Imager sCMOS
(S/N: 61000464)
scientific imaging breakthrough
16 bit, 50 frames/s, 2560x2160 pixels
120 ns interframe time
Readout noise < 3e-

Device 1 of 3

Figure 10: Camera hardware settings for connecting to correct trigger

2.4 Using the laser

Refer to the up-to-date laser SOPs posted in the lab for instructions on turning on and off the laser. Ensure everyone in the PIV room has laser goggles on. Illuminate the laser warning sign and lock the PIV room door.

Figure 11: Laser sign in front of the PIV room

There are several ways to control the light output of the laser: A shutter can be opened or shut from the laser control box; another shutter control can be found in the DaVis laser settings under the hardware graphical interface; the energy knob on the laser control box adjusts the amount of energy that goes into the laser medium; the black knob on top of the laser head blocks some light output depending on how it is turned; and the laser power setting in the DaVis recording interface controls the timing between exciting the laser medium and releasing the resulting light (called the Q-switch delay). Many of these methods can behave counter-intuitively, so here are some useful notes.

Laser control box shutter: This is a simple on/off control; either the shutter is closed and no light is allowed out, or the shutter is open and all the light comes out.

Laser hardware settings shutter: This option is connected to the camera triggers. It should be set to only open the shutter when a camera is taking an image, reducing the laser safety risk when the laser is not in use for the experiment. This setting may get reset to default if you update DaVis, so you should never rely on it to keep yourself safe. Always wear your laser goggles!

Laser control box energy knobs: These knobs control the energy going into the laser medium, which controls the amount of light coming out of the medium. Note that the knobs are easily warped, so the number showing on the knob control may not be an accurate reflection of the actual laser power.

Laser head knob: This knob does not have any labels, and is therefore hard to control well. Ideally, this knob is always adjusted to give maximum light output, and the actual laser output is controlled using the other control options.

Power settings in DaVis Recording interface: These are boxes where you can input a number from 1 to 100% which adjusts the laser power. Note that the number does not indicate the percent laser output power, but rather the percent difference in Q-switch delay between the optimal time and some different time assumed to give zero output. The optimal times are different for each laser, and can be found in the laser manual under the lab computer. They are set in DaVis in the hardware configuration interface, as shown in 12

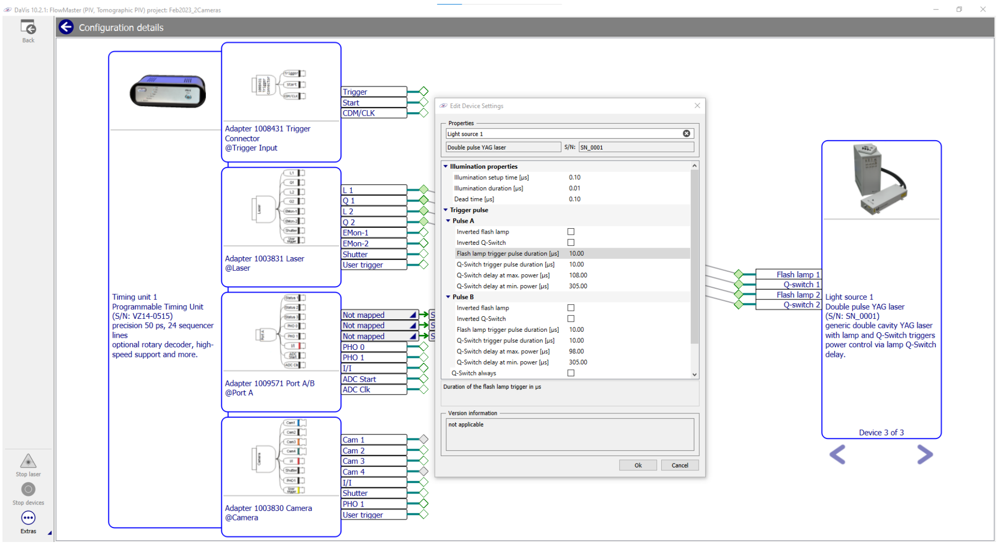

Properties

Light source 1

Double pulse YAG laser S/N: SN_0001

Illumination properties

Illumination setup time [µs] 0.10
Illumination duration [µs] 0.01
Dead time [µs] 0.10

Trigger pulse

Pulse A

Inverted flash lamp ☐
Inverted Q-Switch ☐
Flash lamp trigger pulse duration [µs] 10.00
Q-Switch trigger pulse duration [µs] 10.00
Q-Switch delay at max. power [µs] 108.00
Q-Switch delay at min. power [µs] 305.00

Pulse B

Inverted flash lamp ☐
Inverted Q-Switch ☐
Flash lamp trigger pulse duration [µs] 10.00
Q-Switch trigger pulse duration [µs] 10.00
Q-Switch delay at max. power [µs] 98.00
Q-Switch delay at min. power [µs] 305.00

Q-Switch always ☐

Duration of the flash lamp trigger in µs

Version information

not applicable

Figure 12: Laser hardware settings, showing correctly assigned optimal Q-switch delay

If the laser is on but you can't detect any light, here are some possible solutions:

If the laser is not emitting any light at all:

- Before troubleshooting, put the camera lens caps on and get a board covered in fluorescent tape to help you find the laser sheet.
- Make sure the control panel shutter is open

- Turn the laser on and then press the "Live view" button at the top right of the Recording controls. This will trigger the cameras regularly at the set trigger rate, ensuring that the second shutter is also opening.
- Put the board with fluorescent tape in front of the laser arm. If the laser is firing, you should see the tape fluoresce orange through your safety goggles.
- Look at the laser hardware settings, and make sure that the optimal time for the Q-switch delay matches the optimal time in the laser manuals.
- Turn the power up in the DaVis controls. If at 60% power you still see no light at all, there is a more complex problem.

If the laser is emitting light but the image contrast is still low:

- Make sure the laser is warmed up: With the camera lens caps on and the control box shutter closed, turn the laser on and let it fire for 1-2 minutes. Then open the shutter again and take off the camera lens caps.
- Are there PIV particles in the water? If there aren't, there may not be enough light coming into the cameras to get an image with good contrast.
- Open the camera apertures one setting at a time and see if that improves the image
- Has the coolant water been changed recently? Check the maintenance record sheet posted in the lab. If the coolant water or deionization cartridge needs changing, it may reduce the light output of the laser.
- Get the board with fluorescent tape, and verify that the light sheet is where the cameras are looking
- Look at the laser hardware settings, and make sure that the optimal time for the Q-switch delay matches the optimal time in the laser manuals.
- If all else fails, try adjusting the energy input knobs or the knob on the laser head. Adjust one at a time, and leave each in the position that gives maximum light output.

3 Preparing your experiment

3.1 Clean flume walls

Before doing anything, clean the flume walls where the cameras will be looking through. Use microfiber cloths with glass cleaner. It is also necessary to make sure that there are no fine scratches before filling the flume up. If there are, use fine scratch cleaner to restore the original appearance of the flume walls. Make small, slow circular motions in order to clean without damaging the walls.

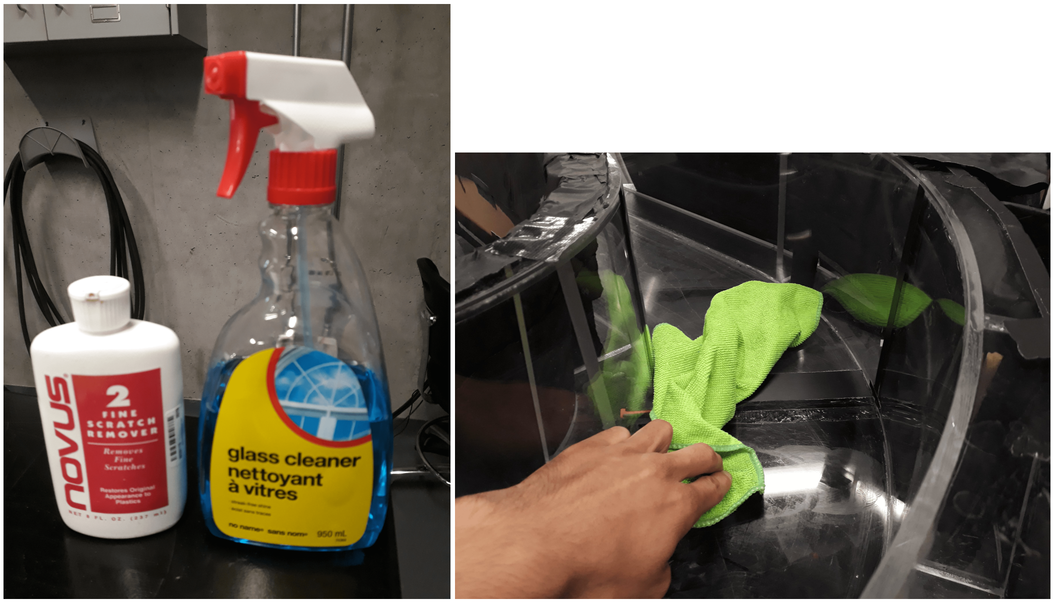

Figure 13: Products and motions to clean the walls

3.2 Fill the tank

Fill the internal tanks with filtered water to ensure good water quality. Pool cartridge filters generally filter out particles greater than about 20 microns in diameter, and operate at a sufficient flow rate to fill the tanks in a reasonable time. Replace the filter every 3 months, or when wear starts to show.

Even if your water quality is perfect, you may have issues if there are bubbles in the water. To avoid bubbles: Fill your tanks at least a day before running your experiment, and let sit for a day. Gently brush the bubbles off of all surfaces including tank walls, flume walls, etc. Once your flow is set up, shake hoses to dislodge bubbles inside them. Position filter bags full of suitable filter media to catch and slow down free-falling water after flume exits and v-notch weirs, preventing air entrainment in the turbulence there. Place a dark background behind your flume so you can see bubbles easily.

3.3 PIV particles

The PIV seeding particles are neutrally buoyant hollow glass spheres 10 microns across. They are kept in a slurry for safe handling. Add PIV particles only after you've established that there are no other large particulates in your water (i.e. after you've taken an image with the laser on and seen what the laser illuminates). You don't need much: roughly one teaspoon of the slurry is enough for the whole small bend flume system.

3.4 Block reflections

Laser light scattered off flume walls and the water surface can be dangerous to the eyes, and interfere with the image quality. It is therefore important to use black covers and black tape in order to block or minimize reflections. Position opaque blocks along the length of the channel, with the exception of the places located in the field of view of the cameras. Additional blocks are placed on top of the flume to prevent light entering from the top and over the end of the flume.

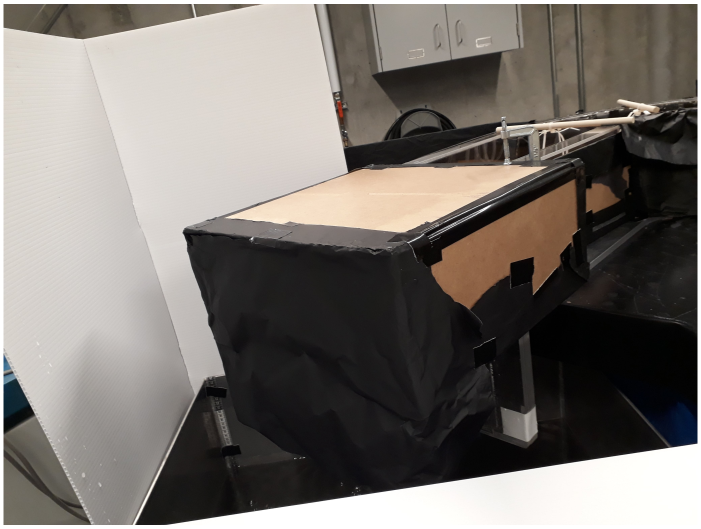

Figure 14: Opaque block at the end of the flume

3.5 Prepare the laser

If the laser has not been used in more than 4 months, it will need to have the deionized coolant water replaced. You can get deionized water from the Environmental Engineering lab. Instructions for changing the laser coolant are in the laser manual. When you replace the water, make sure to record the date on the laser maintenance record sheet posted in the PIV next to the computer.

4 Calibration procedure

The perspective and distortion of the acquired images must be corrected before calculating the velocity. This is done with a spatial calibration using a calibration plate. The principle is to visualize the measurement area with a plate with elements at known locations in order to create a transformation between the real world and picture coordinate systems. Before placing the calibration plate, submerge it and clean it with a paintbrush to remove bubbles.

Figure 15: Calibration procedure

Place the calibration plate in the field of view, where the laser plane will be. Remove the lens caps and laser frequency filters from all cameras. Take a set of images under ambient light, without the laser on, by clicking the "camera" icon on the left of the main DaVis menu and then clicking the "single image" icon at the top right. Save the image by clicking on the "save live image" icon at the top right.

It is not necessary to turn on the laser during calibration, only the cameras. In order to obtain the optimal calibration, the focal plane can be adjusted by turning the Scheimpflug adaptor knobs. One knob adjusts the angle of the image focal plane and one adjusts the axis of rotation of the other knob. These adjustments allow for the calibration plate to be entirely in the camera's focal plane, even when they are at an oblique angle to the camera acquisition plane.

In double exposure mode, each camera takes two images with each measurement, as is needed for PIV. Discard the first frame from each camera, since under ambient light the first frame does not generally have good contrast. Therefore, only the last frame should be retained: Click on the "processing" icon in the main DaVis screen, then select "delete or change order of frames". Select the frames to keep, then click "start".

Once you have a set of images containing one clear image per camera of the calibration plate, select that set in the DaVis main screen, and click on the "calibration" icon on the left of the screen to begin calibration. Most of the calibration is done automatically by DaVis. All that you need to do to begin is make sure the correct calibration plate is indicated.

After you have started the calibration, you must indicate three calibration plate marks on each image: the first defines which mark to use as the origin, the second should be the next mark over in the x direction, and the third should be the mark directly above the first.

The computer will find the rest of the marks automatically. If it cannot find all the marks (or finds many that aren't there), adjust the lighting and the focus and try again.

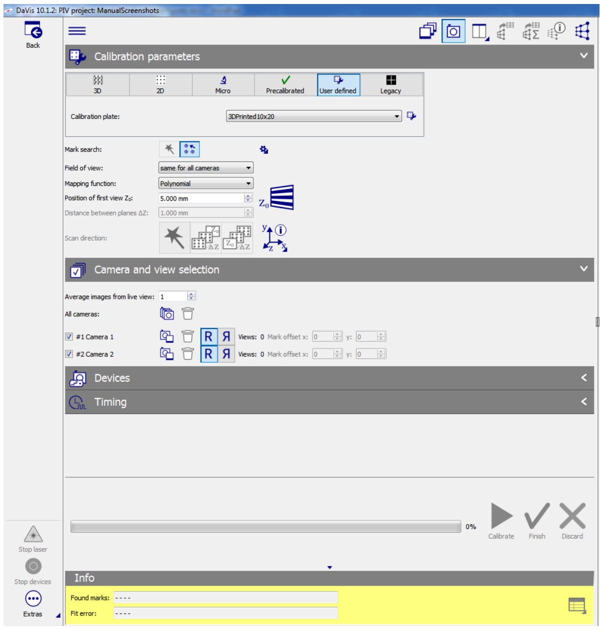

Calibration plate: 3DPrinted10x20

Mark search:

Field of view: same for all cameras

Mapping function: Polynomial

Position of first view Z_0: 5.000 mm

Distance between planes ΔZ: 1.000 mm

Scan direction:

Average images from live view: 1

All cameras:

☑ #1 Camera 1 Views: 0 Mark offset x: 0 y: 0

☑ #2 Camera 2 Views: 0 Mark offset x: 0 y: 0

0%

Found marks: - - - -

Fit error: - - - -

Figure 16: Options in the calibration interface

The DaVis software measures the locations of the calibration marks on the calibration plate and reconstructs the transformation from real space into the camera image. After the transformation is calculated, the software presents a set of distorted images, where the calibration plate is superimposed on a Cartesian plane. These images can be viewed one at a time, or superimposed from each camera to ensure that the cameras agree on which calibration plate point is which.

> In order for the calibration to be good enough to use in measurement, the fit-error associated to each camera must be below 1 pixel.

5 Data Acquisition

5.1 Preparing the acquisition system

To record data, enter the recording interface by clicking the camera icon on the main screen. You will see options like those in figure 17

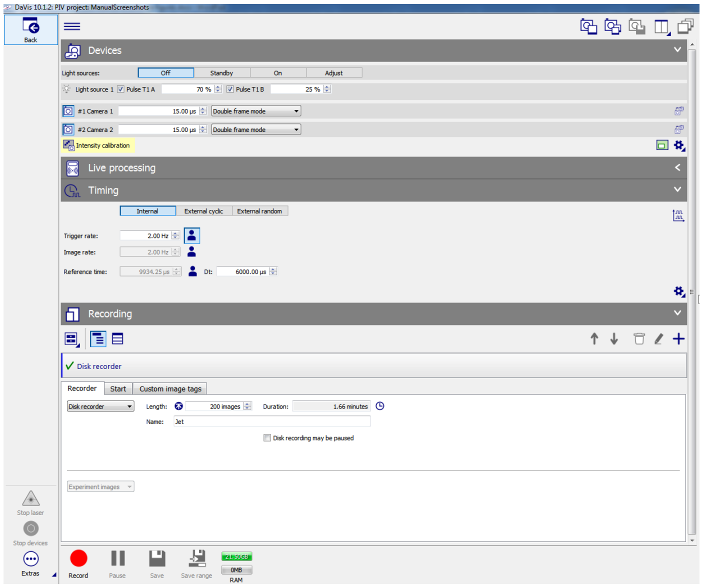

Light sources: Off

Light source 1 ☑ Pulse T1 A 70 % ☑ Pulse T1 B 25 %

#1 Camera 1 15.00 µs Double frame mode

#2 Camera 2 15.00 µs Double frame mode

Trigger rate: 2.00 Hz

Image rate: 2.00 Hz

Reference time: 9934.25 µs Dt: 6000.00 µs

Disk recorder Length: 200 images Duration: 1.66 minutes

Name: Jet

☐ Disk recording may be paused

Figure 17: Recording dialogue

Before acquiring any data, make sure that the cameras are in double frame mode, that the lens caps are off, and that the laser light frequency filters are on. Turn on the laser following the SOPs posted in the lab.

5.2 Initial check with low laser power

When everything is ready, turn off the lights in the lab, making sure you have a portable light ready to help you see what you are doing. Activate the two laser pulses by checking their boxes, and set to low power (about 15%) to begin. Take an image in the DaVis recording interface by pressing "On" in the light source line in the devices panel to activate the laser, and the "single image" icon (leftmost icon at the top right corner) to take the image. Then press "Off" in the light source line to turn off the laser. Click the "max min" icon at the very right (see visualization panel in 18) to adjust the intensity scale of the display into a useful range.

⚠ Always remember to turn the laser off from the light source line of the devices panel once the cameras have taken their images. Otherwise, the laser will continue to fire.

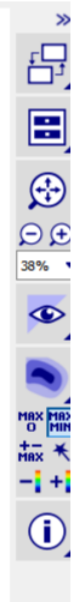

Figure 18: Visualisation panel

If the image at low laser power has no bright spots indicating visible reflections, increase the percentage of power of the two lasers one after the other, checking that there are no areas that are too bright with each increase in power. Make sure to check every frame.

Make sure that as you increase the power in the laser, that you are keeping the maximum intensity count measured by the cameras well below the "danger threshold" of 64 000 counts. Hovering your cursor over the image displays the intensity at that pixel, but this is an inefficient way to monitor the intensity of the whole image. Click the icon under the eye from the visualisation panel on the far right of the screen (see figure 18). You can change the histogram options for the colour scale (set to 100%, and the maximum intensity on the colourbar scale will be the maximum intensity of all pixels in the image), or change the colour scale to highlight the top intensities in red to better monitor the high intensity peaks of the image.

5.3 Image focus and balance

Once the images have enough contrast between the PIV particles and the background, ensure the particles are in focus. If not, adjust the focus of the cameras. You should aim to have approximately equal contrast between all frames and all cameras. If some images are brighter than others, adjust the camera apertures (if one camera's images are brighter) or the relative power of the laser pulses (if one pulse's images are brighter).

While you are checking for reflections and focus, you should also be checking the appearance of the particles. Make sure they are not too big (i.e. several pixels across), which indicates they are either out of focus or they are dust or bubbles rather than PIV particles.

5.4 Set Dt

If you have good contrast in your images, and all the visible particles are small and in focus, toggle between the frames of each camera to see how far each particle travels between frames. The images of the particles should shift by 5 to 10 pixels between frames. If the particles are not at the optimal shift, change the Dt setting to adjust the time between frames. If the particles are too big for you to be confident about how many pixels they shift between frames, there is an issue with the water quality or with bubbles in the water.

> Note: though the previous steps are summarized briefly here, they can be extremely time consuming. The actual data acquisition is very fast; most of the work of PIV is in the setup, especially these steps.

5.5 Record images

Set the trigger frequency to the desired sampling frequency, and the number of samples to the desired value. Once this is done, all that remains is to record the data: click the light source "On", press "Record", wait until the progress bar shows the measurement is complete, then click the light source "Off".

After recording your data, you can turn the lab lights back on and turn the laser off according to the posted SOPs.

6 Self calibration

Once there are images of particles, refine the calibration by doing a self-calibration. This allows the software to cross-reference the images of particles between cameras to get better calibration results. This is a necessary step, and accounts for small differences between the placement of the calibration plate and the final placement of the laser sheet. Enter the self-calibration interface through the icon on the left of the main DaVis screen. Set a large window size (for example, 64 or 128), and click on "Refine calibration". If the new calibration is an improvement over the old (i.e. smaller disparity) click on "Accept".

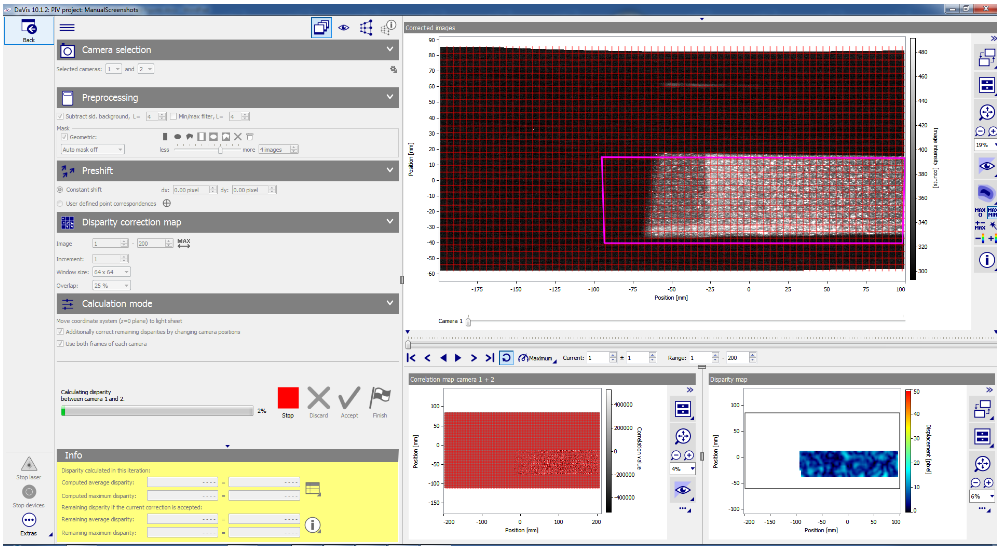

Selected cameras: 1 and 2

☑ Subtract sld. background, L= 4 ☐ Min/max filter, L= 4

Mask
☑ Geometric:
Auto mask off
less — more 4 images

● Constant shift dx: 0.00 pixel dy: 0.00 pixel
○ User defined point correspondences

Image 1 - 200
Increment: 1
Window size: 64 x 64
Overlap: 25 %

Move coordinate system (z=0 plane) to light sheet
☑ Additionally correct remaining disparities by changing camera positions
☑ Use both frames of each camera

Calculating disparity
between camera 1 and 2.
2%

Disparity calculated in this iteration:
Computed average disparity: ---- = ----
Computed maximum disparity: ---- = ----
Remaining disparity if the current correction is accepted:
Remaining average disparity: ---- = ----
Remaining maximum disparity: ---- = ----

Figure 19: Self calibration interface

7 Post-Processing

After recording the images, the DaVis software can process the data to calculate the velocity field. This is done by entering the "Processing" interface, which is shown in figure 20, from the buttons on the left of the DaVis main screen. Once you are in the processing interface, drag processing operations from the list on the left to form a list of operations. Clicking on a step in the sequence brings up the settings for that step in the box below the Operation list. The minimum steps for PIV data processing are outlined here.

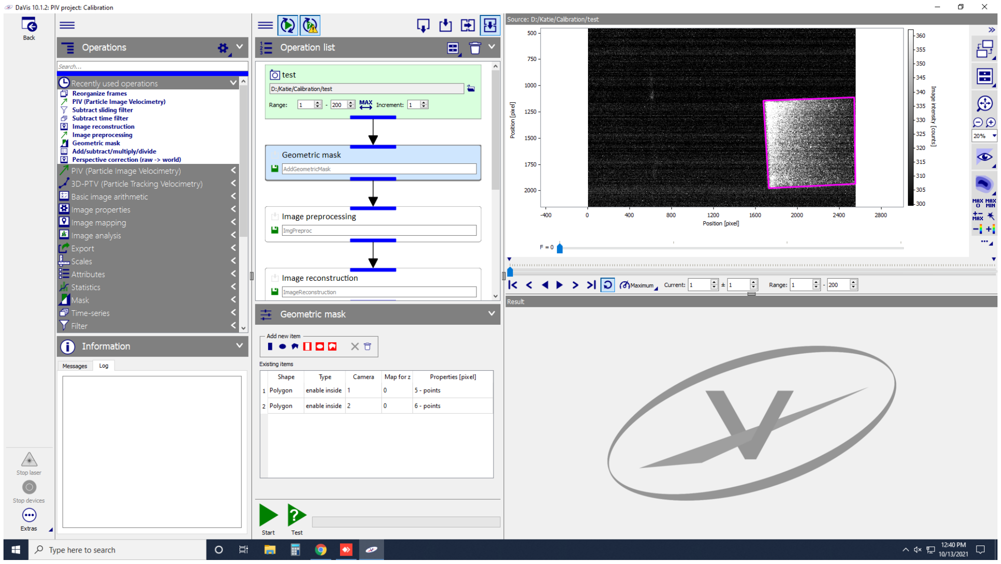

test
D:/Katie/Calibration/test
Range: 1 - 200 Increment: 1

Geometric mask
AddGeometricMask

Image preprocessing
ImgPreproc

Image reconstruction
ImageReconstruction

Geometric mask

Existing items

	Shape	Type	Camera	Map for z	Properties [pixel]
1	Polygon	enable inside	1	0	5 - points
2	Polygon	enable inside	2	0	6 - points

Figure 20: Geometric mask step

7.1 Add a Geometric Mask

Masks remove the parts of the image that are not within the desired field of view. The mask can be defined frame by frame but also by camera. You can add a mask by finding the "geometric mask" operation, or from within the setting of the image preprocessing or PIV operations

Define a region by clicking and selecting each points of the desired geometric shape.

7.2 Image Preprocessing

Basic image preprocessing can be done from within the settings of the PIV operation, but more detailed options are available by calling operations such as the "Image preprocessing" or "Subtract time filter" opertations. Most of the preprocessing options are filters which increase the contrast or resolution of the particle images.

7.3 Image Reconstruction

This step applies the calibration to the recorded images to transform them into real world coordinates. You do not have to input any settings.

7.4 Particle Image Velocimetry

This is the operation that actually calculates the velocity. You can control the interrogation window size, multipass options, and other such settings, but the default options are very good.

Make sure to set the file name to a descriptive name that will help you find your data later.

7.5 Test Processing

Because processing a whole measurement can take a very long time (approximately twenty minutes per hundred samples), test your processing sequence by pressing the "test" button before actually starting the process.

7.6 Exporting results

Once you have a velocity field, if you need to do any calculations outside of DaVis you can export your data using the "Vector field export" operation.

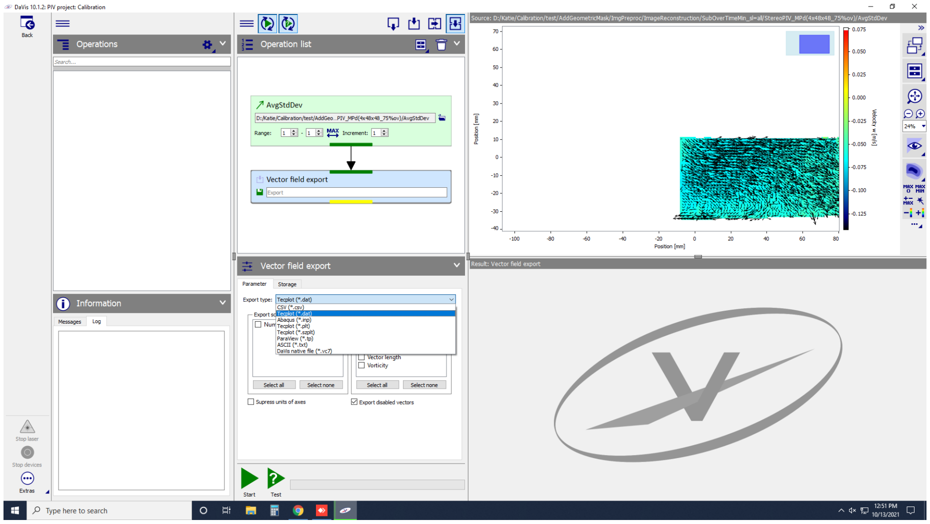

DaVis 10.1.2: PIV project: Calibration

Source: D:/Katie/Calibration/test/AddGeometricMask/ImgPreproc/ImageReconstruction/SubOverTimeMin_sl=all/StereoPIV_MPd(4x48x48_75%ov)/AvgStdDev

AvgStdDev
D:/Katie/Calibration/test/AddGeo...PIV_MPd(4x48x48_75%ov)/AvgStdDev
Range: 1 - 1 Increment: 1

Vector field export
Export

Export type: Tecplot (*.dat)

☐ Supress units of axes
☑ Export disabled vectors

Figure 21: Exporting the results in Tecplot format

8 Precautions to take when leaving the laboratory

When the experiment is finished, it is important to leave the lab clean and tidy as you found it. This involves putting the components used back in their place and adopting different preventive measures according to the nature of each one (for example, electrical components). This is a way to prevent and manage the potential risks present in the PIV room but also within the laboratory.The attitudes to adopt for each type of component or object are described below:

- Laser: Follow the posted SOPs for thorough instructions on turning off the laser.
- Electronics: After finishing the experiment, the Programmable Timing Unit (PTU) and the transformer on its power cord should be turned off and all high voltage cables unplugged if the laser will be disabled for a long time.
- Optical systems: All the cameras must be turned off. Place lens caps on the cameras to avoid light damage.

Figure 22: Reflecting objects

Remember that poor housekeeping can create physical hazards. Remove any reflective objects from the experiment table (pliers, tools, pens and rulers, etc.). They can be kept on a camera table covered with black cloth. Keep flammable objects out of the beam path (paper, fabrics, solvents, etc.) Make sure all necessary valves are closed and hoses removed from tanks so that water does not siphon into unexpected places.

References

[1] Particle Image Velocimetry - LaVision.
https://www.lavision.de/en/techniques/piv-ptv/.

Appendix D

Investigation of air-water interface treatment in simulations of open channel bend flow

Investigation of water surface treatments in DES simulations and their effects on outer bank cell production in river bends

H. K. Schreiner, C. D. Rennie & A. Mohammadian
University of Ottawa

ABSTRACT: Simulations of flow in river bends, especially at the outer bank, can differ based on the treatment of the air-water interface and on the turbulence model used. Here, four detached eddy simulation (DES) models and one large eddy simulation (LES) model are compared based on their ability to reproduce experimental results in a channel bend, with a specific focus on the reproduction of the outer bank cell. The Multidimensional Universal Limiter with Explicit Solution (MULES) interface model and the LES rigid lid models are able to reproduce the outer bank cell of secondary circulation, while the rigid lid models employing DES are not. The combination of the k-omega SST turbulence model (which is employed at the wall boundaries of the DES simulations) together with the symmetry condition applied at the rigid lid boundary, appears to disrupt the production of the outer bank cells in these simulations.

1 INTRODUCTION

Secondary flow in river bends is driven by a buildup of water at the outer bank, called superelevation. In scaled-down river model systems, the superelevation is often small enough that it is not easily captured in numerical simulations. It is common practice to use a flat rigid lid to model the surface in these situations, as it has been shown to generate adequate secondary circulation (Booij 2003). However, this practice necessitates the use of different surface treatments for different flow conditions, which becomes problematic when simulations using different surface treatments are directly compared. This project investigates the comparability of different surface treatments for flow in a river bend.

The main secondary circulation cell in river bends brings water toward the outer bank on the surface (driven by the centrifugal force) and toward the inner bank on the bottom of the flow (driven by the pressure gradient caused by superelevation). In addition, there is a counter-rotating cell at the outer bank driven by Reynolds stress anisotropy. This cell is more difficult to model because it tends to have lower velocity, and because some turbulence models cannot reproduce the necessary Reynolds stress anisotropy.

The superelevation can be found using the formula (Bridge 1992):

$$E = \frac{BU}{gR} \tag{1}$$

Where E is the difference between water surface elevation at the outer bank and inner bank, B is the channel width, U is the average streamwise velocity, g is gravitational acceleration, and R is the channel's radius of curvature.

The rigid lid model has been widely studied using large eddy simulation (LES) (Kashyap, Constantinescu, Rennie, Post, & Townsend, 2012; van Balen, Blanckaert, & Uijttewaal, 2010a; van Balen, Uijttewaal, & Blanckaert, 2010). LES is generally accepted to be accurate for Froude numbers below 0.5, and produces the outer bank cell. It has also been used by Constantinescu, Koken, & Zeng, (2011) in a detached eddy simulation (DES) model (employing LES away from wall boundaries and Reynolds averaged Navier Stokes (RANS) near the boundaries) that successfully produced the outer bank cell. Although it is tempting to interpret this result as indicating that DES simulations can be expected to produce the outer bank cell, one should proceed with extreme caution: the outer bank cell is known to stem from Reynolds stress anisotropy at the upper outer bank corner of the flow (van Balen, Blanckaert, & Uijttewaal, 2010b), which because of its proximity to the wall may fall into the RANS mode of a DES simulation. Given that most of the RANS models employed by DES simulations do not accurately predict Reynolds stress anisotropy, one should not assume a DES simulation will produce the outer bank cell. Rather, one should test the desired model for the given mesh and turbulence model to ensure the production of an outer bank cell. This paper aims to emphasize the importance of this fact by comparing interface models in DES and LES simulations, with a specific focus on the production of the outer bank cell.

Four treatments of the air-water interface are investigated using openFOAM DES simulations of a scaled-down river bend model. The models investigated are a flat rigid lid, a rigid lid with an imposed superelevation, the default volume of fluid (VOF) interFOAM algorithm using Multidimensional Universal Limiter with Explicit Solution (MULES), and the isoAdvector method for advecting sharp interfaces. The rigid lid models are also investigated with a pure LES model. To evaluate the models, the superelevation (in the cases where it is directly simulated) is compared to the predicted superelevation using Equation 1, and velocity results at the bend 90° cross section are compared to experimental data.

Though only MULES and the flat rigid lid models are in general use for modelling river bends, the inclusion of the other models allows for a better understanding of the numerical processes causing differences in the model results. One can distinguish artifacts of the rigid lid boundary condition from artifacts of imposing a flat surface by comparing the flat and simulated rigid lid models. Likewise, comparing different surface advection models will distinguish the benefits (or detriments) of modelling the interface in general from those of the specific algorithm used.

2 METHODS

This project investigates flow through an open channel of 1 m width with a 135° bend with radius of curvature 1.5 m. The channel includes a 12 m approach to the bend and a 2.4 m exit. The simulated flow has a depth of 20 cm, average streamwise velocity of 12.8 cm/s, and Froude number 0.093, well within the range of Froude numbers for which rigid lid approximations are generally accepted. The computational domain was approximately 1.5 million cells for the rigid lid simulations. This is a similar resolution to the mesh used by Kashyap et al. (2012) to model the same flume in LES. The VOF meshes required more cells in order to model the interface and air above the water.

The turbulence model used for most of the simulations is a DES model that uses the Smagorinsky LES for the inner flow field and k-omega Reynolds Averaged Navier Stokes turbulence closure at the boundaries.

The MULES interface model is the default model in the OpenFOAM solver interFOAM. It is a VOF model that assigns to each cell a value alpha representing the fraction of the cell filled with water, from which the surface can be reconstructed. At each time step, the surface is advected by applying a transport equation to alpha. The MULES model also has an option for interface compression. In this project, interface compression was triggered by setting the interface compression parameter (cAlpha) to 2 in order to counteract numerical diffusion of alpha which was observed with no compression. The IsoAdvector model is also a VOF model, but unlike the MULES model it defines a surface explicitly at each time step, and therefore does not allow the interface to numerically diffuse.

As previously mentioned, the flat rigid lid approximation is a common simplification in modelling flow in river bends, and has been shown to yield consistent good results for LES models. In the DES flat rigid lid model, the same principle is applied to a DES model. The water surface is modelled as a flat rigid symmetry plane at the elevation of the average surface height. In order to differentiate the effects of superevelation from the effects of a symmetry boundary condition, a second rigid lid model is included using the time-averaged water surface from the MULES model.

An LES model is also included here for the sake of a consistent comparison with a previously studied model. It uses the same mesh and boundary conditions as the flat rigid lid DES model.

A summary of the simulations investigates is presented in Table 1.

The experiments used for validation are detailed in a previous study (Schreiner, Rennie, and Mohammadian, 2018).

Table 1. Summary of simulation methods.

Simulation name	Turbulence model	Interface model
DES MULES	DES	MULES VOF
DES IsoAdvector	DES	IsoAdvector VOF
DES flat rigid lid	DES	Flat symmetry plane
DES simulated RL	DES	Symmetry plane with superelevation
LES	Smagorinsky	Flat symmetry plane

3 RESULTS

The main secondary circulation cell and the outer bank cell were both visible in the MULES simulation. The time-averaged secondary circulation at 90° from the MULES simulation is shown in Figure 1. The superelevation toward the outer bank was reproduced, with a total difference of water height of 1.25 mm, which overestimates the predicted superelevation of 1.15 mm by 8.7%.

The IsoAdvector model did not produce suitably shaped secondary circulation cells: the main cell was confined to the bottom of the flow, with the counter-rotating cell occupying the upper part of the flow not just at the outer bank but entirely across the channel. Since the qualitative results were so different from expected and experimental results, no meaningful quantitative comparison of secondary circulation strength could be made. The simulated water surface showed a superelevation of 0.9 mm, underestimating the calculated value by 22%.

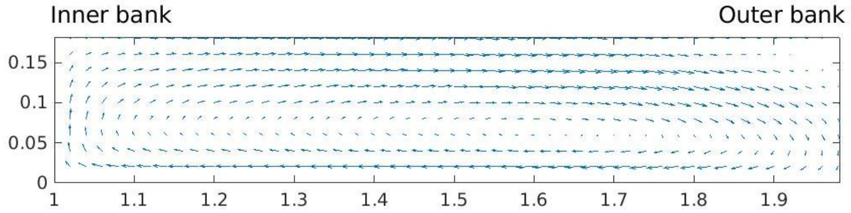

Figure 1. MULES 90° cross section showing main secondary circulation and small outer bank cell. Horizontal axis is measured outward from the inner bank starting at 1.0 m.

The DES rigid lid simulations gave very similar results to each other. Neither DES model produced the outer bank counter-rotating cell. The models did produce the main secondary circulation cell, though the strength of the secondary circulation was somewhat overestimated in both rigid lid cases.

The LES rigid lid models did produce both the main and outer bank circulation cells, though again the secondary velocity was slightly greater than that observed in experiments.

A summary of the outer bank circulation cell simulation results is presented in Table 2.

Table 2. Summary of outer bank cell appearance in selected simulations.

Case	Wall model	Interface model	Outer bank cell
LES	LES	Symmetry plane	Yes
DES MULES	RANS	MULES governed	Yes
DES rigid lid	RANS	Symmetry plane	No

4 CONCLUSIONS

One important takeaway from this comparison is the inability of the presented DES rigid lid models to produce the outer bank cells. Given that the above DES rigid lid models cannot produce the outer bank cell but the otherwise equivalent DES MULES and LES models do produce the outer bank cell, one can conclude that the k-omega model can stifle the outer bank cell development, even when applied on only a small boundary region.

The outer bank cell is driven by Reynolds Stress anisotropy, which is not well captured by k-omega turbulence closure. The above results suggest that the Reynolds Stress anisotropy specifically at the air-water interface is necessary for the production of an outer bank cell.

In order to produce the outer bank cell in the geometry studied, one has the choice of pure LES models or DES combined with MULES interface modelling. Both models are sufficient to produce the outer bank cell, and therefore the choice between them should rely on other project requirements. LES models generally require finer grid resolution at boundaries than DES models, and can be difficult to implement over some boundaries. MULES models require additional mesh above the water surface in order to simulate the air directly. They also have an additional step for the alpha advection at each time step, which can be computationally demanding. In this particular case the MULES simulations took more time to complete than the LES equivalent. However, in many cases the requirement of simulating the outer bank cell easily justifies the increased computational demands of either model.

In general, this study should serve as an example that DES rigid lid models are not guaranteed to produce the outer bank cell even when equivalent LES models have been shown to do so. The success of a DES model is highly dependent on the specific model used and the geometry under study.

REFERENCES

Bridge, J.S. 1992. A revised model for water flow, sediment transport, bed topography and grain size sorting in natural river bends. *Water Resources Research* 28(4):999-1013

Booij, R. 2003. Measurements and large eddy simulations of the flows in some curved flumes. *Journal of Turbulence* 4

Constantinescu, G., Koken, M., & Zeng, J. 2010. The structure of turbulent flow in an open channel bend of strong curvature with deformed bed: Insight provided by detached eddy simulation. *Water Resources Research* 47(5)

Kashyap, S., Constantinescu, G., Rennie, C. D., Post, G. C., & Townsend, R. D. 2012. *Journal of Hydraulic Engineering* 138:1045-1060

Schreiner H. K., Rennie, C. D., & Mohammadian, A. 2018. Trajectory of a jet in crossflow in a channel bend. *Environmental Fluid Mechanics* 18:1301-1319

Van Balen, W., Blanckaert, K., & Uijttewaal, W. 2010 Analysis of the role of turbulence in curved open channel flow at different water depths by means of experiments, LES and RANS. *Journal of Turbulence* 11(1)

Van Balen, W., Uijttewaal, W., Blanckaert, K. 2010. Large eddy simulation of a curved open-channel flow over topography. *Physics of Fluids* 22(7)

Appendix E

OpenFOAM files

system/controldict

```
/*---------------------------------*- C++ -*----------------------------------*\
| =========                 |                                                 |
| \\      /  F ield         | OpenFOAM: The Open Source CFD Toolbox           |
|  \\    /   O peration     | Version:  2.1.0                                 |
|   \\  /    A nd           | Web:      www.OpenFOAM.org                      |
|    \\/     M anipulation  |                                                 |
\*---------------------------------------------------------------------------*/
FoamFile
{
version     2.0;
format      ascii;
class       dictionary;
location    "system";
object      controlDict;
}
// * * * * * * * * * * * * * * * * * * * * * * * * * * * * * * * * * * * * * //

application     pisoFoam;

startFrom       latestTime;

startTime       0;

stopAt          endTime;

endTime        190;
```

```
deltaT          0.001;

writeControl    runTime;

writeInterval   0.5;

purgeWrite      0;

writeFormat     ascii;

writePrecision  6;

writeCompression uncompressed;

timeFormat      general;

timePrecision   6;

runTimeModifiable yes;

adjustTimeStep  off;

maxCo           1;
maxDeltaT       1;
functions
{
#includeFunc yPlus
#includeFunc Q
#includeFunc R
turbulenceFields1
{
// Mandatory entries (unmodifiable)
type            turbulenceFields;
libs           ("libsolverFunctionObjects.so");
// Mandatory entries (runtime modifiable)
// Either field or fields entries
field           epsilon;
executeControl      writeTime;
executeInterval     1;
writeControl        writeTime;
writeInterval       1;
}
```

```
Tracer
{
type    scalarTransport;
libs ("libutilityFunctionObjects.so");
outputControl outputTime;
active         true;
autoSchemes    false;
nCorr          0;
resetOnStartUp false;
fvOptions
{

}
schemesField    U;
}

}
// ************************************************************************* //
```

system/fvSchemes

```
/*--------------------------------*- C++ -*----------------------------------*\
=========                 |
\\      /  F ield         | OpenFOAM: The Open Source CFD Toolbox
\\    /   O peration     | Website:  https://openfoam.org
\\  /    A nd           | Version:  6
\\/     M anipulation  |
\*---------------------------------------------------------------------------*/
FoamFile
{
version     2.0;
format      ascii;
class       dictionary;
location    "system";
object      fvSchemes;
}
// * * * * * * * * * * * * * * * * * * * * * * * * * * * * * * * * * * * * * //

ddtSchemes
{
default         backward;
```

```
}

gradSchemes
{
default         Gauss linear;
}

divSchemes
{
default         none;
div(phi,U)      Gauss LUST grad(U);
div(phi,k)      Gauss limitedLinear 1;
div(phi,B)      Gauss limitedLinear 1;
div(phi,nuTilda) Gauss limitedLinear 1;
div(B)          Gauss linear;
div((nuEff*dev2(T(grad(U))))) Gauss linear;
}

laplacianSchemes
{
default         Gauss linear corrected;
}

interpolationSchemes
{
default         linear;
}

snGradSchemes
{
default         corrected;
}


// ************************************************************************* //
```

system/fvSolution

```
/*--------------------------------*- C++ -*----------------------------------*\
=========                 |
\\      /  F ield         | OpenFOAM: The Open Source CFD Toolbox
\\    /   O peration     | Website:  https://openfoam.org
```

```
\\  /    A nd           | Version:  6
\\/     M anipulation  |
\*---------------------------------------------------------------------------*/
FoamFile
{
version     2.0;
format      ascii;
class       dictionary;
location    "system";
object      fvSolution;
}
// * * * * * * * * * * * * * * * * * * * * * * * * * * * * * * * * * * * * * //

solvers
{
p
{
solver          GAMG;
tolerance       1e-07;
relTol          0.1;
smoother        GaussSeidel;
}

pFinal
{
$p;
smoother        DICGaussSeidel;
tolerance       1e-6;
relTol          0;
};

"(U|k|B|nuTilda)"
{
solver          smoothSolver;
smoother        GaussSeidel;
tolerance       1e-05;
relTol          0;
}
}

PISO
{
```

```
nCorrectors     2;
nNonOrthogonalCorrectors 0;
}


// ************************************************************************* //
```

system/parameters

```
/*--------------------------------*- C++ -*----------------------------------*\
=========                 |
\\      /  F ield         | OpenFOAM: The Open Source CFD Toolbox
\\    /   O peration     | Website:  https://openfoam.org
\\  /    A nd           | Version:  6
\\/     M anipulation  |
\*---------------------------------------------------------------------------*/

RadiusRatio 1.5;
h 0.05;
baseRefinement 2;

ztop 0.12;
L 20;
Lz #calc "2*(2*std::floor((0.06/0.2*$L)/2)+1)";
// ************************************************************************* //
```

system/blockMeshDict

```
/*--------------------------------*- C++ -*----------------------------------*\
| =========                 |                                                 |
| \\      /  F ield         | OpenFOAM: The Open Source CFD Toolbox           |
|  \\    /   O peration     | Version:  2.1.0                                 |
|   \\  /    A nd           | Web:      www.OpenFOAM.org                      |
|    \\/     M anipulation  |                                                 |
\*---------------------------------------------------------------------------*/
FoamFile
{
version     2.0;
format      ascii;
class       dictionary;
object      blockMeshDict;
```

```
}
// * * * * * * * * * * * * * * * * * * * * * * * * * * * * * * * * * * * * * //
#include "parameters"
convertToMeters 1;

i 1; //Divisions in jet entrance box
BendRB $RadiusRatio; //ratio of bend radius to cross channel width

InR #calc "$BendRB*0.2-0.1"; //Radius of inner bank
negInR #calc "-($BendRB*0.2-0.1)"; //negative radius of inner bank
OutR #calc "$BendRB*0.2+0.1"; //Radius of outer bank
negOutR #calc "-($BendRB*0.2+0.1)"; //Radius of outer bank

j #calc "$L-$i"; //Coarse divisions cross stream from jet entrance box to inner bank
mid #calc "$InR+0.2*$j/$L"; //Radius to jet entrance box
negmid #calc "-$InR-0.2*$j/$L"; //ditto but negative

Pi 3.1415926535; //Pi
Insin45 #calc "$InR*sin($Pi/4)"; //x or y coordinate of inner bank at end of bend
Outsin45 #calc "$OutR*sin($Pi/4)"; //x or y coordinate of outer bank at end of bend
xInR #calc "($InR-0.5)*sin($Pi/4)"; //x coordinate of inner bank at end of flume
xOutR #calc "($OutR-0.5)*sin($Pi/4)"; //x coordinate of outer bank at end of flume
yInR #calc "($InR+0.5)*sin($Pi/4)"; //y coordinate of inner bank at end of flume
yOutR #calc "($OutR+0.5)*sin($Pi/4)"; //y coordinate of outer bank at end of flume

r 0.002381; //jet nozzle radius
x0 -0.438; //jet nozzle x coordinate
x1 #calc "$x0-0.2*$i/(2*$L)"; //x coordinate at beginning of jet entrance block
x2 #calc "$x0+0.2*$i/(2*$L)"; //x coordinate at end of jet entrance block
x0plus #calc "$x0+$r";
x0M_{pt}us #calc "$x0-$r";
z0 0.03; //jet nozzle z coordinate
z0plus #calc "$z0+0.79*$r";//$r*sin($Pi/4)";
z0M_{pt}us #calc "$z0-0.79*$r";//$r*sin($Pi/4)";
z1 #calc "max($z0-$ztop/2*$i/$Lz,0)"; //z coordinate of bottom of jet entrance box
z2 #calc "$z1+$ztop*$i/$Lz"; //z coordinate of top of jet entrance box
jdown #calc "max(std::floor(($z0/$ztop)*$Lz-$i/2),0)"; //coarse vertical divisions bel
jup #calc "$Lz-$i-$jdown"; //coarse vertical divisions above jet boxcrest
yprot #calc "2*$r-$OutR"; //y coordinate of protrusion within jet box
yjin #calc "$negOutR-0.05";
xent #calc "std::ceil(9.82*$L-$i/2)"; //streamwise divisions in flume entrance to jet
xent2 #calc "std::floor(2.19*$L-$i/2)"; //streamwise divisions in flume entrance after
```

```
xbend #calc "std::floor(2.356*$BendRB*$L)"; //streamwise divisions in bend
xexit #calc "std::floor(2.5*$L)"; //streamwise divisions in exit
cellratio #calc "40*$i/$L"; //
invcellratio #calc "0.025*$L/$i"; //at weir
layer_cell_absolute 2.0;
b 3;
layer_portionZ #calc "1/($Lz+0.0)";
layer_cellsZ #calc "($layer_cell_absolute+1)/($Lz+$layer_cell_absolute)";
layer_portionj #calc "1/($jdown+0.0)";
layer_cellsj #calc "($layer_cell_absolute+1)/($jdown+$layer_cell_absolute)";

vertices
(
($x0M_{pt}us $yjin $z0M_{pt}us) //0
($x0M_{pt}us $yjin $z0plus) //1
($x0plus $yjin $z0plus) //2
($x0plus $yjin $z0M_{pt}us) //3
($x0M_{pt}us $negOutR $z0M_{pt}us) //4
($x0M_{pt}us $negOutR $z0plus) //5
($x0plus $negOutR $z0plus) //6
($x0plus $negOutR $z0M_{pt}us) //7
($x0M_{pt}us $yprot $z0M_{pt}us) //8
($x0M_{pt}us $yprot $z0plus) //9
($x0plus $yprot $z0plus) //10
($x0plus $yprot $z0M_{pt}us) //11
($x1 $negOutR $z2) //12
($x2 $negOutR $z2) //13
($x2 $negOutR $z1) //14
($x1 $negOutR $z1) //15
($x1 $negmid $z2) //16
($x2 $negmid $z2) //17
($x2 $negmid $z1) //18
($x1 $negmid $z1) //19
($x1 $negInR $z2) //20
($x2 $negInR $z2) //21
($x2 $negInR $z1) //22
($x1 $negInR $z1) //23
($x1 $negOutR $ztop) //24
($x2 $negOutR $ztop) //25
($x1 $negmid $ztop) //26
($x2 $negmid $ztop) //27
($x1 $negInR $ztop) //28
```

```
($x2 $negInR $ztop) //29
($x1 $negOutR 0) //30
($x2 $negOutR 0) //31
($x1 $negmid 0) //32
($x2 $negmid 0) //33
($x1 $negInR 0) //34
($x2 $negInR 0) //35
(-2.402 $negOutR 0) //36
(-2.402 $negInR 0) //37
($x1 $negInR 0) //38
($x1 $negOutR 0) //39
(-2.402 $negOutR $ztop) //40
(-2.402 $negInR $ztop) //41
($x1 $negInR $ztop) //42
($x1 $negOutR $ztop) //43
($x2 $negOutR 0) //44
($x2 $negInR 0) //45
(0 $negInR 0) //46
(0 $negOutR 0) //47
($x2 $negOutR $ztop) //48
($x2 $negInR $ztop) //49
(0 $negInR $ztop) //50
(0 $negOutR $ztop) //51
($Outsin45 $Outsin45 0) //52
($Insin45 $Insin45 0) //53
($Outsin45 $Outsin45 $ztop) //54
($Insin45 $Insin45 $ztop) //55
($Outsin45 $Outsin45 0) //56
($Insin45 $Insin45 0) //57
($xInR $yInR 0) //58
($xOutR $yOutR 0) //59
($Outsin45 $Outsin45 $weirApprx) //60
($Insin45 $Insin45 $weirApprx) //61
($xInR $yInR $weirApprx)//$weirHeight) //62
($xOutR $yOutR $weirApprx)//$weirHeight) //63
($Outsin45 $Outsin45 $ztop) //64
($Insin45 $Insin45 $ztop) //65
($xInR $yInR $ztop) //66
($xOutR $yOutR $ztop) //67
);

edges
```

```
(
arc 51 54 ($OutR 0 $ztop)
arc 50 55 ($InR 0 $ztop)
arc 47 52 ($OutR 0 0)
arc 46 53 ($InR 0 0)
);

blocks
(
hex (0 3 7 4 1 2 6 5) ($i #calc "std::floor(0.025*$i/$r)" $i) simpleGrading (1 1 1)
// jet inlet
hex (4 7 11 8 5 6 10 9) ($i $i $i) simpleGrading (1 1 1) //jet protrusion
hex (8 11 18 19 9 10 17 16) ($i 1 $i) simpleGrading (1 1 1) //nozzle box 0
hex (5 6 10 9 12 13 17 16) ($i $i 1) simpleGrading (1 1 1) //nozzle box 1
hex (7 14 18 11 6 13 17 10) (1 $i $i) simpleGrading (1 1 1) //nozzle box 2
hex (15 14 18 19 4 7 11 8) ($i $i 1) simpleGrading (1 1 1) //nozzle box 3
hex (15 4 8 19 12 5 9 16) (1 $i $i) simpleGrading (1 1 1) //nozzle box 4
hex (19 18 22 23 16 17 21 20) ($i $j $i) simpleGrading (1 1 1) //across from jet nozzl
hex (30 31 33 32 15 14 18 19) ($i $i #calc"$jdown+$layer_cell_absolute") simpleGrading
//below jet nozzle 0
hex (32 33 35 34 19 18 22 23) ($i $j #calc"$jdown+$layer_cell_absolute") simpleGrading
//below jet nozzle 1
hex (12 13 17 16 24 25 27 26) ($i $i $jup) simpleGrading (1 1 1) //above jet nozzle 0
hex (16 17 21 20 26 27 29 28) ($i $j $jup) simpleGrading (1 1 1) //above jet nozzle 1
hex (36 39 38 37 40 43 42 41) ($xent $L #calc"$Lz+$layer_cell_absolute") simpleGrading
//entrance
hex (44 47 46 45 48 51 50 49) ($xent2 $L #calc"$Lz+$layer_cell_absolute") simpleGradin
//downstream entrance
hex (47 52 53 46 51 54 55 50) ($xbend $L #calc"$Lz+$layer_cell_absolute") simpleGradin
//bend
hex (52 59 58 53 54 67 66 55) ($xexit $L #calc"$Lz+$layer_cell_absolute") simpleGradin
//outlet no weir
);

boundary
(
inlet
{
type mappedPatch;
offset (0.5 0 0);
sampleMode nearestCell;
samplePatch none;
```

```
faces
(
(36 37 41 40)
);
}
outlet
{
type patch;
faces
(
(66 67 59 58)
);
}
weir
{
type wall;
faces
(
);
}
jet
{
type patch;
faces
(
(0 3 2 1)
);
}
jetWall
{
type wall;
faces
(
(1 2 6 5)
(0 4 7 3)
(0 1 5 4)
(2 3 7 6)
);
}
lowerWall
{
type wall;
```

```
faces
(
(36 37 38 39)
(30 32 33 31)
(32 34 35 33)
(44 45 46 47)
(47 46 53 52)
(53 58 59 52)
);
}
sideWall
{
type wall;
faces
(
(36 39 43 40)
(30 31 14 15)
(15 14 7 4)
(7 14 13 6)
(5 6 13 12)
(15 4 5 12)
(12 13 25 24)
(44 47 51 48)
(47 52 54 51)
(52 59 67 54)
(58 53 55 66)
(46 50 55 53)
(46 45 49 50)
(35 34 23 22)
(22 23 20 21)
(21 20 28 29)
(38 37 41 42)
);
}

top
{
type symmetryPlane;
faces
(
(41 40 43 42)
(26 24 25 27)
```

```
(28 26 27 29)
(49 48 51 50)
(50 51 54 55)
(55 54 67 66)
);
}
merge1a
{
type empty;
faces
(
(12 16 19 15)
(24 26 16 12)
(26 28 20 16)
(16 20 23 19)
(15 19 32 30)
(19 23 34 32)
);
}
merge1b
{
type empty;
faces
(
(43 42 38 39)
);
}
merge2a
{
type empty;
faces
(
(44 45 49 48)
);
}
merge2b
{
type empty;
faces
(
(31 33 18 14)
(33 35 22 18)
```

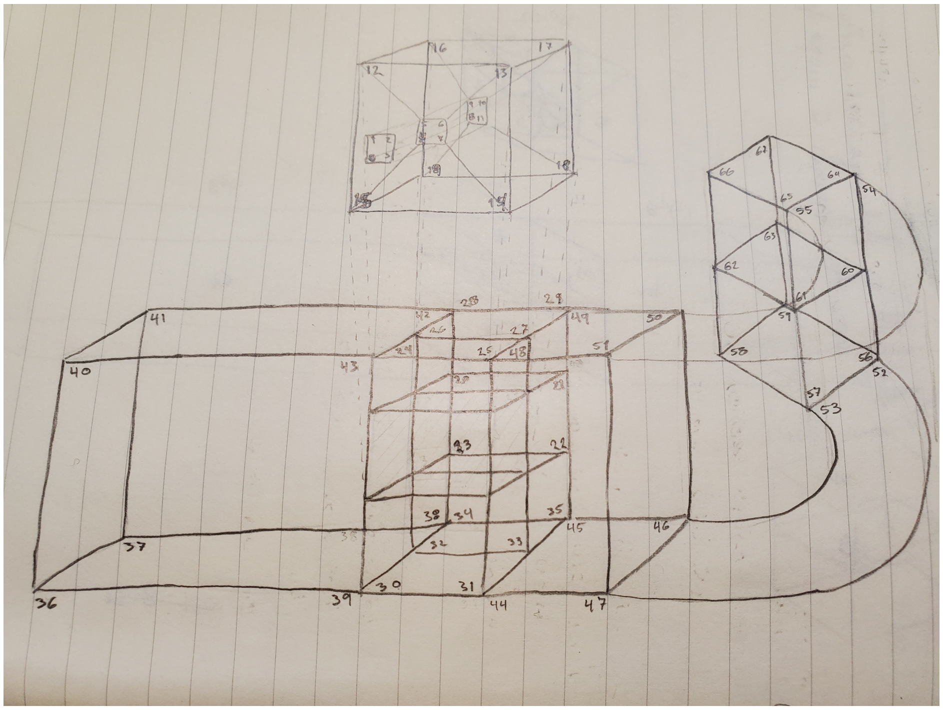

Figure E.1: Diagram of points in blockmeshDict file

```
(14 18 17 13)
(18 22 21 17)
(13 17 27 25)
(17 21 29 27)
);
}
);

mergePatchPairs
(
(merge1a merge1b)
(merge2a merge2b)
);

// ************************************************************************* //
```

system/snappyHexMeshDict

```
/*--------------------------------*- C++ -*----------------------------------*\
| =========                 |                                                 |
```

```
| \\      /  F ield         | OpenFOAM: The Open Source CFD Toolbox           |
|  \\    /   O peration     | Version:  2.1.0                                 |
|   \\  /    A nd           | Web:      www.OpenFOAM.org                      |
|    \\/     M anipulation  |                                                 |
\*---------------------------------------------------------------------------*/
FoamFile
{
version     2.0;
format      ascii;
class       dictionary;
object      autoHexMeshDict;
}
// * * * * * * * * * * * * * * * * * * * * * * * * * * * * * * * * * * * * * //

#include "parameters"

BendRB $RadiusRatio;
OutR #calc "$BendRB*0.2+0.1";
negOutR #calc "0-$OutR";
yjin #calc "$negOutR-0.05";
Pi 3.1415926535;
BendEnd #calc "($OutR-0.1)*sin($Pi/4)";

castellatedMesh true;
snap  true;
addLayers  true;
mergeTolerance 1e-06;

geometry
{
EntranceBox
{
type searchableBox;
M_{pt} (-3 $yjin 0);
max ($OutR 0 0.12);
}

ExitBox
{
type searchableBox;
M_{pt} (-3 0 0);
max ($OutR #calc "$OutR+0.35" 0.12);//
```

```
}

Cylinder
{
type searchableCylinder;
point1 ($BendEnd $BendEnd 0.06);
point2 (#calc "2*$BendEnd" 0 0.06);//
radius 0.2;
}
upperWall
{
type searchablePlane;
planeType       pointAndNormal;

pointAndNormalDict
{
basePoint       (0 0 $h);
normal          (0 0 1);
}
}

}

castellatedMeshControls
{
//Refinement parameters
maxLocalCells 20000000;//max cells on one processor
maxGlobalCells 20000000;//including outside flume
M_{pt}RefinementCells 1;//stops iteration when only a few cells refined
nCellsBetweenLevels 1;//higher number = gradual mesh changes
resolveFeatureAngle 5;
allowFreeStandingZoneFaces true;
refinementSurfaces
{
upperWall
{
level (0 0);
patchInfo
{
type patch;
}
}
```

```
}
features
(

);
//regionrefinement
refinementRegions
{
EntranceBox
{
mode inside;
levels (($baseRefinement $baseRefinement));
}
ExitBox
{
mode inside;
levels ((#calc"$baseRefinement" #calc"$baseRefinement"));
}
Cylinder
{
mode inside;
levels (($baseRefinement $baseRefinement));
}
}

//MeshSelection
locationInMesh (-0.438 #calc "$negOutR+0.01" 0.03);
}

snapControls
{
nSmoothPatch 0;//Number of patch smoothing iterations before finding correspondence to
tolerance 4;//relative distance to snap to edge, in local edge lengths
nSolveIter 0;//Number of mesh displacement relaxation iterations
nRelaxIter 5;
nFeatureSnapIter 0; //number of morph iterations within snapping step
implicitFeatureSnap false;
explicitFeatureSnap false;
}

addLayersControls
{
```

```
mergeFaces true;
expansionRatio 1.5;//growth factor between layers
relativeSizes true;
firstLayerThickness 1.2;
M_{pt}Thickness 0.00001;
layers
{
sideWall
{
expansionRatio 1.2;
nSurfaceLayers 4;
firstLayerThickness 2;
}
jetWall
{
nSurfaceLayers 3;
firstLayerThickness 0.3;
expansionRatio 1.5;
}
}
featureAngle 120;
nGrow 0;
maxFaceThicknessRatio 0.5;
nSmoothSurfaceNormals 0;
nSmoothThickness 0;
M_{pt}MedianAxisAngle 0;
maxThicknessToMedialRatio 3;
nSmoothNormals 3;
nRelaxIter 5;
nBufferCellsNoExtrude 0;
nLayerIter 50;

}

meshQualityControls
{
maxNonOrtho 70;
M_{pt}Vol 1.00E-13;
M_{pt}TetQuality 1e-15;
maxConcave 80;
maxInternalSkewness 4;
maxBoundarySkewness 20;
```

```
M_{pt}FaceWeight 0.05;
M_{pt}VolRatio 0.01;
M_{pt}Twist 0.02;
M_{pt}DeterM_{pt}ant 0.001;
M_{pt}Area -1;
M_{pt}TriangleTwist -1;
M_{pt}Flatness 0.5;
nSmoothScale 4;
errorReduction 0.75;
}
```

constant/g

```
/*--------------------------------*- C++ -*----------------------------------*\
| =========                 |                                                 |
| \\      /  F ield         | OpenFOAM: The Open Source CFD Toolbox           |
|  \\    /   O peration     | Version:  2.1.0                                 |
|   \\  /    A nd           | Web:      www.OpenFOAM.org                      |
|    \\/     M anipulation  |                                                 |
\*---------------------------------------------------------------------------*/
FoamFile
{
version     2.0;
format      ascii;
class       uniformDimensionedVectorField;
location    "constant";
object      g;
}
// * * * * * * * * * * * * * * * * * * * * * * * * * * * * * * * * * * * * * //

dimensions      [0 1 -2 0 0 0 0];
value           (0  0 -9.81);


// ************************************************************************* //
```

constant/transportProperties

```
/*--------------------------------*- C++ -*----------------------------------*\
| =========                 |                                                 |
| \\      /  F ield         | OpenFOAM: The Open Source CFD Toolbox           |
```

```
|  \\    /   O peration     | Version:  2.1.0                                 |
|   \\  /    A nd           | Web:      www.OpenFOAM.org                      |
|    \\/     M anipulation  |                                                 |
\*---------------------------------------------------------------------------*/
FoamFile
{
version     2.0;
format      ascii;
class       dictionary;
location    "constant";
object      transportProperties;
}
// * * * * * * * * * * * * * * * * * * * * * * * * * * * * * * * * * * * * * //

transportModel Newtonian;
nu              [0 2 -1 0 0 0 0] 1e-06;
rho             [1 -3 0 0 0 0 0] 1000;

//sigma           [1 0 -2 0 0 0 0] 0.07;
// ************************************************************************* //
```

constant/turbulenceProperties

```
/*--------------------------------*- C++ -*----------------------------------*\
| =========                 |                                                 |
| \\      /  F ield         | OpenFOAM: The Open Source CFD Toolbox           |
|  \\    /   O peration     | Version:  2.1.0                                 |
|   \\  /    A nd           | Web:      www.OpenFOAM.org                      |
|    \\/     M anipulation  |                                                 |
\*---------------------------------------------------------------------------*/
FoamFile
{
version     2.0;
format      ascii;
class       dictionary;
location    "constant";
object      turbulenceProperties;
}
// * * * * * * * * * * * * * * *  * * * * * * * * * * * * * * * * * * * * * //

simulationType LES;
```

```
LES
{
LESModel dynamicKEqn;

turbulence on;

printCoeffs on;

delta cubeRootVol;

dynamicKEqnCoeffs
{
filter simple;
}

cubeRootVolCoeffs
{
deltaCoeff      1;
}
}// ************************************************************************* //
```

0/k

```
/*--------------------------------*- C++ -*----------------------------------*\
| =========                 |                                                 |
| \\      /  F ield         | OpenFOAM: The Open Source CFD Toolbox           |
|  \\    /   O peration     | Version:  2.1.1                                 |
|   \\  /    A nd           | Web:      www.OpenFOAM.org                      |
|    \\/     M anipulation  |                                                 |
\*---------------------------------------------------------------------------*/
FoamFile
{
version     2.0;
format      ascii;
class       volScalarField;
location    "0";
object      k;
}
// * * * * * * * * * * * * * * * * * * * * * * * * * * * * * * * * * * * * * //

#include "include/initialConditions"
```

```
dimensions      [0 2 -2 0 0 0 0];

internalField   uniform 0;

boundaryField
{
inlet
{
type                mapped;
value               uniform 2e-05;
interpolationScheme cell;
setAverage          false;
average             2e-05;
}
outlet
{
type            inletOutlet;
inletValue      uniform 0;
value           uniform 0;
}
jet
{
type            fixedValue;
value           uniform $jetKE;
}
upperWall
{
type            symmetryPlane;
}
lowerWall
{
type            fixedValue;
value           uniform 0;
}
sideWall
{
type            fixedValue;
value           uniform 0;
}
jetWall
{
type            fixedValue;
```

```
value           uniform 0;
}

}

// ************************************************************************* //
```

0/nut

```
/*--------------------------------*- C++ -*----------------------------------*\
| =========                 |                                                 |
| \\      /  F ield         | OpenFOAM: The Open Source CFD Toolbox           |
|  \\    /   O peration     | Version:  2.1.1                                 |
|   \\  /    A nd           | Web:      www.OpenFOAM.org                      |
|    \\/     M anipulation  |                                                 |
\*---------------------------------------------------------------------------*/
FoamFile
{
version     2.0;
format      ascii;
class       volScalarField;
location    "0";
object      nut;
}
// * * * * * * * * * * * * * * * * * * * * * * * * * * * * * * * * * * * * * //

#include "include/initialConditions"

dimensions      [0 2 -1 0 0 0 0];

internalField   uniform 0;

boundaryField
{
inlet
{
type                zeroGradient;
}
outlet
{
type            zeroGradient;
}
```

```
jet
{
type zeroGradient;
}
upperWall
{
type            symmetryPlane;
}
lowerWall
{
type            zeroGradient;
}
sideWall
{
type            zeroGradient;
}
jetWall
{
type            zeroGradient;
}
}

// ************************************************************************* //
```

0/p

```
/*--------------------------------*- C++ -*----------------------------------*\
| =========                 |                                                 |
| \\      /  F ield         | OpenFOAM: The Open Source CFD Toolbox           |
|  \\    /   O peration     | Version:  4.1                                   |
|   \\  /    A nd           | Web:      www.OpenFOAM.org                      |
|    \\/     M anipulation  |                                                 |
\*---------------------------------------------------------------------------*/
FoamFile
{
version     2.0;
format      ascii;
class       volScalarField;
location    "0";
object      p;
}
// * * * * * * * * * * * * * * * * * * * * * * * * * * * * * * * * * * * * * //
```

```
#include "include/initialConditions"

dimensions      [0 2 -2 0 0 0 0];

internalField   uniform 0;

boundaryField
{
inlet
{
type            zeroGradient;
}
outlet
{
type            fixedValue;
value uniform 0;
}
jet
{
type            fixedFluxPressure;
}
upperWall
{
type symmetryPlane;
}
lowerWall
{
type zeroGradient;
}
sideWall
{
type  zeroGradient;
}
jetWall
{
type  zeroGradient;
}
}


// ************************************************************************* //
```

0/s

```
/*--------------------------------*- C++ -*----------------------------------*\
| =========                 |                                                 |
| \\      /  F ield         | OpenFOAM: The Open Source CFD Toolbox           |
|  \\    /   O peration     | Version:  2.3.x                                 |
|   \\  /    A nd           | Web:      www.OpenFOAM.org                      |
|    \\/     M anipulation  |                                                 |
\*---------------------------------------------------------------------------*/
FoamFile
{
version     2.0;
format      ascii;
class       volScalarField;
object      s;
}
// * * * * * * * * * * * * * * * * * * * * * * * * * * * * * * * * * * * * * //

dimensions      [0 0 0 0 0 0 0];

internalField   uniform 0;

boundaryField
{
inlet
{
type fixedValue;
value uniform 0;
}
outlet
{
type inletOutlet;
inletValue uniform 0;
value uniform 0;
}
jet
{
type fixedValue;
value uniform 1;
}
```

```
upperWall
{
type symmetryPlane;
}
lowerWall
{
type zeroGradient;
}
sideWall
{
type zeroGradient;
}
jetWall
{
type zeroGradient;
}
}

// ************************************************************************* //
```

0/U

```
/*--------------------------------*- C++ -*----------------------------------*\
| =========                 |                                                 |
| \\      /  F ield         | OpenFOAM: The Open Source CFD Toolbox           |
|  \\    /   O peration     | Version:  4.1                                   |
|   \\  /    A nd           | Web:      www.OpenFOAM.org                      |
|    \\/     M anipulation  |                                                 |
\*---------------------------------------------------------------------------*/
FoamFile
{
version     2.0;
format      ascii;
class       volVectorField;
location    "0";
object      U;
}
// * * * * * * * * * * * * * * * * * * * * * * * * * * * * * * * * * * * * * //

#include "include/initialConditions"

dimensions      [0 1 -1 0 0 0 0];
```

```
internalField   uniform (0 0 0);

boundaryField
{
inlet
{
type                mapped;
value               uniform ($velIn 0 0);
interpolationScheme cell;
setAverage          true;
average             ($velIn 0 0);
}
outlet
{
type inletOutlet;
inletValue uniform (0 0 0);
value uniform (0 0 0);
}
jet
{
type                flowRateInletVelocity;
volumetricFlowRate  constant $jetFlowRate;
}
upperWall
{
type symmetryPlane;
}
lowerWall
{
type            noSlip;
}
sideWall
{
type            noSlip;
}
jetWall
{
type            noSlip;
}
}
```

```
// ************************************************************************* //
```

0/include/initialConditions

```
/*--------------------------------*- C++ -*----------------------------------*\
=========                 |
\\      /  F ield         | OpenFOAM: The Open Source CFD Toolbox
\\    /   O peration     | Website:  https://openfoam.org
\\  /    A nd           | Version:  6
\\/     M anipulation  |
\*---------------------------------------------------------------------------*/

h      0.04;
inletFlowRate        0.000556;
velIn      0.07075;
pressure             0;
turbulentKE          0;
turbulentEpsilon     0;
turbulentNut 0;
jetFlowRate 0.0000022;
jetKE 0;
jetNut 0;

// ************************************************************************* //
```

Bibliography

Abduo, Shaimaa S., Ashraf M. Elmoustafa, and Mahmoud Samy Abdel Salam (2021). “Study of counteracting the secondary flow in open channel bends”. In: *Ain Shams Engineering Journal* (xxxx). ISSN: 20904479. DOI: `10.1016/j.asej.2021.01.011`.

Aghababaei, Mohammad, Amir Etemad-Shahidi, Ebrahim Jabbari, and Milad Taghipour (2017). “Estimation of Transverse Mixing Coefficient in Straight and Meandering Streams”. In: *Water Resources Management* 31.12, pp. 3809–3827. ISSN: 15731650. DOI: `10.1007/s11269-017-1708-4`.

Ajeel Fenjan, S., H. Bonakdari, A. Gholami, and A.A. Akhtari (2016). “Flow variables prediction using experimental, computational fluid dynamic and artificial neural network models in a sharp bend”. In: *International Journal of Engineering, Transactions A: Basics* 29.1, pp. 14–22. ISSN: 17281431. DOI: `10.5829/idosi.ije.2016.29.01a.03`.

Akan, Recep and Sıddıka Nilay Keskin (2019). “The effect of data size of ANFIS and MLR models on prediction of unconfined compression strength of clayey soils”. In: *SN Applied Sciences* 1.8, pp. 1–11. ISSN: 25233971. DOI: `10.1007/s42452-019-0883-8`.

Azamathulla, H. Md and Z. Ahmad (2012). “Gene-expression programming for transverse mixing coefficient”. In: *Journal of Hydrology* 434-435, pp. 142–148. ISSN: 00221694. DOI: `10.1016/j.jhydrol.2012.02.018`.

Baek, Kyong Oh and Il Won Seo (2013). “Empirical equation for transverse dispersion coefficient based on theoretical background in river bends”. In: *Environmental Fluid Mechanics* 13.5, pp. 465–477. ISSN: 15677419. DOI: `10.1007/s10652-013-9276-5`.

Bai, Ruonan, Dejun Zhu, Huai Chen, and Danxun Li (2019). “Laboratory Study of Secondary Flow in an Open Channel Bend by Using PIV”. In: *Water* 11.4, p. 659. ISSN: 2073-4441. DOI: `10.3390/w11040659`.

Bali, Meysam, Morteza Kolahdoozan, Amir Reza Zarrati, and Majid Jandaghi Alaee (2019). “Vertical velocity in rectangular channel bends: numerical study and development of a prediction formula”. In: *Journal of the Brazilian Society of Mechanical Sciences and Engineering* 41.11, pp. 1–14. ISSN: 18063691. DOI: `10.1007/s40430-019-1990-6`.

— (2020). “Transverse velocity in rectangular channel bends: numerical study and development of a prediction formula”. In: *Journal of the Brazilian Society of Mechanical Sciences and Engineering* 42.8, pp. 1–17. ISSN: 18063691. DOI: `10.1007/s40430-020-02483-3`.

Barros, Julio M. and Kenneth T. Christensen (Apr. 2014). “Observations of turbulent secondary flows in a rough-wall boundary layer”. In: *Journal of Fluid Mechanics* 748 (2), R1–R13. ISSN: 14697645. DOI: `10.1017/jfm.2014.218`.

Bathurst, J C, R D Hey, and C R Thorne (1979). “Secondary Flow and Shear Stress at River Bends”. eng. In: *Journal of hydraulic engineering (New York, N.Y.)* 105.10, pp. 1277–1295. ISSN: 0733-9429.

Bathurst, J.C., C.R. Thorne, and R.D. Hey (1977). “Direct measurement of secondary currents in river bends”. In: *Nature* 269, pp. 504 –506.

Ben Meftah, M., D. Malcangio, F. de Serio, and M. Mossa (2017). “Vertical dense jet in flowing current”. In: *Environmental Fluid Mechanics* 18.1, pp. 75–96. ISSN: 15731510. DOI: `10.1007/s10652-017-9515-2`.

Biringen, Sedat (1993). “Direct Numerical Simulation of Turbulent Flow in a Square Duct”. In: *Journal of Fluid Mechanics* 257, pp. 65–95. ISSN: 14697645. DOI: `10.1017/S002211209300299X`.

Blanckaert, K. (2009). “Saturation of curvature-induced secondary flow, energy losses, and turbulence in sharp open-channel bends: Laboratory experiments, analysis, and modeling”. In: *Journal of Geophysical Research: Solid Earth* 114.3, pp. 1–23. ISSN: 21699356. DOI: `10.1029/2008JF001137`.

— (2010). “Topographic steering, flow recirculation, velocity redistribution, and bed topography in sharp meander bends”. In: *Water Resources Research* 46.9, pp. 1–23. ISSN: 00431397. DOI: `10.1029/2009WR008303`.

— (2015). “Flow separation at convex banks in open channels”. In: *Journal of Fluid Mechanics* 779, pp. 432–467. ISSN: 14697645. DOI: `10.1017/jfm.2015.397`.

Blanckaert, K. and H. J. de Vriend (2003). “Nonlinear modeling of mean flow redistribution in curved open channels”. In: *Water Resources Research* 39.12, n/a–n/a. ISSN: 00431397. DOI: `10.1029/2003WR002068`.

— (2005). “Turbulence structure in sharp open-channel bends”. In: *Journal of Fluid Mechanics* 536, pp. 27–48. ISSN: 0022-1120. DOI: `10.1017/S0022112005004787`.

Blanckaert, Koen (2003). “Flow and Turbulence in Sharp Open-Channel Bends”. PhD thesis.

Blanckaert, Koen and Walter H Graf (2001). “Mean Flow and Turbulence in Open-Channel Bend”. In: *Journal of Hydraulic Engineering* 10.October, pp. 835–847.

Blanckaert, Koen and Walter H. Graf (2004). “Momentum Transport in Sharp Open-Channel Bends”. In: *Journal of Hydraulic Engineering* 130.3, pp. 186–198. ISSN: 0733-9429. DOI: `10.1061/(ASCE)0733-9429(2004)130:3(186)`.

Blanckaert, Koen et al. (2013). “Flow separation at the inner (convex) and outer (concave) banks of constant-width and widening open-channel bends”. In: *Earth Surface Processes and Landforms* 38.7, pp. 696–716. ISSN: 01979337. DOI: `10.1002/esp.3324`.

Bolotin, A (1999). “Quantum Mechanical Approach to Fuzzy Logic Modelling”. In: 7177.01.

Booij, R. (2003). “Measurements and large eddy simulations of the flows in some curved flumes”. In: *Journal of Turbulence*, pp. 1–17. ISSN: 14685248. DOI: `10.1088/1468-5248/4/1/008`.

Booij, R and J Tukker (1996). “Development in Laser Techniques and Applications to Fluid Mechanics”. In: ed. by RJ Adrian, DFG Durão, MV Durst Fand Heitor, M Maeda, and JH Whitelaw. Springer Berlin Heidelberg. Chap. Three-Dimensional Laser-Doppler Measurements in a Curved Flume, pp. 98–114.

Boxall, J B and I Guymer (2003). “Analysis and Prediction of Transverse Mixing Coefficients in Natural Channels”. In: *Journal of Hydraulic Engineering* 129.2, pp. 129–139. ISSN: 07339429. DOI: `10.1061/(ASCE)0733-9429(2003)129:2(129)`.

Brand, Andreas, Christian Noss, Christian Dinkel, and Markus Holzner (2016). “High-resolution measurements of turbulent flow close to the sediment-water interface using a bistatic acoustic profiler”. In: *Journal of Atmospheric and Oceanic Technology* 33.4, pp. 769–788. ISSN: 15200426. DOI: `10.1175/JTECH-D-15-0152.1`.

Burchard, Hans (2008). “Turbulence spectra”. In: *Marine Turbulence* 0, pp. 38–51.

Cambonie, Tristan and Jean Luc Aider (2014). “Transition scenario of the round jet in crossflow topology at low velocity ratios”. In: *Physics of Fluids* 26.8. ISSN: 10897666. DOI: `10.1063/1.4891850`. arXiv: `1405.4777`.

Carr, Meredith L and Chris R Rehmann (2007). “Measuring the Dispersion Coefficient with Acoustic Doppler Current Profilers”. In: *J. Hydraul. Eng. ASCE* 133.8, pp. 977–982.

Celik, I. B., Z. N. Cehreli, and I. Yavuz (2005). “Index of resolution quality for large eddy simulations”. In: *Journal of Fluids Engineering, Transactions of the ASME* 127 (5), pp. 949–958. ISSN: 00982202. DOI: `10.1115/1.1990201`.

Chamani, R, N Rajaratnam, M K Beirami, and Shivaji V Sakhalkar (2011). “Redistribution of velocity and Bed-shear stress in straight and curved open channels by means of a bubble screen”. In: *Journal of Hydraulic Engineering* 134 (10), pp. 1532–1535. DOI: `10.1061/(ASCE)0733-9429(2008)134`.

Chang, Kuang-An and Edwin a. Cowen (2002). “Turbulent Prandtl Number in Neutrally Buoyant Turbulent Round Jet”. In: *Journal of Engineering Mechanics* 128.10, pp. 1082–1087. ISSN: 0733-9399. DOI: `Doi10.1061/(Asce)0733-9399(2002)128:10(1082)`.

Chang, Kuang-An, Y Ryu, and N Mori (2009). “Parameterization of Neutrally Buoyant Horizontal Round Jet in Wave Environment”. In: *Journal of Waterway, Port, Coastal, and Ocean Engineering* 135.3, pp. 100–107. ISSN: 0733-950X. DOI: `10.1061/(ASCE)0733-950X(2009)135:3(100)`.

City of Ottawa (n.d.). *Drinking water-Frequently asked questions*. URL: `\url{https://ottawa.ca/en/living-ottawa/drinking-water-stormwater-and-wastewater/drinking-water/drinking-water-frequently-asked-questions#section-e7f46105-3762-4411-a795-b215f94f6553}`.

Constantinescu, George, S. Kashyap, T. Tokyay, C. D. Rennie, and R. D. Townsend (2013a). “Hydrodynamic processes and sediment erosion mechanisms in an open channel bend of strong curvature with deformed bathymetry”. In: *Journal of Geophysical Research: Earth Surface* 118.4, pp. 2308–2324. ISSN: 21699011. DOI: `10.1002/2013JF002760`.

— (2013b). “Hydrodynamic processes and sediment erosion mechanisms in an open channel bend of strong curvature with deformed bathymetry”. In: *Journal of Geophysical Research: Earth Surface* 118.4, pp. 2308–2324. ISSN: 21699011. DOI: `10.1002/2013JF002760`.

Constantinescu, George, S. Kashyap, T. Tokyay, C.D. Rennie, and R D Townsend (2013c). “Hydrodynamic processes and sediment erosion mechanisms in an open channel bend of strong curvature with deformed bathymetry”. In: *Journal of Geophysical Research: Earth Surface* 118.4, pp. 2308–2324. ISSN: 21699011. DOI: `10.1002/2013JF002760`.

Constantinescu, George, Mete Koken, and Jie Zeng (2011). "The structure of turbulent flow in an open channel bend of strong curvature with deformed bed: Insight provided by detached eddy simulation". In: *Water Resources Research* 47.5. ISSN: 00431397. DOI: `10.1029/2010WR010114`.

de Vriend, H. J. (1977). "A Mathematical Model Of Steady Flow In Curved Shallow Channels". In: *Journal of Hydraulic Research* 15.1, pp. 37–54. ISSN: 0022-1686. DOI: `10.1080/00221687709499748`.

— (1981). "Velocity redistribution in curved rectangular channels". In: *Journal of Fluid Mechanics* 107.HY10, pp. 423–439. ISSN: 14697645. DOI: `10.1017/S0022112081001833`.

de Vriend, H. J. and H. J. Geldof (1983). "Main Flow Velocity in Short River Bends". In: *Journal of Hydraulic Engineering* 109.7, pp. 991–1011.

Dean, W.R. (1927). " Note on the motion of fluid in a curved pipe ". In: *The London, Edinburgh, and Dublin Philosophical Magazine and Journal of Science* 4.20, pp. 208–223. ISSN: 1941-5982. DOI: `10.1080/14786440708564324`.

— (1928). "The stream-line motion of fluid in a curved pipe (Second paper) ". In: *The London, Edinburgh, and Dublin Philosophical Magazine and Journal of Science* 5.30, pp. 673–695. ISSN: 1941-5982. DOI: `10.1080/14786440408564513`.

Dietrich, William E and J Dungan Smith (1983). "Influence of the Point Bar on Flow Through Curved Channels". In: 19.5, pp. 1173–1192. DOI: `10.1029/WR019i005p01173`.

Dow, Karen E, Peter M Steffler, and David Z Zhu (2009). "Case Study: Intermediate Field Mixing for a Bank Discharge in a Natural River". In: *Journal of Hydraulic Engineering* 135.1, pp. 1–12. ISSN: 0733-9429. DOI: `10.1061/(ASCE)0733-9429(2009)135:1(1)`.

Dugué, Violaine, Koen Blanckaert, Qiuwen Chen, and Anton J. Schleiss (2015). "Influencing flow patterns and bed morphology in open channels and rivers by means of an air-bubble screen". In: *Journal of Hydraulic Engineering* 141 (2), pp. 1–13. ISSN: 19437900. DOI: `10.1061/(ASCE)HY.1943-7900.0000946`.

Elhadi, N, A Harrington, I Hill, Y L Lau, and B G Krishnappan (1984). "River mixing-A state-of-the-art report". In.

Ester, Martin, Hans-Peter Kriegel, Jörg Sander, and Xiaowei Xu (1996). "A Density-Based Algorithm for Discovering Clusters in Large Spatial Databases with Noise". In: *Proceedings of the Second International Conference on Knowledge Discovery and Data Mining*. KDD'96. Portland, Oregon: AAAI Press, 226–231.

Fang, Xingjun, Zixuan Yang, Bing Chen Wang, Mark F. Tachie, and Donald J. Bergstrom (2017). "Large-eddy simulation of turbulent flow and structures in a square duct roughened with perpendicular and V-shaped ribs". In: *Physics of Fluids* 29.6. ISSN: 10897666. DOI: `10.1063/1.4985715`.

Farhadi, Alireza, Christine Sindelar, Michael Tritthart, Martin Glas, Koen Blanckaert, and Helmut Habersack (2018). "An investigation on the outer bank cell of secondary flow in channel bends". In: *Journal of Hydro-Environment Research* 18.September 2017, pp. 1–11. ISSN: 15706443. DOI: `10.1016/j.jher.2017.10.004`.

Fischer, B (1978). "On the tensor form of the bulk dispersion coefficient in a bounded skewed shear flow". In: 83.C5.

Fischer, Hugo B. (1969). "The effect of bends on dispersion in streams". In: *Water Resources Research* 5.2, pp. 496–506. ISSN: 19447973. DOI: `10.1029/WR005i002p00496`.

— (1972). "A Lagrangian Method For Predicting Pollutant Dispersion in Bolinas Lagoon, Marin County, California". In.

Fischer, Hugo B. and E. R. Holley (1971). "Analysis of the Use of Distorted Hydraulic Models for Dispersion Studies". In: *Water Resources Research* 7.1, pp. 46–51.

Foerst, Markus and Nils Rüther (2018). "Bank retreat and streambank morphology of a meandering river during summer and single flood events in Northern Norway". In: *Hydrology* 5.68. ISSN: 23065338. DOI: `10.3390/hydrology5040068`.

Garson, G. David (1991). "Interpreting Neural-Network Connection Weights". In: *AI Expert* 6.4, 46–51. ISSN: 0888-3785.

Germano, Massimo, Ugo Piomelli, Park Moin, and William H Cabot (1991). "A dynamic subgrid-scale eddy viscosity model". In: *Physics of Fluids* 3.7.

Gholami, Azadeh, Hossein Bonakdari, Amir Hossein Zaji, and Ali Akbar Akhtari (2015a). "Simulation of open channel bend characteristics using computational fluid dynamics and artificial neural networks". In: *Engineering Applications of Computational Fluid Mechanics* 9.1, pp. 355–369. ISSN: 1997003X. DOI: `10.1080/19942060.2015.1033808`.

— (2020). "A comparison of artificial intelligence-based classification techniques in predicting flow variables in sharp curved channels". In: *Engineering with Computers* 36, pp. 295–324. ISSN: 14355663. DOI: `10.1007/s00366-018-00697-7`.

Gholami, Azadeh, Hossein Bonakdari, Amir Hossein Zaji, Ali Akbar Akhtari, and Saeed Reza Khodashenas (2015b). "Predicting the velocity field in a 90 ° Open channel bend using a gene expression programming model". In: *Flow Measurement and Instrumentation* 46, pp. 189–192. ISSN: 09555986. DOI: `10.1016/j.flowmeasinst.2015.10.006`.

Gholami, Azadeh, Hossein Bonakdari, Amir Hossein Zaji, Salma Ajeel Fenjan, and Ali Akbar Akhtari (2016a). "Design of modified structure multi-layer perceptron networks based on decision trees for the prediction of flow parameters in 90 ° open-channel bends". In: *Engineering Applications of Computational Fluid Mechanics* 10.1, pp. 194–209. ISSN: 1997003X. DOI: `10.1080/19942060.2015.1128358`.

Gholami, Azadeh, Hossein Bonakdari, Amir Hossein Zaji, David G. Michelson, and Ali Akbar Akhtari (2016b). "Improving the performance of multi-layer perceptron and radial basis function models with a decision tree model to predict flow variables in a sharp 90 ° bend". In: *Applied Soft Computing Journal* 48, pp. 563–583. ISSN: 15684946. DOI: `10.1016/j.asoc.2016.07.035`.

Gopalan, Shridhar, Bruce M. Abraham, and Joseph Katz (2004). "The structure of a jet in cross flow at low velocity ratios". In: *Physics of Fluids* 16.6, pp. 2067–2087. ISSN: 10706631. DOI: `10.1063/1.1697397`.

Grace, Robert A. (2009). *Marine Outfall Construction*. American Society of Civil Engineers. ISBN: 9780784407417.

Graftieaux, L., M. Michard, and G. Nathalie (2001). "Combining PIV, POD and vortex identification algorithms for the study of unsteady turbulent swirling flows". In: *Measurement Science and Technology* 12 (9), pp. 1422–1429. ISSN: 09570233. DOI: `10.1088/0957-0233/12/9/307`.

Hajibehzad, Manoochehr Shokrian, Mahmood Shafai Bejestan, Vito Ferro, and Rahim Avarand (2022). “Mean flow, secondary currents and bed shear stress at a 180-degree laboratory bend with and without enhanced permeable groins as an Eco-friendly river structure”. In: *Journal of Hydro-Environment Research* 44.March 2021, pp. 12–22. ISSN: 15706443. DOI: `10.1016/j.jher.2022.07.004`.

Hersberger, Daniel S., Mário J. Franca, and Anton J. Schleiss (2016). “Wall-Roughness Effects on Flow and Scouring in Curved Channels with Gravel Beds”. In: *Journal of Hydraulic Engineering* 142.1, pp. 1–11. ISSN: 0733-9429. DOI: `10.1061/(asce)hy.1943-7900.0001039`.

Hill, Tim, Leorey Marquez, Marcus O’Connor, and William Remus (1994). “Artificial neural network models for forecasting and decision making”. In: *International Journal of Forecasting* 10.1, pp. 5–15. ISSN: 01692070. DOI: `10.1016/0169-2070(94)90045-0`. arXiv: `arXiv:1011.1669v3`.

Hodgson, J E, N Rajaratnam, and A K Moawad (1999). “Circular jets in crossflows of finite depth”. In: *Proceedings of the Institution of Civil Engineers: Water, Maritime, and Energy* 136.Mar. Pp. 35–42.

Huai, Wenxin, Haoran Shi, Zhonghua Yang, and Yuhong Zeng (2018). “Estimating the Transverse Mixing Coefficient in Laboratory Flumes and Natural Rivers”. In: *Water Air Soil Pollution*, 229:252. DOI: `10.1007/s11270-018-3893-zEstimating`.

Hunt, J C R, A A Wray, and P Moin (1988). “Eddies, streams, and convergence zones in turbulent flows”. In: *Center for Turbulence Research, Proceedings of the Summer Program*, pp. 193–208. ISBN: CTR-S88.

Iliescu, Traian and Paul Fischer (2004). “Backscatter in the rational LES model”. In: *Computers and Fluids* 33.5-6, pp. 783–790. ISSN: 00457930. DOI: `10.1016/j.compfluid.2003.06.011`.

Iyer, Prahladh S. and Krishnan Mahesh (2016). “A numerical study of shear layer characteristics of low-speed transverse jets”. In: *Journal of Fluid Mechanics* 790, pp. 275–307. ISSN: 0022-1120. DOI: `10.1017/jfm.2016.7`.

Jamieson, E C, G. C. Post, and C. D. Rennie (2010). “Spatial variability of three-dimensional Reynolds stresses in a developing channel bend”. In: *Earth Surface Processes and Landforms* 35.9, pp. 1029–1043. DOI: `10.1002/esp.1930`.

Jamieson, Elizabeth Clare (2011). “The role of vorticity , turbulence and three-dimensional flow structure on the development of scour”. PhD thesis. University of Ottawa. ISBN: 9780494983133.

Jeon, Tae Myoung, Kyong Oh Baek, and Il Won Seo (2007). “Development of an empirical equation for the transverse dispersion coefficient in natural streams”. In: *Environmental Fluid Mechanics* 7.4, pp. 317–329. ISSN: 15677419. DOI: `10.1007/s10652-007-9027-6`.

Jeong, Jinhee and Fazle Hussain (1995). “On the identification of a vortex”. In: *Journal of Fluid Mechanics* 285, pp. 69–94. ISSN: 00483893. DOI: `10.1007/BF02380836`.

Jirka, Gerhard H. and Robert L. Doneker (1992). “Hydrodynamic Classification of Submerged Single Port Discharges”. In: *Journal of Hydraulic Engineering,* 117.9, pp. 1095–1112.

Jones, Gilbert R., Jonathan D. Nash, Robert L. Doneker, and Gerhard H. Jirka (2007). “Buoyant Surface Discharges into Water Bodies . I : Flow Classification and Prediction Methodology”. In: *Journal of Hydraulic Engineering* 133.September, pp. 1010–1021. ISSN: 0733-9429. DOI: `10.1061/(ASCE)0733-9429(2007)133:9(1010)`.

Kashyap, S. (2012). “A 3-D Numerical Study of Flow, Coherent Structures, and Mechanisms Leading to Scour in a High Curvature 135 ° Channel Bend With and Without Submerged Groynes”. PhD thesis. University of Ottawa.

Kashyap, S., George Constantinescu, Colin D. Rennie, Gavin Charles Post, and R D Townsend (2012). “Influence of Channel Aspect Ratio and Curvature on Flow, Secondary Circulation, and Bed Shear Stress in a Rectangular Channel Bend”. In: *Journal of Hydraulic Engineering* December, pp. 1045–1060. ISSN: 07339429. DOI: `10.1061/(ASCE)HY.1943-7900.0000643.`.

Kawahara, Genta, Markus Uhlmann, and Lennaert Van Veen (2011). “The significance of simple invariant solutions in turbulent flows”. In: *Annual Review of Fluid Mechanics* 44, pp. 203–225. ISSN: 00664189. DOI: `10.1146/annurev-fluid-120710-101228`.

Kazemi, Mohammad Amin, Mary Pa, Mohammad Nasir Uddin, and Mashallah Rezakazemi (2023). “Adaptive neuro-fuzzy inference system based data interpolation for particle image velocimetry in fluid flow applications”. In: *Engineering Applications of Artificial Intelligence* 119.June 2022, p. 105723. ISSN: 09521976. DOI: `10.1016/j.engappai.2022.105723`.

Kemp, Stanley J., Patricia Zaradic, and Frank Hansen (2007). “An approach for determining relative input parameter importance and significance in artificial neural networks”. In: *Ecological Modelling* 204.3-4, pp. 326–334. ISSN: 03043800. DOI: `10.1016/j.ecolmodel.2007.01.009`.

Kim, Jun Song, Donghae Baek, and Inhwan Park (2020). “Evaluating the Impact of Turbulence Closure Models on Solute Transport Simulations in Meandering Open Channels”. In: *Water* 12.

Kim, Won-Wook and Suresh Menon (1995). “A new dynamic on-equation subgrid-scale model for large eddy simulations”. In: *American Institute of Aeronautics and Astronautics*. DOI: `https://doi.org/10.2514/6.1995-356`.

Lee, Myung Eun and Il Won Seo (2012). “Spatially Variable Dispersion Coefficients in Meandering Channels”. In: *Journal of Hydraulic Engineering* 139.February, p. 120831032340008. ISSN: 0733-9429. DOI: `10.1061/(ASCE)HY.1943-7900.0000669`.

Leeder, M. R. and P. H. Bridges (1975). “Flow separation in meander bends”. In: *Nature* 253, pp. 338–339. DOI: `https://doi.org/10.1038/253338a0`.

Li, Bingdong and Xinhua Zhang (Aug. 2022). “Evolution of outer bank cell in open-channel bends”. In: *Environmental Fluid Mechanics*. ISSN: 15731510. DOI: `10.1007/s10652-022-09865-2`.

Li, Yalin, Xikun Wang, Bo Zhou, Shouqi Yuan, and Soon Keat Tan (2017). “Dean instability and secondary flow structure in curved rectangular ducts”. In: *International Journal of Heat and Fluid Flow* 68.October 2018, pp. 189–202. ISSN: 0142727X. DOI: `10.1016/j.ijheatfluidflow.2017.10.011`.

Li, Zhi Wei, Wen Xin Huai, and Zhong Dong Qian (2012). “Study on the flow field and concentration characteristics of the multiple tandem jets in crossflow”. In: *Science China Technological Sciences* 55.10, pp. 2778–2788. ISSN: 16747321. DOI: `10.1007/s11431-012-4964-9`.

Lyman, F. A. (1990). “Vorticity production at a solid boundary”. In: *Applied Mechanics Reviews* 43 (8), pp. 157–158.

Malcangio, Daniela and Michele Mossa (2016). “A laboratory investigation into the influence of a rigid vegetation on the evolution of a round turbulent jet discharged within a cross flow”. In: *Journal of Environmental Management* 173, pp. 105–120. ISSN: 10958630. DOI: `10.1016/j.jenvman.2016.02.044`.

Markovich, Dmitriy M., Vladimir M. Dulin, Sergey S. Abdurakipov, Leonid A. Kozinkin, Mikhail P. Tokarev, and Kemal Hanjalić (2016). "Helical modes in low- and high-swirl jets measured by tomographic PIV". In: *Journal of Turbulence* 17.7, pp. 678–698. ISSN: 1468-5248. DOI: `10.1080/14685248.2016.1173697`.

MATLAB (2021). *MATLAB version 9.10.0.1602886 (R2021a)*. The Mathworks, Inc. Natick, Massachusetts.

Meyer, K. E., J. M. Pedersen, and O. Ozcan (2007). "A turbulent jet in crossflow analysed with proper orthogonal decomposition". In: *Journal of Fluid Mechanics* 583, pp. 199–227. DOI: `10.1017/S0022112007006143`.

Michaelis, Dirk, Douglas R. Neal, and Bernhard Wieneke (2016). "Peak-locking reduction for particle image velocimetry". In: *Measurement Science and Technology* 27.10. ISSN: 13616501. DOI: `10.1088/0957-0233/27/10/104005`.

Milani, Pedro M., David S. Ching, Andrew J. Banko, and John K. Eaton (2020). "Shear layer of inclined jets in crossflow studied with spectral proper orthogonal decomposition and spectral transfer entropy". In: *International Journal of Heat and Mass Transfer* 147, p. 118972. ISSN: 00179310. DOI: `10.1016/j.ijheatmasstransfer.2019.118972`.

Mittal, Kash L., ed. (2003). *Contact angle, wettability and adhesion. Volume 3*. eng. First edition. Boca Raton, FL: CRC Press, an imprint of Taylor and Francis. ISBN: 9780429088124.

Moncho-Esteve, Ignacio J., Frederik Folke, Manuel García-Villalba, and Guillermo Palau-Salvador (2017). "Influence of the secondary motions on pollutant mixing in a meandering open channel flow". In: *Environmental Fluid Mechanics* 17, pp. 695–714. ISSN: 15731510. DOI: `10.1007/s10652-017-9513-4`.

Montorfano, A., F. Piscaglia, and G. Ferrari (2013). "Inlet boundary conditions for incompressible LES: A comparative study". In: *Mathematical and Computer Modelling* 57 (7-8), pp. 1640–1647. ISSN: 08957177. DOI: `10.1016/j.mcm.2011.10.077`.

Morton, B. R. (1984). "The Generation and Decay of Vorticity". In: *Geophysical & Astrophysical Fluid Dynamics* 28 (3-4), pp. 277–308. ISSN: 10290419. DOI: `10.1080/03091928408230368`.

Muto, Y (1997). "Turbulent flow in two-stage meandering channels". PhD thesis. University of Bradford.

Nezu, I. and H. Nakagawa (1993). *Turbulence in open-channel flows*. IAHR. ISBN: 9054101180.

Nikitin, N. V., N. V. Popelenskaya, and A. Stroh (July 2021). "Prandtl's Secondary Flows of the Second Kind. Problems of Description, Prediction, and Simulation". In: *Fluid Dynamics* 56 (4), pp. 513–538. ISSN: 15738507. DOI: `10.1134/S0015462821040091`.

Nortek (2012). *Nortek Quick Guide to Vectrino Profiler*.

Odgaard, A Jacob (1986). "Meander Flow Model. I: Development". In: *Journal of Hydraulic Engineering* 112.12, pp. 1117–1135.

Ottevanger, W., K. Blanckaert, and W. S J Uijttewaal (2012). "Processes governing the flow redistribution in sharp river bends". In: 163-164, pp. 45–55. ISSN: 0169555X. DOI: `10.1016/j.geomorph.2011.04.049`.

Paik, Joongcheol and Fotis Sotiropoulos (2005). "Coherent structure dynamics upstream of a long rectangular block at the side of a large aspect ratio channel". In: *Physics of Fluids* 17.11, pp. 1–14. ISSN: 10706631. DOI: `10.1063/1.2130743`.

Park, Inhwan and Il Won Seo (2018). “Modeling non-Fickian pollutant mixing in open channel flows using two-dimensional particle dispersion model”. In: *Advances in Water Resources* 111.November 2017, pp. 105–120. ISSN: 03091708. DOI: `10.1016/j.advwatres.2017.10.035`.

Peng, Xinzai, Yiying He, Yijun Zhao, and Wenming Zhang (2022). “A novel pre-dilution, swirling jet diffuser to enhance effluent mixing: Hydrodynamics and dilution performance”. In: *Journal of Hydro-Environment Research* 45.September, pp. 1–14. ISSN: 15706443. DOI: `10.1016/j.jher.2022.08.002`.

Pilechi, A., A. Mohamadian, C. D. Rennie, and David Z. Zhu (2016). “Efficient Method for Coupling Field Data and Numerical Modeling for the Estimation of Transverse Mixing Coefficients in Meandering Rivers”. In: *ASCE Journal of Hydraulic Engineering* 142.July. ISSN: 0733-9429. DOI: `10.1061/(ASCE)HY.1943-7900`.

Pilechi, Abolghasem, Colin D. Rennie, Abdolmajid Mohammadian, and David Z. Zhu (2014). “In situ spatially distributed field measurements of transverse dispersion of a wastewater effluent in an extended natural meandering river”. In: *Journal of Hydraulic Research* 53.1, pp. 20–35. ISSN: 0022-1686. DOI: `10.1080/00221686.2014.950611`.

Pinelli, Alfredo, Markus Uhlmann, Atsushi Sekimoto, and Genta Kawahara (Feb. 2010). “Reynolds number dependence of mean flow structure in square duct turbulence”. In: *Journal of Fluid Mechanics* 644, pp. 107–122. ISSN: 14697645. DOI: `10.1017/S0022112009992242`.

Post, Gavin Charles GC (2007). “The Measurement of Reynolds Stresses in a Model River Bend using Acoustic Doppler Velocimeters”. PhD thesis. University of Ottawa. ISBN: 9780494492659.

Prandtl, Ludwig (1952). *Essentials of Fluid Mechanics*.

Pratte, B. D. and W. D. Baines (1967). “Profiles of the round turbulent jet in a cross flow”. In: *Journal of the Hydraulics Division, Proceedings of the American Society of Civil Engineers* 93.HY6, pp. 53–64.

Rajaratnam, N. and John K. Langat (1995). “Mixing Region of Circular Turbulent Wall Jets in Cross Flows”. In: *Journal of Hydraulic Engineering* 121.10, pp. 694–698.

Ramamurthy, A S, S S Han, and P M Biron (2013). “Three-Dimensional Simulation Parameters for 90 degrees Open Channel Bend Flows”. In: *Journal of Computing in Civil Engineering* 27.3, pp. 282–291. ISSN: 0887-3801. DOI: `Doi10.1061/(Asce)Cp.1943-5487.0000209`.

Rhee, Shin Hyung, Boris P. Makarov, H. Krishinan, and Vladimir Ivanov (2005). “Assessment of the volume of fluid method for free-surface wave flow”. In: *Journal of Marine Science and Technology* 10.4, pp. 173–180. ISSN: 09484280. DOI: `10.1007/s00773-005-0205-2`.

Rosovskii, I. L. (1961). *Flow of water in bends of open channels*. Jerusalem: Israel Program for Scientific translations.

Russell, P. and R. Vennell (2019). “High Resolution Observations of an Outer-Bank Cell of Secondary Circulation in a Natural River Bend”. In: *Journal of Hydraulic Engineering* 145.5, p. 04019012. ISSN: 19437900. DOI: `10.1061/(ASCE)HY.1943-7900.0001584`.

Rutherford, J. C. (1994). *River Mixing*. Chichester England ; New York : Wiley.

Schreiner, H. K., C. D. Rennie, and A. Mohammadian (2023). “Insights into secondary flow structure from clusters of instantaneous vortices”. In: *Environmental Fluid Mechanics*. ISSN: 15731510. DOI: `10.1007/s10652-022-09907-9`.

Schreiner, K., C. D. Rennie, and Abdolmajid Mohammadian (2018). “Trajectory of a jet in crossflow in a channel bend”. In: *Environmental Fluid Mechanics*.

Seo, Il Won, Hwang Jeong Choi, Young Do Kim, and Eun Jin Han (2016). “Analysis of Two-Dimensional Mixing in Natural Streams Based on Transient Tracer Tests”. In: *Journal of Hydraulic Engineering* 142.8. DOI: `10.1061/(ASCE)HY.1943-7900.0001118.`.

Seo, Il Won, Hong Sik Kim, Daeyoung Yu, and Dong Soo Kim (2001). “Performance of Tee Diffusers in Shallow Water with Crossflow”. In: *Journal of Hydraulic Engineering,* 127.1, pp. 53–61.

Seo, Il Won, Myung Eun Lee, and Kyong Oh Baek (2008). “2D Modeling of Heterogeneous Dispersion in Meandering Channels”. In: *Journal of Hydraulic Engineering* 134.2, pp. 196–204. ISSN: 0733-9429. DOI: `10.1061/(ASCE)0733-9429(2008)134:2(196)`.

Shamlo, Nima Bigdely (2005). “Matlab toolbox for high resolution vector field visualization with application in improving the understanding of crack propogation mechanisms”. San Diego State University.

Shao, Dongdong and Adrian Wing Keung Law (2011). “Boundary impingement and attachment of horizontal offset dense jets”. In: *Journal of Hydro-Environment Research* 5.1, pp. 15–24. ISSN: 15706443. DOI: `10.1016/j.jher.2010.11.003`.

Shiono, K. and Y. Muto (1998). “Complex flow mechanisms in compound meandering channels with overbank flow”. In: *Journal of Fluid Mechanics* 376, pp. 221–261. ISSN: 00221120. DOI: `10.1017/S0022112098002869`.

Smith, J. Dungan and S. R. Mclean (1984). “A Model for Flow in Meandering Streams”. In: *Water Resources Research* 20.9, pp. 1301–1315. ISSN: 19447973. DOI: `10.1029/WR020i009p01301`.

Smith, S. H. and M. Mungal (1998). “Mixing, structure and scaling of the jet in crossflow”. In: *Journal of Fluid Mechanics* 357. DOI: `10.1017/S0022112097007891`.

Stroh, A., K. Schäfer, B. Frohnapfel, and P. Forooghi (Feb. 2020). “Rearrangement of secondary flow over spanwise heterogeneous roughness”. In: *Journal of Fluid Mechanics* 885, R5. ISSN: 0022-1120. DOI: `10.1017/jfm.2019.1030`.

Tamoradi, Zeinab, Javad Ahadiyan, Mohsen Najarchi, Houshang Hasounizadeh, and Mohammad Mahdi Najafizadeh (2019). “Reducing bend scour using in-phase and out-of-phase hydraulic jets”. In: *Water Science and Technology: Water Supply* 19 (5), pp. 1446–1453. ISSN: 16070798. DOI: `10.2166/ws.2019.014`.

Terrington, S. J., K. Hourigan, and M. C. Thompson (2021). “The generation and diffusion of vorticity in three-dimensional flows: Lyman’s flux”. In: *Journal of Fluid Mechanics* 915. ISSN: 14697645. DOI: `10.1017/jfm.2021.179`.

Thomson, James (1877). “Experimental Demonstration in Respect to the Origin of Windings of Rivers in Alluvial Plains , and to the Mode of Flow of Water round Bends of Pipes”. In: *Proceedings of the Royal Society of London* 26.1877, pp. 356–357.

Thorne, C R, W Zevenbergen, J C Pitlickt, S Raist, J B Bradley, and P Y Julient (1985). “Direct measurement of secondary currents in a meandering sand-bed river”. In: *Nature* 315 (27), pp. 746–747.

Uhlmann, Markus, Genta Kawahara, and Alfredo Pinelli (Nov. 2010). “Traveling-waves consistent with turbulence-driven secondary flow in a square duct”. In: *Physics of Fluids* 22. DOI: `10.1063/1.3466661`.

Uhlmann, Markus, Alfredo Pinelli, Genta Kawahara, and Atsushi Sekimoto (Oct. 2007). “Marginally turbulent flow in a square duct”. In: *Journal of Fluid Mechanics* 588, pp. 153–162. ISSN: 14697645. DOI: `10.1017/S0022112007007604`.

Vaghefi, Mohammad, Kumars Mahmoodi, Saeed Setayeshi, and Maryam Akbari (2020). “Application of artificial neural networks to predict flow velocity in a 180° sharp bend with and without a spur dike”. In: *Soft Computing* 24.12, pp. 8805–8821. ISSN: 14337479. DOI: `10.1007/s00500-019-04413-5`.

van Balen, W., W. S J Uijttewaal, and K. Blanckaert (2010). “Large-eddy simulation of a curved open-channel flow over topography”. In: *Physics of Fluids* 22.7, pp. 1–18. ISSN: 10706631. DOI: `10.1063/1.3459152`.

van Balen, W., W. S.J. Uijttewaal, and K. Blanckaert (2009). “Large-eddy simulation of a mildly curved open-channel flow”. In: *Journal of Fluid Mechanics* 630, pp. 413–442. ISSN: 00221120. DOI: `10.1017/S0022112009007277`.

Vanderwel, C., A. Stroh, J. Kriegseis, B. Frohnapfel, and B. Ganapathisubramani (Mar. 2019). “The instantaneous structure of secondary flows in turbulent boundary layers”. In: *Journal of Fluid Mechanics* 862, pp. 845–870. ISSN: 14697645. DOI: `10.1017/jfm.2018.955`.

Voulgaris, G. and J. H. Trowbridge (1998). “Evaluation of the Acoustic Doppler Velocimeter (ADV) for Turbulence Measurements”. In: *Journal of Atmospheric and Oceanic Technology* 15.1, pp. 272–289. ISSN: 0739-0572. DOI: `10.1175/1520-0426(1998)015<0272:EOTADV>2.0.CO;2`.

Wang, Xueming, Abdolmajid Mohammadian, and Colin D. Rennie (2022a). “Influence of Negatively Buoyant Jets on a Strongly Curved Open-Channel Flow Using RANS Models with Experimental Data”. In: *Water (Switzerland)* 14.3. ISSN: 20734441. DOI: `10.3390/w14030347`.

Wang, Xueming, Colin D. Rennie, and Abdolmajid Mohammadian (2022b). “Experimental Studies on the Influence of Negatively Buoyant Jets on Flow Distribution in a 135-Degree Open Channel Bend”. In: *Water (Switzerland)* 14.12. ISSN: 20734441. DOI: `10.3390/w14121898`.

Wei, Miao, K. Blanckaert, Joris Heyman, Danxun Li, and Anton J. Schleiss (2016). “A parametrical study on secondary flow in sharp open-channel bends: Experiments and theoretical modelling”. In: *Journal of Hydro-Environment Research* 13, pp. 1–13. ISSN: 15706443. DOI: `10.1016/j.jher.2016.04.001`.

Weisstein, E. W. (accessed July 2017). *Levenberg-Marquardt Method*. URL: `http://mathworld.wolfram.com/Levenberg-MarquardtMethod.html`.

Wit, Lynyrd de, Cees van Rhee, and Geert Keetels (2014). “Turbulent Interaction of a Buoyant Jet with Cross-Flow”. In: *Journal of Hydraulic Engineering* 140.12, p. 04014060. ISSN: 0733-9429. DOI: `10.1061/(ASCE)HY.1943-7900.0000935`.

Wu, Zhao, Dominique Laurence, Sergey Utyuzhnikov, and Imran Afgan (2019). “Proper orthogonal decomposition and dynamic mode decomposition of jet in channel crossflow”. In: *Nuclear Engineering and Design* 344.October 2018, pp. 54–68. ISSN: 00295493. DOI: `10.1016/j.nucengdes.2019.01.015`.

Yalin, M. Selim (Mehmet Selim) (1971). *Theory of hydraulic models*. eng. Macmillan civil engineering hydraulics. London: Macmillan. ISBN: 0333035577.

Yang, Yang et al. (2022). “An efficient DBSCAN optimized by arithmetic optimization algorithm with opposition-based learning”. In: *Journal of Supercomputing* 78.18, pp. 19566–19604. ISSN: 15730484. DOI: `10.1007/s11227-022-04634-w`.

Yoshizawa, Akira (1986). “Statistical theory for compressible turbulent shear flows, with the application to subgrid modeling”. In: *Physics of Fluids* 29.7. DOI: `10.1063/1.865552`.

Yotsukura, Nobuhiro and William W. Sayre (1976). “Transverse mixing in natural channels”. In: *Water Resources Research* 12.4, pp. 695–704. ISSN: 19447973. DOI: `10.1029/WR012i004p00695`.

Yuan, Junjie, Zhihao Weng, and Yanguang Shan (2021). “Modelling of double bubbles coalescence behavior on different wettability walls using LBM method”. In: *International Journal of Thermal Sciences* 168.November 2020, p. 107037. ISSN: 12900729. DOI: `10.1016/j.ijthermalsci.2021.107037`.

Yuan, Lester L. and Robert L. Street (1998). “Trajectory and entrainment of a round jet in crossflow”. In: *Physics of Fluids* 10.9, pp. 2323–2335. ISSN: 1070-6631. DOI: `10.1063/1.869751`.

Zadeh, L.a. (1965). “Fuzzy sets”. In: *Information and Control* 8.3, pp. 338–353. ISSN: 00199958. DOI: `10.1016/S0019-9958(65)90241-X`.

Zahiri, Javad and Hosein Nezaratian (2020). “Estimation of transverse mixing coefficient in streams using M5, MARS, GA, and PSO approaches”. In: *Environmental Science and Pollution Research*. ISSN: 16147499. DOI: `10.1007/s11356-020-07802-8`.

Zeng, Jie, George Constantinescu, Koen Blanckaert, and Lany Weber (2008). “Flow and bathymetry in sharp open-channel bends: Experiments and predictions”. In: *Water Resources Research* 44.9. ISSN: 00431397. DOI: `10.1029/2007WR006303`.

Zhang, Liwei and Vigor Yang (2017). “Flow Dynamics and Mixing of a Transverse Jet in Crossflow Part I: Steady Crossflow”. In: *Journal of Engineering for Gas Turbines and Power* 139 (August). ISSN: 0742-4795. DOI: `10.1115/1.4035808`.

Zhang, Wenming and David Z. Zhu (2011). “Transverse Mixing in an Unregulated Northern River”. In: *Journal of Hydraulic Engineering* 137.NOVEMBER, pp. 1426–1440. ISSN: 0733-9429. DOI: `10.1061/(ASCE)HY.1943-7900.0000453`.

Zheng, Jingxu and Shide Mao (2019). “A thermodynamic model for the solubility of N2, O2 and Ar in pure water and aqueous electrolyte solutions and its applications”. In: *Applied Geochemistry* 107.January, pp. 58–79. ISSN: 18729134. DOI: `10.1016/j.apgeochem.2019.05.012`.